Dissertation

submitted to the

Combined Faculty of Natural Sciences and Mathematics

of Heidelberg University, Germany

for the degree of

Doctor of Natural Sciences

Put forward by
Therese Weißbach
born in: Karl - Marx - Stadt now Chemnitz

Oral examination: 17.06.2020

Spectroscopic isotope ratio analysis on speleothem fluid inclusions - analytics and paleoclimatic case studies

Referees:

Dr. Tobias Kluge
Prof. Dr. Norbert Frank

Zusammenfassung In dieser Arbeit wurde die Rekonstruktion von klimatischen Bedingungen und Paläotemperaturen mittels der Analyse von Sauerstoff (δ^{18}O) und Wasserstoff (δ^{2}H) aus Flüssigkeitseinschlüssen von Speläothemen für zwei unterschiedliche klimatische Zonen (gemäßigte Breiten und Tropen) untersucht. Zu diesem Zweck wurde ein Fluidextraktions- und Messsystem aufgebaut, welches Cavity Ring-Down Spektroskopie zur Messung verwendet. Ich konnte Memory- und Mengeneffekte ausschließen und eine Genauigkeit von 0.5 ‰ für δ^{18}O und 1.5 ‰ für δ^{2}H bei wiederholten Messungen mit Wasservolumen $> 0.2\,\mu$l erreichen. Die Analyse stabiler Wasserisotope erlaubt die Bestimmung von Paläotemperaturen mit dem klassischen Karbonat Thermometer, sowie mit der Anwendung der δ^{2}H/T-Beziehung mit einer Genauigkeit von bis zu $\pm\,0.45\,$°C. Für den westlichen tropischen Atlantik konnte ich eine Abkühlung von $\sim 3\,$°C während der Heinrich Stadiale (2 und 3) ermitteln. Über die direkte Temperaturbestimmung hinaus, liefert die Analyse von Fluideinschlüssen Informationen über die Verfügbarkeit von Karstwasser während der Stalagmitenbildung. Die δ^{18}O und δ^{2}H Werte von zwei Speläothemenen aus Deutschland und Puerto Rico zeigen z.B. Steigungen von $+2.3 \pm 1.1$ bzw. $+3.7 \pm 0.2$, welche signifikant niedriger sind als die von typischen meteorischen Wasserlinien (Steigung ~ 8). Damit zeigt sich ein klares Verdunstungssignal in der stabilen Isotopenzusammensetzung der Flüssigkeitseinschlüsse, welches wahrscheinlich auf Verdunstungseffekte in der Höhle oder dem Epikarst hindeutet. Ich konnte zeigen, dass unter trockeneren Klimabedingungen die beobachteten Verdunstungssignale verstärkt auftreten.

Abstract In this thesis the reconstruction of climatic conditions and paleotemperatures by the analysis of oxygen (δ^{18}O) and hydrogen (δ^{2}H) isotopes of fluid inclusions in speleothems from two different climatic zones (mid-latitudes and tropics) was performed. An extraction and processing system for fluid inclusion analysis with laser spectroscopy was developed and characterized with respect to the memory or amount effect. I could exclude disturbance effects and achieve a precision of 0.5 ‰ for δ^{18}O and 1.5 ‰ for δ^{2}H in replicated measurements with water volumes $> 0.2\,\mu$l. The analysis of stable water isotopes allows the determination of paleotemperatures using the classic carbonate thermometer as well as the application of the δ^{2}H/T-relationship with a precision down to $\pm\,0.45\,$°C. For the western tropical Atlantic I identified a cooling during the Heinrich stadials (2 and 3) of $\sim 3\,$°C applying the classic carbonate oxygen isotope thermometer. Beyond direct temperature determination, the analysis of fluid inclusions provides information about karst water availability during stalagmite formation. For instance, the δ^{18}O and δ^{2}H values of two speleothems from Germany and Puerto Rico, show slopes of $+2.3 \pm 1.1$ and $+3.7 \pm 0.2$, respectively, that are significantly lower compared to meteoric water lines (slope of ~ 8). This clear evaporation signal in the related fluid inclusions probably indicates evaporation effects (cave or epikarst), which are enhanced during drier climate conditions.

Contents

1 Introduction

1.1 Motivation

One central element of climate change is the impact on the Earth's hydrological cycle. The prediction of water availability is highly uncertain, but at the same time the water demand continues to rise, leading to an increase in water stress[1] worldwide (see figure 1.1). Changes in average precipitation are much more difficult for climate models to predict than temperature. While the projection of temperature changes and global warming is generally predicted with a *high* degree of confidence using climate models, the forecast of precipitation changes can only be determined with *medium* certainty [*IPCC*, 2013]. It is certain that as the temperature rises the water-holding capacity of the air increases, according to the Clausius-Clapeyron equation with generally 7 % more water vapour in the atmosphere for every 1°C of temperature rise [*Oltmans and Hofmann*, 1995]. However, corresponding precipitation is not evenly distributed across

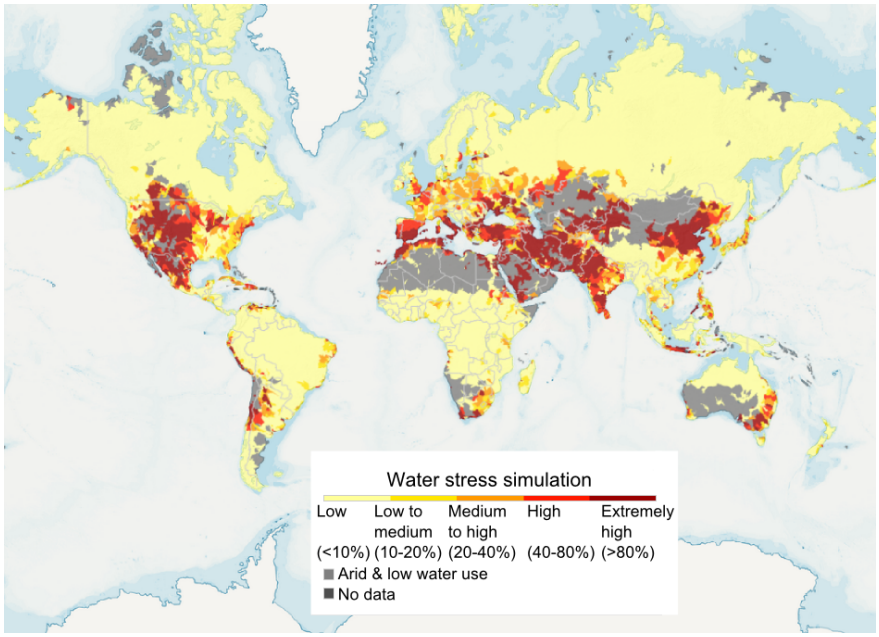

Figure 1.1: Aqueduct - Water Risk Atlas with the predicted water stress simulation according to the business as usual scenario for 2040 [*WRI*, accessed March 19, 2020].

[1] Groundwater stress measures the ratio of total water withdrawals to the available renewable surface and groundwater resources. In this context, water abstraction is defined as the use of water by agriculture, livestock, households and industry. For the available renewable water resources, the impact of dams or industry consuming water must be taken into account [*WRI*, accessed March 19, 2020].

the planet. Some regions will likely experience an increase in extreme precipitation, while in other, already arid regions, droughts will be more pronounced both spatially and temporally [*IPCC*, 2013]. In order to assess future changes in the climate system, it is important to integrate palaeo-data into the model-based projections and thus contribute to the improvement of climate models. Thus, the key to predicting future changes in precipitation is a well-founded knowledge and understanding of paleo-rainfall variations in the past.

A well understood archive, which preserves information on rainfall is needed for the reconstruction of paleo-precipitation. This work focusses on speleothems, which represent a potential high-resolution and continuous terrestrial archive besides tree rings, lake sediments and pollen records. Stalagmites are the perfect archive for this task, as they contain water-filled (*fluid*) inclusions, which are potentially unchanged aliquots of the original drip water that was enclosed during the period of calcite growth and consequently relics of past precipitation [*Schwarcz et al.*, 1976; *Van Breukelen et al.*, 2008]. Therefore, they represent a direct record for paleo-precipitation that can be found worldwide in regions with karstified carbonate bedrock (see figure 1.2) [*Fairchild and Baker*, 2012]. Speleothems allow climatic reconstructions in the same time range as ice cores, but are not restricted to polar regions, since they are formed under a variety of hydroclimatic conditions, from extremely cold climates to very dry regions as long as liquid water is available. The decay of uranium into a series of daughter isotopes is one

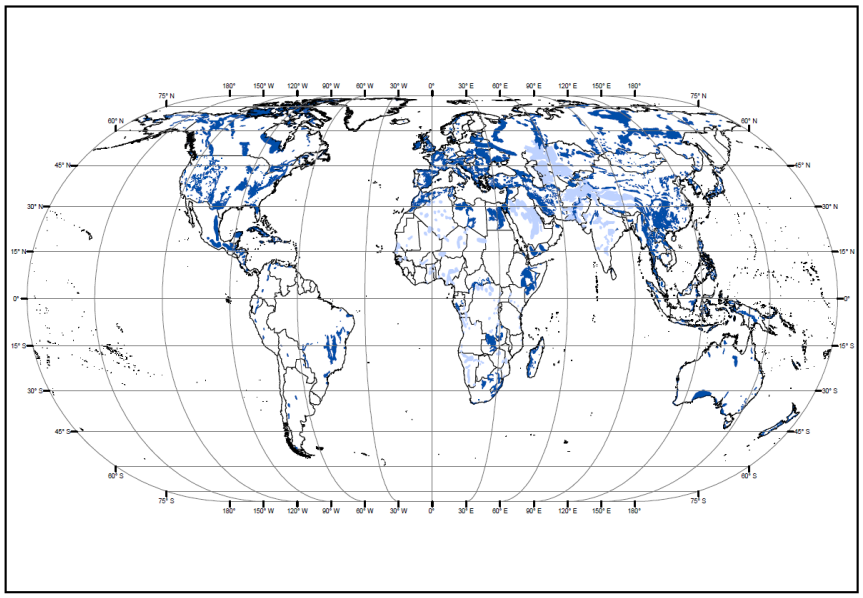

Figure 1.2: Global distribution of carbonate rocks. In karstified areas (blue) caves could potentially form and thus also speleothems could be found [*The University of Auckland*, accessed March 20, 2020].

of the main chronometers of palaeoclimatology. The principle of $^{230}Th/^{234}U$ dating is based on the observation that the ^{238}U decay series in a speleothem sample return from an initial state of imbalance to a secular equilibrium, which can be expressed as a function of time using the decay constants of the radioactive isotopes [*Richards and Dorale*, 2003]. As the $^{230}Th/^{234}U$ ratio will change over time after the growth layer has been deposit because the speleothem contains some uranium (^{234}U decays via alpha decay to ^{230}Th) from aqueous solution during growth, but not the insoluble element thorium [*Fairchild and Baker*, 2012]. Due to the high precision of uranium-series dating, speleothems can be dated back up to 600 000 years and offer the possibility to retrieve information about climate change and the timing of regional hydrological responses to global events [*Genty et al.*, 2002; *Lachniet et al.*, 2009; *Van Breukelen et al.*, 2008]. Using the multi-proxy approach, which combines the analysis of highly resolved carbon ($\delta^{13}C_{calcite}$) and oxygen ($\delta^{18}O_{calcite}$) isotope data from speleothem calcite with the additional analysis of various trace elements, climatic changes of the past can be reconstructed [*Fairchild et al.*, 2000; *McDermott*, 2004; *Dreybrodt and Scholz*, 2011]. By means of isotope analysis of the fluid inclusions, not only the $\delta^{18}O_{fluid}$ value of the paleo-drip water but also its $\delta^{2}H_{fluid}$ composition can be reconstructed. This in turn provides information about the origin of the water masses (using the deuterium excess) and can help to better classify changes in the isotopic composition of the drip water (possible evaporation) [*Gat et al.*, 1994; *Pfahl and Sodemann*, 2014]. If the formation conditions of the carbonate precipitation are known, i.e. whether the mineral was formed under equilibrium conditions, paleotemperatures can be reconstructed by simultaneous measurement of the oxygen isotopes in the calcite and in the fluid inclusions [*Kim and O'Neil*, 1997; *Tremaine et al.*, 2011].

1.2 Outline of this thesis

This thesis focuses on tow main aspects, (i) to design, construct and calibrate the *fluid inclusion line*, which uses absorption spectroscopy to measure the water stable isotopes of fluid inclusions and (ii) to apply this new technique in different case studies. For the first objective an extraction line was developed and further improved, which is based on the principle of *Affolter et al.* [2014] and produces a continuous vapour water background on which the aliquot of water released from the crushed speleothem is measured. This setup allows the simultaneous measurement of $\delta^{18}O_{fluid}$ and $\delta^{2}H_{fluid}$ isotopes by means of cavity ring-down spectroscopy, which has a comparable precision to traditional mass spectrometry, but is much less expensive. In chapter 3, the setup of the line, the calibration using independently measured in-house standards and the newly developed water amount calibration method with glass capillaries is described. This also includes an advanced evaluation software for the measurement of the stable isotopes, which takes into account the unavoidable variation of the water vapour background (see section 3.4). Furthermore, the influence of possible disturbance effects on

the actual measurement of the isotopic signal in fluid inclusions of speleothems was investigated, which include absorption on freshly crushed calcite surfaces and the amount or memory effect (see section 3.7). Inter - laboratory comparison measurements were performed to test and verify the accuracy and reliability of the stable isotope analysis.

For the second objective this new technique was applied to three climatological different speleothem case studies: (i) Stam 4 from the Cloşani Cave (Romania), (ii) Bu4 from Bunker Cave (Germany), (iii) LA-1 from Cueva Larga (Puerto Rico) and comprises the second part of this thesis. The climate of central Europe is affected for example by the variability of the North Atlantic Oscillation (NAO) [*Hurrell*, 1995; *Wanner et al.*, 2001], whereas the precipitation for tropical regions mainly depends on the position of the Intertropical Convergence Zone (ITCZ) [*Lachniet et al.*, 2009; *Stríkis et al.*, 2011].

The selected stalagmites cover three very different time scales, from decadal variations to multicentury and millennial timescale. Since 1979, Europe sees a more pronounced warming trend [*Böhm et al.*, 2010]. Therefore, I selected the fast growing stalagmite Stam 4 from Cloşani Cave (Romania), which covers the 20th century between 1911 - 2010 to test if the application of the δ^2H/T relationship on stable isotope measurements of fluid inclusions is feasible for temperature reconstructions. I can directly compare my findings with local mean annual air temperature records and check if this method provides reliable temperatures for the temperature increase for parts of the late Holocene (1911 - 2008) (see chapter 4). The second stalagmite, from a continental climatic environment, was collected from the Bunker Cave (Germany) and covers parts of the Holocene (present - 8.6 ka BP), whose climatic variability of winter precipitation may be stored in the fluid inclusions. The stalagmite Bu4 has already been intensively investigated and it has been shown that drier and more humid periods can be identified in the stable isotopes of the carbonate [*Fohlmeister et al.*, 2012]. In this study, I analysed to what extent the stable isotopes of the fluid inclusions and their abundance can be used to predict changing precipitation conditions (see chapter 5). As a final case study I have chosen a tropical stalagmite covering parts of the Last Glacial. The stable isotope analysis of the stalagmite (LA-1) carbonate suggests rapid climatic fluctuations on Puerto Rico from cold (stadial) to warmer (interstadial) conditions and strong variations in precipitation. Since it is still unclear how pronounced this climatic variations were in the tropics, the water stable isotope signal stored in the fluid inclusions was applied to reconstruct precipitation changes (drier or wetter periods) and determine the strength of the possible cooling trend during Heinrich events (see chapter 6).

2 | Theoretical background

This chapter focuses on the processes, which influence the composition of stable isotopes (δ^{18}O and δ^{2}H) in precipitation and accordingly in drip water, which is the signal that is stored in fluid inclusions of speleothems. The summary given here is mainly based on the work of *Clark and Fritz* [1997] and *Mook and Rozanski* [2000]. Furthermore, it discusses the formation and growth of stalagmites and how fluid inclusions are formed, using the work of *McDermott* [2004], *Lachniet* [2009] and *Fairchild and Baker* [2012] as a basis. Most classic studies on speleothems focus on the stable isotopes of calcite (δ^{18}O and δ^{13}C) and trace elements to reconstruct climatic conditions and variations during speleothem growth *Fairchild and Baker* [2012]. This thesis, however, aims on the fractionation between carbonate and water as an application of the paleo - thermometer. The versatility of the interpretation of the stable water isotopes is demonstrated by three very different case studies, each representing an unique speleothem record influenced by different climatic backgrounds on different time scales. In addition, the focus of this work is on the methodology and measurement techniques of stable water isotopes by means of laser absorption spectroscopy, more precisely cavity ring - down spectroscopy (CRDS). Here a short overview of the basics of technology and the current state of research is given.

2.1 Stable isotopes

Isotopes are elements that contain the same number of electrons and protons, but differ in the number of neutrons. This leads to a difference in mass which causes different physical properties, the so - called *isotope effect*, and makes it possible to use isotopes as tracers of environmental processes. They can be categorized in stable and radioactive isotopes. While radioactive isotopes are mainly used for dating as their concentration diminishes with time, the composition of stable isotopes provides information about the fractionation conditions during proxy formation.

2.1.1 Isotope notation

For water there are two stable isotopes for hydrogen (^{1}H and ^{2}H) and three stable isotopes for oxygen (^{16}O, ^{17}O and ^{18}O). The isotope ^{2}H is called Deuterium and often given the symbol D. For light elements one isotope is generally predominant, while the others are only found in trace amounts [*Hoefs*, 2009]. In case of water molecules, the two isotopes that are most abundant are ^{1}H and ^{16}O and the three rare stable isotopes are ^{2}H, ^{17}O and ^{18}O (natural abundance see table 2.1).

hydrogen		oxygen	
isotope	mole fraction	isotope	mole fraction
^{1}H	0.99985	^{16}O	0.99757
^{2}H	0.00015	^{17}O	0.00038
		^{18}O	0.00205

Table 2.1: Average terrestrial abundance of the stable isotopes of hydrogen and oxygen [*Coplen et al.*, 2000].

When these isotopes form molecules, the compounds are called isotopologues. Numerous species can exist with the most common isotopologues in decreasing abundance: $^{1}H^{1}H^{16}O$, $^{1}H^{1}H^{18}O$ and $^{1}H^{2}H^{16}O$ [*Mook and Rozanski*, 2000]. Isotopic concentrations or abundance ratios are often very small and, therefore, not given in absolute values, but related to those of a specially selected standard in the form of deviations, the so-called $\delta - notation$. Thus, for the oxygen isotopic composition of a sample, it gives [*Clark and Fritz*, 1997]:

$$\delta^{18}O\,(\text{in }‰) = \left(\frac{\left(\frac{^{18}O}{^{16}O}\right)_{sample}}{\left(\frac{^{18}O}{^{16}O}\right)_{standard}} - 1 \right) \cdot 1000 \tag{2.1}$$

The abundance of stable isotopes is generally expressed in ‰ (per mil) and defines the relative deviation from an internationally accepted standard, which is Vienna Standard Mean Ocean Water (VSMOW) for the hydrogen and oxygen isotope ratios of water [*Coplen*, 1994]. In the calcite system the internationally accepted standard is Vienna PeeDee Belemnite (VPDB) [*Coplen*, 1994]. Thereby, the relationship for the δ^{18}O value of a sample between the VSMOW and VPDB scales can be expressed as [*Kim et al.*, 2015]:

$$\delta^{18}O_{\text{VSMOW}} = 1.03092 \cdot \delta^{18}O_{\text{VPDB}} + 30.92\ (‰) \tag{2.2}$$

2.1.2 Isotope fractionation

Isotopes have the same number of electrons, but can be distinguished by their physicochemical properties due to their different mass. The difference in mass leads to two properties in which the isotopes differ from one another:

- Physicochemical fractionation: Different bond strengths for reaction compounds varying only by the isotopes of the same element have an effect on the corresponding reaction rates. The heavier the isotope, the lower the zero-point energy (with few exceptions for specific isotopologues[1]), which represents the

[1] For carbon dioxide (CO_2) the lighter isotopologue $^{13}C^{16}O^{16}O$ (atomic mass constant u = 45) has a lower zero-point energy than the heavier isotopologue $^{12}C^{18}O^{16}O$ (atomic mass constant u = 46) [*Prokhorov et al.*, 2019].

minimum potential energy of a molecular bond in a vibrating molecule. This difference in binding energies implies that heavier isotopes are statistically more likely to remain in the bound state than lighter isotopes [*Mook and Rozanski*, 2000]. For the stable water isotopologues this implies that the lighter isotopologues evaporate more easily and the heavier ones are more likely to remain in the liquid phase.

- Diffusive fractionation: Fractionation arises from the different diffusive velocities between isotopes [*Mook and Rozanski*, 2000]. Thereby lighter and therefore faster molecules have a higher diffusion velocity and a higher frequency to collide with other molecules, which can be one of the drivers for chemical reactions.

The isotope separation during phase transitions is much stronger for lighter elements, such as hydrogen, where the difference in mass between two isotopes relative to the mass of the element is larger. However, all these isotope effects decrease with increasing temperature, as the energy of the vibrating molecules becomes independent of mass and binding energy [*Mook and Rozanski*, 2000].

Isotope fractionation leads to a partial separation of isotopic species during physical or chemical processes, which results in a disproportional concentration of one isotope over the other on one side of the reaction [*Clark and Fritz*, 1997]. The fractionation factor α describes the fractionation from state A to state B:

$$\alpha_{B/A} = \frac{R_B}{R_A} \tag{2.3}$$

where R is the isotope ratio of the rare isotope over the abundant isotopes. Since isotope effects are small and resulting in $\alpha \approx 1$, the fractionation is referred to as deviation of α from 1 [*Mook and Rozanski*, 2000], called ϵ:

$$\epsilon = \alpha_{B/A} - 1 = \frac{R_B}{R_A} - 1 \tag{2.4}$$

here $\epsilon > 0$ refers to an enrichment and $\epsilon < 0$ to a depletion of the rare isotope. The fractionation of the isotopes can take place under equilibrium conditions, under non-equilibrium conditions (kinetic) or under disequilibrium conditions, which are explained below [*Clark and Fritz*, 1997]:

- Equilibrium fractionation: Fractionation is generally regarded as equilibrium fractionation when A and B are in chemical equilibrium. The reaction between A and B is completely reversible, and the effective mass transport is identical in both directions. Equilibrium conditions exist in a closed system, for example for water and water vapour in a closed volume, with the lighter isotope enriched in the vapour phase. Here the equilibrium fractionation factor α is temperature dependent, which is an important property for paleoclimatic studies with stable isotopes.

- Kinetic fractionation: Kinetic fractionation is associated with incomplete and unidirectional processes, which can be caused by a sudden change in temperature or the additional removal of the reactant. This means that the reaction from A to B is irreversible, the effective mass transport is permanent from A to B and the mass is immediately removed from the system. In a purely kinetic process no mass transport from B to A can take place. An example is the freezing of water under a varying temperature.

- Disequilibrium fraction: This fraction is similar to kinetic fractionation, but mass transfer between A and B can occur in both directions, with one direction dominating. An example is the evaporation of water in an open volume. Even under evaporative conditions it is almost impossible to prevent a flux into the water reservoir.

2.1.3 Oxygen and hydrogen in the hydrological cycle

Isotopic fractionation of water molecules occurs during different processes in the hydrological cycle. The isotopic composition of the precipitation depends on relevant meteorological parameters and thus serves as an important tool in palaeoclimatology. It was found that in general there is a strong correlation between the temperature of surface air and the stable isotope ratios of oxygen or hydrogen in precipitation at locations for mid and high latitudes [*Dansgaard*, 1964; *Rozanski et al.*, 1992]. However, the isotopic composition of precipitation is not always only temperature dependent, but also the product of significant changes in atmospheric circulation patterns [*Sonntag et al.*, 1979; *Leng*, 2006]. These different factors, which have an influence on the δ^{18}O and δ^{2}H composition of the precipitation, are discussed in the following.

Isotopic composition of precipitation

Different processes influence and control the isotopic compositions of atmospheric water vapour and precipitation in the troposphere (see figure 2.1). When water evaporates from the ocean surface, it becomes depleted in ^{2}H and ^{18}O because isotopically lighter isotopologues (e.g. $^{1}H^{1}H^{16}O$) evaporate more easily than the heavier ones [*Craig and Gordon*, 1965]. The overall isotopic composition of ocean water can significant vary between -7 up to $+2\,‰$ for δ^{18}O, for example, due to local evaporation in tropical latitudes or in zones with freshwater discharge [*Rohling*, 2013]. Thereby the isotopic composition of the vapour is determined by the isotopic composition of the ocean surface, sea - surface temperature, relative humidity of the atmosphere and wind regime [*Leng*, 2006]. After evaporation, the water vapour is transported both vertically and horizontally until saturation conditions are reached and cloud formation begins. During the vertical transport, the isotopic composition of the water vapour in the cloud can be modified, e.g. by mixing with additional and isotopically different water vapour. When the rising vapour reaches the dew point, it condenses, which can be achieved by an orographic upward movement or a frontal cooling. During the movement of an

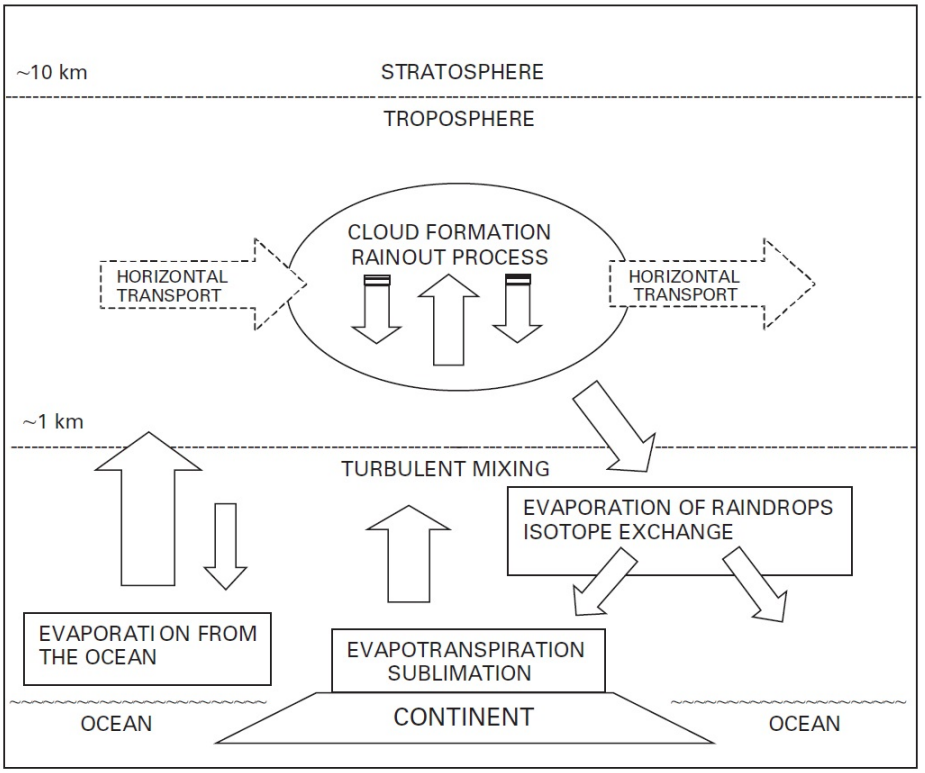

Figure 2.1: Effects controlling the isotopic composition of atmospheric water vapour and precipitation [*Leng*, 2006].

air parcel towards the poles, the residual water vapour becomes progressively lighter with each successive precipitation event, and consequently the precipitation of the residual vapour becomes lighter, which is the so-called *rainout effect* (see figure A.1). The isotopic composition of rainfall collected at the ground is close to isotopic equilibrium, because raindrops leaving the cloud continuously re-equilibrate isotopically with surrounding moisture during falling [*Leng*, 2006]. So the progressive condensation of water vapour on a global scale can be represented as a continuous *Rayleigh distillation* process (see figure A.3), because the process of rainout *distils* the heavy isotopes from the vapour [*Gat*, 1996]. *Dansgaard* [1964] described a number of empirical relationships between observed isotopic composition of monthly precipitation and environmental parameters (temperature, latitude and altitude) using the *Rayleigh model*[2]. However, the isotopic composition of the annual precipitation at any point

[2]The isotope fractionation process can be described using the Rayleigh equation, which is a exponential relation that describes the stable isotopic evolution of a homogeneous reservoir from which a phase is continuously extracted [*Rayleigh*, 1896]. The state in a closed system undergoing isotopic fractionation can be described as: $R = R_0 \cdot f^{\alpha-1}$, where R_0 is the initial isotope ratio, R is the product of the reaction process, α is the fractionation factor and f is the fraction of the reaming substrate.

on the Earth's surface is not only determined by the continuous rainout towards the poles, but also depends on many other effects, which are explained in detail below.

On a global scale, a differentiation can be made between the temperature, latitude and continental effects, and on a local scale between the altitude, seasonal and amount effects.
The *temperature effect* is the observed positive correlation between the isotopic composition of precipitation and the local air temperature (with an annual mean for mid to high latitudes of $d\delta^{18}O/dT = 0.69\,‰/T$) [*Dansgaard*, 1964]. In fact, it is the temperature in the cloud that controls the condensation and thus the isotopic fractionation. Under typical atmospheric conditions, the saturation water vapour pressure in the cloud depends exponentially on the temperature (Clausius – Clapeyron relation). More precisely, there is a temperature dependent isotope exchange between condensate and water vapour at the cloud base [*Gat*, 1996]. The cloud base temperature is closely related to the surface temperature and falling raindrops equilibrate with the surrounding water vapour, whereby the degree of isotopic re-equilibration depends on raindrop size, relative humidity and cloud height [*Leng*, 2006]. However, the $\delta^{18}O$-T relationship is only an approximation and strongly variable, depending on the location with gradients between $0.17\,‰/T$ for marine stations up to $0.90\,‰/T$ for the Antarctica peninsula [*Rozanski et al.*, 1992; *Mook and Rozanski*, 2000].
The *latitude effect* is strongly related to the $\delta^{18}O$-T relationship, hence more depleted isotope values are expected for precipitation at higher latitudes (for $\delta^{18}O$ $-0.6\,‰$ per degree of latitude). For polar regions, this is due to the low temperatures and the fact that they are at the end of the *Rayleigh rainout* effect resulting in a steeper $\delta^{18}O/T$ gradient (of about $-2\,‰$ per degree of latitude). For the tropics, the recycling of moisture due to evapotranspiration in tropical forest can vary these gradients [*Salati et al.*, 1979].
The *continental effect* describes the decrease of $\delta^{18}O$ and $\delta^{2}H$ values in precipitation with distance from the ocean [*Dansgaard*, 1964; *Clark and Fritz*, 1997]. As an air mass moves across a continent, the land mass causes a progressive cooling and rainout of the air mass. The isotope signal of precipitation can be influenced by recycling of water over continents by evapotranspiration, the so-called continental recycling [*Koster et al.*, 1993; *Bowen et al.*, 2019]. In the tropics, moisture recycling is a dominant effect and leads to a lower slope of the $\delta^{18}O$/distance gradient along the advection path. Plants may also lead to a re-introduction of moisture into the atmosphere, but no isotopic fractionation occurs. However, increased d-values (deuterium excess) of precipitation indicate evaporation of a terrestrial moisture source [*Salati et al.*, 1979; *Gat and Matsui*, 1991].
The *amount effect* is relevant for coastal areas and islands in tropical regions, where a seasonal variation of temperature is minimal and deep vertical convection is common. It is associated with strongly depleted $\delta^{18}O$ and $\delta^{2}H$ values for increased rainfall amounts [*Dansgaard*, 1964]. The more it rains, the more the remaining water vapour is depleted of heavy isotopes, and precipitation becomes isotopically lighter. However,

the exact physical context for these observations remains unclear and various theoretical approaches, such as cloud height or precipitation types, are currently under investigation to explain the amount effect in detail. In more arid regions, the *amount effect* refers to a negative correlation between local monthly precipitation amounts and precipitation isotope ratios. The evaporation during rainfall leads to isotopic values, which are shifted away from the GMWL towards meteoric water lines with an evaporation slope less than 8 [*Clark and Fritz*, 1997].
The *altitude effect* is associated with an increased depletion for the heavier isotopes of precipitation with altitude, since any kind of relief forces the air mass to rise [*Clark and Fritz*, 1997]. Decreasing temperatures with increasing altitude in mountainous regions usually lead to increased condensation, as the vapour air mass expands during rising due to adiabatic cooling and thus causes rainout [*Siegenthaler and Oeschger*, 1980]. The progressive Rayleigh distillation produces orographic precipitation. All these effects influence the isotopic composition of the precipitation and thus produce a unique fingerprint of rainfall on a global scale (see figure A.2).

Global meteoric water line (GMWL) and deuterium excess

Considering the different effects on the isotopic composition of the precipitation, it is notable that a global correlation between δ^{18}O and δ^{2}H values was found in fresh water. *Craig* [1961] and *Dansgaard* [1964] stated the relation

$$\delta^2 H \approx 8 \cdot \delta^{18} O + 10‰ \tag{2.5}$$

which is named the *Global Meteoric Water Line* (GMWL), where the term *meteoric* refers to *meteorological* and has nothing to do with fiery objects from space [*Clark and Fritz*, 1997]. Both, oxygen and hydrogen are influenced by the same isotopic effects and are linearly correlated with a slope of ~ 8, which results from the ratio of the equilibrium fractionation factors for ^{2}H and ^{18}O. If the water evaporates at a relative humidity below saturation, condensation no longer takes place under equilibrium conditions, resulting in slopes of less than 8 [*Gat*, 1996]. The evaporation of water leads to an enrichment of heavier isotopes in the residual water (evaporative loss see figure 2.2), which in turn depends on the humidity of the ambient air and can reach a slope of about 4 under very dry conditions (relative humidity $h = 0.25$) [*Gat*, 1971]. The isotopic composition of δ^{18}O and δ^{2}H in precipitation is generally predictable at the global scale, with water containing highly depleted δ^{18}O and δ^{2}H values associated with colder regions and vice versa (see figure 2.2). This key observation of *Craig* [1961] is the basis of many palaeoclimatology studies. *Rozanski et al.* [1993] observed significant deviations from this global relationship at the local scale, which is mainly explained by variable climatic conditions and geographical parameters, resulting in specific local *MWL*.

A proxy suitable to describe the hydrological cycle of moisture is the deuterium excess, which is defined as $d = \delta^2 H - 8 \cdot \delta^{18} O$ [*Dansgaard*, 1964]. The deuterium excess is a consequence of the slower movement of the ${}^1H^1H^{18}O$ ($H_2^{18}O$) molecule during diffusion, which leads to a relative enrichment of the ${}^1H^2H^{16}O$ (HDO) molecule in the water vapour. During evaporation, non-equilibrium fractionation is intrinsically dominant since the diffusive transport into the free atmosphere above is caused by a strong gradient of relative humidity above the water surface and by winds that transport the evaporate away from the water surface [*Pfahl and Sodemann*, 2014]. The global average deuterium excess in precipitation is 10 ‰ [*Craig*, 1961], reflecting the fact that the ocean is generally out of equilibrium with the atmosphere and the mean relative humidity of air at the evaporating ocean surface is $< 100\,\%$. The value of deuterium excess (d-value) is a proxy for the physical conditions at the oceanic moisture source, mainly relative humidity (h_s) and sea surface temperature (SST). If the evaporation of the ocean is the only moisture source for the atmospheric boundary layer, then d in the evaporation flux increases with decreasing h_s and increasing SST [*Merlivat and Jouzel*, 1979]. It is even possible to see well defined climatic changes with deuterium profiles from Greenland and Antarctic ice cores, if the deuterium signature of the evaporation conditions is preserved at least partially along the trajectory of the

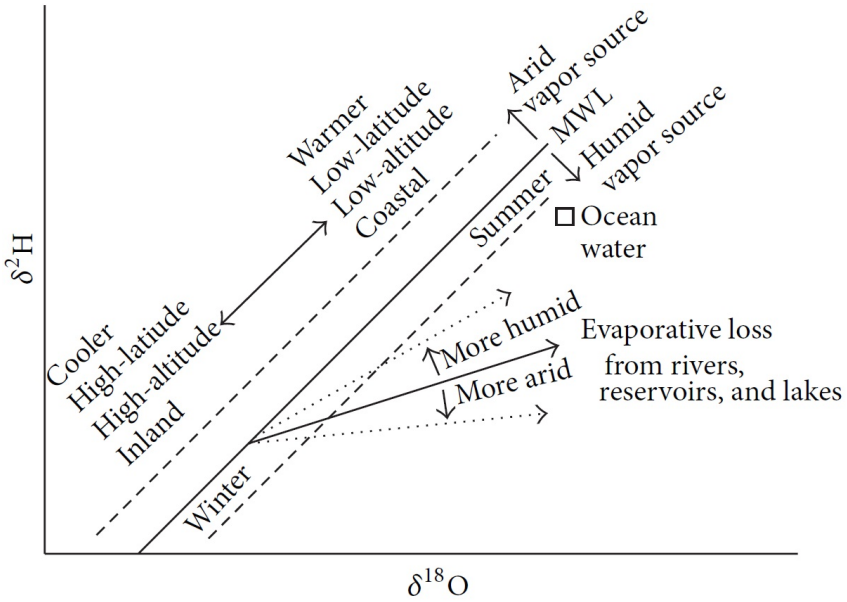

Figure 2.2: Schematic plot of δ^{18}O versus δ^2H showing the different effects which can influence the *Global Meteoric Water Line*. Precipitation from colder regions and higher latitudes is more likely to have a lower isotopic composition than precipitation from warmer regions. The slope of the *MWL* can be influenced by evaporation and is characteristic for local climatic conditions. The deuterium excess in precipitation increases in response to enhanced moisture recycling, whereas the deuterium excess is reduced when water is lost through enhanced evaporation [*Froehlich et al.*, 2002].

advected vapour until precipitation [*Jouzel et al.*, 2007]. There are other processes that influence the deuterium excess in precipitation, such as the re-evaporation of falling raindrops and moisture exchange with the ambient air in the subcloud layer, which leads to lower d-values [*Guan et al.*, 2013]. Also the type of weather system producing precipitation can vary the d-values, because the moisture source area is very different for frontal or cyclonic precipitation than for purely convective or orographic precipitation [*Aemisegger et al.*, 2014; *Scholl and Murphy*, 2014]. In tropical regions, deuterium excess may also be an indicator of continental moisture recycling, which is a well-known phenomenon for the Amazon basin, where large amounts of recycled moisture contribute to the air masses transported by the trade winds [*Salati et al.*, 1979; *Gat and Matsui*, 1991; *Risi et al.*, 2013]. In this context, increased deuterium values during the dry season indicate an additional contribution to local precipitation due to the evapotranspiration of the forest [*Ampuero et al.*, 2020].

2.2 Speleothems as paleoclimatic archive

Speleothems are formed by precipitation of carbonate-saturated seepage water originating from meteoric water. They provide continental archives in caves where the climate signal can be conserved very well, as they are protected by their location from erosion by chemico-physical processes occurring at the surface [*Fairchild and Baker*, 2012]. Stalagmites can be dated absolutely and precisely, e.g. with the $^{230}Th/^{234}U$ method [*Edwards et al.*, 1987; *Scholz and Hoffmann*, 2008; *Cheng et al.*, 2013] or in some cases with layer counting [*Shen et al.*, 2013].

2.2.1 Speleothem evolution and growth

Moore [1952] defined speleothems as secondary cave deposit of calcium carbonate ($CaCO_3$), which consist of the minerals calcite and/or aragonite. The origin of the precipitated mineral lies above the cave within the karst zone or the carbonate bedrock (typically limestone ($CaCO_3$) and/or dolomite ($CaMg(CO_3)_2$)) where carbonate is dissolved by the percolating water [*Fairchild and Baker*, 2012]. Speleothem growth (see figure 2.3) starts when a rainfall event occurs in a region with sufficient CO_2 supply and which is characterized by a soluble and porous rock (epikarst). The increased CO_2 concentration in the percolation water compared to the atmosphere above (400-4 000 ppm) is a consequence of the CO_2 rich soil zone (up to 100 000 ppm) due to root respiration and microbial decomposition. The percolating water dissolves gaseous CO_2 until it is in equilibrium with soil air pCO_2 and produces carbonic acid (H_2CO_3), which is a weak acid and progressively dissociates into HCO_3^- (bicarbonate) and CO_3^{2-}

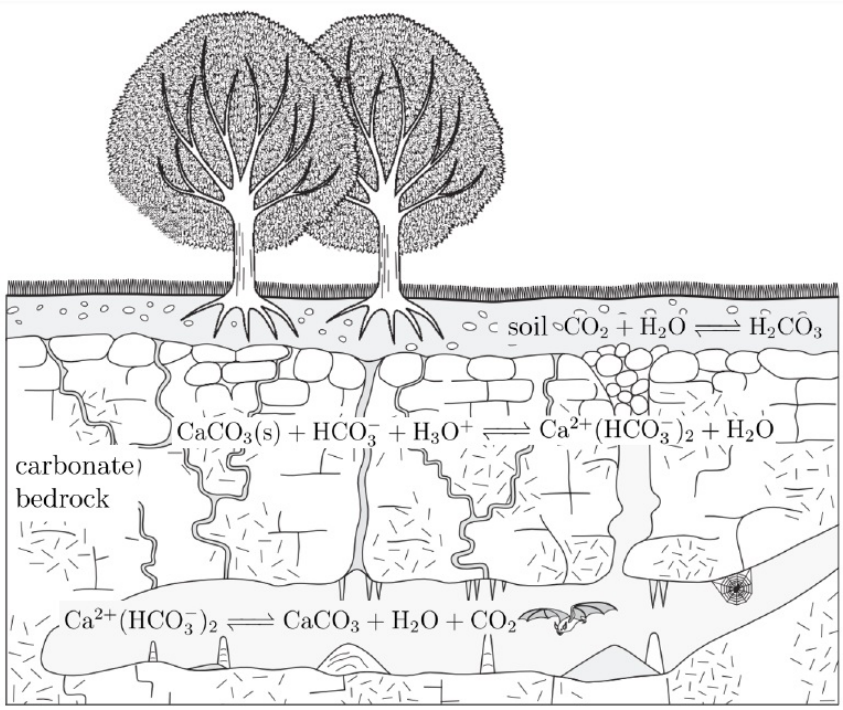

Figure 2.3: Illustration of natural cave system in a karst environment with the dissolution and precipitation regime and the corresponding chemical reactions (illustration from *Arps* [2017] after *Fairchild and Baker* [2012]).

(carbonate ions) [*Fairchild and Baker*, 2012]:

$$CO_2^{(g)} \rightleftharpoons CO_2^{(aq)} \tag{2.6}$$

$$CO_2^{(aq)} + H_2O \rightleftharpoons H_2CO_3 \tag{2.7}$$

$$H_2CO_3 + H_2O \rightleftharpoons H_3O^+ + HCO_3^- \tag{2.8}$$

$$HCO_3^- + H_2O \rightleftharpoons H_3O^+ + CO_3^{2-} \tag{2.9}$$

The concentration of total dissolved inorganic carbon (DIC) depends on the pH value of the solution, with HCO_3^- being the dominant species at nearly neutral pH values. The resulting acid solution percolates through the soil zone to the epikarst where it is able to dissolve the surrounding carbonate ($CaCO_3^{(s)}$) host rock [*Dreybrodt*, 1980] following the chemical reaction:

$$CaCO_3^{(s)} + HCO_3^- + H_3O^+ \rightleftharpoons Ca^{2+\,(aq)} + CO_3^{2-\,(aq)} + HCO_3^- + H_3O^+ \tag{2.10}$$

$$\rightleftharpoons Ca^{2+}(HCO_3^-)_2 + H_2O \tag{2.11}$$

The solubility of the calcium carbonate depends on the pCO_2 and the temperature [*McDermott*, 2004]. With the entry of the carbonate saturated water into the cave, the

pCO_2 drops suddenly, because a sufficiently ventilated cave has a much lower partial pressure as the soil. The drip water entering the cave atmosphere begins to degas the dissolved CO_2 in the solution and subsequently becomes supersaturated with respect to Ca^{2+}, resulting in a shift of the solution equilibrium towards calcite precipitation ($CaCO_3$) [*Fairchild and Baker*, 2012], which can be described as:

$$Ca^{2+}(HCO_3^-)_2 \rightleftharpoons CaCO_3 + H_2O + CO_2 \tag{2.12}$$

Over the time the accumulation of these precipitates forms speleothems (see figure 2.3), whereby the growth rate (typically varies from 0.01 to 1 mm/year) of stalagmites depends on the following factors: (i) drip rate, (ii) degree of supersaturation of drip water with respect to Ca^{2+}, (iii) gradient between cave air and drip water pCO_2 and (iv) cave temperature [*Dreybrodt*, 1980, 2012]. Here an increase in drip rate leads to increased calcite precipitation if the same super - saturation is given. If the drip rate is too high and the drop tends to flow continuously, the time for degassing is not sufficient so the calcite precipitation will stop, called hiatus [*Mühlinghaus et al.*, 2007]. A hiatus can also be caused by drying out of the stalagmite surface. However, the growth of the stalagmites is mainly dependent on the supersaturation of drip water with respect to calcium carbonate, which is related to the CO_2 content of the soil, the subsequent dissolution of the host rock, the cave air temperature, the gradient between cave air and drip water pCO_2 [*Baker et al.*, 2016]. These parameters are linked to the outside climate and thus the precipitation of cave carbonate minerals reflects climate variations.

The most common speleothems are stalagmites and stalactites [*Frisia*, 2019], with stalactites hanging from the ceiling and growing to the cave floor and stalagmites growing from the cave floor upwards. Stalagmites are usually fed by water dripping from an overhead stalactite. Further forms of cave deposit are flowstone, which do not show a clear age structure, or tubular soda straws, which are characterized by a central hollow tube and a translucent wall structure. Commonly found in caves are so - called pools, which can also contain calcite deposits, these are called pool spars and form at or under the water surface. Speleothems can be found where carbonate rock is present although growth may be slow in regions with dry or frozen environments, but they are typically found worldwide and record the regional climate of the past.

2.2.2 Fluid inclusions

Stalagmites usually contain microscopically small water - filled cavities called *fluid inclusions* (see figure 2.4), which are filled with cave water from the time of stalagmite growth [*Schwarcz et al.*, 1976; *Harmon et al.*, 1979]. They are formed by the incomplete growth process of neighbouring crystallites, whereby a micro - cavity is created which is filled with the remains of the former calcite - precipitating drip water [*Kendall and Broughton*, 1978]. Thus, they are of primary origin and their age corresponds to that of the surrounding host calcite [*Fairchild and Baker*, 2012]. They generally present an

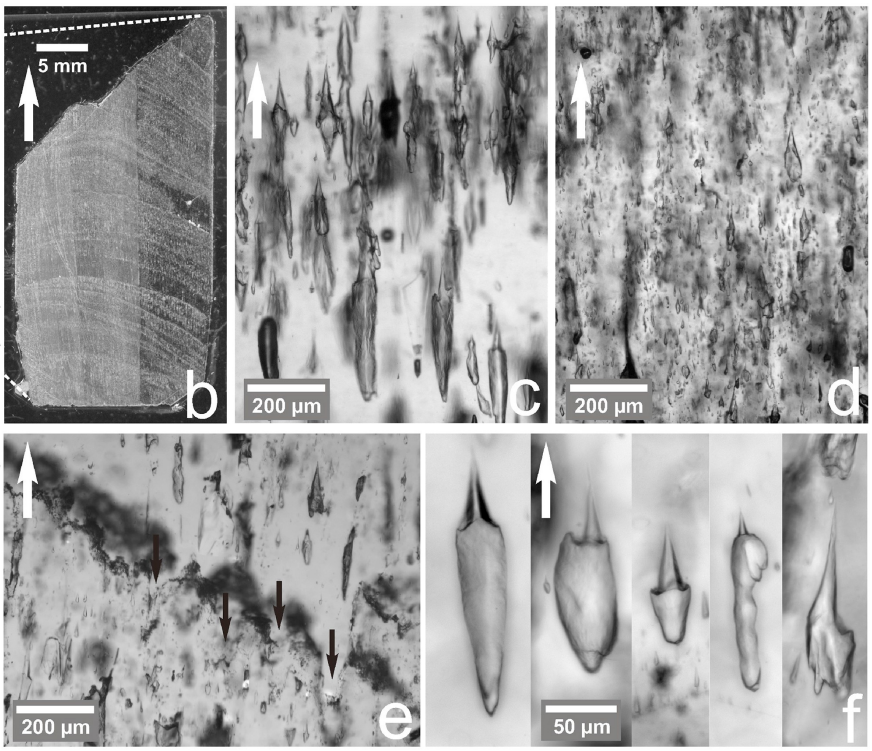

Figure 2.4: Thin sections with clearly visible fluid inclusion, adapted from *Meckler et al.* [2015]. The picture shows a columnar calcite fabric (b) with an abundance of large single-phase fluid inclusions of elongated shape (c) and very small fluid inclusions (d). Air-filled inclusions appear darker than water-filled inclusions. The single images show the typical inclusion shapes (f) and a growth hiatus, which shows evidence of a slight calcite dissolution (black arrows in e).

elongated shape (or sometimes irregular shape) and are typically arranged perpendicular to the growth layers and parallel to the crystallites boundaries [*Schwarcz et al.*, 1976]. The length of the elongated inclusions (see (f) at figure 2.4) can vary from 1 to 100 micrometers (sometimes up to 1 cm), as well as the water content can vary between 0.005 to 5.0 μl per g calcite [*Kendall and Broughton*, 1978]. Within a stalagmite, the distribution is inhomogeneous and can vary between layers with many water-filled inclusions (milky whitish calcite) and inclusion free layers (transparent calcite) [*Genty et al.*, 2002]. The reasons for the variable water content within a stalagmite and the presence of water-filled inclusions is due to crystal growth. *Boch et al.* [2011] found, that transparent calcite were interpreted as having developed during times of increased water excess and high drip rates, whereas the milky whitish calcite is formed by rapid crystal growth from highly oversaturated solutions [*Frisia et al.*, 2000]. Therefore, fabrics of calcite precipitates are controlled by host rock parameters and in particular by the amount of surface precipitation and temperature [*Frisia and Borsato*, 2010;

Frisia, 2014]. Presumably a strongly changing water content is an indirect indicator for changing climatic conditions [*Vogel et al.*, 2013].

It has been established that the drip water isotopic composition generally represents the weighted mean of local precipitation [*Yonge et al.*, 1985; *Genty et al.*, 2014], but can deviate from rainwater due to evaporation in the epikarst or cave under dry climatic conditions [*Bar-Matthews et al.*, 1996; *Denniston et al.*, 1999]. Cave drip water is incorporated into the calcite at the time of its precipitation and can therefore be stratigraphically related to the time of dripping, so fluid inclusions represent past drip water [*Schwarcz et al.*, 1976; *McDermott et al.*, 2006]. Therefore, measurements of the stable water isotopes in fluid inclusions provide a direct proxy of moisture history of past precipitation above the cave [*Van Breukelen et al.*, 2008; *Griffiths et al.*, 2010] and/or paleotemperature using the relationship between $\delta^{18}O_{fluid}$ and $\delta^{18}O_{calcite}$ fractionation for calcite precipitation at equilibrium (more details see section 2.2.3) [*Kim and O'Neil*, 1997; *Tremaine et al.*, 2011]. In order to interpret the fluid inclusion record, they must preserve the isotopic signal of the drip water. However, there are processes, which can alter the isotopic signal recorded in the fluid inclusions after enclosure, which are discussed in the following:

- *Schwarcz et al.* [1976] noticed, that a post - depostional alteration of fluid inclusions may occur through oxygen isotope exchange between trapped water and surrounding $CaCO_3$. However, it is questionable to what extent this isotopic exchange actually plays a role. On the one hand, it is a slow diffusive process, which is negligible on Quaternary time scales at Earth surface temperatures [*McDermott et al.*, 2006]. On the other hand, the oxygen reservoir of the carbonate is much larger than that of the water inclusions. Nevertheless, a possible oxygen exchange between $\delta^{18}O_{fluid}$ and $\delta^{18}O_{calcite}$ would be recognizable, because it would affect the δ^{18}O - δ^{2}H relationship of the fluid inclusions and accordingly lead to values located away from the GMWL.

- Another effect that may influence the isotopic compositions of inclusion - hosted water is disequilibrium fraction during dissolution or recrystallization after deposition at the water - calcite interface. Additionally, this subsequent modification would alter the stable isotope and trace element compositions of the carbonate [*Frisia and Borsato*, 2010; *McDermott et al.*, 2006]. [*Frisia*, 1996] investigated the recrystallization in stalagmites in detail by optical microscopy and defined the evolution of the main fabric types. The columnar structure of calcite crystals appears to be primary, without evidence of dissolution or recrystallisation after deposition [*Kendall and Broughton*, 1978].

- Another possible alteration of the isotopic composition of fluid inclusions compared to the original drip water is the evaporation of the water before the voids are closed, which depends on the relative humidity in the cave and the cave ventilation. This evaporation would influence $\delta^{18}O_{fluid}$ as well as $\delta^{2}H_{fluid}$ and lead

to values on a waterline with a slope significantly lower than 8 [*Gat et al.*, 1994].

- To what extent PCP (Prior Calcite Precipitation) changes $\delta^{18}O_{fluid}$ value is not yet known in detail due to the significantly higher abundance of oxygen atoms in the water solvent than in the dissolved carbonate. However, PCP is a clear indication of non - equilibrium fractionation during carbonate precipitation, which may bias the reconstructed paleotemperatures [*Riechelmann et al.*, 2013].

2.2.3 The $\delta^{18}O_{calcite}$ signal

Stable isotope data records ($\delta^{18}O_{calcite}$ and $\delta^{13}C_{calcite}$) from speleothem calcite are often used as paleoclimatic proxies [*Duplessy et al.*, 1970; *Bar-Matthews et al.*, 1999; *Wang et al.*, 2001; *Fairchild et al.*, 2006a; *Lachniet*, 2009]. The detection of isotope signals in calcite depends on the isotopic composition of the oxygen and carbon sources, their modification on the way to the cave (see figure 2.5) and fractionation during calcite precipitation [*Lachniet et al.*, 2009]. Therefore, the original climate signal can be altered by the development in the percolating water and the conditions at the dissolution of the calcite and furthermore at the time of deposition. Accordingly, measured signals in the stalagmite are diminished, attenuated, or even overprinted progressively through these factors, e.g. the seasonal variability of isotopic composition in precipitation is smoothed in the soil reservoir [*Fairchild and Baker*, 2012]. Here I will be

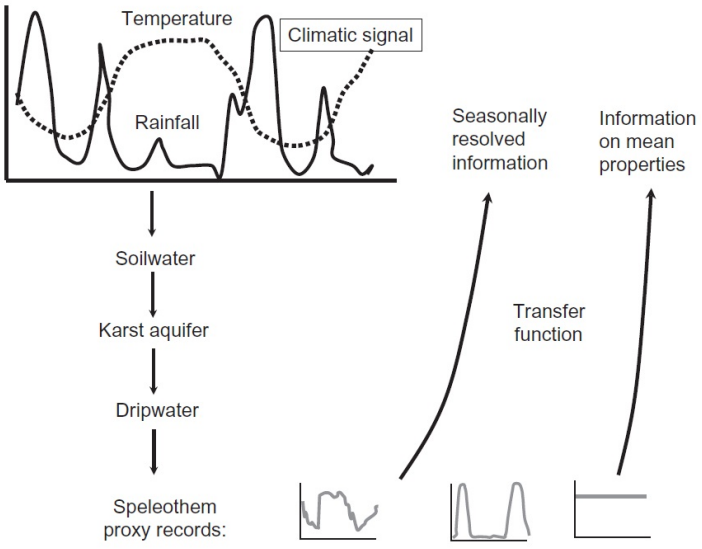

Figure 2.5: The encoded proxy parameters in a speleothem are the result of various processes that change and smooth the climate signal. Information about the original conditions can be reconstructed by reversing the coding process, which is called transfer function [*Fairchild and Baker*, 2012].

focusing on oxygen, as it is essential for calcite precipitation and thus for the application of the classical carbonate thermometer. The role of carbon will be briefly explained later (see section 2.2.4).

The complexity of the interpretation of the $\delta^{18}O_{calcite}$ signal depends on external factors outside the cave, which control the isotopic composition of the rainwater (see section 2.1.3). While percolating into the soil, the drip water δ^{18}O signal is typically modified by mixing of meteoric water of several months and the recycling of seepage water by evapotranspiration. A minor effect on the oxygen signal of the water is caused by the dissolution of old carbonate in the epikarst/host rock and through prior calcite precipitation (PCP) [*McDermott*, 2004; *Lachniet*, 2009]. For the $\delta^{18}O_{calcite}$ signal, the effect of carbonate dissolution is only relevant if the water percolates through the soil very fast. If the solution remains in the soil for more than several days, the residence time is long enough to regain the isotopic equilibrium after carbonate dissolution [*Dreybrodt and Scholz*, 2011]. As the drip water enters the cave, dissolved CO_2 degases and causes calcite precipitation, which is controlled by cave properties such as temperature, relative humidity or partial pressure of CO_2. The moment of CO_2 outgassing can occur even before the actual stalagmite is formed, and early calcite precipitation, known as PCP, can appear in the epikarst or at the drip point.

The classic carbonate thermometer

Isotope thermometry has become well established since the classic paper of *Urey* [1948] on the thermodynamic properties of isotopic substances, because the oxygen isotopic fractionation between water and calcite during calcite precipitation is temperature dependent [*McCrea*, 1950; *Epstein et al.*, 1953]. In this process, fractionation depends fundamentally on difference in mass with the heavy isotope preferably being incorporated into the calcite [*Dreybrodt and Scholz*, 2011], but becomes insignificant at higher temperatures. Theoretical studies show that the fractionation factor α(calcite - water) for isotope exchange between minerals and water on a logarithmic scale is a linear function of $1/\mathrm{T}^2$ (see figure 2.6), where T is the temperature at which the carbonate/mineral is precipitated and can be expressed as [*Bottinga and Javoy*, 1973]:

$$1000 \cdot ln(\alpha) = \mathrm{A}(10^6/T^2) + \mathrm{B}(10^3/T) + \mathrm{C} \tag{2.13}$$

For calcite precipitation under equilibrium conditions many equations have been developed describing the fractionation between H_2O and $CaCO_3$ with different parametrization based on theoretical calculations [*Schauble et al.*, 2006; *Chacko and Deines*, 2008], experimental determinations in the laboratory [*Kim and O'Neil*, 1997; *Dietzel et al.*, 2009; *Hansen et al.*, 2019] or empirical/semi - empirical calibrations [*Coplen*, 2007; *Tremaine et al.*, 2011; *Johnston et al.*, 2013].

Paleotemperatures can be calculated if mineral formation conditions similar to the parametrization reference are present. Depending on the selected parametrization,

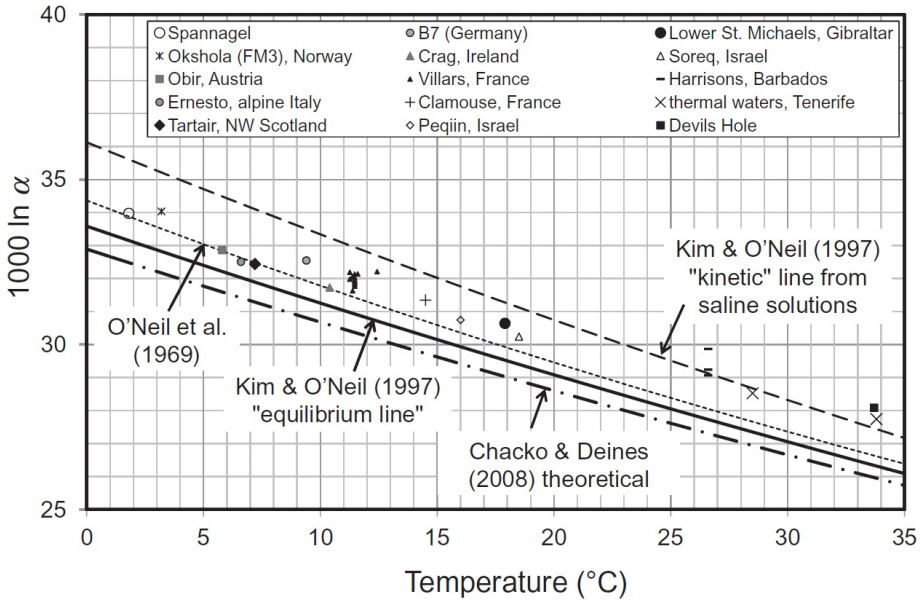

Figure 2.6: The temperature dependence for the oxygen isotope fractionation between water and calcite, according to *Fairchild and Baker* [2012]. Different parametrization based on theoretical calculations, experimental work and a selection of field data are compared. It should be noted here that this parametrization is only valid for low temperatures (0 - 40°C).

the calculated temperatures differ by an offset, for example *Kim and O'Neil* [1997] proposed for synthetic carbonates produced in the laboratory at low temperatures the following expression: $1000 \cdot ln(\alpha) = 18.03 \cdot (10^3/T) - 32.42$. *Tremaine et al.* [2011] found $\delta^{18}O_{calcite}$ values in in - situ cave calibrations that were systematically too high for laboratory based predictions. In this study, the authors found an empirical relationship for cave specific water – calcite oxygen isotope fractionation over a realistic temperature range and for different cave environments as $1000 \cdot ln(\alpha) = 16.1 \cdot (10^3/T) - 24.6$ [*Tremaine et al.*, 2011]. The study of active growing speleothems at different latitudes and altitudes worldwide after *Johnston et al.* [2013] gives the following parametrization: $1000 \cdot ln(\alpha) = 17.66 \cdot (10^3/T) - 30.16$. The selection of the parametrization must be made individually for each cave and is preferably checked with recently precipitated calcite. Most paleotemperature equations are based on calcite, although it is also possible that the deposit consists of aragonite, which would lead to a temperature - independent offset from the calcite value [*Grossman et al.*, 1986].

In order to interpret speleothem isotopic records, it is crucial to evaluate whether the calcite was deposited in nominal isotopic equilibrium. Provided that sufficient time is available for the exchange of isotopes, equilibrium conditions are likely to occur. Whether a stalagmite has grown in isotopic equilibrium can be investigated by

analysing $\delta^{18}O_{calcite}$ and $\delta^{13}C_{calcite}$ along a laminae, the so-called Hendy test [*Hendy*, 1971]. Constant isotope values along a growth layer are an indicator of equilibrium fractionation, while the simultaneous increase of $\delta^{18}O_{calcite}$ and $\delta^{13}C_{calcite}$ values is an indication of a disequilibrium. However, recent studies show that the Hendy test can be ambiguous and insufficient [*Dorale and Liu*, 2009; *Mühlinghaus et al.*, 2009]. Kinetic fractionation significantly affects the isotopic composition of speleothem calcite, with higher $\delta^{18}O_{calcite}$ values than expected according to *Kim and O'Neil* [1997], and can obscure the originally imprinted environmental signals [*Tremaine et al.*, 2011]. Kinetic fractionation occurs especially for fast or incomplete reactions, such as fast CO_2 degassing from drip water, fast calcite precipitation [*Mickler et al.*, 2004; *Dreybrodt and Scholz*, 2011] or rapidly changing growth rates [*Watkins and Hunt*, 2015]. Another important control mechanism is the occurrence of PCP, which leads to a shift in the super saturation at the stalagmite surface and favours disequilibrium [*Riechelmann et al.*, 2013]. Not only fast dripping can influence fractionation, but also too slow drip rates can favour evaporation in the cave and thus lead to kinetic fractionation during calcite precipitation [*Mickler et al.*, 2004].

2.2.4 Other proxies in speleothems

Speleothems record environmental information such as climate signals and offer the analysis of multiple proxies, where the stable isotopes of calcite provide information on the isotopic composition of precipitation (variation of $\delta^{18}O_{calcite}$) and changes in vegetation (variation of $\delta^{13}C_{calcite}$) [*McDermott*, 2004]. Further proxies encoded in the fluid inclusions, like $\delta^{18}O_{fluid}$ and $\delta^{2}H_{fluid}$, noble gases [*Kluge et al.*, 2008; *Scheidegger et al.*, 2010] and the liquid – vapour homogenisation temperature of the inclusions [*Krüger et al.*, 2011] can provide information about paleotemperatures [*Affolter et al.*, 2019; *Arienzo et al.*, 2015] and precipitation [*Fleitmann et al.*, 2003b]. Nevertheless, it is preferable for paleoclimatic interpretations if the calcite has precipitated under equilibrium conditions, however, is this not the case, clumped isotopes are a sensitive indicator for disequilibrium effects [*Affek et al.*, 2008; *Kluge and Affek*, 2012]. In addition to the oxygen isotopes of calcite, several other proxies can be used to decode climate signals from speleothem records. For example, the $\delta^{13}C$ isotopic composition of speleothems can be used to infer the isotopic composition of atmospheric CO_2 [*Baskaran and Krishnamurthy*, 1993] or the type and density of vegetation growing above the cave [*Dorale et al.*, 1992], because the main driver of $\delta^{13}C$ variability in the soil is the primary carbon production by plants (C3 or C4), which have a very different $\delta^{13}C$ signature and transfer processes. Furthermore, another important source of carbon is the dissolution of the carbonate bedrock, which has a different isotopic signature than the carbon in the soil and atmosphere and, therefore, can provide information on the formation of the stalagmite [*Hendy*, 1971; *Genty et al.*, 1998].

The growth rate of a stalagmite is controlled by the saturation state of the drip water, drip rate, temperature and pCO_2 in the cave and thus can be used as indicator

for a number of environmental parameters, such as cave air circulation or amount of precipitation [*Baker et al.*, 1993; *Genty and Quinif*, 1996]. In addition, speleothems not only consist of pure calcite, but also incorporate traces of other elements into their crystal structure, such as Mg (magnesium), Na (sodium), Sr (strontium), Ba (barium), P (phosphor) or U (uranium) which are becoming increasingly important in multi - proxy analyses of speleothems [*Fairchild and Treble*, 2009]. The source of these trace elements is in the atmosphere or soil and their concentration in the speleothem is controlled by recycling processes in the soil and by calcite precipitation process. For example, Mg/Sr ratios are used as a proxy for precipitation changes [*Roberts et al.*, 1998; *Sinclair et al.*, 2012] and phosphorus concentrations provide information about the seasonal hydrological variability [*Lewis et al.*, 2011].

2.3 Cavity Ring - Down Spectroscopy (CRDS)

2.3.1 Basics of absorption spectroscopy and CRDS

Absorption spectroscopy by measuring the decay time of an optical resonator, also known as "Cavity Ring - Down Spectroscopy", attributes absorption measurement to a time measurement [*Zalicki and Zare*, 1995; *Demtröder*, 2013]. Of fundamental importance is the Lambert - Beer law, which describes the relationship between the attenuation of light through a substance and the properties of that substance. Considering the ring - down time measurement of the CRDS technique, the exponential loss of light intensity at the photodetector is defined over the Lambert - Beer law, which can be written as follows [*Picarro*, accessed February 28, 2020]:

$$I(t, \lambda) = I_0 \cdot e^{-t/\tau(\lambda)} \tag{2.14}$$

with the initial light intensity I_0 and the wavelength of the laser λ. When the laser is switched off, the ring - down time constant $\tau(\lambda)$ indicates the time until the intensity has decreased with 1/e below an adjustable threshold. For CRDS, a laser pulse is stored in a high - quality optical cavity containing the sample, and the pulse decay is monitored with the aid of a photodetector that measures the intensity of light transmitted through one of the mirrors [*Zalicki and Zare*, 1995]. The optical cell (cavity) consists of two or more spherical mirrors (three for the *L2130-i* analyser) with very high reflectivity $R > 0.995\,\%$. This technique allows the laser beam to perform a large number of reflections within a cavity. Thus, achieving average absorption path lengths (l) of up to several kilometres ($\sim 20\,\text{km}$ for the *L2130-i* analyser) and exceeding the actual cavity length (L) by a factor of 10^5 [*Berden et al.*, 2000]. For a measurement, light from a continuous wave laser is first injected into the cavity (see right panel of figure 2.7). The light intensity builds up inside the cavity due to the high degree of reflectance of the mirrors and is monitored by a photodetector. The ring-down measurement is performed by quickly switching off the laser and measuring the light intensity in the cavity, as this decays exponentially over time. When the cavity contains an absorbing

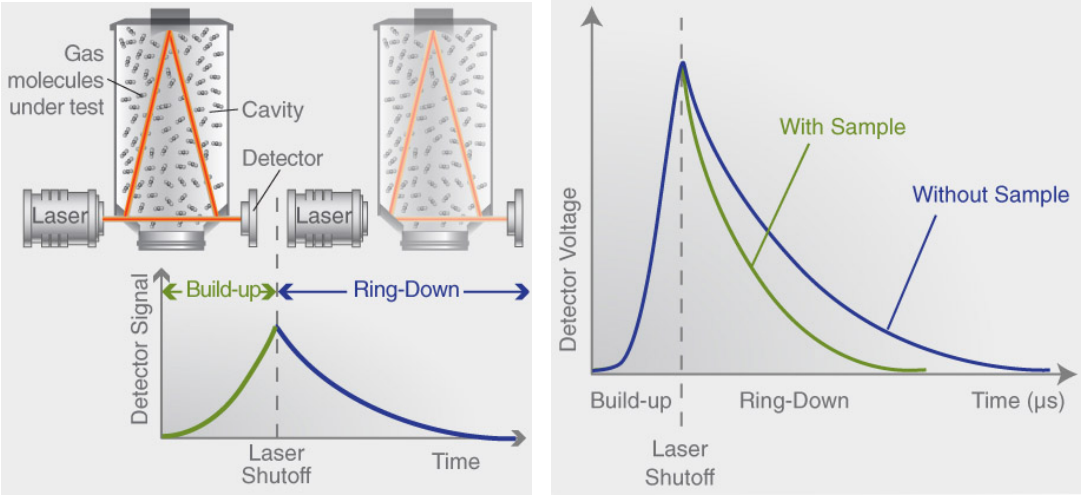

Figure 2.7: Left: Principle of cavity ring - down spectroscopy for a Picarro analyser with three reflecting mirrors with a reflectivity of 99.995 %, which circulate the laser beam and exceed the optical path length (l) to $\sim$20 km. The laser is switched off when a threshold intensity is reached and the ring - down time (τ) of the laser pulse is subsequently measured. Right: The ring - down time varies depending on the cavity contents, with an absorbing species τ is reduced [*Picarro*, accessed February 28, 2020].

gas, an additional optical loss occurs which causes a decrease in the ring - down time (see left panel of figure 2.7). The difference of the measured photon decay time with (τ) and without (τ_0) an absorbing species in the cavity can be described as follows [*Yu and Lin*, 1993]:

$$\frac{1}{\tau} - \frac{1}{\tau_0} = \frac{\alpha \cdot c \cdot l}{n \cdot L} \tag{2.15}$$

where c is the speed of light, l is the length of the absorbing medium, L is the cavity length, n is the index of refraction of the absorbing medium and α is the absorption coefficient, which is the product of the extinction coefficient ϵ and the sample concentration C. For a more detailed derivation of the difference of the reciprocal decay times see *Demtröder* [2013].

By scanning the wavelength of the laser over the relevant wavelength range (spectral range 7 183.5 - 7 184.0 cm^{-1}) of the water isotopologues ($^1H^1H^{16}O$, $^1H^2H^{16}O$, and $^1H^1H^{18}O$) and measuring the decay time (optical loss), an optical spectrum and thus the detailed spectral profile is generated [*Gianfrani et al.*, 2003]. The concentration of each isotopologue is then proportional to the area under each measured isotopologue spectral feature [*Brand et al.*, 2009]. The advantage of using the three mirror cavity to extend the effective absorption path is that the signal to noise ratio is significantly reduced compared to a two mirror cavity which favours a standing wave [*Demtröder*, 2013]. In addition, with the effective path length of many kilometres, the sensitivity of

the infrared spectrometers can be significantly increased, which also allows to detect rare isotopologues with a natural abundance in the per mil range [*Picarro*, accessed February 28, 2020]. Another advantage of this technique is that infrared laser can be used to detect the unique near - infrared absorption spectrum of the water isotopologues. These lasers can be operated at room temperature and require no additional nitrogen cooling [*Lis et al.*, 2008].

The known wavelength of the continuous wave laser of the *L2130-i* analyser is tuned over (in $0.01\,\mathrm{cm}^{-1}$ steps) the absorption spectra of the ${}^{1}H^{1}H^{16}O$, ${}^{1}H^{2}H^{16}O$, and ${}^{1}H^{1}H^{18}O$ isotopologues with lines around $7\,183\,\mathrm{cm}^{-1}$ [*Gianfrani et al.*, 2003]. During the measurement, the pressure and temperature in the cavity are continuously monitored and maintained constant at $50.00 \pm 0.02\,\mathrm{torr}$ and $80.00 \pm 0.02\,°\mathrm{C}$, respectively [*Picarro*, 2015]. To completely minimize the instrumental measurement drift of the *L2130-i* analyser, the sample cavity is surrounded by layers of thermally insulating material to provide a high degree of passive thermal stability and further stabilized by means of a solid state heating system. Comparison of the measured relative intensity of the peaks for the water isotopologues with those of the respective standards (VSMOW for this study) gives $\delta^{18}\mathrm{O}$ and $\delta^{2}\mathrm{H}$ values [*Picarro*, 2015]. At low water vapour concentrations, the overlapping absorption of other species (e.g. CH_4) may interfere with the actual water isotope absorption spectra. The *L2130-i* analyser corrects for these overlapping spectra, by analysing and evaluating each species which interferes with water isotopologue measurements. This correction enables an accurate and precise measurement of the water stable isotopes with low or even varying water vapour concentration (see figure A.9) [*Aemisegger et al.*, 2012].

2.3.2 State of the art for stable water isotope measurements of fluid inclusions of speleothems

Two physically different measuring principles allow the determination of the isotopic composition of fluid inclusions of speleothems. Laser spectroscopic systems use the difference in the structure of the rotational - vibration energy level of the individual isotope molecules, resulting in isotopic characteristic absorption peaks in the near - infrared region. The traditional technique to measure stable isotopes is by isotope ratio mass spectrometry (IRMS), which utilizes the different mass - to - charge ratios of the isotopes. Before the stable water isotopes are measured they must be released, which can be done either by crushing [*Schwarcz et al.*, 1976] or thermal decrepitation [*Yonge*, 1982]. Thermal decrepitation releases water by heating the fluid bearing sample to a high temperature ($\sim 550°\mathrm{C}$). This method has the disadvantage that the extraction temperature and isotope exchange may vary during extraction resulting in large fractionation of up to 30 ‰ for $\delta^{2}\mathrm{H}$ in comparison to parent cave drip water [*Yonge*, 1982; *Matthews et al.*, 2000; *McGarry et al.*, 2004], which can be avoided by crushing the sample mechanically. In the 1970´s [*Schwarcz et al.*, 1976; *Harmon et al.*,

1978, 1979], pioneering work was carried out to measure stable isotopes of fluid inclusions using mass spectrometry (IRMS). For this purpose, the water was extracted by crushing the sample under vacuum conditions and then subsequently converted into water vapour of molecular species suitable for O and H isotopic analysis. The first combined method for oxygen and hydrogen measurements with an off - line crushing method and dual - inlet isotope mass spectrometer was developed by *Dennis et al.* [2001], achieving good precisions but requiring a large sample size of 1 to 3 μl [*Matthews et al.*, 2000]. A reduction of sample size down to 0.1 μl , which correspondence to 0.1 g of calcite [*Fleitmann et al.*, 2003b], was achieved by *Vonhof et al.* [2006] by combining off - line preparation and continuous - flow mass spectrometry. This technique enables a faster analysis of smaller sample sizes with comparable precision of 0.5 ‰ for δ^{18}O and 1.5 ‰ for δ^{2}H of 0.1 - 0.2 μl of released water to dual - inlet IRMS [*Vonhof et al.*, 2006; *Dublyansky and Spötl*, 2009].

Laser spectroscopy does not require any additional water treatment, like the reduction of H_2O in a pyrolysis reactor into measurable molecules like H_2 or CO. It is less expensive and allows a reliable, precise and easy technique to measure stable water isotopes [*Brand et al.*, 2009; *Gupta et al.*, 2009]. The first application using cavity ring - down spectroscopy to measure fluid inclusions in speleothems was developed by *Arienzo et al.* [2013] using a *L2130-i* analyser from Picarro. The Miami Device, with a stainless steel line heated to 115 °C and constantly flushed with dry nitrogen as a carrier gas, achieves comparable precisions as the traditional IRMS technique, with 0.5 ‰ for oxygen and 2.0 ‰ for hydrogen. The application of another analyser using off - axis integrated cavity output spectroscopy (OA-ICOS) achieve comparable precisions [*Czuppon et al.*, 2014] and newest developments are able to measure released water volumes in the nano litre range (50 to 260 nl) by using the CRDS technique with a precision of 0.33 ‰ for δ^{18}O and 1.6 ‰ for δ^{2}H [*Uemura et al.*, 2016].

All these lines [*Arienzo et al.*, 2013; *Czuppon et al.*, 2014; *Uemura et al.*, 2016] are working with a dry carrier gas and low water vapour concentrations in the analyser cavity, which can influence the stable isotope measurements. The measured isotopic signal needs to be corrected for these disturbance effects, e.g. the isotopic dependency on the water vapour content [*Uemura et al.*, 2016] or the memory effect. Regarding the so - called memory effect, the cavity remembers the previously measured sample, which results from the fact that the cavity of the CRDS analyser cannot be completely evacuated between two measurements. Thus, the sample signal of the previously measured sample remains in the cavity due to adsorption of water molecules on the cavity walls. This can be avoided by injecting the desired water sample multiple times, then the measured signal converges exponentially to the actual sample signal. However, multiple injections are not feasible for fluid inclusion measurements of speleothems since the amount of water of these samples is too low (μl range). This issue was handled by *Affolter et al.* [2014] with an extraction line that is always kept under humid conditions, therefore an artificial water vapour background is generated, which contains

a known δ^{18}O and δ^{2}H isotopic composition. The permanently saturated line allows the measurement of fluid inclusions of speleothems by the instantaneous evaporation of the released water followed by spectroscopic analysis of the resulting mixture of water vapour background and sample signal. The advantages of the line are: (i) it is easy to build, (ii) the operational costs are low compared to vacuum and IRMS systems and (iii) it avoids additional corrections of the measured water stable isotopes with standard deviations smaller than 0.4 ‰ for $\delta^{18}O_{fluid}$ and 1.5 ‰ $\delta^{2}H_{fluid}$. The achieved precision is comparable with the traditional IRMS technique [*Vonhof et al.*, 2006; *Dublyansky and Spötl*, 2009] and CRDS setups working with a dry carrier gas [*Arienzo et al.*, 2013; *Czuppon et al.*, 2014].

2.4 Climatological setting of the three different study sites concerning the time scale of the speleothem records

2.4.1 The transitional climatic zone (Romania) - present day

The Carpathian mountains are located in a transitional climatic zone between central Europe, western Eurasia and the Mediterranean. By their position and the main morphological features, they divide the country into two major regions of different climatic characteristics: with colder and wetter climatic conditions in the north, whereas the south is dominated by a drier and warmer climate [*Micu et al.*, 2016]. Winter climate in Romania is strongly affected by the North Atlantic Oscillation (NAO) [*Bojariu and Paliu*, 2001; *Micu et al.*, 2016], which is characterized by a meridional displacement in the atmospheric pressure between the Icelandic Low and the Azores High [*Wanner et al.*, 2001] and associated with changes in the westerlies across the Atlantic onto Europe [*Hurrell*, 1995]. For central and northern Europe, NAO + years are associated with relatively humid and mild winters, while NAO − conditions lead to less precipitation and colder temperatures during European winter (position of atmospheric patterns see figure A.4) [*Dai et al.*, 1997; *Trouet et al.*, 2009]. For the Mediterranean region another teleconnection pattern affects the weather process, the East Atlantic West Russia (EAWR) pattern [*Krichak and Alpert*, 2005]. Positive trends in the NAO and the EAWR are associated with drier than normal weather conditions in the Mediterranean region [*Bojariu and Paliu*, 2001].

For an inland continental site, like the location of the cave, the dominant control on the isotopic composition of the precipitation is the *Rayleigh rainout* effect. The air masses follow an eastward progressing rainout trajectory over the European land mass with an isotopic composition of the precipitation, which becomes more depleted if regional temperatures are decreased and vice versa [*Rozanski et al.*, 1993]. The direct link of fluid inclusions to drip water and therefore to paleoprecipitations, enables the reconstruction of temperatures based on the relationship between δ^{18}O and accordingly δ^{2}H in precipitation and air temperature for continental climate [*Rozanski*

et al., 1992]. For Hungary, *Demény et al.* [2017] showed that the application of the δ^2H/T relationship on stable isotope measurements of fluid inclusions led to reliable temperature reconstructions for the last interglacial. At present, there are indications of progressive climate change from global observation data sets, which suggests visible changes in the average values or the overall variability of climate characteristics. In general, Europe has shown a greater warming trend since 1979 compared to the global mean and the related climate trends in mountainous regions are even more pronounced [*Böhm et al.*, 2010].

2.4.2 Central Europe (Germany) - Holocene

The weather system of central Germany (location of the Bunker Cave) is, like most of the climate in Europe, determined by the NAO (see section 2.4.1), which dominates the mid - latitude westerly wind systems and thus influences the precipitation and temperature pattern [*Hurrell*, 1995]. The present interglacial, the Holocene, covers the period of the last 11 700 years and marks the rapid transition from the cold period (Younger Dryas) to a subsequent, generally warmer period with relatively small temperature variations [*Dansgaard et al.*, 1989; *Mayewski et al.*, 2004]. For the Holocene on the multidecadal to multicentury timescale, periods of more stable and warmer climate were interrupted by several cold relapses. These cold interruptions were most likely favoured by decreasing solar insolation combined with a possible slowdown of the thermohaline circulation and in some cases also combined with a series of tropical volcanic eruptions [*Wanner et al.*, 2011]. One pronounced cooling event during the Holocene is the 8.2 ka event, which was triggered by cooler conditions in the North Atlantic due to a slowdown of the thermohaline circulation [*Fohlmeister et al.*, 2012]. For the Atlantic episode of the Holocene (9.6 - 5.5 ka), [*Niggemann et al.*, 2003b] found an increased stalagmite growth for a cave in central Germany, which is associated with variations in precipitation. The mainly wet and warmer period of the Holocene was interrupted by colder and drier conditions. Stalagmites offer the possibility to study variation in precipitation with the analysis of stable isotopes in fluid inclusions, but are biased towards autumn and winter in Central Europe, as the drip sites are mainly active in winter due to evapotranspiration in summer [*Wackerbarth et al.*, 2010].

2.4.3 The tropical west Atlantic (Puerto Rico) - millennial timescale

Puerto Rico, as the easternmost island of the Greater Antilles, is a tropical island in the north - eastern Caribbean and lies between the high pressure cell over the Atlantic and the Inter - Tropical Convergence Zone (ITCZ). The surface temperature of the sea, which averages around 27 °C has a direct effect on the climate through large amounts of latent and sensible heat transfer throughout the year [*Granger*, 1985]. This ocean - atmosphere coupling is of great importance for the climate in the Caribbean since the area is dominated by sea surface and the numerous islands are not large

enough to cause strong climatic fluctuations. The climate is, therefore, predominantly maritime, which nowadays leads to comparatively small temperature variations [*Schellekens et al.*, 2004]. The seasonal weather patterns for the Caribbean region are broadly divided into dry winter (December - March) and rainy summer (June - November) seasons [*Grist*, 2002] with the climate strongly dominated by easterly trade winds especially in the winter months [*Scholl et al.*, 2009]. Thereby, the rain isotopic signature of precipitation differ between rain and dry season due to a varying source or different climate patterns. The dry season in the Caribbean is characterized by orographic precipitation from frontal system rain (cold fronts from North America, trade winds and sea breeze showers) which occasionally pass over the island. In contrast, during the rainy season convective rainfall, which originates from the passage of tropical easterly wave and is formed by low pressure system (tropical storms and hurricanes) accounts for half of the total precipitation [*Scholl and Murphy*, 2014].

On millennial timescale, rainfall variability in the tropical regions of the western Atlantic dependence on the latitudinal position of the ITCZ [*Lachniet et al.*, 2009], which effects the strength and track of easterly trade winds. For the tropics, the increased input of freshwater into the North Atlantic and the weakening of the AMOC (Atlantic Meridional Overturning Circulation) during Heinrich events led to a southward shift of the ITCZ. The consequences are colder and drier climate conditions for westerly Atlantic tropics during stadials as has been shown in various paleostudies of stalagmites, ocean sediment or lake sediment cores [*Lachniet et al.*, 2009; *Hodell et al.*, 2012; *Grauel et al.*, 2016; *Escobar et al.*, 2012; *Deplazes et al.*, 2013; *Arienzo et al.*, 2015]. In contrast, a northward shift of the ITCZ is expected during the interstadials, which will be accompanied by warmer and wetter climatic conditions [*Deplazes et al.*, 2013]. It is questionable how pronounced these rapid climatic fluctuations from cold (stadial) to warmer (interstadial) conditions appear in the Caribbean tropics, since in some stalagmite records no characteristic of D/O events can be found, although HS events are very clearly represented [*Carolin et al.*, 2013; *Arienzo et al.*, 2017].

3 | *Fluid inclusion line* - setup, data evaluation, calibration and intercomparison

Fluid inclusions archive the drip water from which the speleothem formed and can therefore provide valuable insights into the paleo-hydrological conditions. Here I present a setup that measures oxygen and hydrogen simultaneously with the laser absorption technique. Technical advances now allow to determine $\delta^{18}O_{fluid}$ and $\delta^{2}H_{fluid}$ of microliter water amounts with high precision and accuracy. The construction of the *Fluid inclusion line* located in Heidelberg is based on the prototype developed by *Affolter et al.* [2014] in Bern, but has been modified and further developed as described in the following section. Moreover, I have developed a protocol for data evaluation, which can be downloaded here: `https://github.com/bhemmer/IsoFluid`. In the following I will describe the setup and investigate precision and accuracy. Furthermore, I discuss possible effects, which could disturb the stable isotope measurement of fluid inclusion water. For example the memory effect, the effect of adsorption and desorption on the stalagmite surface or the effect of isotopic composition of the water vapour background. Finally, I will show the robustness of the measurements and the reproducibility by performing first speleothem test measurements. The inter-laboratory comparison (Max Planck Institute for Chemistry, Mainz and University of Bern) shows that the measurements with a CRDS (Cavity ring-down spectroscopy) analyser attached to this extraction line achieves an accuracy comparable to mass spectrometry.

For this setup, I used a CRDS analyser from the company Picarro (Santa Clara, USA). The *L2130-i* isotope and gas concentration instrument is used regularly in many fields of environmental studies, such as hydrology, oceanography or palaeoclimatology [*Benetti et al.*, 2014; *von Freyberg et al.*, 2017; *Affolter et al.*, 2019; *Gao et al.*, 2019]. I discuss the principle of laser spectrometric isotope and water vapour mixing ratio measurements in section 2.3. Here I will focus on the specifications of the *L2130-i* analyser, which is based on cavity-ring down spectroscopy.

3.1 Preparation line

To enable a reproducible and precise analysis of stable isotopes of fluid inclusions, an artificial water vapour background is generated, which contains a known δ^{18}O and δ^{2}H isotopic composition. This allows the measurement of fluid inclusions of speleothems by the instantaneous evaporation of the released water followed by spectroscopic analysis of the resulting mixture of water vapour background and sample signal. More precisely,

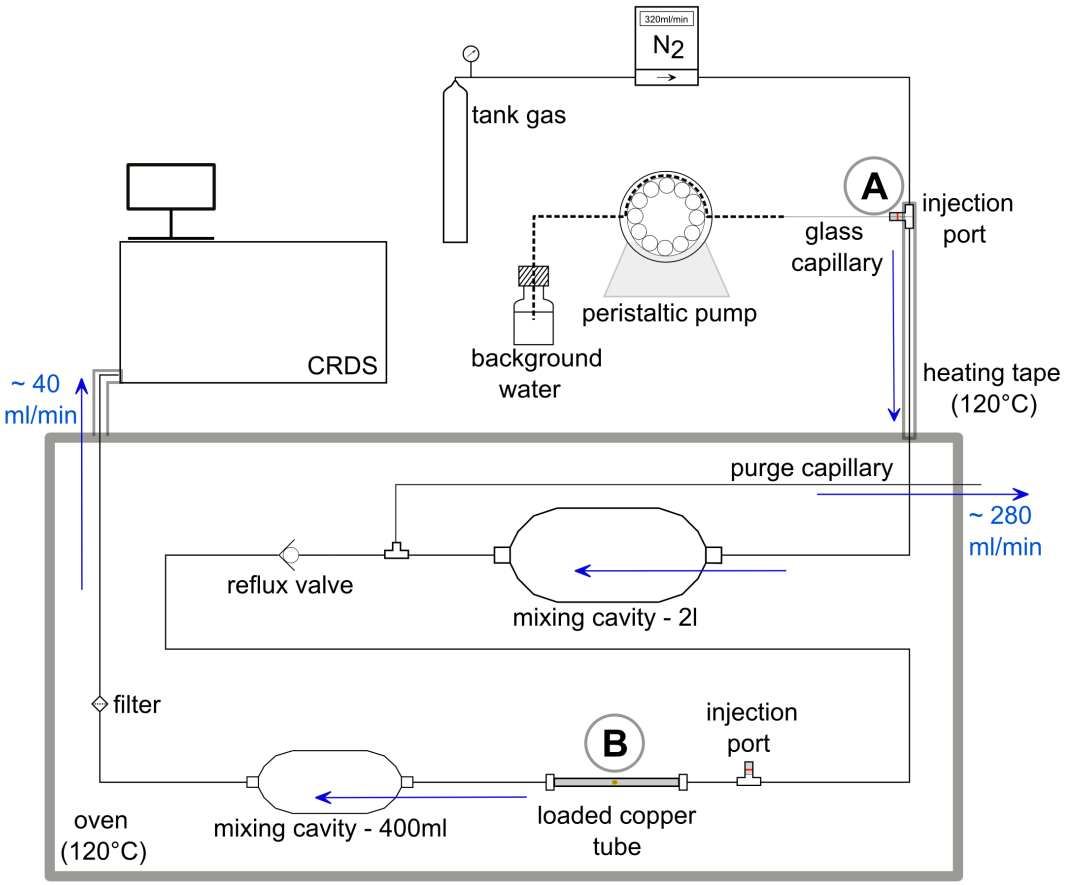

Figure 3.1: The *Fluid inclusion line* for the measurement of stable isotopes of fluid inclusions in speleothems. Water with a known isotope composition is mixed into a nitrogen gas flow to create a stable water vapour background (see point A). The purge capillary reduces the background vapour flow from 280 to 40 ml/min as required for the CRDS analyser. The two volumes provide a smoothing of the background vapour signal and an adjustment of the measurement signal. The speleothem sample is placed in a copper tube and installed at position B. In order to prevent the backflow of the water vapour signal from the freshly crushed sample, a reflux valve is installed. Thereby the respective flow directions are shown as blue arrows. All used components and the corresponding companies are listed in table A.1 and A.2.

the preparation line (figure 3.1) generates a stable water vapour background by mixing water of a known isotopic composition into a nitrogen gas flow. A peristaltic pump (Ismatec - REGLO *Digital* (Wertheim, Germany)) continuously supplies small amounts of water (1 μl) to the line through the injection port. Instant evaporation is enabled via a fused silica capillary, which slightly touches the heated base of the port. The nitrogen flow of 300 ml/min is controlled by an Analyt - MTC - mass flow controller (Müllheim, Germany). This causes a constant overpressure of 0.5 bar above atmosphere in the preparation line, with a flow rate of 40 ml/min of the CRDS analyser the surplus gas stream is vented through the purge capillary. Thus, it is possible to create a background with a low water vapour concentration in the range of 6 000 to 8 000 ppmV (details about precision see section 3.6).

Details - setup preparation line

The vaporizing unit consists of an injection port with a septum, enabling the fused silica capillary to penetrate without atmospheric disturbance. The capillary itself is connected to the peristaltic pump tube without a further adapter. The selected inner (tube with 0.13 mm) and outer (capillary with 0.36 mm) diameter allow an airtight connection. The mixing cavity with a volume of 2 l enables a stable water vapour background and compensates fluctuations caused by pump cycles of the peristaltic pump. While crushing of the speleothem sample the water in the fluid inclusions immediately evaporates. This leads to a sudden volume increase, which produces a gas flow in both flow directions. Therefore, I installed a reflux valve between mixing cavity and sample mounting to prevent a backflow and thus, a loss of the sample signal. The reproducibility is largely influenced by the installation of the reflux valve. For a test measurement with six 1.0 μl injections the actual measured signal varies between 0.1 and 0.8 μl (see figure A.5). In order to perform test measurements as e.g. memory effect tests (see section 3.7), I placed a second injection port directly in front of the sample inlet. This allows syringes to access the closed line, enabling faster measurements as the water vapour background remains under stable conditions. The majority of the line is heated to a constant temperature of 120°C by an oven (see section 3.1.2). Connecting parts between vaporizing unit and oven or oven and CRDS analyser are heated via a heating tape to the same temperature. A temperature of 120°C ensures a total and instantaneous evaporation of the water without any fractionation.

Details - sample mounting

The speleothem sample does not require any special preparation, only the edge length must correspond to the inner diameter of the copper tube (8 mm) through which it is mounted in the line. Compact pieces are preferred as the sample is crushed from the outside by a hydraulic crusher, the position of the sample is marked and fixed with glass wool. An additional small mixing cavity (400 ml) is installed directly behind the sample inlet. This converts the generated sample signal into a measurable signal. With

the additional mixing cavity the duration of the sample signal is extended from less than a minute to 30 minutes (0.5 μl) or even to 60 minutes (2 μl), whereby the duration of the sample signal depends on the released water volume. The CRDS analyser records one data point every 0.8 seconds, but light isotopes reach the analyser within the first seconds due to fractionation. With a very small cavity (2 ml) the actual isotope signal of the sample is only partially recorded and important information about the complete evolution of the isotope signal is lost (see figure A.6). In addition, a filter is installed to protect the laser cell against small calcite particles.

3.1.1 Hydraulic crusher

The copper tube, equipped with the desired sample, is installed at position B as shown in figure 3.1. Hereby an airtight connection between line and copper tube is enabled using a brass ferrule nut set (Swagelok), which is used for each sample once. The hydraulic crusher, as shown in figure 3.2 exerts a pressure of 200 - 300 bar onto the copper tube. A small barrier (2 mm height) prevents a complete compression of the tube, which would lead to an interruption of the water vapour flow. The piston in the stainless steel jack is moved by a hydraulic hand pump. Since the piston has a diameter of 4 cm, very large samples require crushing in two steps. To crush the

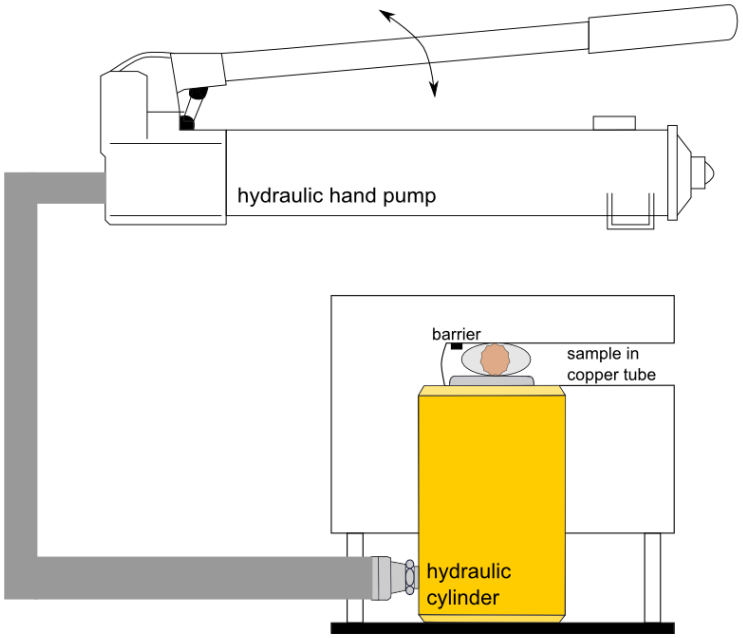

Figure 3.2: Schematic illustration of the hydraulic crusher, which consist of a piston fixed in a stainless steel jack and a hydraulic hand pump. It exerts a pressure of 200 - 300 bar onto the sample, whereby a small barrier prevents a complete compression of the tube. All used components and corresponding companies are listed in table A.2.

sample the oven door must be opened, which results in a decrease in temperature and disturbs the water vapour background signal (see figure 3.4). An experienced user can complete this process in less than 30 seconds. Then the disturbance has no effect on the measurement signal as it reaches the analyser with a 90 second delay and is taken into account in the evaluation (see section 3.4). For the analysis of the sample signal, this intermediate interval is set to two minutes, which ensures that the undisturbed water vapour background is used to calculate the background signal.

Particle size analysis

I carried out a grain size analysis at the *Institute of Earth Sciences Heidelberg* to test the efficiency of the hydraulic crusher. The samples were analysed with the *Analysette 22 Micro Tec* (Fritsch - Achern, Germany) based on the principle of laser diffraction analysis. It follows the fundamental that particles of different sizes produce different diffraction patterns. Thus a simple and fast measurement of the geometrical dimensions of the particle is possible [*Beuselinck et al.*, 1998]. For particles with a diameter above 10 μm the laser diffraction analysis is based on the Fraunhofer diffraction, whereas Mie diffraction plays a role for smaller particles, which will not be discussed here [*de Boer et al.*, 1987]. The Fraunhofer diffraction theory states that the intensity of light, scattered by a particle, is directly proportional to the size of the particle. Thus, the grain size can be determined by measuring the diffraction angle of the laser beam. The relation is inversely proportional: the smaller the particle, the larger the diffraction angle. The detailed measurement process is described in the appendix A.2.

I have selected five already crushed and measured samples for fluid inclusion to determine the particle size. The results of the particle size analysis are shown in figure 3.3 and listed in table 3.1, with each sample measured ten times. The left side of figure 3.3 shows the development of the median over the number of measurements. Here the median or *d50* describes the average grain size. There is a decrease in the median with progressive measurements, indicating a change in the particle size distribution. This observation implies that some particles stick together and only gradually separate

sample #	name	weight [g]	median [μm]
1	Closani II C1	0.251	26.56
2	Closani II B2	0.261	57.63
3	LA-1-24 B	0.303	36.67
4	LA-1-13 B	0.309	29.86
5	LA-1-1 A	0.315	36.36

Table 3.1: Five samples already crushed and measured for fluid inclusion were analysed for particle size analysis. The mean value or *d50* is the value of the particle diameter at 50 % in the cumulative distribution.

with running an ultrasonic bath. During crushing a high pressure (up to 300 bar) is performed on the sample. This pressure leads to crushing of the stalagmite as well as to a compression and compaction of the fine material.

Due to the non constant median, I used the last five measurements of each sample to determine the mean particle size distribution (figure 3.3 right panel). Here the mass fraction in % is plotted against the particle diameter in μm. Two peaks have to be distinguished. *Peak I* at a particle diameter of about 20 - 30 μm represents the mean diameter of single particles, whereas *peak II* rather correspondence to several particles that stick together due to the high pressure exerted during crushing. As the grain size measurement progresses a decrease of the *peak II* is visible, corresponding to a dissolution of the clumping particles, at the same time *peak I* increases. All samples are showing a similar particle size distribution, which speaks for a homogenous and reproducible crushing routine. With a mean grain size around 30 μm, it is feasible to open almost all fluid inclusions as they have typically a size from 1 to 50 μm [*Scheidegger et al.*, 2010] or 10 to 50 μm [*Schwarcz et al.*, 1976].

Compared to other techniques, the hydraulic crusher of the *fluid inclusion line* achieves a very good crushing efficiency with an average *d50* value of 37 μm. A similar crushing procedure developed by *Affolter et al.* [2014] results in a *d50* value of 495 μm with the

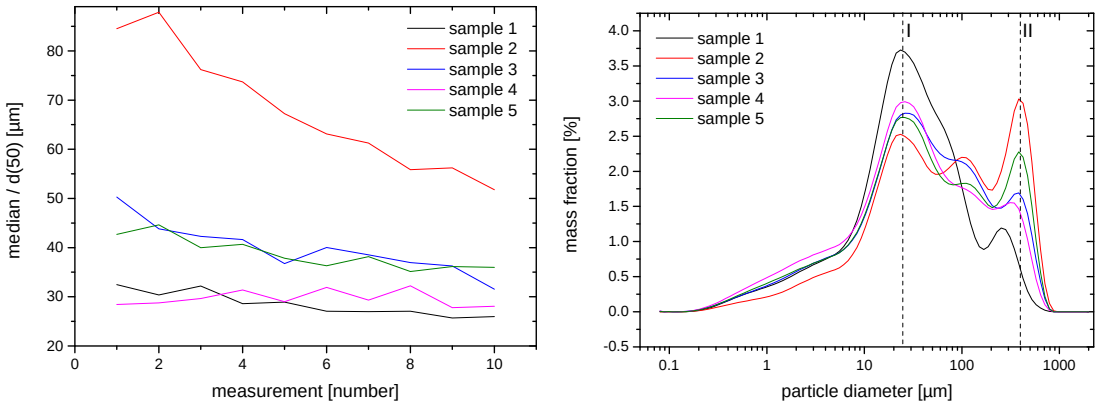

Figure 3.3: Left: Median or *d50* with progressive measurements for five different samples illustrated in different colours. The median measurement was repeated ten times. A decrease of the median indicates a change in the particle size distribution. Right: Grain size distribution for all five samples, whereby the last five measurements were taken into account. Two particle diameters are dominant with peaks at 20 - 30 μm (*peak I*) and 400 μm (*peak II*), while *peak II* does not correspond to a single particle size, but to the size of several particles clumping together due to the high pressure exerted during crushing. The mean diameter of single particles is dominant at a particle diameter of about 20 - 30 μm indicated as *peak I*. Detailed data for all samples and the 10 individual measurements are listed in the appendix (A.4, A.5, A.6, A.7, A.8 and A.9).

difference that the barrier is adjusted to a higher level and therefore the copper tube is not compressed as much as for this setup. *Kluge et al.* [2008] has developed a crushing method for noble gas analysis, where they achieved an average grain size of 630 μm. With the *Amsterdam Device* of *Vonhof et al.* [2006] a grain size distribution from 100 up to 1000 μm was achieved.

3.1.2 Temperature control

A constant temperature at 120°C ensures a complete and immediate evaporation, which is important to avoid fractionation by partial evaporation. The majority of the preparation line is heated by an oven, whose temperature can be recorded by a temperature sensor (pt1000). A representative temperature profile is shown in figure 3.4, with a constant temperature at 120°C. Temporary temperature decreases are due to the necessary opening of the oven door during sample crushing or changing samples, as the heating must be deactivated briefly. In this case, the temperature decreases below 100°C, but returns to the initial value after approximately 20 minutes. The actual measurement, which takes place about 90 minutes after sample change, is not disturbed by sample exchange. The time interval of 90 minutes is required for

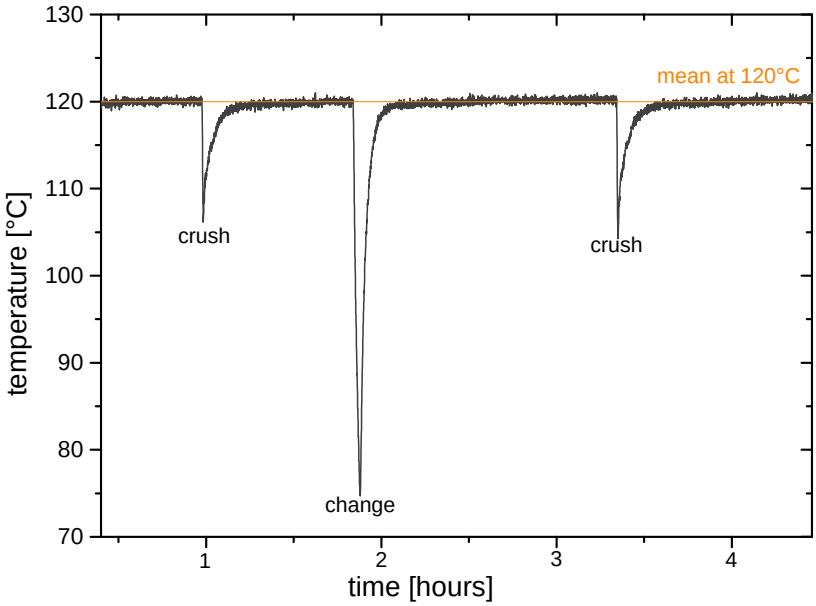

Figure 3.4: A representative temperature profile of the oven with which the main part of the extraction line is heated. When crushing the sample the oven door has to be opened, which is shown as the first and third drop. The temperature does not decrease below 100°C during crushing so condensation can be excluded. For a sample change the heating must be switched off temporarily, which leads to a strong temperature decrease whereby a constant temperature of 120°C is reached again after approximately 20 minutes.

the water vapour background to reach stable conditions (standard deviation below 20 ppmV) again and for the desorption of water molecules from the sample surface to be completed. As the desorption of water molecules would lead to a measurable shift of the isotopic composition towards lighter values, since due to fractionation isotopically heavier molecules preferentially adsorb onto an active grain surfaces [*Dennis et al.*, 2001]. I have investigated the effect of adsorption in detail in section 3.7.3.

3.2 Picarro analyser - *L2130-i*

In this thesis a cavity ring - down spectrometer *L2130-i* from the company Picarro is used as CRDS analyser. Picarro analysers use time - based optical absorption spectroscopy to determine the concentration or isotopic composition of the sample gases (more details see section 2.3). It is based on wavelength - scanned cavity ring - down spectroscopy (WS-CRDS), a method in which the laser beam passes through the sample many times, creating a long effective path length for the interaction of the light with the sample. *L2130-i* provides high quality measurements of $\delta^{18}O$ and $\delta^{2}H$, which are measured simultaneously every 0.8 seconds with a measurement range of vapour samples from 1 000 to 50 000 ppmV. The guaranteed precision at 2 500 ppmV for an integration period of 100 seconds is 0.080/0.500 ‰ for $\delta^{18}O/\delta^{2}H$. With a higher water vapour concentration of 12 500 ppmV the precision increases to 0.040/0.100 ‰ for $\delta^{18}O/\delta^{2}H$. The CRDS technology provided by Picarro guarantees a temperature and pressure controlled analyser, with a typical 24 h drift of 0.082/0.336 ‰ VSMOW for $\delta^{18}O/\delta^{2}H$ when measuring liquid samples [*Picarro*, 2015].

3.2.1 Short - term stability - 24 hours

Infrared spectrometers generate data that are affected by different types of noise (usually white noise), which can be significantly reduced by time averaging. As the integration time increases, it is expected that the precision of the measurements will initially improve by reducing the white noise up to the point where the instrumental drift becomes visible [*Casado et al.*, 2016]. This can be shown in a so - called Allan - Werle plot (see figure A.8). Here a 24 h experiment was performed with a water vapour mixing ratio of 15 700 ppmV. *Aemisegger et al.* [2012] has found the optimal integration time τ_0 to 100 min for oxygen and to 170 min for hydrogen.

I also performed a long - term measurement (22 h) where a significant lower water vapour concentration compared to *Aemisegger et al.* [2012] was established with a mean value and corresponding standard deviation of $6\,961 \pm 18$ ppmV for the last 30 min (detailed data is listed in table A.10). The isotopic signals for both $\delta^{18}O$ and $\delta^{2}H$ for the last 30 min obtained a mean value of -11.00 ± 0.21 ‰ and -54.01 ± 0.76 ‰, respectively (see figure 3.5). It is important to mention here that two systemic uncertainties appear for this *fluid inclusion line*. On the one hand, the water vapour concentration decreases during the course of the day by about 250 - 500 ppmV (see figure A.14), and

on the other hand, the isotopic composition of the background water changes (see figure 3.5).

The water standard that is used to generate the water vapour background concentration is stored in a bottle next to the oven. This is necessary because the line is constructed with the smallest possible volumes and, therefore, the setup is spatially limited. Even if this effect is small it leads to shorter optimal integration times than those found by *Aemisegger et al.* [2012]. The lowest standard deviations for oxygen and hydrogen were achieved for an integration time of 60 minutes (see table A.10), whereby the standard deviation barely changes after 100 seconds. For this setup a standard deviation of 0.208/0.731 ‰ VSMOW for $\delta^{18}O/\delta^{2}H$ is achieved for an integration time of 60 min, which is comparable to other CRDS systems operating in a constant flow mode. For example, *Gupta et al.* [2009] using WS - CRDS technology obtained a precision of 0.2/1.0 ‰ VSMOW for $\delta^{18}O/\delta^{2}H$ when measuring liquid samples evaporated onto a dry background. Considering once again the variation of the water vapour concentration, *Aemisegger et al.* [2012] found that for the *L2130-i* analyser the precision of the isotope measurements barely depends on the water vapour mixing ratio (see figure A.9). Therefore, if the isotopic measurements are not performed under dry conditions (< 500 ppmV), no correction due to different water vapour concentrations of the isotope signal are required.

For the calibration of the isotope signal, the measurement signal is integrated over a period of 60 min with a constant water vapour concentration. The resulting drift

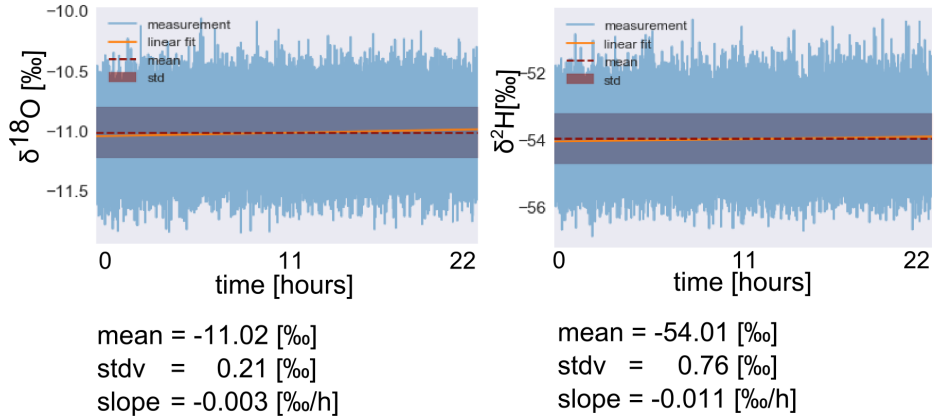

Figure 3.5: For the 22 h measurement of the *fluid inclusion line* a trend in the isotopic composition of the water vapour background is measurable. The isotope values of oxygen and hydrogen shift to heavier values due to evaporation in the supplying water bottle. Overall, a total deviation of 0.066/0.242 ‰ VSMOW for $\delta^{18}O/\delta^{2}H$ can be measured for the 22 h measurement. The mean value with associated standard deviation refers to the last 30 min of the measurement.

due to evaporation is 0.003/0.011 ‰ for $\delta^{18}O/\delta^{2}H$ and is thus, far below the uncertainty resulting from the standard deviation of 0.21/0.75 ‰. For the evaluation of the sample signal, the isotope signal is averaged over 30 min before each measurement and then calibrated with the independently measured standard (see section 3.5). Thus, for each measurement a relative calibration instead of an absolute calibration is carried out, accordingly drifts can be observed very well throughout the day.

3.2.2 Long - term drift - for several months

Since the *L2130-i* analyser is not calibrated daily, it must be ensured that no drift of the isotope signal occurs over a longer period of time. Therefore, it is verified if the calibration remains valid for several months. In fact, the calibration is repeated at regular intervals and the results of a selection of different standards are listed in table A.11. It shows, that the measurements agree within the standard deviation and only deviate by less than 0.1 ‰ for $\delta^{18}O$ and 0.5 ‰ for $\delta^{2}H$, respectively (see table A.11), even if there are several months or even one year between the respective measurements. Accordingly, a drift for this setup over a period of several months to a year can be excluded.

3.3 Measurement routine - daily and weekly

3.3.1 Daily routine

The daily routine of a measurement sequence follows the course shown in figure 3.6. Starting the nitrogen flow, the water supply and the heating causes a decrease of the water vapour concentration. After connecting the first sample, the setup requires approximately 90 minutes until the water vapour background has reached stable conditions. I verify this by calculating the standard deviation of the water vapour concentration over 30 minutes. If it is below 20 ppmV the sample is crushed with the hydraulic crusher. The oven door must be opened for this, which can be seen as a short dip in the water vapour concentration in figure 3.6. The actual sample measurement runs for 90 minutes to ensure that the complete peak is recorded. Afterwards, the line is opened and a new sample is installed. This can be seen in figure 3.6 as second or fourth increase in water vapour concentration, labelled *sample change*. This peak indicates desorption of water molecules from the speleothem surface. Thereby the peak height varies depending on the characteristics of the sample piece. For example, a pool spar with a larger surface area compared to a compact stalagmite sample desorbs more water. A detailed evolution of the water vapour concentration peak for four different speleothem samples is shown in the appendix in figure A.15. Since no spikes on the desorption signal are observed, thermal decrepitation of fluid inclusions can be excluded. This is a further proof that the chosen temperature (120°C) is not too high. After sample crushing, the initial water vapour concentration is reached again after approximately 1 h and the next speleothem sample can be measured 90 min after

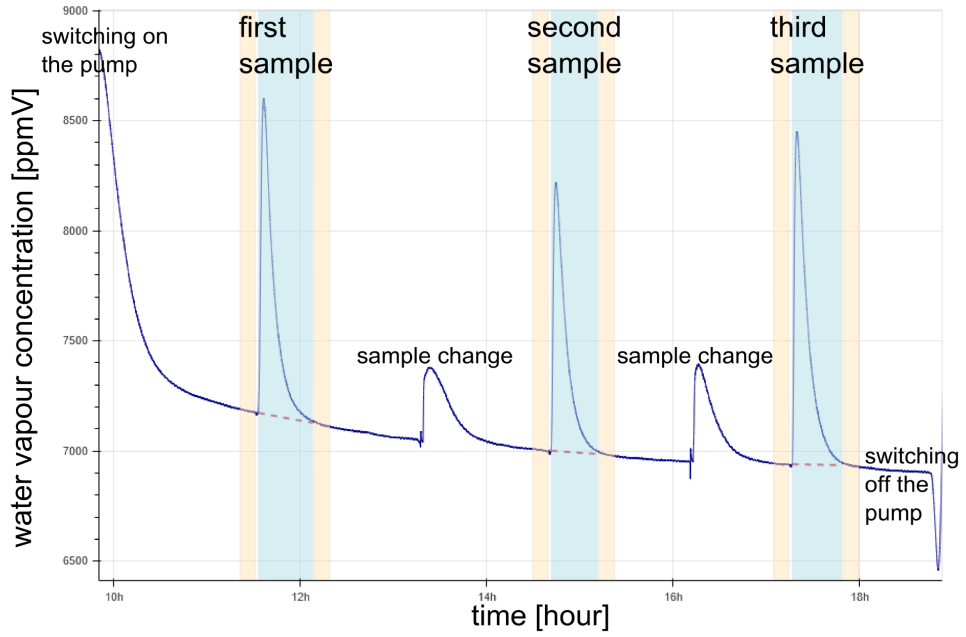

Figure 3.6: Water vapour concentration record of a measurement routine for a standard day on which three speleothem samples were measured. The actual measurement peak of the sample is shown in blue, the corresponding background in light brown with the linear regression of the background as a red dotted line. Installing fresh samples increases the water vapour concentration due to desorption of water molecules from the speleothem surface.

placement in the oven. Before crushing of the next sample the stability of the water vapour background is checked by calculating the standard deviation (< 20 ppmV). Typically three speleothem samples can be measured per day. Over night the CRDS analyser measures atmospheric air to avoid accidental flooding. Therefore, the heating, the water and nitrogen supply is switched off.

3.3.2 Weekly routine

On a weekly basis the calibration for the *Fluid inclusion line* is verified by isotope and volume calibration measurements. For this purpose, glass capillaries (see section 3.5.2) filled with water of known isotopic composition and volume are measured regularly. In addition, parts of the line to wear and tear are renewed on a weekly basis, this includes especially the pump tube of the peristaltic pump and the *FS* capillary, because the pump tube guarantees a constant volume delivery for a working time of 35 hours [*ISMATEC*, accessed January 09, 2020]. Other parts of the line, like the two septa of the injection ports, must be checked regularly and replaced if necessary. In addition, a fresh water standard to produce the water vapour background is filled up once a week.

3.4 Data Evaluation

The evaluation software provided by Picarro cannot be used for the stable isotope measurements of speleothems containing fluid inclusions. As mentioned before, liquid samples are measured by default with the CRDS analyser, but if operated in a constant flow mode the actual measured signal must be integrated over the corresponding time interval. With the isotope signal of oxygen and hydrogen, a splitting into light and heavy isotopes takes place (see figure 3.8). The light isotopes reach the analyser first due to fractionation. Simultaneously, the water vapour concentration changes (see figure 3.7). The released water is recognizable as a peak with a sharp increase and an exponential decrease. For this reason, I developed an evaluation protocol, which is partly based on *Affolter et al.* [2014]. Necessary for the evaluation are: water vapour concentration in ppmV, δ^{18}O in ‰ VSMOW and δ^{2}H in ‰ VSMOW over time, covering 40 min prior to the sample crushing and 40 min after the crushing. With the assistance of the Python script *IsoFluid*, which can be downloaded here `https://github.com/bhemmer/IsoFluid`, the import of the data and the actual evaluation can be carried out.

3.4.1 Peak detection

If a speleothem sample is crushed and contains water - filled fluid inclusions, a peak will appear in the water vapour concentration (see figure 3.7). The main evaluation step is to separate this sample signal from the manually generated water vapour background. I defined a slope criterion (dH_2O/dt) to detect the peak, which is generated by the released water. Therefore, peak - start is defined as a positive slope that must be above a threshold, with exemplary parameter setting see figure A.16. The same applies for peak - end, whereby the slope here is negative. Typically, the increase in water vapour concentration at the beginning of a peak takes place in small intervals of only a few data points (n = 5 and t = 4 s). Whereas the falling edge follows an exponential decrease, larger intervals are chosen (n = 300 and t = 240 s). In addition, at shallow slopes, the measured sample - based signal is superimposed by the signal of the peristaltic water pump. These pump cycles can also be seen in figure 3.7 as regular periodic waves. In order to filter out this disturbing signal, I apply the running mean method to calculate the undisturbed end criterion.

For the calculation of the peak - end criterion the water vapour background has to be considered. Because, the background water vapour concentration cannot be assumed constant during ongoing measurements (see figure 3.6) as it shows a decreasing trend through time. At the beginning of a measurement day, the slope is steeper than at the end, where the water vapour background can sometimes even rise. I take these background changes into account when fitting peak - start and peak - end, which is referred to as *water vapour background correction* (see section 3.4.1). Increase in water vapour concentration at peak - start is significant and happens between two to four

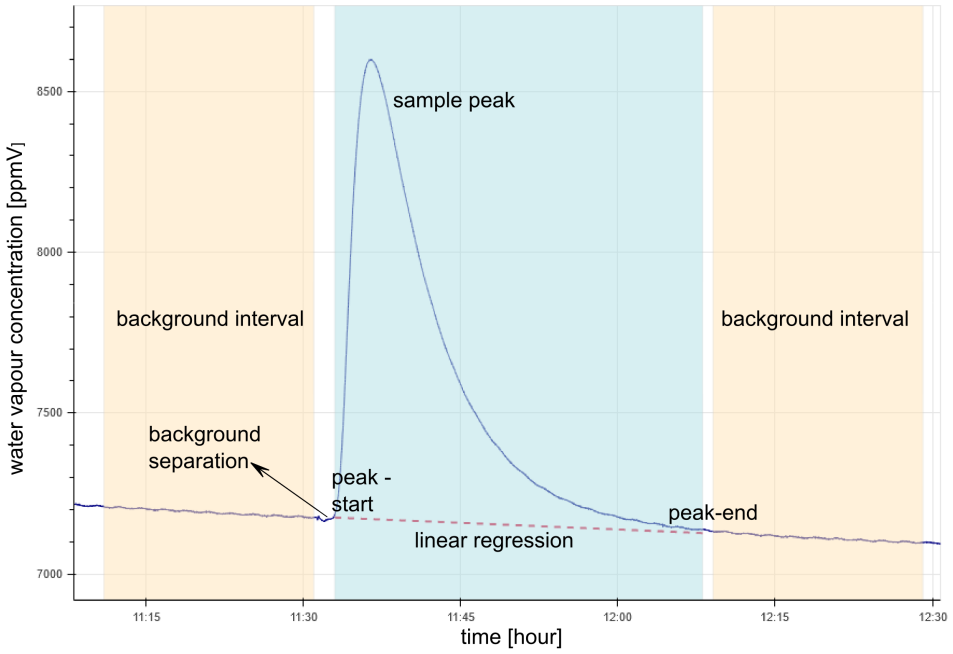

Figure 3.7: Peak evaluation of the water vapour concentration for a stalagmite sample. The sample - based signal interval is shown in blue and the corresponding background intervals in light brown. A superposition of the background signal with the signal of the peristaltic water pump (regular periodic waves) can be identified, which is considered by calculating the peak - end criterion. The linear decrease of the water background is fitted with a linear regression (dashed line).

data points (data points are recorded every 0.8 s). Therefore, the effect of background changes on the sample signal is negligible for the starting conditions. For the peak - end however, the sample signal needs to be corrected for the slope of the background.

Water vapour background correction

For the calculation of the water vapour background I selected two intervals, one directly before the peak and one afterwards. The duration of the intervals is set to 20 minutes, which has proven to be sufficient with the best fit - probability. Before the peak rises a drop in the water vapour concentration can be observed, which occurs due to the opening of the oven door. This cannot be avoided, but will be considered during the evaluation. It can be seen in figure 3.7 as a white space between background interval and peak - start. This intermediate interval is set to two minutes, which ensures that the undisturbed water vapour background is used to calculate the background signal. Once the two intervals are fixed, the background during the sample peak is simulated with a linear regression. The assumption of a constant mean value

is not adequate for calculating the water vapour background as it would underestimate the actual measured signal. An exact determination of the background and thus, of the sample signal is especially important for the accuracy of small amounts of water.

After peak - start (t_0), peak - end (t_1) and the corresponding water vapour background of the peak are defined, the water vapour concentration is integrated over the time interval t_0 - t_1 and corrected for the background (see equation (3.3)). The computed signal in ppmV·s can be converted to a water volume using the associate calibration described in section 3.5. In order to ensure a consistent evaluation of a data record, the specified parameters for the individual samples should not be changed. An example on how to select these parameters is given in section A.2, along with a brief explanation of how to use the *IsoFluid* script.

3.4.2 Transfer of t_0 and t_1 to isotope signal

Figure 3.8 shows the temporal evolution of the isotope ratios, which can be explained as follows: Due to isotope fractionation, the light isotopes evaporate first, which leads to a shift to more negative (lighter) values. Followed by the heavier isotopes, which leads to the opposite effect. This behaviour can be observed so clearly in figure 3.8, because a stalagmite sample (Stam 4 - Cloşani) was measured here with an isotope ratio similar to the one of the water vapour background (VE).

To evaluate the isotope signal, the start and end positions of the water vapour peak are transferred to the oxygen and hydrogen peak. However, the background of the isotope signal is calculated differently. As shown in figure 3.8, the background of the isotope signal is much more stable than that of the water vapour background. For this reason,

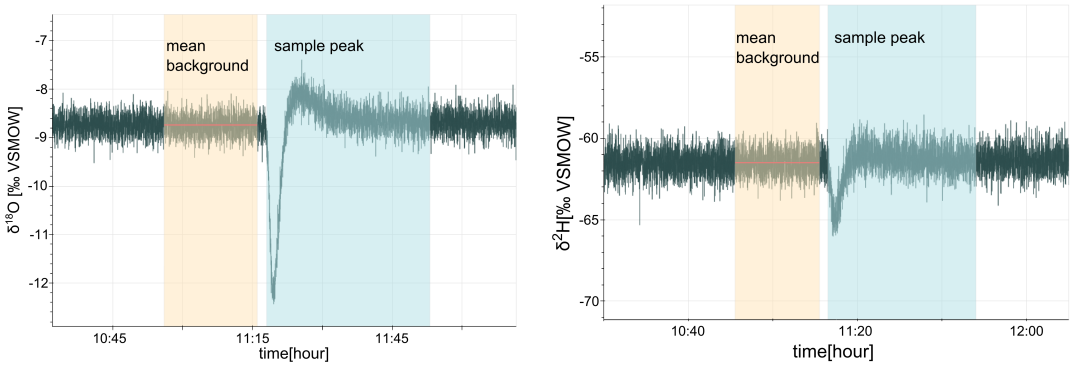

Figure 3.8: δ^{18}O evolution during sample crushing on the left and δ^{2}H on the right. The interval of the peak duration is shown in blue, the background interval in light yellow and the corresponding mean isotope signal of the background in red. A strong isotope fractionation can be observed, which leads first to a shift to more negative isotope values (lighter) and subsequently to more positive values (heavier).

the mean value method is adequate for this calculation. Only the interval before the peak is used to compute the mean background during the isotope peak of the sample. Similar to the calculation of the water background, there is an intermediate interval (related to the opening of the oven door) to exclude from the evaluation. When the isotope signal reaches equilibrium conditions again depends strongly on the deviation between sample signal and used isotopic composition of the background as well as on the amount of released water. Therefore, the duration until the isotopic equilibrium is reached again can vary between 10 and 45 min. For example shown in figure 3.8 the duration is approximately 20 min.

To calculate the isotope signal, the actual water volume must be taken into account. The evaluation for δ^{18}O and δ^{2}H is equivalent and illustrated exemplarily for oxygen:

$$\delta^{18}O_{sample} = \frac{\overbrace{\int_{t0}^{t1} \delta^{18}O_{sample}(t) \cdot H_2O_{sample}(t) \cdot \mathrm{d}t}^{\mathrm{A}}}{\underbrace{\int_{t0}^{t1} H_2O_{sample}(t) \cdot \mathrm{d}t}_{\mathrm{B}}} \tag{3.1}$$

with:

$$\mathrm{A} = \int_{t0}^{t1} \delta^{18}O_{mix}(t) \cdot H_2O_{mix}(t) \cdot \mathrm{d}t - \int_{t0}^{t1} \delta^{18}O_{back}(t) \cdot H_2O_{back}(t) \cdot \mathrm{d}t \tag{3.2}$$

and:

$$\mathrm{B} = \int_{t0}^{t1} H_2O_{mix}(t) \cdot \mathrm{d}t - \int_{t0}^{t1} H_2O_{back}(t) \cdot \mathrm{d}t \tag{3.3}$$

where A is the corrected isotope signal of the sample and B is the corresponding water signal. The measured signal of $\delta^{18}O_{mix}$ and H_2O_{mix} is a mixture of sample and background, with $\delta^{18}O_{back}$ and H_2O_{back} resulting from the background fit using the mean method for the isotope signal and a linear regression for the water vapour concentration, respectively. The time interval, t_0 to t_1, indicates the start and end point of the sample peak. Subsequently, the measured sample signal is calibrated as described in the following section.

3.5 Calibration

For the analysis of speleothem samples, both the isotope signal of oxygen and hydrogen and the amount of released water is relevant. For this purpose I have developed a new water amount calibration method using glass capillaries. This can also be used for inter - laboratories comparison, because the capillaries can be filled with water of a known isotopic composition and volume. This would allow the internal calibration of different laboratories working with similar setups to be analysed independently. For the calibration of the isotope signal I used five independently measured in - house standards.

3.5.1 Isotopic calibration

The five different standards used for calibration are listed in table 3.2. They were measured independently with the *LGR*[1] analyser at GGWI Group Heidelberg. The *LGR* analyser calibration procedure includes three in - house standards (DI, Colle and Alpen) spanning a range between -8.01 and -22.74 ‰ for δ^{18}O and -49.7 and -176.3 ‰ for δ^{2}H in VSMOW. At least once per year, the in - house standards are analysed against the international primary reference material VSMOW2 and SLAP2. In 2016, the IAEA has organized a worldwide comparison of stable isotopes in water [*Wassenaar et al.*, 2018]. Four unknown water samples were analysed in a routine sequence with the *LGR* analyser of the GGWI group. The reported results were within the uncertainty given by the IAEA. Offsets between the reported and the true value were smaller than 0.08/0.7 ‰ VSMOW for δ^{18}O/δ^{2}H [personal correspondence Martina Schmidt, 03.12.2019]. The desalinated deep sea water - *Kona* was measured in Mainz using mass spectrometry to -0.01/0.39 ‰ VSMOW for δ^{18}O/δ^{2}H [personal correspondence with

	δ^{18}O [‰ VSMOW]	error [‰ VSMOW]	δ^{2}H [‰ VSMOW]	error [‰ VSMOW]
Kona - ocean water	-0.05	0.08	0.54	0.70
VE - tap water	-8.75	0.08	-61.65	0.70
VCL - Alps	-13.04	0.08	-98.32	0.70
CC - Colle Alps	-15.13	0.08	-110.58	0.70
NG - North Greenland	-26.54	0.08	-212.11	0.70

Table 3.2: In - house water standards for isotopic calibration, which were independently measured at the *Institute of Environmental Physics* with the *LGR* analyser at GGWI Group Heidelberg [personal correspondence Martina Schmidt, 03.12.2019].

[1] Triple isotope water analyser TIWA - 45EP from Los Gatos Research company. In contrast to conventional CRDS, the laser beam is directed off - axis with respect to the cavity axis hence, the name Off - Axis Integrated Cavity Output Spectroscopy (OA-ICOS).

Hubert Vonhof, 25.07.2018]. This independent measurement shows a very good agreement within the uncertainty compared to the measurements on the *LGR*, which gives for *Kona* δ^{18}O values to -0.05 ± 0.08 ‰ and for δ^{2}H values to 0.54 ± 0.70 ‰ in VSMOW, respectively. Five water standards were selected to calibrate the *fluid inclusion line* spanning an isotope range of -26.5 up to 0.1 ‰ for δ^{18}O and -212.1 up to 0.5 ‰ for δ^{2}H in VSMOW, which includes the relevant range for speleothem samples.

The five different isotope background levels are realized by adding the corresponding standard water to the supplying water bottle of the peristaltic pump. Once a stable water vapour concentrations is achieved in the preparation line (stdv below 20 ppmV) the isotope signal is averaged over 60 minutes, which results in a standard deviation of 0.2/0.7 ‰ for δ^{18}O/δ^{2}H. In figure 3.9 the measured isotope signal with the standard deviation is plotted against the expected value that is based on independent analyses of the GGWI Group. Over a period of one year, the respective standards were measured twice without any significant discrepancies (see section 3.2.2). The data is fitted with a linear regression taking x- and y-uncertainties into account, resulting in $y = (0.99 \cdot x + 2.30)$ ‰ for oxygen and $y = (0.98 \cdot x - 7.77)$ ‰ for hydrogen. In the upper part of figure 3.9 the residuals for both calibrations are shown. Thereby, the residual is a quantity for the deviation from the measured value to the expected one and can be used to asses the quality of the regression.

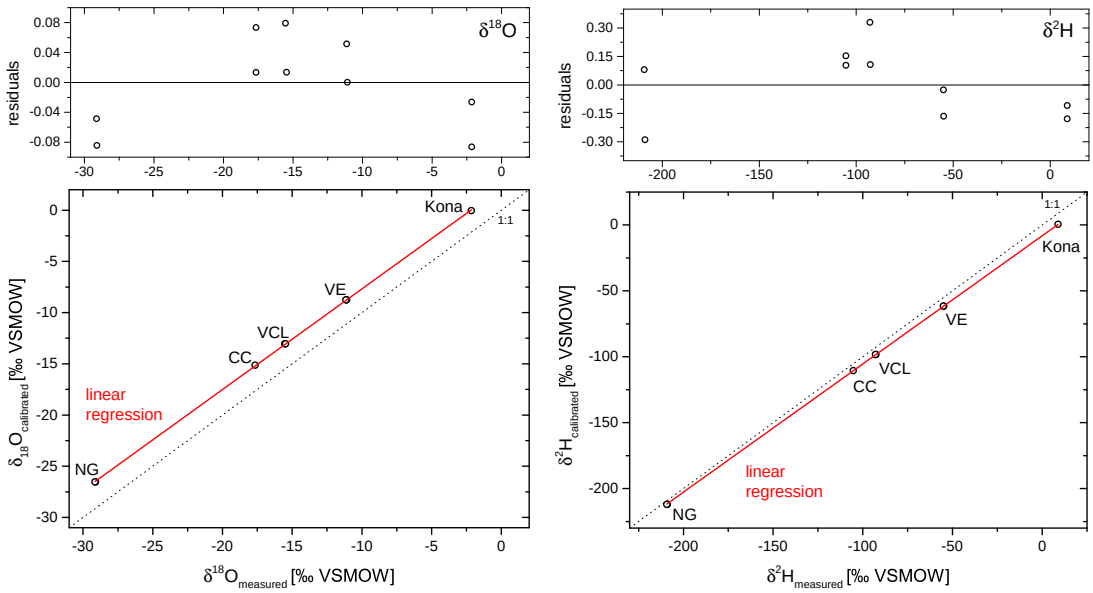

Figure 3.9: The calibration for oxygen and hydrogen results in a linear regression, where the uncertainties of x and y are taken into account. The calibration equation is $y = (0.99 \cdot x + 2.30)$ ‰ for oxygen and $y = (0.98 \cdot x - 7.77)$ ‰ for hydrogen, which have remained constant over time. The upper section shows the residuals.

Even if only a limited number of data points are available, it shows that the residuals are randomly distributed around zero. This proves that the selected linear regression model is appropriate.

3.5.2 Water amount calibration

Knowing the exact amount of released water from the crushed speleothem requires a precise water amount calibration. The standard volume calibration is carried out by injecting water in the μl range with syringes. At a more detailed analysis, however, the large uncertainty for this method becomes obvious (see section 3.5.3). Therefore, I have developed an individual water amount calibration method with glass capillaries, which can additionally be used for comparison between laboratories.

The glass capillary (borosilicate, see figure 3.10) can be filled with water of desired volume (0.1 - 5.0 μl) and isotopic composition. It is closed airtight by melting the edges off and the exact volume is defined by scanning the capillary and comparison with the 1 μl labels. This procedure is repeated five times and the mean value gives the exact volume with an volume uncertainty of 0.025 μl. In total 45 capillaries (table A.12 and A.13) were measured to calibrate a volume spanning a range from 0.2 up to 4.3 μl (see figure 3.10), which yielded a linear regression as $y = (5.9 \times 10^{-10} \cdot x - 0.011)\,\mu$l. The capillaries are measured weekly to monitor the stability of the calibration.

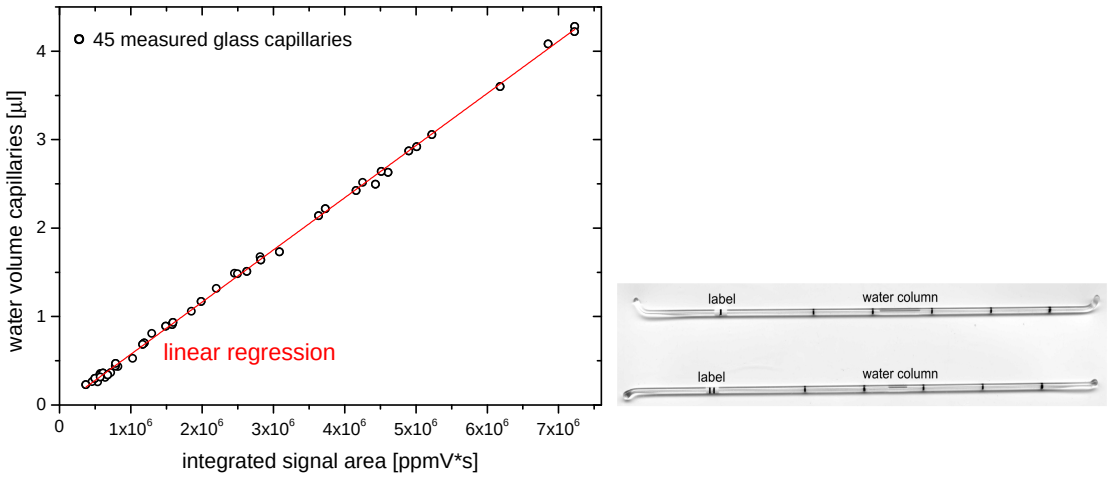

Figure 3.10: Left: The integrated measured volume signal in ppmV is plotted against the water volume in μl derived form the glass capillaries. The resulting linear regression $y = (5.9 \times 10^{-10} \cdot x - 0.011)\,\mu$l is used to determine the released amount of water from speleothem samples. Right: Picture scan of two glass capillaries at which the black labels indicate one microlitre steps. The added water is clearly visible as a dark column.

3.5.3 Volume accuracy of syringes compared to glass capillaries

The standard method for calibrating the water amount is by manual injection of various water volumes in the range of typical fluid inclusions. This has the advantage that the preparation line does not have to be opened and injections can be performed sequentially. With an injection port directly in front of the sample inlet (see point *B* in figure 3.1), an actual sample is simulated. I found, however, that different syringe brands have varying volume accuracies and do not achieve the accuracy of glass capillaries regarding the water amount. Therefore, I have selected two brands *Hamilton* and *SGE*, which are common for water amount calibration and tested them more intensively for accuracy and reproducibility.

To cover a volume range from 0.1 to 5 μl, two syringes with different volumes were used of both *Hamilton* and *SGE*. The 1 μl-syringe for all injections up to 1 μl and the 5 μl-syringe for all larger injections. The 1 μl-syringe from *SGE* is equipped with an additional injection help, which enables homogeneous injection and thus, achieves a higher volume accuracy. However, various problems with the handling of the syringes appeared. In some cases it was difficult to penetrate the septum or septum residues remained in the syringe needle and blocked it. Furthermore, the later evaluation showed that the actual injected volume deviates from the measured one. This is visible in figure 3.11, where the actual injected volume in μl is plotted against the evaluated volume in ppmV $\cdot$ s. Both syringe brands vary significantly in the evaluated signal, i.e. in the actual signal measured with the CRDS analyser and integrated over the peak duration (evaluation details see section 3.4), compared to the glass capillaries. From

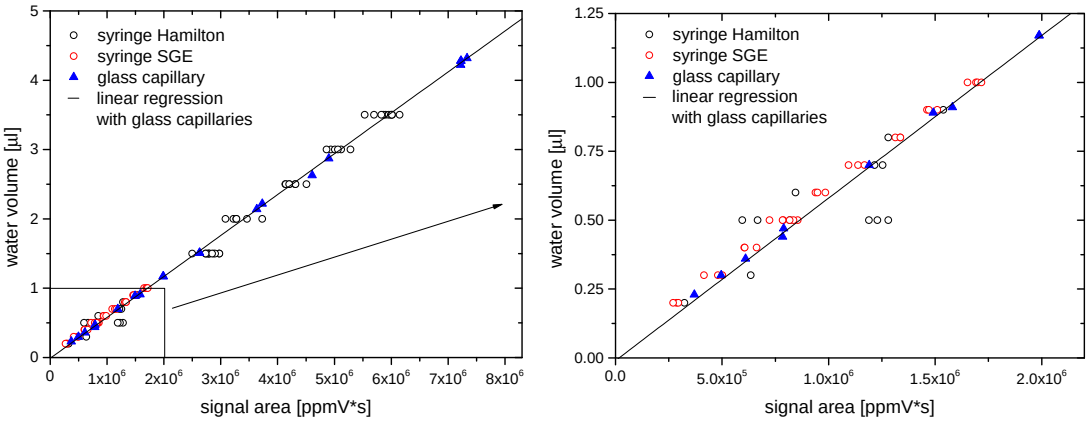

Figure 3.11: Left: The injected volume of the syringes is plotted against the integrated measurement signal ppmV $\cdot$ s for the *Hamilton* syringe (black circles), the *SGE* syringe (red circles) and the glass capillaries (blue triangles) with linear regression (black line). The actually injected volume of the syringes does not reproduce adequately. For a better overview, no error bars are included. Right: A zoom for the small volume range below 1 μl is shown.

figure 3.11, it is recognizable that especially *Hamilton* can not reproduce the desired volume and show significant scatter. The volume uncertainties of the syringes are: $\pm 0.02\,\mu$l for $1\,\mu$l - syringes and $\pm 0.1\,\mu$l for $5\,\mu$l - syringes. The volume accuracy of the glass capillaries from the graphic evaluation is much better with $\pm 0.0025\,\mu$l.

I have found that with the assistance of syringes only an approximate calibration for the released water amount is possible. Therefore, I decided to use the calibration method with water - filled glass capillaries for the water amount.

3.6 Precision of isotope measurement

The precision of isotopic measurements for the *fluid inclusion line* is quantified using the amount of variation in the data set based on the calculated standard deviation (see figure 3.12). For this purpose, water of a known isotopic composition, in this case *VE*,

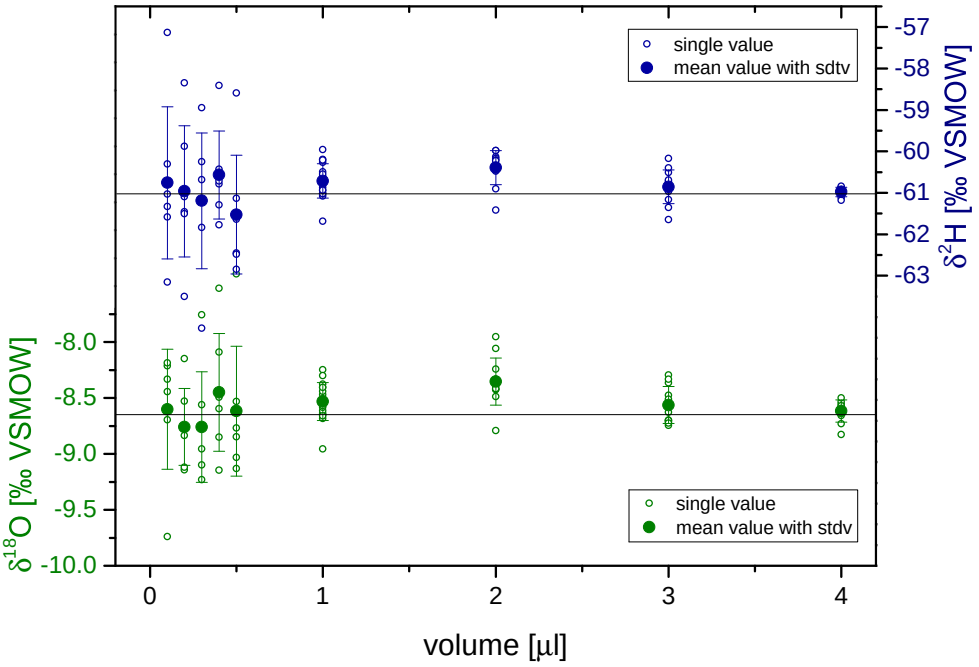

Figure 3.12: Precision of the isotope measurements with the individual injections (circles) shown over the gradually volume increase from 0.1 to $4.0\,\mu$l. The resulting mean values with associated standard deviation are shown as dots in green for oxygen and in blue for hydrogen. The standard deviation decreases with increasing volume. Thus, the precision of the isotope measurement improves with increasing volume. The black line gives the expected values for *VE* - tap water, which are: $\delta^{18}O = -8.57\,‰$ and $\delta^{2}H = -61.04\,‰$ in VSMOW. The results of the individual measurements are listed in table A.14.

was injected several times. The volume of the injection is gradually increased from 0.1 to 4.0 μl. Even if the number of injections is not equal for all volumes, a clear decrease of the standard deviation with increasing volume becomes apparent. For volumes above 1.0 μl, the standard deviation reduces from 0.50 to 0.15 ‰ for δ^{18}O and from 1.5 to 0.4 ‰ for δ^{2}H in VSMOW, respectively. For small volumes, i.e. below 1 μl, the individual values scatter significantly around the expected value (δ^{18}O = - 8.57 ‰ and δ^{2}H = - 61.04 ‰ in VSMOW). This indicates that small volumes have a higher standard deviation than larger ones. Accordingly, the precision of the isotope measurement improves with increasing volume.

The measurements shown in figure 3.12 demonstrate a high reproducibility of isotope ratios determined from μl water aliquots. However, this alone is not sufficient to conclude the actual uncertainty of a single measurement. Systematic errors must also be taken into account. For example does the difference in isotopic signal between the water vapour background used and the sample signal (see section 3.7.4) affect the actually measured isotopic composition of the sample? Even though the reproducibility for larger volumes above 1 μl decreases to less than 0.2/0.4 ‰ VSMOW for δ^{18}O/δ^{2}H, we have decided in favour of a conservative estimate of the uncertainty. The uncertainty for a single measurement of the isotope signal is 0.50 ‰ for δ^{18}O and 1.50 ‰ for δ^{2}H in VSMOW.

3.7 Possible disturbance effects during stable isotope measurement

When measuring fluid inclusions in speleothems, processes during sample processing and water extraction occur which can influence the measurement of the actual isotope signal. First, the liquid water in the inclusions is evaporated and then mixed with water vapour, that has a different isotopic composition than the sample. In addition, crushing a speleothem sample produces a large fresh calcite surface to which water molecules are most prone to adhere. Furthermore, the CRDS system used has an internal memory effect [*Gupta et al.*, 2009], which should be excluded with the construction of the preparation line. In the following, I investigated which effects are present and how they can influence or change the actual measurement of the isotopic signal.

3.7.1 Memory effect

If water samples are measured with CRDS system, the cavity is evacuated between each measurement. This leads to an unavoidable memory effect since water molecules from the previous measured sample remain in the cavity and affect the current one. This can be avoided when measuring liquid samples by injecting several times, because the isotopic signal will exponentially converge to the actual sample signal. This procedure is difficult to adapt for speleothem samples as they contain only small amounts of

water and, therefore, only one measurement is possible. *Gupta et al.* [2009] developed a method to quantify the memory effect and to apply this to speleothem samples. Since the memory effect is very consistent, a factor X can be determined with which the measured sample signal is subsequently corrected. In doing so, X is the memory coefficient for the nth injection with $(M-P)/(T-P)$, where M is the measured value of the actual injection, T is the expected value of the actual injection and P is the value of the previous injection. A memory coefficient close to one indicates that the measured value corresponds to the expected one.

To test the memory effect for the *fluid inclusion line*, a set of various standard waters was measured six times each including multiple injections (see table 3.3). It is ensured that the isotopic composition of the second injection is significantly different from that of the first one. Then, a possible memory effect can be quantified. Therefore, I started with the injection of *VE* - tap water, followed by several injections of *NG* - North Greenland water. These two standard waters have a large difference in the isotopic signal (with approximately 22 ‰ for δ^{18}O and 182 ‰ for δ^{2}H) and thus, a

Injections	X (δ^{18}O)	X (δ^{2}H)	Injections	X (δ^{18}O)	X (δ^{2}H)
test A			test D		
1	1.00	1.01	1	0.97	1.00
2	0.99	1.01	2	0.98	0.99
3	0.99	1.01	3	0.98	1.01
4	0.99	1.01	4	0.98	1.00
test B			test E		
1	1.00	1.01	1	0.99	1.01
2	1.01	1.02	2	1.01	1.03
3	1.01	1.01	3	0.99	1.01
test C			test F		
1	0.99	1.00	1	0.98	1.00
2	0.99	1.00	2	0.98	1.00
3	0.99	1.01	3	0.98	1.00

Table 3.3: Measured memory coefficient for the *fluid inclusion line* with six sets of multiple injections denoted by the capital letters A to F. The memory coefficient X is a ratio of (M - P) divided by (T - P), where M is the measured value of the actual injection, T is the value of the actual injection and P is the expected value of the previous injection. A X value close to one indicates that the measured sample corresponds to the expected value and that no memory effect occurs. Detailed data of all individual injections used to characterize the memory effect is listed in table A.15.

high probability of measuring a memory effect. Regarding the *fluid inclusion line*, it proves that the mean memory coefficient with corresponding standard deviation for all measurements is $X(\delta^{18}O) = 0.99 \pm 0.01$ and $X(\delta^{2}H) = 1.01 \pm 0.01$, respectively. Thus, a memory effect can be excluded. For a better classification of the results, *Uemura et al.* [2016] found a system memory for the 1st injection of previous water, expressed as a percentage of the previous sample, to 29.3 % for δ^{2}H and 6.9 % for δ^{18}O.

3.7.2 Amount effect

Recent studies on isotopic measurements in fluid inclusions of speleothems with similar CRDS systems have shown that an amount of water inferior to 1 µl can have a significant effect on the measured isotope signal [*Brand et al.*, 2009; *Arienzo et al.*, 2013; *Uemura et al.*, 2016]. Thus, *Brand et al.* [2009] found a deviation of 0.5 ‰ for $\delta^{18}O$ and even 1.6 ‰ for $\delta^{2}H$ from expected values when the injected water was reduced from 1.0 to 0.5 µl. The deviation increases even further for volumes below 0.5 µl and becomes nonlinear. For the *fluid inclusion line* a deviation of the isotopic composition for volumes below 1 µl is not observed (see figure 3.12 and table A.14). This is demonstrated in the precision measurements (see section 3.6), where injections of 0.1 up to 4.0 µl were measured. The standard deviation for volumes below 1 µl is significantly higher than for larger ones, but no trend can be detected. This is mainly due to the different measurement methods. As already mentioned, the line is operated in a constant flow mode. So a constant water vapour background (approximately 6 000 to 8 000 ppmV) is generated, which leads to a completely saturated surface of the entire line and the cavity in the CRDS analyser. Accordingly, it is not operated with almost dry conditions, which would correspond to a water vapour concentration of 10 up to 500 ppmV [*Picarro*, 2015]. With a cavity close to dry conditions, water molecules tend to adhere to the cavity walls, which may lead to fractionation. This is especially relevant when evaluating small water amounts. With a completely saturated surface of the cavity and the entire line, it is possible to measure even small water amounts down to 0.2 µl with a precision of 0.50/1.50 ‰ VSMOW for oxygen/hydrogen.

3.7.3 Adsorption and/or desorption on calcite surface

When a speleothem is crushed, a large fresh calcite surface is produced to which water molecules are most likely to adhere. This can lead to a large negative isotopic shift for both oxygen and hydrogen, as *Dennis et al.* [2001] showed for crushing at room temperature. *Dennis et al.* [2001] found that the degree of depletion is inversely related to the water/calcite ratio with fractionation of δ^{18}O exceeding -10 ‰ and δ^{2}H -20 ‰. Under vacuum conditions, a temperature around 130°C [*Vonhof et al.*, 2006] or even 110 to 120°C [*Dublyansky and Spötl*, 2009] is sufficient to avoid adsorption. Although, adsorption and/or desorption is less problematic working with a humid water vapour background, because the entire line and the cavity is saturated it should studied carefully.

I used an artificial inclusion calcite system (speleothem analogues) as it is described by *Dennis et al.* [2001] to quantify the influence of adsorption on the actual measured isotopic signal. Therefore, I measured Iceland spar (see figure 3.13) together with a water - filled glass capillary such as those used for water amount calibration. The size of the compact Iceland spar piece as well as the released water of the capillary represent a typical speleothem sample with a water content of 4.3 up to 7.8 μl per g calcite. An exemplary sample composition of the artificial inclusion calcite system is shown in figure A.18 and detailed data is listed in table A.16.

I started with inserting Iceland spar (inclusion free) without additional water in glass capillaries. As it can be seen in figure 3.13, the water vapour concentration decreases during crushing, which is indicative of an adsorption of water molecules on the freshly generated calcite surface. The measurement shown in figure 3.13 included a piece of Iceland spar with a sample weight of 0.25 g and led to an adsorption of 0.023 μl of water from the water vapour background. An effect on the isotopic background signal (see figure A.17) could not be detected. With further measurements of the artificial inclusion calcite system, it is investigated to what extent this limited adsorption of water influences the actually measured isotopic signal. In total, I prepared and compared five such calcite systems with measurements containing only water - filled glass capillaries without additional calcite. As can be seen in figure 3.14, the adsorption of water molecules on the calcite surfaces does not affect the actually measured isotopic signal. Both oxygen (green triangles) and hydrogen (blue triangles) accurately match the expected value.

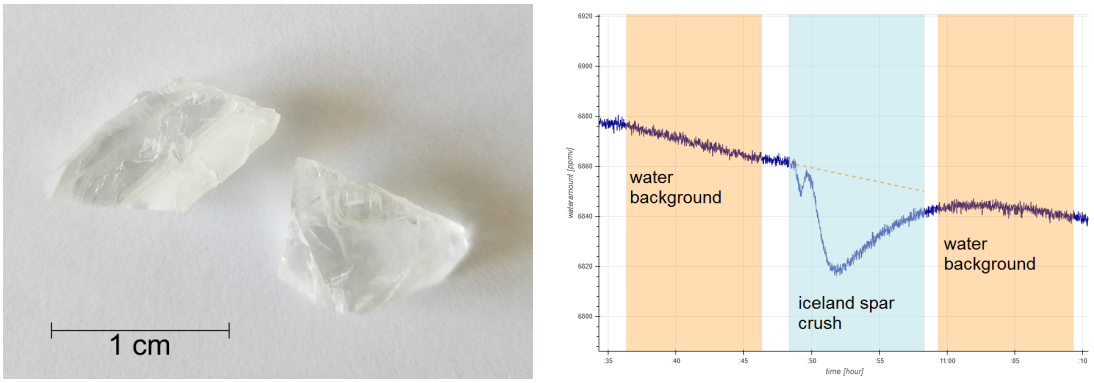

Figure 3.13: Left: Compact piece of transparent and inclusion free Iceland spar. Right: Measurement of the water vapour concentration during crushing of a 0.25 g Iceland spar piece. The decrease of water vapour concentration indicates an adsorption of water molecules on the freshly generated calcite surface. More precisely a depletion of 0.023 μl of water during crushing. The interval to calculate the water vapour background before and after the sample measurement is marked in orange, the actual measurement in blue.

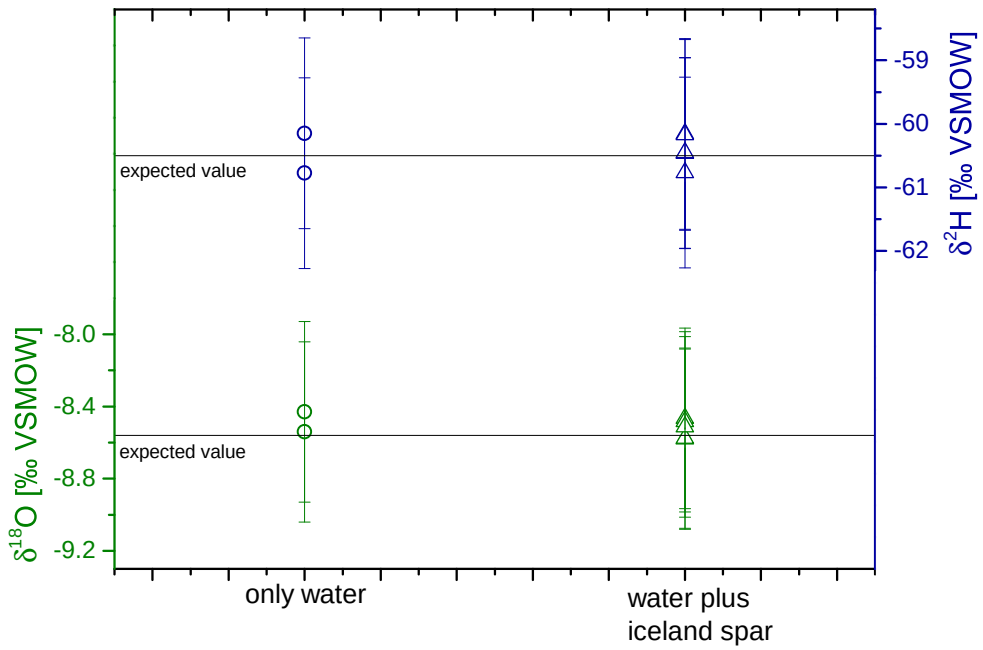

Figure 3.14: Results for the artificial inclusion calcite system, for which compact Iceland spar pieces were measured together with *VE* water - filled glass capillaries, shown as triangles. The circles indicate water - filled glass capillaries (*VE*) without calcite addition measured for comparison, with δ^{18}O data in green and δ^{2}H in blue. A fractionation due to adsorption of water molecules on the calcite surface is not detectable. Detailed data of the individual measurements is listed in table A.16.

With a standard deviation of 0.05 ‰ for δ^{18}O and 0.22 ‰ for δ^{2}H in VSMOW, a very good reproducibility of the individual measurements is achieved.

The artificial inclusion calcite systems selected here correspond to a speleothem analogues with a high water content (4.3 - 7.8 μl/g). In order to conclusively quantify the influence, it is recommended to measure small amounts of water, ranging from 0.2 to 0.5 μl, and Iceland spar samples with a weight of 0.5 g. Here the analysed Iceland spar sample (0.25 g) adsorbed 0.023 μl water, which correspondence to a ratio of approximately 0.1 μl water per g calcite.

Affolter et al. [2014] describes desorption of atmospheric water vapour on the stalagmite sample when it is placed in the copper tube and connected to the line. An increase in water vapour concentration is visible for the first minutes of heating and depends on the sample surface and amount of material. The desorption signal of four different sample changes is shown in figure A.15. The total release of the desorbed water lasts between 30 to 60 minutes and is completed before the actual measurement

takes place. This is ensured by monitoring the background water vapour concentration, because only when the original background value is reached again, the sample is crushed and measured.

3.7.4 Effect of isotopic background

I have investigated to what extent the isotope signal of the background vapour influences the actually measured sample signal. This is especially relevant for speleothem samples whose isotopic composition strongly differs from that of *VE* - water that is used as the standard background.

For this test measurement, I injected *VE* - tap water on four different water vapour isotope backgrounds (see figure 3.15). The used standard background waters are: *NG* - North Greenland, *CC* - Alps Colle, *VE* - tap water and *WW* - lake water (Willersinnweiher). In addition, I decided to use *VE* - water as injection, because its isotopic composition is comparable to the majority of mid - latitudes speleothems. In total, five times 3.0 μl of *VE* - water were injected, the results of the individual measurements are listed in table A.17. This time the standard deviation is not used as an uncertainty. Since the uncertainty of the expected value must also be taken into account, with 0.08/0.7 ‰ for $\delta^{18}O/\delta^{2}H$, which are measured independently with the *LGR* analyser (see section 3.5). If the isotope signal of the sample to be measured corresponds to that of the background (see figure 3.15) no deviation can be detected. Therefore, the mean value corresponds to the expected value, which for example is the case if

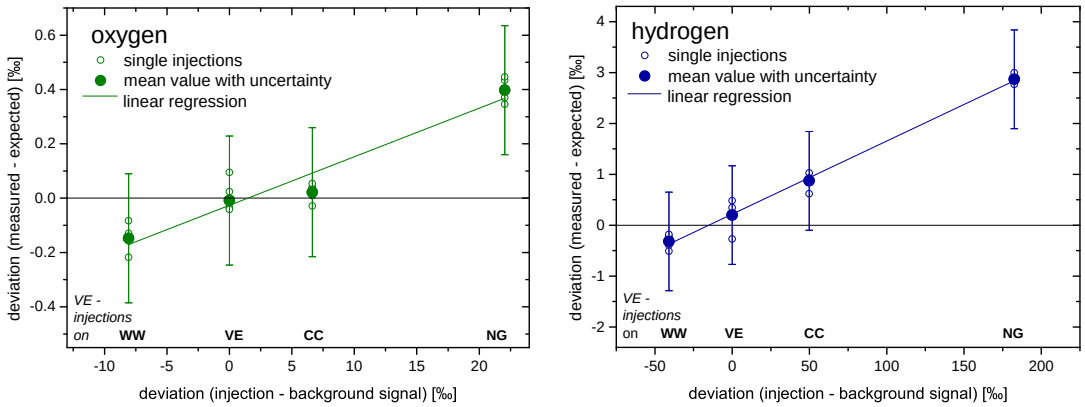

Figure 3.15: The deviation of the measured injected isotope signal to the expected value is shown depending on the difference of the injection to the isotope signal of the background. Single injections are shown as circles and the corresponding mean values as dots, with oxygen in green and hydrogen in blue. The green/blue line indicates the linear regression of the single measurements. No deviation is detectable if the measured isotopic signal corresponds to the one of the water vapour background. Whereas, if the deviation between the measured isotopic signal and that of the background increases, a deviation becomes obvious.

VE - water is injected on *VE* background water vapour. However, if the deviation between the measured isotopic signal and that of the background increases a deviation is obvious. For example, with *VE* injections on *NG* water vapour background, a deviation of +0.40 ‰ for δ^{18}O and even +2.87 ‰ for δ^{2}H, both in VSMOW, is measurable.

It is debatable why such a characteristic arises. Intuitively one would assume that the isotopic signal of the background affects the actual measurement. The preparation line is completely saturated with the background water vapour and is, therefore, dominated by this isotope signal. For a relatively light background water like *NG* this would mean that the measured *VE* signal should shift to lighter and thus more negative values. Considering that *North Greenland* with an isotopic composition of −26.54 ‰ for δ^{18}O and −212.11 ‰ for δ^{2}H in VSMOW, is much lighter than *VE tap water* with $\delta^{18}\mathrm{O} = -8.75$ ‰ and $\delta^{2}\mathrm{H} = -61.65$ ‰ in VSMOW. In fact, exactly the opposite is true. The measured signal of a *VE* injection on a *NG* background becomes heavier (more positive). It seems that the isotope signal of the injection dominates and the background signal is superimposed at the moment of injection. The water vapour background is generated by the peristaltic pump, which supplies 1 µl per minute to the line. The injection, however, introduces 3 µl into the line within a few seconds. Thus, at the moment of injection the dominant isotopic signal is that of the injection. In the case of a *VE* - injection on *NG* - background, the isotopic signal of *North Greenland* water vapour background is superimposed by relatively heavier water and thus, the actually measured injection signal is shifted to heavier (more positive) values.

To test this hypothesis and actually determine a correction factor for the isotope measurements in fluid inclusions, further measurements need to be performed. In doing so, the volume of the injections should be varied (0.2 - 5 µl) in order to test whether the injection itself actually has an influence on the measured isotope signal. If this hypothesis is correct a clear volume dependence should be detectable, i.e. a stronger deviation of the measured isotope signal for larger injected volumes. Hence, an intensive study have to be performed to quantify the effect accurately and apply this correction to real speleothem samples. Indeed, this deviation is only relevant for speleothem samples with an significantly different isotopic composition of the fluid inclusions compared to the background (± 10 ‰ for δ^{18}O and ± 50 ‰ for δ^{2}H). Otherwise it is covered by the conservative uncertainty estimation.

3.7.5 Implication for fluid inclusion measurements

I investigated how possible disturbance effects could influence or change the actual measurement of the isotopic signal of fluid inclusions. Thus, I was able to show that both a memory effect and an amount effect can be excluded. In addition, the adsorption of water during crushing is observed, but this has no effect on the measured isotope signal of the speleothem sample. However, the selection of the water vapour background used has an impact. It is important to ensure that the isotope signal of the

water vapour background corresponds to that of the fluid inclusion of the speleothem to be measured ($\pm 10\,‰$ for δ^{18}O and $\pm 50\,‰$ for δ^{2}H). Although, a considerably lower standard deviation is observed for released volumes above $1\,\mu$l. I have decided on a conservative estimate of the error of the individual measurement, with $0.5\,‰$ for δ^{18}O and $1.5\,‰$ for δ^{2}H in VSMOW. This uncertainty can be reduced by measuring replicates.

3.8 First test speleothem samples - reproducibility and accuracy measurements

After successfully construction and calibrating the *fluid inclusion line* the first measurements were performed. For testing purpose different speleothem types were investigated, e.g. soda straws, stalactites and pool spars from German caves. These first measurements were mainly used to become familiar with the measurement routine and to optimally adapt the evaluation software. In order to verify the accuracy of the *fluid inclusion line*, I exchanged reference samples with Hubert Vonhof (Max Planck Institute for Chemistry in Mainz) and wit Stéphane Affolter (University of Bern). The speleothem measurements performed in Mainz were conducted with a standard Thermo Finnigan TC - EA pyrolysis unit with an additional crusher and cold trap unit [*Vonhof et al.*, 2006], while the measurements in Bern were performed with the analogue CRDS setup [*Affolter et al.*, 2014].

3.8.1 Different types of speleothem samples - reproducibility measurements

I selected three different speleothem samples for the first test measurements: soda straws, stalactites and pool spars. For all three samples sufficient material was available to perform several replicate measurements. The Bunker Cave (soda straw), as well as the Dechen Cave (sinter) and also the Hüttenbläserschacht Cave (pool spar) are located close to Iserlohn. All three caves are part of extensive DFG funded research group DAPHNE. Moreover, in section 5 I examined the stalagmite Bu4 from the Bunker Cave in more detail.

Sinter and soda straws from Dechen Cave and Bunker Cave

The sinter (left side of figure 3.16) has grown on a power cable accordingly, a recent growth can be assumed. Overall six replicate measurements (see table 3.4) were carried out with a mean value and the corresponding standard deviation of $\delta^{18}O = -6.01 \pm 0.65\,‰$ and $\delta^{2}H = -48.58 \pm 0.66\,‰$ in VSMOW. For a better classification of the measured isotope values the mean drip water composition for the Dechen Cave is given here: $\delta^{18}\mathrm{O} = -8.4\,‰$ VSMOW [*Wurth*, 2003]. It is evident that the measured fluid inclusion value for oxygen deviates significantly from the expected drip water composition. A reason for the shift of the oxygen isotopic composition to

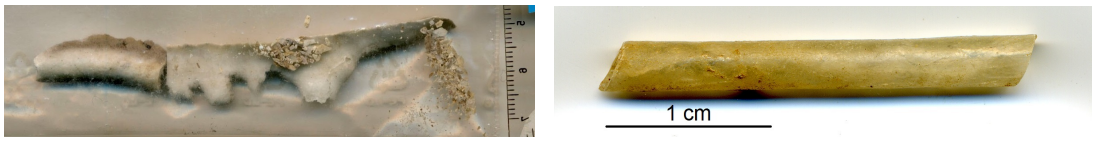

Figure 3.16: Left: A sample picture of a recent precipitate growing on a power cable in the Dechen Cave. Right: Picture from a soda straw growing in the Bunker Cave.

heavier (more positive) values could be, that the sinter experienced additional heating during calcite precipitation. Because the sinter grew on a power cable, which is used for lighting. Therefore, it can be assumed that the cable heats up under electricity flow and accordingly, also the drip water from which the stalactite precipitates. Nevertheless, the replicate measurements show good reproducibility with a standard deviation of 0.65/0.66 ‰ VSMOW for δ^{18}O/δ^{2}H.

As a second set of test samples, four replicates of the soda straws (right side of figure 3.16) from the Bunker Cave were analysed. The resulting mean values with corresponding standard deviation are given to $\delta^{18}O = -5.80 \pm 1.11$ ‰ and to $\delta^{2}H = -47.52 \pm 2.76$ ‰ in VSMOW (see table 3.4). In direct comparison to the sinter sam-

	sample ID	mass [g]	water volume [μl]	water content [μl/g]	δ^{18}O [‰]	error [‰]	δ^{2}H [‰]	error [‰]
Dechen Cave								
	A	1.2	0.66	0.5	-6.20	0.50	-47.90	1.50
	B	0.5	0.27	0.5	-6.45	0.50	-49.44	1.50
	C	0.6	0.30	0.5	-5.57	0.50	-48.99	1.50
	D	0.6	0.34	0.6	-6.17	0.50	-48.75	1.50
	E	0.5	0.27	0.5	-4.81	0.50	-47.51	1.50
	F	1.2	0.61	0.5	-6.83	0.50	-48.87	1.50
	mean	-	-	-	-6.01	0.65	-48.58	0.66
Bunker Cave								
	A	1.3	0.63	0.5	-7.26	0.50	-50.19	1.50
	B	1.4	0.26	0.2	-4.53	0.50	-47.18	1.50
	C	2.7	1.01	0.4	-6.47	0.50	-49.57	1.50
	D	1.6	0.18	0.1	-4.95	0.50	-43.15	1.50
	mean	-	-	-	-5.80	1.11	-47.52	2.76

Table 3.4: Results of water stable isotope measurements (in VSMOW) of fluid inclusions for sinter (Dechen Cave) and soda straws (Bunker Cave) are given as well as the mean values with corresponding standard deviation.

ples a stronger variability of the individual measurements becomes noticeable. Here the standard deviation increases from 0.65 to 1.11 ‰ (1σ) for δ^{18}O and from 0.66 to 2.76 ‰ (1σ) for δ^{2}H. For the soda straw samples no further information like $\delta^{18}O_{calcite}$ or age distribution is available. However, if the results are compared with current drip water data from the Bunker Cave a distinct deviation is noticed. Current drip water data is given to -8.0 ± 0.2 ‰ for δ^{18}O and -54.5 ± 1.5 ‰ for δ^{2}H, in VSMOW [*Riechelmann et al.*, 2011]. Soda straws are narrow, hollow tubes of stalactites in which the drip water flows along the length of the soda straw growing down from the cave ceiling. Depending on the drip interval, the length of the flow path and the humidity in the cave, it is not clear how fluid inclusions are formed. Therefore, also evaporation effects during soda straw formation are possible and it is questionable whether a drip water isotope composition is to be expected at all.

Pool spar from Hüttenbläserschacht Cave

I selected pool spars from three different ponds out of the Hüttenbläserschacht Cave to analyse them as a third set of test samples. Pool spars are speleothem formation, which precipitate below the water surface. The entrapped fluid inclusions should therefore correlate to the isotopic composition of the pond. It is possible that the ponds may experience evaporation effects as well. Also for these samples no further information about age distribution or calcite composition is available.

Nevertheless, I compared the stable isotope results with the LMWL (see figure 3.17), which is computed from rain water samples collected at the German Cave Museum Iserlohn. It shows that the respective individual measurements (see table A.18) of the different ponds reproduce and scatter around the LMWL. The fact, that the data fits to the LMWL excludes evaporation effects in the pond water and proves that the measurements are reliable. Since no drip water data is available for this cave, the data of the Bunker Cave (blue triangle) is shown for a better comparison. The uncertainties of the mean values plotted in figure 3.17 are calculated after the propagation of uncertainty. The standard deviation appears to be meaningless for a mean value consisting of two individual measurements. In particular, the composition of the oxygen isotopes of pool spar and drip water agrees very well. The mean value of all pool spars from the different pond results to -7.62 ± 0.23 ‰ for δ^{18}O and -50.87 ± 1.47 ‰ for δ^{2}H. Compared with the mean drip water of the Bunker Cave, -8.0 ± 0.2 ‰ for δ^{18}O and -54.5 ± 1.5 ‰ for δ^{2}H, especially the δ^{18}O data corresponds within the uncertainty.

In summary, the *fluid inclusion line* is able to measure different types of speleothem samples with high reproducibility, e.g. for the sinter growing on power cable with a standard deviation of 0.65/0.66 ‰ for δ^{18}O/δ^{2}H. The measurement of the pool spar and the comparison with the LMWL shows that reliable stable isotope values are produced for fluid inclusions of speleothems. Furthermore, the conservative uncertainty estimation of 0.5/1.5 ‰ for δ^{18}O/δ^{2}H chosen for this purpose proves to be realistic.

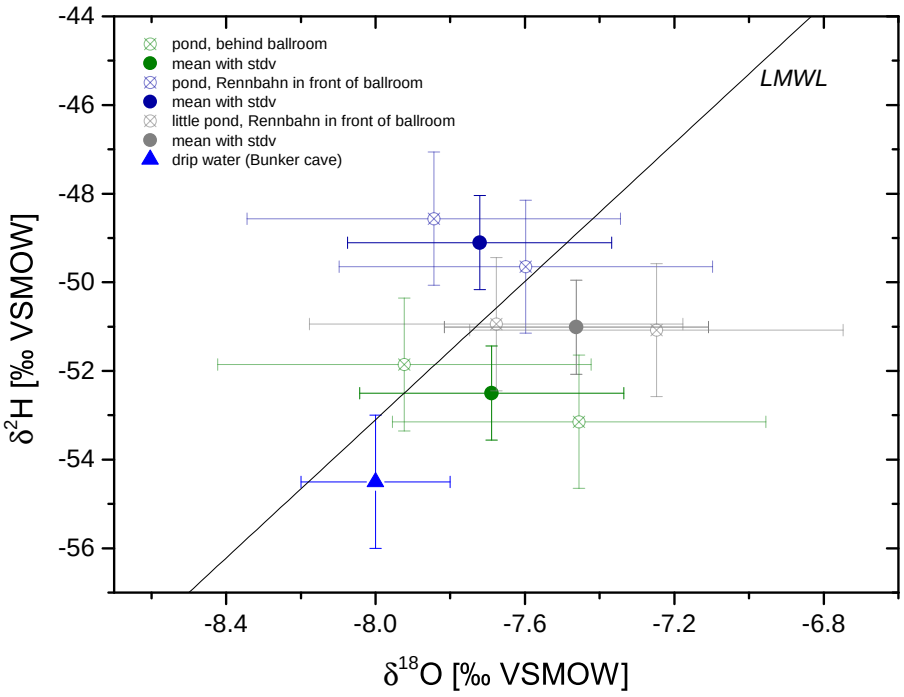

Figure 3.17: Results of stable isotope measurements of fluid inclusions for pool spar speleothems from Hüttenbläserschacht Cave. The mean values for the three different ponds are shown as dots and the corresponding individual measurements as circles. The isotopic composition of the mean drip water (blue triangle) for the Bunker Cave is shown as well as the LMWL (black line) with $\delta^2 H = 7.72 \cdot \delta^{18} O + 7.14\,‰$ VSMOW [*Riechelmann et al.*, 2017].

3.8.2 Comparison between laboratories - accuracy measurements

Two different types of speleothem samples were selected for the comparison measurements with Hubert Vonhof (Max Planck Institute for Chemistry in Mainz) and with Stéphane Affolter (CRDS analogous in Bern). The stalagmite from the Huagapo cave in the Peruvian Andes was measured with both setups, whereas the flowstone from the Scladina cave in Belgium was only measured with IRMS. I measured a series of five replicates in the case of Huagapo and four of Scladina with the *fluid inclusion line*. The results for each measurement as well as the mean value and the corresponding standard deviation are listed in table 3.5.

It proves, that the individual measurements of Huagapo reproduce within a standard deviation of $0.75/1.35\,‰$ for $\delta^{18}\mathrm{O}/\delta^{2}\mathrm{H}$ and of Scladina with a standard deviation of $0.48/0.35\,‰$ for $\delta^{18}\mathrm{O}/\delta^{2}\mathrm{H}$. In a direct comparison Heidelberg/Mainz the results for Scladina correspond within the uncertainty, with $-5.49/-5.51\,‰$ for $\delta^{18}\mathrm{O}$ and $-44.59/-42.50\,‰$ for $\delta^{2}\mathrm{H}$. For Huagapo the oxygen isotope data reproduces as well

	sample #	δ^{18}O VSMOW [‰]	error VSMOW [‰]	δ^{2}H VSMOW [‰]	error VSMOW [‰]	water content [μl/g]
Huagapo						
	a	-16.61	0.5	-122.18	1.50	1.92
	b	-17.34	0.5	-125.81	1.50	1.72
	c	-16.84	0.5	-124.47	1.50	2.03
	d	-15.68	0.5	-123.62	1.50	1.59
	e	-17.92	0.5	-125.66	1.50	1.62
mean with stdv		-16.88	0.75	-124.35	1.35	
IRMS (Mainz)		*-16.25*	*0.40*	*-118.00*	*3.00*	
Picarro (Bern)		*-16.1*	*0.5*	*-124.2*	*1.5*	
Picarro (Bern)		*-16.3*	*0.5*	*-124.5*	*1.5*	
Scladina						
	a	-5.70	0.50	-44.76	1.50	1.57
	b	-5.86	0.50	-45.03	1.50	2.97
	c	-5.80	0.50	-44.50	1.50	2.77
	d	-4.68	0.50	-44.09	1.50	1.70
mean with stdv		-5.51	0.48	-44.59	0.35	
IRMS (Mainz)		*-5.49*	*0.40*	*-42.50*	*3.00*	

Table 3.5: Results of the inter laboratory comparison for the stable isotope measurements of fluid inclusions. With the *fluid inclusion line* a series of replicates was measured for Huagapo as well as for Scladina. The mean values with the corresponding standard deviation are given in direct comparison to the single measurements performed with IRMS or CRDS.

with $-16.88/-16.25\,‰$ measured at Heidelberg/Mainz. Indeed, for hydrogen the expected value is not precisely reached and deviates significantly with almost 6 ‰. This could also be explained by the natural heterogeneity in the samples, which is already recognizable in the larger standard deviation for Huagapo in comparison to Scladina. In fact, two bands were measured for Huagapo (data listed in table A.19), which differ from each other by about 4 ‰. Since stalagmites are natural samples it is difficult to measure actual replicates. All units are given relative to VSMOW.

If Heidelberg and Bern are compared, a very good correspondence between the two setups is shown. With the CRDS analogous based in Bern the fluid inclusions of the stalagmite Huagapo were measured to - 16.2 ‰ for δ^{18}O and - 124.35 ‰ for δ^{2}H. This is in excellent agreement with the mean values of this *fluid inclusion line*, which are $-16.88 \pm 0.75\,‰$ for δ^{18}O and $-124.35 \pm 1.35\,‰$ for δ^{2}H, with all units relative to VSMOW.

This inter laboratory comparison shows that with the *fluid inclusion line* based in Heidelberg it is possible to perform very accurate stable isotope measurements, with e.g. for Scladina a deviation below 0.1/2.0 ‰ for δ^{18}O/δ^{2}H. These results are particularly important as two different measurement methods, IRMS and CRDS, were compared. Comparing the same measurement technique with the CRDS analogous based in Bern, accurate stable isotope results were achieved.

3.9 Technical conclusion

- Advantages of the CRDS method (with *L2130-i* analyser) compared to IRMS
  - The CRDS method is less expensive than the classical method with IRMS (factor 3 - 5).
  - The measurement setup (preparation line) is mechanically more robust, because it is not operated in vacuum but with an overpressure of about 0.5 bar.
  - *L2130-i* analyser from Picarro provides accurate and precise stable isotope measurements with a guaranteed precision of 0.080/0.500 ‰ for δ^{18}O/δ^{2}H at a water vapour concentration of 2 500 ppmV and with an integration time of 100 s [*Picarro*, 2015].
  - The *L2130-i* analyser shows no dependence of the precision of the stable isotope measurements regarding the water vapour concentration [*Aemisegger et al.*, 2012].

- Advantages of operation with a saturated water background
  - The isotope and volume calibration for the preparation line with connected *L2130-i* analyser remains valid for several months.
  - I could prove with direct comparison measurements that the adsorption of water molecules on the speleothem surface has no effect on the measured isotope signal.
  - I could exclude an amount effect as well as the memory effect for this system. However, when choosing the water vapour background it should be taken into account that the isotope signal of the sample and that of the background do not deviate significantly in the isotopic composition (± 10 ‰ for δ^{18}O and ± 50 ‰ for δ^{2}H).
- Precision and accuracy of the *fluid inclusion line*
  - I achieve a precision of isotope measurements for aliquots of water from speleothem fluid inclusions to 0.5 ‰ for δ^{18}O and 1.5 ‰ for δ^{2}H relative to VSMOW.
  - This precision is comparable to other CRDS systems such as *Arienzo et al.* [2013] (0.5/2.0 ‰ for δ^{18}O/δ^{2}H) and *Affolter et al.* [2014] (0.5/1.5 ‰ for δ^{18}O/δ^{2}H).
  - The precision is also comparable to traditional measurement techniques, like IRMS, which achieve a precision to ± 0.5 ‰ for δ^{18}O and 2.0 ‰ for δ^{2}H for a single measurement [*Dublyansky and Spötl*, 2009].
  - The inter laboratory comparison measurements with IRMS [*Vonhof et al.*, 2006] and the CRDS analogous [*Affolter et al.*, 2014] show the accuracy of the isotope measurements performed with *fluid inclusion line*.

4 Case study I: Late Holocene stalagmite (1911 - 2010) in the transitional climatic zone - Romania, Cloșani Cave

I selected Stam 4 for a first detailed fluid inclusion study on a late Holocene stalagmite covering the 20th century between 1911 - 2010. The stalagmite was collected by an expedition conducted by Sylvia Riechelmann in the Cloşani Cave, which is one of the most famous caves in Romania. The cave was first cited scientifically in 1913 and has been part of intensive scientific studies [*Diaconu*, 1990; *Constantin and Lauritzen*, 1999; *Warken et al.*, 2018]. Located on the southern slope of the Carpathians, the cave is in a climatic transition zone between Central Europe and the Mediterranean. Thus, the mountain range divides Romania into two main regions with different climatic characteristics by blocking the mixing of the northern polar/Arctic and southern Mediterranean air flows. For the Carpathians temperature reconstruction of the late Holocene are mainly based on tree rings [*Levanič et al.*, 2013; *Popa and Kern*, 2009], which are biased towards the growing season (summer months). However, *Warken et al.* [2018] showed that speleothem growth in the Cloşani Cave is favoured in autumn and winter. The actively and fast growing stalagmite Stam 4 contains many water - filled inclusions (mean water content of 0.90 μl/g), making it a perfect research object for studying the stable isotope composition in fluid inclusions for a modern stalagmite. Due to the continental location of the cave, the relationship between the isotopic composition of precipitation and air temperature (δ^2H/T) [*Rozanski et al.*, 1992] can be used to determine cave temperatures by measuring the $\delta^2 H_{fluid}$ signal [*Demény et al.*, 2017; *Affolter et al.*, 2019]. The results can be directly compared with the local mean annual air temperature records [*Micu et al.*, 2016] and checked whether this method provides reliable temperatures for the more pronounced warming trend in Europe since 1979 [*Böhm et al.*, 2010]. This first application was also part of a bachelor project carried out by Marie-Christin Juhl in 2019.

4.1 Site description - the Cloșani Cave

The Cloşani Cave is located on the southern slope of the Carpathians (see figure A.19) at an altitude of 433 m above sea level close to the village Cloşani. The cave developed in massive limestones of Upper Jurassic-Aptian age [*Constantin and Lauritzen*, 1999], whereby the limestone mainly consist of calcite (93 %) and dolomite (7 %) [*Diaconu*, 1990]. The cave is divided into two main passages (see figure A.19), which split shortly

after the entrance and sum up to a total length of 1458 m. While the *Crystal Passage* is located at an upper level, approximately 8 m in average above the other passage, Stam 4 was collected in the deeper sector of the *Laboratory Passage*. The stalagmite was removed at a maximum distance of one meter from the drip site CL3, where the host rock overburden is approximately 100 m.

A detailed monitoring programme in the years 2010 to 2012 and 2015 showed remarkable microclimate stability for the Cloşani Cave, with a mean air temperature of 11.4 °C varying with inner annual variations of 0.5 °C and a relative humidity close to 100 % [*Warken et al.*, 2018]. The cave air pCO_2 pattern follows a strong seasonal cycle with high values in late summer (up to 8000 ppmV) and low values during winter (2000 ppmV). The winter time (October - March) is also the period where 75 to 100 % of the meteoric precipitation is available for infiltration, which almost disappears during summer due to evapotranspiration. *Warken et al.* [2018] showed, that calcite precipitation is strongly favoured in winter and suppressed in summer, as both pH and Ca^{2+} of the drip water follows the seasonal cycle of cave air pCO_2. The isotopic composition of the drip water for CL3 shows no seasonal cycle and is rather constant with a mean value of -9.62 ± 0.20 ‰ for oxygen and -66.32 ± 1.68 ‰ for hydrogen in VSMOW, detailed data see table A.20. Mean annual air temperature records for three stations close to the cave are shown in figure A.20. The meteorological station with the longest record (1896 - 2008) is located in the city of Drobeta Turnu Severin and gives a MAAT (Mean Annual Air Temperature) of 11.7 °C for the last 100 years [*Klein Tank et al.*, 2002]. The LMWL is determined using stable istope data from the nearest GNIP station in Cluj-Napoca (336 m above sea level), which is 260 km from the Cloşani Cave at a comparable altitude above sea level [*Cozma et al.*, 2017].

4.2 Late Holocene stalagmite - Stam 4

The relatively small and fast - growing stalagmite Stam 4 has a total length of 6 cm and an average growth rate of 510 μm per year. The stalagmite has grown on solidified cave floor, which is clearly visible as brown colouring in the lower part (see left side of figure 4.1). The available piece (light red coloured) to study fluid inclusions is taken from the edge of Stam 4 with an approximate distance of 1 to 1.5 cm from the actual growth axis. This must be taken into account when determining an age distribution of the sample levels. In doing so, I attempted to follow the respective growth layers as well as possible, which are marked exemplarily as red lines on the left in figure 4.1. The stalagmite was dated by layer counting and additional radiocarbon dating (personal correspondence with Dana Riechelmann and Jens Fohlmeister). Here the measurements show an increase in ^{14}C activity (see figure A.22), which confirms that Stam 4 grew at the time of the ^{14}C bomb - peak. This increase of the atmospheric radiocarbon concentration (pmC) in the late 1950s can be identified between 1.9 and 3.9 cm distance from top. Accordingly, the ^{14}C dating supports the age depth model

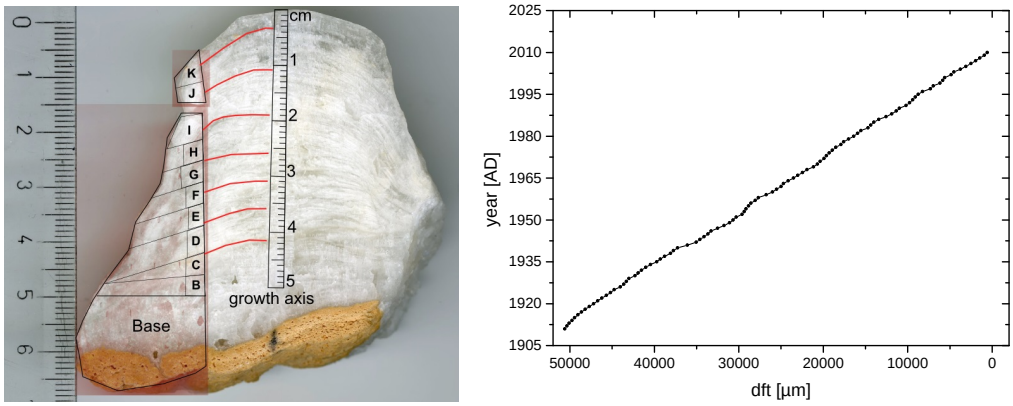

Figure 4.1: Left: Stalagmite Stam 4 with light red colouration of the sample piece, which was analysed for stable isotopes in fluid inclusions. The individual sample levels range form B to K starting at the base of the stalagmite. Right: Age depth model with dft (distance from top) in μm. The stalagmite was dated by layer counting and additional ^{14}C measurements, unpublished data provided by Dana Riechelmann and Jens Fohlmeister.

derived from layer counting (right side of figure 4.1), which shows a constant growth over the period from 1911 to 2010 without any significant hiatus. Both summer and winter layers are clearly detectable in the thin - sections (left side figure A.21), whereas winter layers show a compact structure with less inclusions and summer layers contain air - and water - filled ones. The uniform growth is also reflected in the crystal structure, as Stam 4 consists mainly of columnar fabrics (right side of figure A.21).

4.2.1 Sampling strategy for Stam 4

In order to determine the water content (μl/g) of Stam 4 and thus estimate how much sample material is required per measurement, the piece was divided into two parts (see left side of figure 4.2). *Part II* is the smaller piece (length of 2.5 cm), which was divided into 13 cubes of equal size with a band saw. The sample levels ranging from *B* (close to base) to *G* (top). Since it is the outermost edge of Stam 4, *part II* is also called the edge. A diamond wire saw was used to cut *part I* and to follow the growth layers as closely as possible. Thereby, in total 28 samples were cut with the sample levels ranging from B up to K.

Those samples closest to the growth axis are numbered with *1*, which can be seen on the right in figure 4.2.

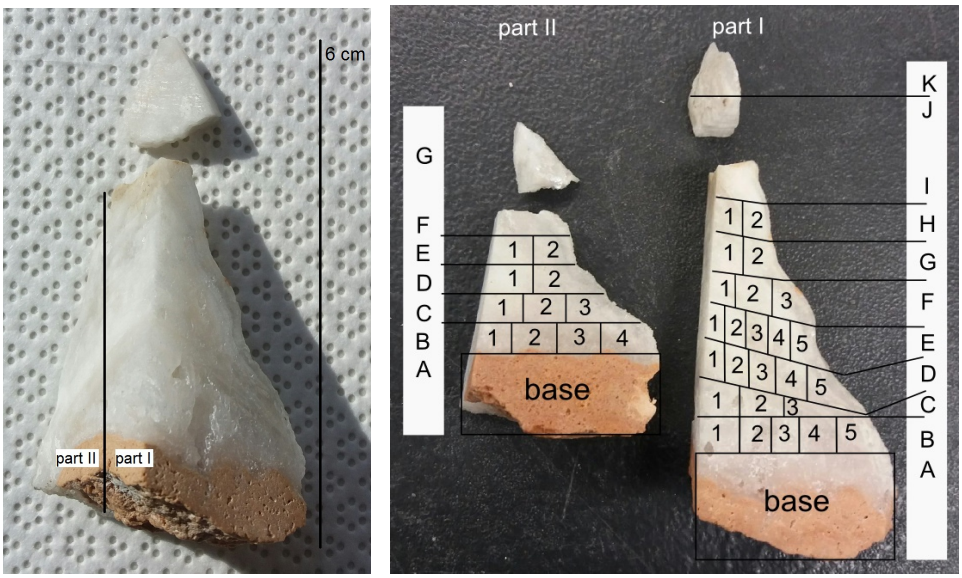

Figure 4.2: Left: The piece of Stam 4 with the subdivision into *part I* and *II*. Right: *Part I* and *II* with sample mapping and corresponding labelling. *Part II* was measured first as a test and therefore cut into cubic sample blocks. For the detailed fluid inclusion study of *part I* I tried to follow the growth layers as good as possible.

4.3 Results

4.3.1 δ^{18}O and δ^{2}H of fluid inclusions for *part II* - the edge

Since growth layers in the marginal section of a stalagmite can no longer be resolved, an age classification is not possible. Due to the drip water running off at the edge of the stalagmite, it can be assumed that younger calcite precipitates there and accordingly, younger drip water is enclosed in the fluid inclusions. For this reason, I compared the fluid inclusion data of *part II* (see figure 4.3) with the current drip water. Figure 4.3 shows the individual stable isotope measurements for *part II* in direct comparison with the drip water data for the drip site CL3. The resulting mean for the fluid inclusions of *part II* is given as $\delta^{18}\mathrm{O} = -9.47 \pm 0.49\,‰$ and $\delta^{2}\mathrm{H} = -64.57 \pm 1.16\,‰$ and the resulting mean of the drip site CL3 to $\delta^{18}\mathrm{O} = -9.62 \pm 0.20\,‰$ and $\delta^{2}\mathrm{H} = -66.32 \pm 1.68\,‰$ in VSMOW. The 13 individual measurements of *part II* reproduce with a standard deviation of $0.49/1.16\,‰$ for $\delta^{18}\mathrm{O}/\delta^{2}\mathrm{H}$.

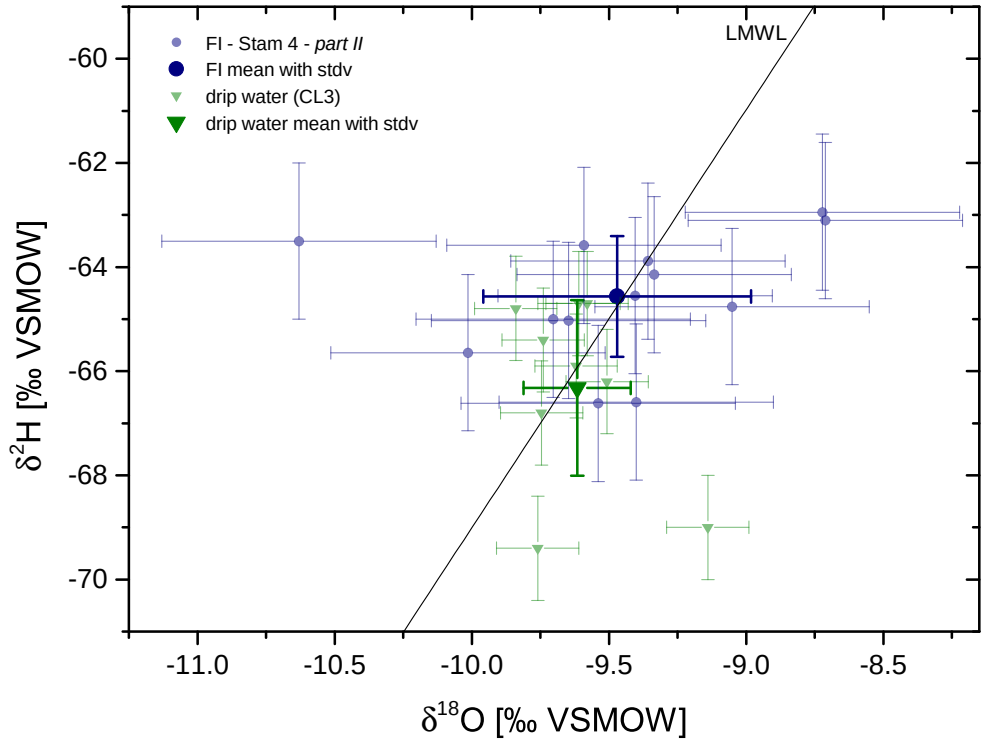

Figure 4.3: Fluid inclusion results for *part II* shown as light blue dots, with the corresponding mean value and standard deviation as dark blue dot. The drip water data of CL3 is shown as light green triangles, with the corresponding mean value and stdv as dark green triangle [*Warken et al.*, 2018]. Additionally, the measurements match to the LMWL of Cluj-Napoca given to $\delta^2H = 8.03 \cdot \delta^{18}O + 11.29\,‰\text{VSMOW}$ [*Cozma et al.*, 2017]. The results of the respective individual measurements with corresponding water content are listed in table A.21.

4.3.2 δ^{18}O and δ^2H of fluid inclusions for *part I* - relative temperature determination

Part I of Stam 4 contains sections where the edge of the growth plateau is still identifiable. Thus, I attempt to match the age ranges to the corresponding sample levels (see figure A.23). This was done visually and only partly growth lines could be followed. It should be explicitly pointed out that this does not lead to clearly defined ages, but age ranges were associated to the individual sample levels (B to K). Samples near the base (level B) are definitely older than samples close to the top (level K). Due to the large uncertainties in the age distribution, only sample levels (B to K) are given in the following figures. The complete data set of all 28 individual stable isotope measurements is listed in table A.22.

In the following I will determine temperature changes using two methods. First, with the classic approach of temperature dependence of the oxygen fraction during calcite precipitation, called ΔT_α. Second, with the temperature dependence of hydrogen, called $\Delta T_{\delta D}$. Since an absolute temperature reconstruction is difficult and some assumptions are required, I only examined the relative temperature change ($\Delta(T)$) in the following. Therefore, I relate this temperature change to the start of stalagmite growth, thus to sample level B.

Classic carbonate thermometer ΔT_α

The fractionation factor α (calcite - water) can be calculated by the concurrent measurement of $\delta^{18}O_{calcite}$ and $\delta^{18}O_{fluid}$. In order to calculate α, I averaged the calcite oxygen isotope measured at a considerably higher resolution than the $\delta^{18}O_{fluid}$ data. This is shown in figure 4.4 as light green dots which are smoothed with an interval corresponding to the edge length (0.5 cm) of the stalagmite samples measured for fluid inclusions. Here the same constraint appears as with the age distribution, since $\delta^{18}O_{calcite}$ was analysed at the growth axis and needs to be translated to the position of the fluid sample piece, resulting in a relative large depth uncertainty. To verify the reproducibility of the individual measurements, fluid inclusion samples with both numbering *1* and *2* are shown. Although only samples with numbering *1* are used for further analysis, as they are located closest to the growth axis. This is particularly relevant for level C, which shows significantly higher values then the surrounding samples. Since *C1* and *C2* were measured independently and confirm the same value, *C1* must be considered in the data set. For sample level D, only sample *D2* is utilized because *D1* is below the evaluation limit with a sample water volume of 0.18 μl. In summary, all $\delta^{18}O_{fluid}$ measurements reproduce within the uncertainty of 0.5 ‰ and on average the samples numbered with *1* and *2* deviate from each other by -0.07 ± 0.44 ‰ for oxygen, in VSMOW.

The temperature dependence of the fractionation factor α (calcite - water), which is defined as $(1000 + \delta^{18}O_{calcite})/(1000 + \delta^{18}O_{fluid})$ becomes visible when using the natural logarithmic as a scale. This is shown as grey squares in figure 4.4, which varies between 30.67 and 32.76. For synthetic carbonates at low temperatures *Kim and O'Neil* [1997] proposed the following expression: $\Delta = 18.03(10^3/T) - 32.42$ which can be used to calculate absolute temperatures. The use of a calibration of ${}^{18}\alpha_{cc/w}$, based on the composition of extremely slow growing calcites from Devils Hole and Laghetto Basso, would lead to different absolute temperatures [*Daëron et al.*, 2019]. However, the temperature dependence of the fractionation factor is comparable to the one of *Kim and O'Neil* [1997]. With this calibration the temperature change in relation to sample level B is determined. In figure 4.4, the relative temperature change (orange dots) varies in the range of approximately 10 K. If this is transferred to the age of the stalagmite, it would result in a temperature variation of 10°C over the last 100 years.

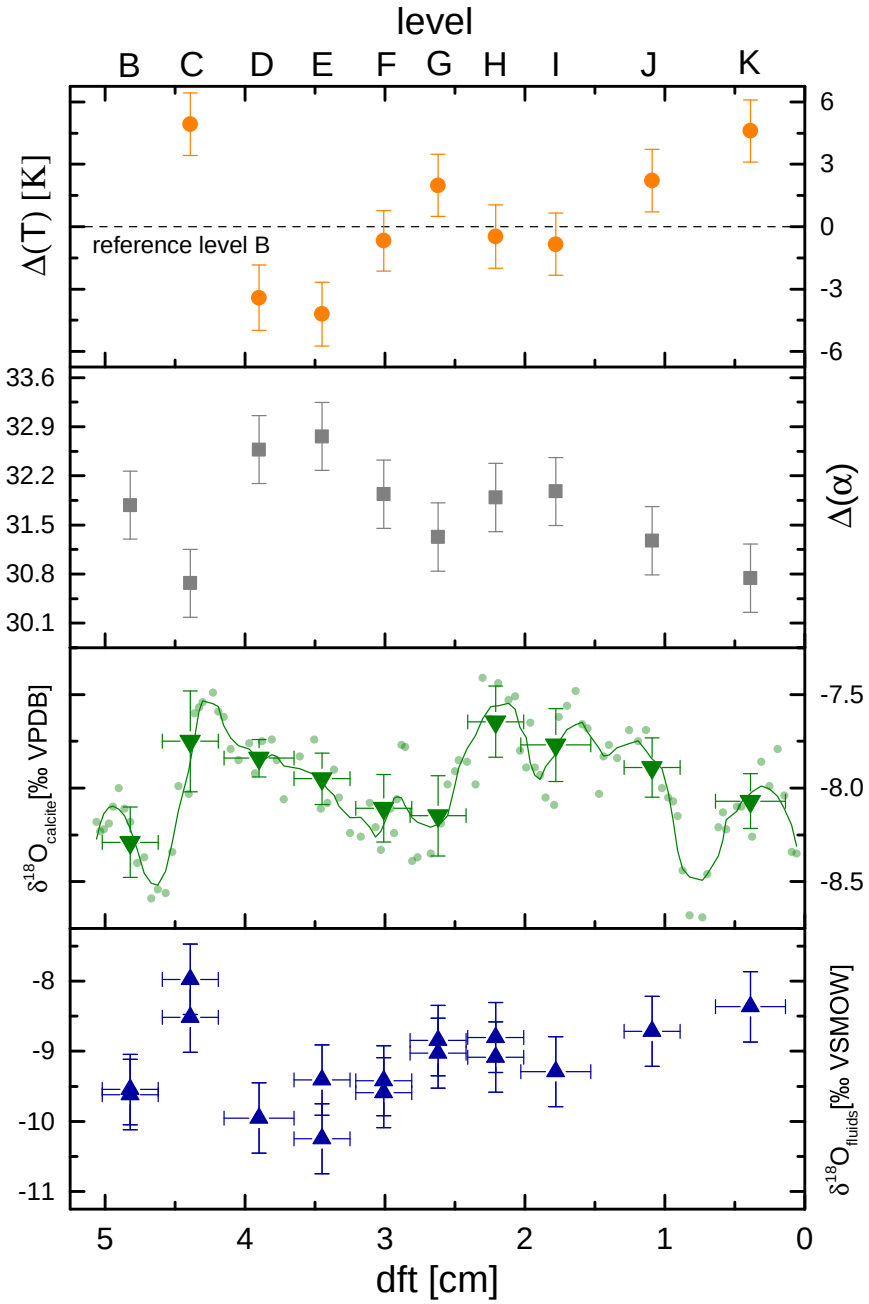

Figure 4.4: *Part I* - data of $\delta^{18}O_{fluid}$ (blue triangles), as well as $\delta^{18}O_{calcite}$ (green triangles) and the resulting fractionation factor $\Delta(\alpha)$ (grey squares) are shown. Smoothed calcite data (green line) with an interval corresponding to the edge length (0.5 cm) of the fluid inclusion sample piece. The relative temperature change derived form $\Delta(\alpha)$ related to sample level B is shown as orange dot. For a better overview the depth (dft) errors of $\Delta(\alpha)$ and $\Delta(T)$ are not shown, but are the same as for $\delta^{18}O_{fluid}$. The exact calculation of the respective fractionation factors with the corresponding propagation of errors is listed in table A.23.

Temperature calculation based on hydrogen isotopes $\Delta T_{\delta D}$

The relationship between the isotopic composition of precipitation and temperature was investigated by *Rozanski et al.* [1992] for Central Europe to $+0.59 \pm 0.04$ ‰ /T for oxygen and thus $+4.72 \pm 0.32$ ‰ /T for hydrogen, in VSMOW. Since the stalagmite Stam 4 from the Cloşani Cave grew under continental climatic influence, the mean value for Europe seems to be the best estimate to determine the relative temperature change with the δD_{fluid}/T relationship (see figure 4.5). As in the immediate environment, all GNIP stations only have very short time series (2012 - 2016) of isotopic measurements in precipitation and are therefore not adequate to calculate an exact local hydrogen - temperature dependency.

Figure 4.5 shows the fluid inclusion data of δD_{fluid} as blue triangles over the depth of Stam 4. As it is the case for ΔT_{α}, the individual measurements with numbering *1* and *2* are shown to prove the reproducibility. On average, the δD_{fluid} results of the samples with numbering *1* and *2* deviate by 0.14 ± 0.84 ‰, which is within the uncertainty of the single measurement of 1.5 ‰, in VSMOW. Again, the data in level C appears significantly higher than the surrounding data points, but as it reproduces an outlier can be excluded. For level D, only sample *D2* is used, because *D1* is excluded due to a released water volume below the threshold value for evaluation. The relative deviation of deuterium $\Delta(D)$ to sample level B is shown as a grey square, whereby the uncertainty of depth is equal to δD_{fluid}, but not shown for a better overview. I could identify a significant increase for $\Delta(D)$ of $+4.76 \pm 2.12$ ‰ between sample level F and K (see figure 4.5), which using the relation given by *Rozanski et al.* [1992] can be transferred to a temperature change with a total increase of $+1.01 \pm 0.63$ °C.

4.4 Discussion

4.4.1 *Part II* - verification of the current drip water isotopy

For *Part II* of the recent stalagmite Stam 4, I could show that with the *fluid inclusion line* it is feasible to measure the stable isotopic composition of fluid inclusions, which corresponds to the isotopic composition of the actual drip water within the uncertainty. A direct comparison of the mean values of inclusion/drip shows the following results for δ^{18}O with $(-9.47 \pm 0.49)/(-9.62 \pm 0.20)$ ‰ and for δ^{2}H with $(-64.57 \pm 1.16)/(-66.32 \pm 1.68)$ ‰, in VSMOW. The sampling of Stam 4 *part II* does not allow to assign the individual samples to an absolute age or an age range. Therefore, only mean values are discussed here, which are very consistent within the uncertainty. Furthermore, with the analysis of *Part II* I could achieve a good reproducibility of measurements of stable isotopes in fluid inclusions with a standard deviation of 0.49/1.16 ‰ for δ^{18}O/δ^{2}H.

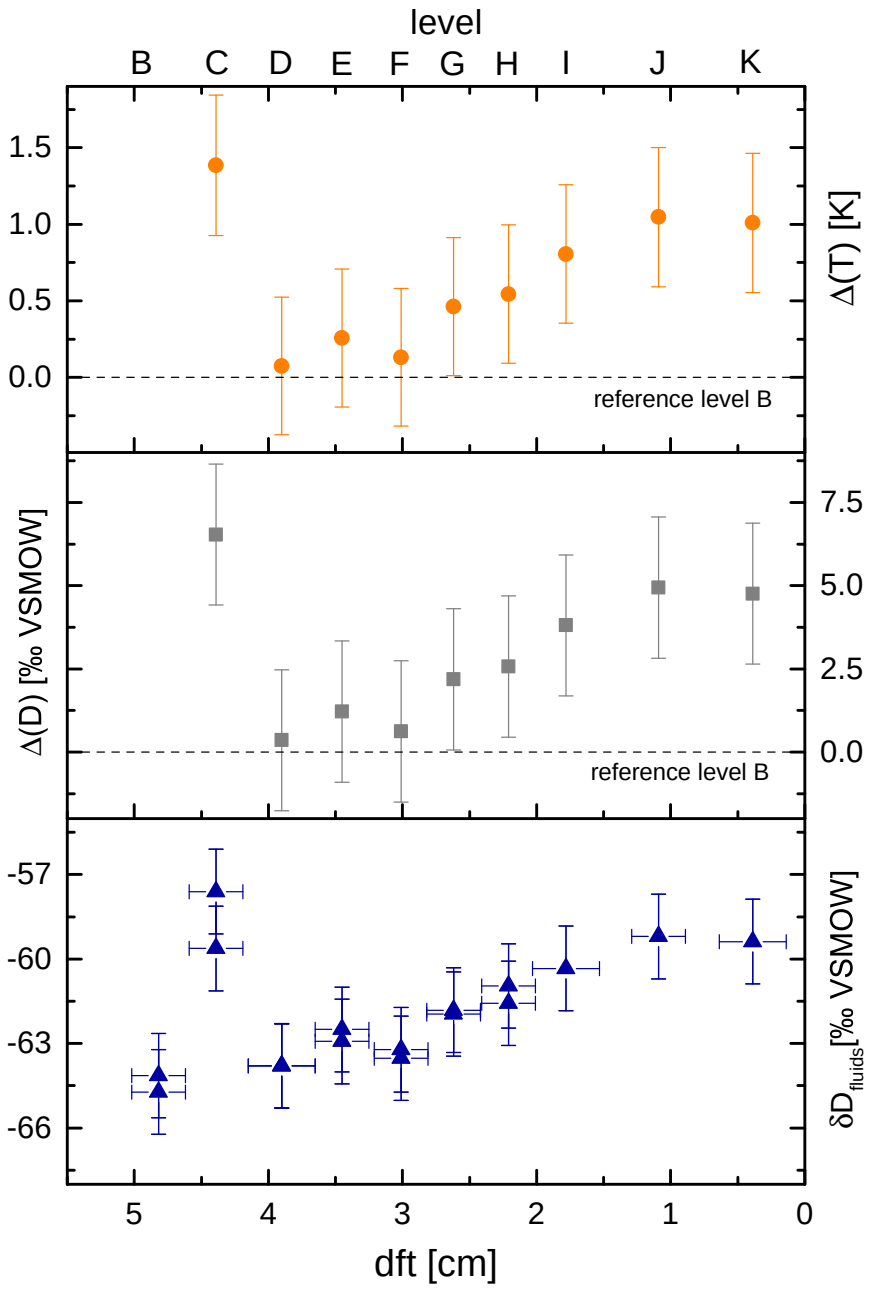

Figure 4.5: Stam 4 *part I* - data of δD_{fluid} (blue triangles) and the resulting deuterium deviation $\Delta(D)$ (grey squares) relative to level B. For δD_{fluid} samples with both numbering *1* and *2* are shown. An increasing trend is visible for $\Delta(D)$ as well as for $\Delta(T)$. Using the δD/T relationship of 4.72 ± 0.32 ‰ VSMOW/T [*Rozanski et al.*, 1992] a total increase of $\Delta(T) = 1.01 \pm 0.63$ °C is obtained.

4.4.2 *Part I* - relative temperature determination

First, the relative temperature variation was determined for *part I* using the fractionation factor approach for oxygen - ΔT_α. In Central Europe, I expect a temperature increase towards a modern age due to anthropogenic climate change. Accordingly, with the proportionality of $\Delta\,(10^3 ln(\alpha))$ to temperature, a linear decrease towards the top of the stalagmite should be recognizable. This decrease ($\Delta(\alpha)$ as grey square) can be detected in figure 4.4 starting at sample level D, i.e. with the exception of sample levels B and C. However, if I consider the relative temperature variation to sample level B with the calibration according to *Kim and O'Neil* [1997], the relative temperature change varies by $\pm\,5\,\mathrm{K}$. Transferring the sample levels to an age range, this temperature variation would be obtained for the period from 1919 to 2005. One reason for this unrealistic temperature determination is the fact that the isotopes of the calcite were measured at the growth axis and the isotopes for the fluid inclusions at the edge. Accordingly, the measurements do not reflect the fractionation between calcite and water at the same position. Furthermore, the assumption of equilibrium fractionation for calcite precipitation is insufficient. Another reason that the precipitation took place in a non - equilibrium regime is the variation in growth rate. The strong seasonal cycle of the cave air CO_2 leads to a stalagmite growth restricted to the cold season, which results in rapidly changing growth rates that may favour isotopic disequilibrium [*Watkins and Hunt*, 2015]. Exactly this becomes obvious when considering the large variation of the fractionation factor α, shown as $\Delta\,(10^3 ln(\alpha))$ in figure 4.4. Consequently, a temperature determination according to the temperature dependency by calcite precipitation is therefore not suitable and leads to an inadequate estimation.

In contrast, hydrogen is not involved in calcite precipitation and therefore an undisturbed signal [*Affolter et al.*, 2019; *Uemura et al.*, 2020]. It is directly linked to the drip water compositions and features a temperature dependence. The characterization of the slope of this relationship varies according to the location and altitude, but can be approximated with a mean value for Europe. Figure 4.6 shows the relative temperature change (orange dots) derived from the deuterium - temperature relation of $4.72 \pm 0.64\,‰/\mathrm{T}$ [*Rozanski et al.*, 1992]. Here sample level C was not considered due to the higher δ^2H value, which will be discussed later. As already mentioned, an absolute age determination is difficult due to the peripheral position of the sample piece. However, it is clear that from the base to the top (B to K) the stalagmite is getting progressively younger. Because of the consistent growth of Stam 4 (see right side of figure 4.1), I decided to visually transfer the age distribution to the sample levels, which only applies for samples with numbering *1*. Details about this procedure are shown in figure 4.6. As a result, I have assigned samples level D to the year 1930 and the peak of the stalagmite piece to the year 2010, with correspondingly large uncertainty. It can be seen that $\Delta(T)$ is close to zero till a depth of 3 cm or an age of 1950, followed by an increase of $1.01 \pm 0.63\,°\mathrm{C}$ till the top of the stalagmite or to the year 2010. On the right side of figure 4.6 a local MAAT record (grey line) of the station Drobeta is shown

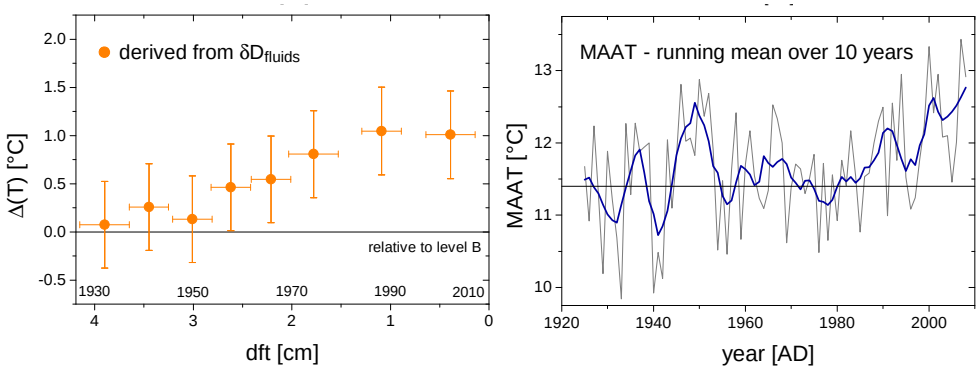

Figure 4.6: Left: Relative temperature change derived from deuterium (orange dots) over the depth (distance from top). No absolute age determination is possible, but the possible age range of Stam 4 is given. Right: The mean annual air temperature of Drobeta (grey line) for the last 100 years with the smoothed signal (blue line) and the mean temperature as black line is given [*Klein Tank et al.*, 2002]. The interval (10 years) of the running mean is the age range that the fluid inclusion samples sum up on average.

[*Klein Tank et al.*, 2002]. The signal is smoothed (blue line) with a time interval of 10 years, which equals the time frame of the stalagmite pieces. The mean annual air temperature for the time period from 1928 to 2008 is shown as black line, whereby an increase in temperature can be identified from 1980 until 2008. This is supported by findings of *Micu et al.* [2016] that the temperature for the Romanian Carpathian have risen by up to 1 °C from 1960 to 2010 (see figure A.25). Additionally, the 6th climate report of the Ministry of Environment and Climate Change claims a mean temperature increase for Romania of 0.8 °C for the period of 1901 - 2012 [*Ministry of Environment and Climate Change*, 2013]. Considering the ΔT derived from deuterium, it seems that around 1950 a temperature increase begins which is not reflected in the local MAAT. One reason for this could be that the sample section measured here is an edge piece of the stalagmite, which is located at the margin of the growth plateau. Accordingly, the growth layers are not distinguishable and a mixing of drip water of different ages can occur. During precipitation of the calcite at the edge, younger and heavier drip water is enclosed in the fluid inclusions, which would lead to an earlier and much higher relative temperature change.

For oxygen isotopes the $\delta^{18}O/T$ relationship can vary from 0.17 ‰°C^{-1} (marine stations) to 0.90 ‰°C^{-1} (Antarctic Peninsula), with an average slope for continental Europe of 0.58 ± 0.08 ‰°C^{-1} [*Rozanski et al.*, 1992; *Clark and Fritz*, 1997]. In the following I will compare the slope and the resulting temperature changes with local studies. For example, a stable isotope study from Hungary found a relation of 0.37 ± 0.03 ‰°C^{-1} for present - day precipitation for a 9 year record [*Vodila et al.*, 2011]. Another study in Hungary by *Varsányi et al.* [2011], which used noble gases

in groundwater, derived a slope of $0.47\,‰°C^{-1}$ (with the isotopic correction due to changing sea levels). According to *Vodila et al.* [2011] I would obtain a relative temperature change of $1.61 \pm 0.73\,°C$, which corresponds within the uncertainty to the one determined previously to $1.01 \pm 0.63\,°C$. However, I decided on the $\delta^{18}O/\Delta T$ dependence according to *Rozanski et al.* [1992], as he considered 47 stations in Europe with the longest record in Vienna over 30 years. If *Rozanski et al.* [1992] focuses on seasonal changes, a much smaller slope for Europe with a mean of $0.34 \pm 0.02\,‰°C^{-1}$ is obtained, which is similar to that of *Vodila et al.* [2011]. Since there is a wide range of "climates" within an annual cycle, the temperature coefficient for long - term temperature changes is advantageous for paleoclimatic reconstructions [*Siegenthaler and Oeschger*, 1980]. It shows that the conservative error approximation of the single measurement for the stable water isotopes in fluid inclusions is reasonable, even if the uncertainty seems to be overestimated for deuterium when considering figure 4.6.

Although I did not obtain absolute temperatures, the relative temperature change is in excellent agreement with the increase of the mean annual air temperature for Romania. This proves that the $\Delta(D)$ approach is a reliable method to determine mean annual air temperatures via fluid inclusions.

Part I - sample level C

For figure 4.6 I have ignored sample level C, because the measurements show significantly higher (more positive) values for oxygen and hydrogen than the surrounding inclusion measurements. Since $\delta^{18}O_{fluid}$ as well as δD_{fluid} were measured independently and reproduce within the uncertainty, *C1* and *C2* must be considered in the data set. If sample level C is translated into an age range. It relates to the period of 1924 to 1932. *Warken et al.* [2018] describes a dry period for the Cloşani Cave during that time interval, characterized by significantly higher Mg/Ca ratios. However, a clear evaporation pattern in the isotopic composition, as observed in other stalagmites (see chapter 5 and 6), could not be conclusively identified for sample level C. Although the stable isotope values are higher (more positive) in both oxygen and hydrogen, they correspond within the uncertainty to the LMWL (see figure A.24).

Another possibility, which might explain the more positive isotope values of sample level C, is the influence of the North Atlantic Oscillation (NAO). *Comas-Bru et al.* [2016] found an effect of the North Atlantic Oscillation on the isotopic composition of precipitation through its control of air temperature and the trajectory of the westerly winds that carry moisture to Europe during the boreal winters. Hence, the NAO index is positively correlated with $\delta^{18}O$ in precipitation and the $\delta^{18}O_{prec}$ value is negatively correlated with the amount of precipitation for South East Europe. This means that with a positive NAO index, also positive $\delta^{18}O_{prec}$ values are expected and at the same time less precipitation (see figure A.26). A decline of the Mediterranean precipitation has been noted for positive trend of the NAO accompanied by a positive trend of the

East Atlantic Western Russia (EAWR) pattern [*Krichak and Alpert*, 2005]. *Warken et al.* [2018] found for the time period between 1926 - 1936 a positive NAO index and a positive EAWR index, resulting in pronounced less winter precipitation in South Romania. Presumably the noticeable higher (more positive) values for $\delta^{18}O_{fluid}$ and $\delta^{2}H_{fluid}$ are a result of a changed circulation pattern, with a strong Azores High and deeper than normal Icelandic Low [*Comas-Bru et al.*, 2016]. As a result, the Atlantic influence is decreasing, which means that warmer air from the Mediterranean is increasingly becoming a source of precipitation [*Baldini et al.*, 2008].

Findings for the late Holocene stalagmite in the transitional climatic zone - Romania

- *Part II* (the edge): $\delta^{18}O_{fluid}$ and $\delta^{2}H_{fluid}$ measurements reflect the isotopic composition of the actual drip water within the uncertainty. Additionally, I was able to achieve a good reproducibility of stable isotope measurements in fluid inclusions with a standard deviation of 0.49/1.16 ‰for δ^{18}O/δ^{2}H in VSMOW.
- *Part II*: The classic carbonate thermometer would led to an unrealistic temperature variation of $\pm 5\,°C$ for the Cloşani Cave over the last 100 years.
- *Part II*: The newly applied deuterium - temperature relation is a reliable method to determine mean annual air temperatures via fluid inclusions for mid - latitude speleothems.
- *Part II*: For the period between 1950 - 2010 I obtained a temperature increase for the Cloşani Cave of $+1.01 \pm 0.63\,°C$, which is in excellent agreement with local temperature records [*Micu et al.*, 2016].

5 Case study II: Holocene stalagmite (present - 8.6 ka BP) from Central Europe - Bunker Cave

The second application of the *Fluid inclusion line* was related to the Holocene stalagmite Bu4 from Bunker cave. A number of stalagmites from Bunker cave were part of the extensive DFG funded research group DAPHNE. Numerous publications have already been published about both the Bunker cave and stalagmite Bu4 [*Mühlinghaus et al.*, 2009; *Wackerbarth et al.*, 2010; *Kluge et al.*, 2010; *Riechelmann et al.*, 2011; *Fohlmeister et al.*, 2012; *Münsterer et al.*, 2012; *Riechelmann et al.*, 2017], which is investigated in terms of water isotopes in fluid inclusions in this thesis. The previous studies are the basis for the interpretation of the fluid inclusion data. I conducted a detailed study of the stable water isotopes in the fluid inclusions embedded in the carbonate lattice of Bu4. It is noticeable that only a small segment of the stalagmite contains water-filled inclusions, which are suitable for a detailed examination. The varying fabrics and facies zones of calcite precipitates of Bu4 are controlled by changing climatic conditions and in particular by the amount of surface precipitation and temperature [*Frisia et al.*, 2000; *Frisia and Borsato*, 2010; *Frisia*, 2014]. The fact that evaporation can occur in caves and has an influence on the isotopic signal is known [*Dreybrodt and Deininger*, 2014], but it is questionable how strong this phenomenon will effect the isotopic composition of the fluid inclusions. In the following I will investigate to what extent the analysis of fluid inclusions from the stalagmite of the Bunker Cave allows to draw conclusion about the changed climatic conditions for Central Europe during the Holocene.

5.1 Site description - the Bunker Cave

The Bunker Cave is located in the Rhenish Slate Mountains close to the city Iserlohn in North Rhine-Westphalia (see map A.27). The cave developed in Middle to Upper Devonian limestone and is part of the large Bunker-Emst cave system [*Riechelmann et al.*, 2011]. The entrance of the cave is located 184 m above sea level and separates into two chambers in the deeper part of the cave (see figure A.29). The thickness of the overburden rocks ranges from 15 to 30 m whereby the vegetation above the cave is a mixture of deciduous forest and scrubs [*Grebe*, 1993]. *Riechelmann et al.* [2011] conducted an intensive monitoring program (2006-2009), where they observed a stable cave air temperature of 10.6 ± 0.2 °C and pCO_2 variation between 900 to 1200 ppmV in chamber 2 (sampling position of Bu4). Since the carbon dioxide concentration in the cave air lacks a clear seasonal cycle, regular changes of the cave air pCO_2 variability are

not a major driving force for calcite precipitation. This is supported by missing annual laminae in speleothems [*Riechelmann et al.*, 2011]. A changing outside temperature causes alternating ventilation inside the cave, enabled by the two entrances. This leads to a homogeneously ventilated cave with a relative humidity varying between 86 and 97 %. Drip water was regularly collected as part of the monitoring programme, although only data from the drip site TS8 are relevant for this study. The drip water isotopic composition of δ^{18}O and δ^{2}H show low variability and no seasonal pattern (see figure A.31) with a mean value of -8.0 ± 0.2 ‰ for δ^{18}O and -54.5 ± 1.5 ‰ for δ^{2}H in VSMOW. Those values fit very well to the infiltration weighted annual mean values of rainwater, which was found to be $\delta^{18}\mathrm{O} = -8.1$ ‰ and $\delta^{2}\mathrm{H} = -55.0$ ‰ in VSMOW. Accordingly, the drip water at TS8 shows no instantaneous response to precipitation events, suggesting a specific water capacity threshold in the soil/karst aquifer with an average residence time of up to a 3 years [*Kluge et al.*, 2010; *Riechelmann et al.*, 2017]. In addition, the δ^{18}O and δ^{2}H drip water values correspond with the LMWL (see figure A.31), thus fractionation effects due to evaporation in the soil, epikarst and cave can be excluded nowadays. However, TS8 is characterized by a very low drip rate (0 - 0.07 drops/min) and a varying drip classification from seasonal drip to seepage flow, corresponding to a drip rate decrease of about 50 % [*Riechelmann et al.*, 2013]. Variations in drip rates can be caused by various factors. For example, an increase in drip rate can be induced by heavy rainfall events, filling the reservoir feeding TS8 to a threshold resulting in more continuous flow. Contrary, the drip rate can be reduced if carbonate deposits originating from prior calcite precipitation (PCP) might change or block the water flow path [*Fairchild et al.*, 2006b]. *Riechelmann et al.* [2013] found evidence that PCP is an important process at the TS8 drip site, which was supported by the analysis of calcite precipitate samples on watch crystals showing clear indications of disequilibrium fractionation for $\delta^{18}O_{calcite}$ and $\delta^{13}C_{calcite}$.

5.2 Holocene stalagmite - Bu4

The stalagmite Bu4 (see figure 5.1) with a length of approximately 21 cm was collected in 2007 under the actively drip site TS8. *Fohlmeister et al.* [2012] dated the oldest part of Bu4 with Th/U - dating to 8 600 years before present. Additional radiocarbon dating from the very top part of Bu4 shows the typical increase and decrease in radiocarbon as would have been expected for the cave carbonates precipitating during the period of tropospheric nuclear bomb testing and the following atmospheric radiocarbon decrease (late 1950 to recent). This proves that the stalagmite was actively growing during the last 60 years. Bu4 shows a constant growth over the last 8 600 years with a growth rate of 20 μm per year in the lower part and an increasing growth velocity in the upper part with a growth rate of 60 - 80 μm per year. The upper part of Bu4 with a relatively fast but constant growth rate shows mainly columnar fabrics (see figure A.30). In contrast, the lower part shows columnar fabrics that merge into dendritic fabrics [*Frisia et al.*, 2000; *Frisia and Borsato*, 2010]. In addition, at 146 and 169 mm distance from top

two coralloid or detrital layers are visible (red lines in figure 5.1), these contain aerosol particles and are associated with drier conditions [*Dreybrodt*, 1980; *Dredge et al.*, 2013]. These layers indicate that the dripping process was interrupted and the stalagmite surface dried out [*Hill and Forti*, 1997]. *Riechelmann* [2010] classified two different *facies zones*, type *A* and *B* which can be seen in figure 5.1. Type *A* is characterized by dark, clear and compact crystals, indicating an continued calcite growth with compact and nearly fluid inclusion free calcite formation. This growth is favoured with a relatively thick water film (1 mm) on the stalagmite surface [*Kendall and Broughton*, 1978]. In contrast the milky, porous and therefore fluid inclusion rich facies type *B* develops during rapid and incomplete calcite formation [*Frisia et al.*, 2000]. This is possible if a thin water film (0.01 mm) stays long enough on the stalagmite surface to form a highly

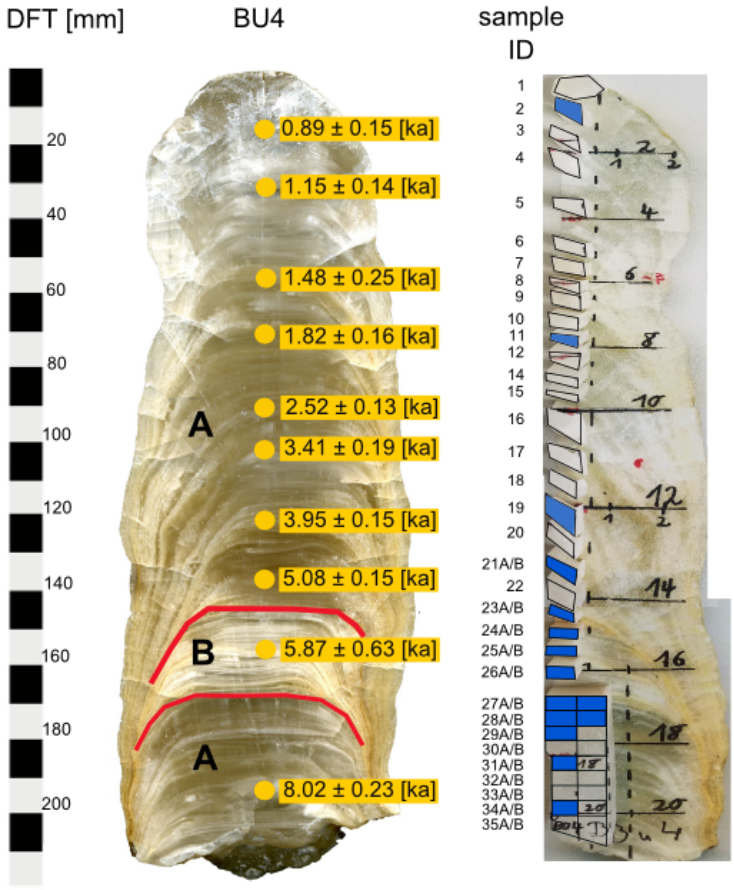

Figure 5.1: Left: Bu4 stalagmite with dating points and resulting age. The two different facies zones are identified with *A* and *B*, the red lines indicating detritus layers. The left picture is adapted from *Riechelmann et al.* [2011] and sample ages after *Fohlmeister et al.* [2012] are added. Right: Samples are shown with corresponding sample ID, with those measured for fluid inclusions marked in blue.

supersaturated solution which leads to an irregular calcite formation and therefore to porous and fluid inclusion rich crystals [*Dreybrodt*, 1980]. This is favoured by a slow drip rate or even if the dripping stopped.

The right side of figure 5.1 shows the Bu4 samples with corresponding sample ID for fluid inclusion measurements. Bu4 was partially pre-cut for a planed noble gas study in 2008. For this application I sawed the lower part (sample ID 27 - 32) with a band saw to the required sample size of ~ 5 mm edge length. Due to the low water content, only a few measurement were conducted for facies zones *A* and mainly samples of the facies zones *B* were analysed. All measured samples for fluid inclusion analysis are marked in blue.

5.3 Results

5.3.1 Water content - stalagmite Bu4

A total of 49 stalagmite samples were available for the analysis of fluid inclusion measurements. At the beginning of the measurement it became apparent that not the complete stalagmite was suitable for a fluid inclusion study as a significant part of the stalagmite contained no water - filled inclusions (see figure 5.2). Therefore, I have performed a total of 19 individual measurements. The water content varies between 0

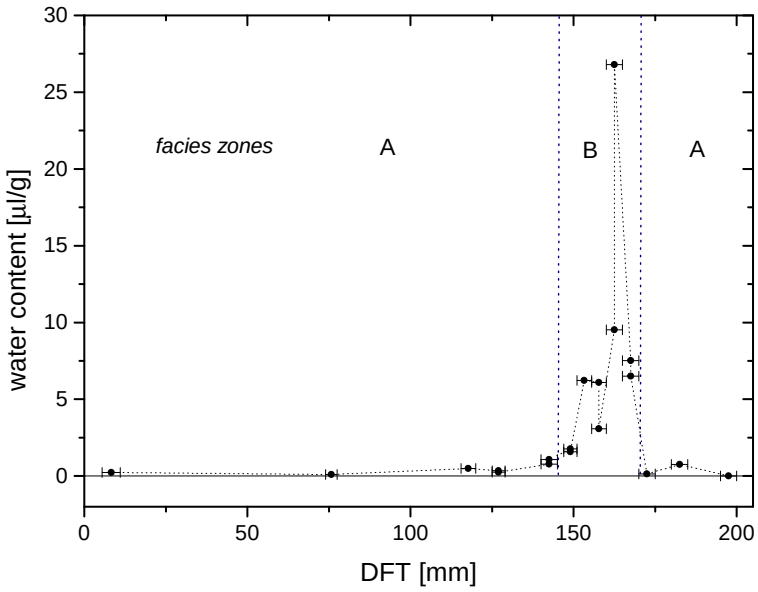

Figure 5.2: The measured water content in μl per g calcite over the depth (distance from top) is shown. The two different facies zones are identified with *A* and *B*, with the two detrital layers illustrated as blue dotted lines.

and up to 27 μl per g calcite. For facies zones *B*, a significant increase in water content can be identified, whereas facies zones *A* is characterized by a very low water content. Overall, within the area of the facies zones *A* less than 0.2 μl water was released in 6 measurements, which is the threshold value for a reliable evaluation. As a consequence, I conducted no further measurements in this section of Bu4. The two detritus layers at 146 and 169 mm are plotted as a blue dotted line and enclose the facies zones *B*.

5.3.2 δ^{18}O and δ^{2}H of fluid inclusions - stalagmite Bu4

The results of the 19 individual measurements of oxygen and hydrogen isotopes in fluid inclusions are shown as blue circles in figure 5.3. For a better comparison of the results, the drip water of TS8 (green triangles) as well as various rainwater data (grey dots) are shown. The rainwater data consists of a data set collected above the Dechen Cave (2007 - 2013) and GNIP data from Bad Salzufern (1978 - 2006) [*Riechelmann et al.*, 2017]. A clear deviation of the measured fluid inclusion data from the GMWL and LMWL can be identified, which is illustrated with the magnification of the dotted square on the right side of figure 5.3. The measured water isotopes of the fluid inclusions do not represent the actual drip water at TS8.

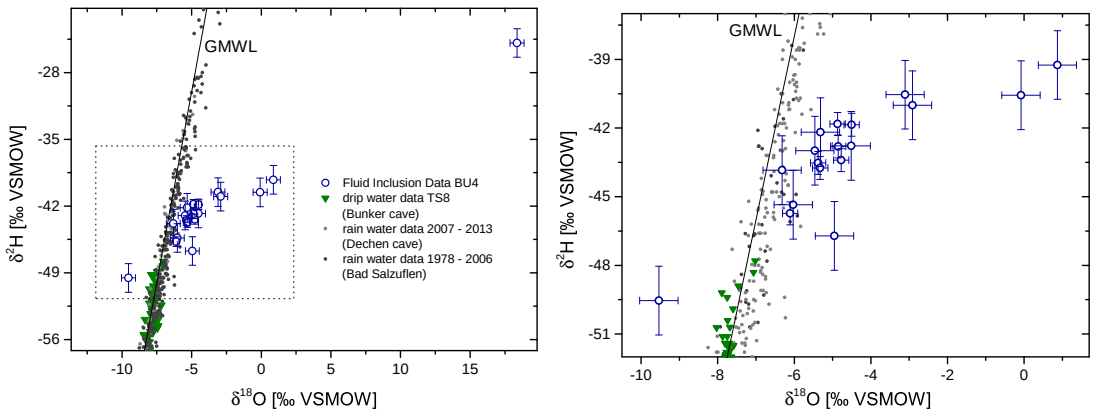

Figure 5.3: Left: Individual measurements of the stable isotopes, δ^{18}O and δ^{2}H, in fluid inclusions (blue circles) of Bu4. Drip water of TS8 (green triangles) as well as rain water data (grey dots) is shown for a better comparison [*Riechelmann et al.*, 2017]. A deviation from the GMWL is obvious. Right: Magnification of the dotted square. The detailed results of the individual measurements are listed in table A.24 and A.25.

5.4 Discussion

5.4.1 Water content - changing climate condition

I found a strong variation in water content for the stalagmit Bu4, with values close to 0 up to 27 μl per g calcite. Facies zone *A* contains almost no water - filled inclusions, whereas facies zone *B* contains a number of them. This coincides with the theoretical considerations of *Riechelmann* [2010], which, based on thin sections, predicted such a pattern of water content over depth (see figure A.30). For the facies zone *A* with its compact crystals resulting from a very regular crystal growth, I found no to very few water - filled inclusions (0.01 up to 0.35 μl/g). The compact crystals formed by a continuous calcite precipitation from a relatively thick water film (1 mm [*Kendall and Broughton*, 1978]), which is favoured at higher and continuous drip rates [*Genty and Quinif*, 1996; *Frisia and Borsato*, 2010]. *Boch et al.* [2011] found that compact/dense laminae developed during times of increased water excess and high drip rates, and therefore during climatic conditions with increased rainfall. These dark facies zone *A* is in strong contrast to the white porous facies zone *B* with a high water content (0.75 up to 26.79 μl/g), which is confined by the two coralloid layers at 146 and 169 mm (5.5 and 7.1 ka before present). This milky, inclusion - rich and porous facies zone is formed by rapid crystal growth from highly oversaturated solutions [*Frisia et al.*, 2000], which is favoured by a thin water film (0.01 mm [*Kendall and Broughton*, 1978]). The strong supersaturation of the solution in this thin water film, which forms under low drip rates [*Dreybrodt*, 1980], enhances the out - gassing of CO_2 due to the long residence time on the stalagmite surface. Low drip rates could be a sign of dry climatic conditions, which is confirmed by the two coralloid layers since only under very dry conditions aerosol particles can deposit on the stalagmite surface and form this type of calcite fabric [*Frisia*, 2014]. Therefore, fabrics and facies zones of calcite precipitates are controlled by host rock parameters and in particular by the amount of surface precipitation and temperature [*Frisia and Borsato*, 2010; *Frisia*, 2014]. Presumably a strongly changing water content is an indirect indicator for changing climatic conditions. This coincides with the findings of [*Niggemann et al.*, 2003b], who observed dark compact laminae to develop preferentially during the wet winter times, whereas the white porous laminae grow in drier cave environments and probably reflect periods of stronger evaporation and/or higher supersaturation. In fact, longer residence time of water in a thin film on the stalagmite surface favours the possibility of evaporation [*Dreybrodt and Deininger*, 2014].

The two coralloid layers (5.5 and 7.1 ka before present) enclose the section with a high water content, whereby the samples in which the two coralloid layers were included, with a water content of $\sim$1.5 and $\sim$7 μl/g, do not exhibit the highest water content measured in this speleothem. However, this period (5.5 - 7.1 ka) is associated with rather dry climatic conditions, which is consistent with the results of *Niggemann et al.* [2003b], who found light - porous micro facial laminae with a high water content for the

period between 9.6 and 5.5 ka BP (Atlantic episode of the Holocene). In this case the water content of two stalagmites from the Sauerland was not measured directly, but qualitatively determined by thin sections. Furthermore, *Niggemann et al.* [2003a] has recently observed the formation of white, porous facies zones where the speleothem sites are characterized by a stronger air flow and the surfaces dry out completely in summer and autumn. A rather dry period of the Holocene between 7 and 5 ka before present was also observed in other stalagmites from various German caves, followed by moister climatic conditions from 5 ka until today [*Wurth*, 2003]. This coincides with the low water content of the upper part of Bu4 (5.5 ka until present), where facies zone *A* is dominant. The seasonal variability of climatic conditions would be reflected in the alternation of annually deposited white porous and dark compact laminae [*Genty and Quinif*, 1996] due to the strong seasonal fluctuations of the water excess (dark compact lamellae in years with high water excess). Since the facies zone of Bu4 does not fluctuate on an annual time scale, it can be assumed that growth conditions were rather constant over a longer period of time (e.g. 5.5 and 7.1 ka before present) for sections with uniform crystal structure.

Comparing the water content with the isotope ($\delta^{13}C_{calcite}$ and $\delta^{18}O_{calcite}$) and trace element (Mg/Ca) measurements of *Fohlmeister et al.* [2012] reveals only a limited accordance. The purple box in figure 5.4 shows the section with highest water content of Bu4 and thus the period in which I assume dry climate conditions. The findings of cold and dry climate periods after *Fohlmeister et al.* [2012] are illustrated as green boxes and are mainly based on the Mg/Ca ratios. Higher Mg/Ca ratios are interpreted as periods with less precipitation and accordingly periods with rather dry climate conditions. For the time span from 7.1 to 5.5 ka, with a high water content this is only partially the case. *Fohlmeister et al.* [2012] suggest dry and cold climate conditions for the period of 7.7 - 7.3 ka and around 5.6 ka. This corresponds to the segment of the two coralloid layers, which confirms our results. However, I would also assume dry climate conditions between these two layers, which is not consistent with *Fohlmeister et al.* [2012]. For the $\delta^{13}C_{calcite}$ signal, more positive values indicate a lower drip rate, which I would expect for facies zone *B*. This facies zone is assumed to form under a very thin water film on the stalagmite surface or temporary drying. Accordingly, the drip rate must have been reduced or even completely stopped, which is supported by the two coralloid layers. This hypothesis is consistent with the findings of *Fohlmeister et al.* [2012], who measured more positive $\delta^{13}C_{calcite}$ values for this section from 7.1 to 5.5 ka and, in particular, the coralloid layer. *Fleitmann et al.* [2003a] found that the enrichment of heavier stable isotopes of the calcite ($\delta^{13}C_{calcite}$ and $\delta^{18}O_{calcite}$) may be used as an indicator of lower humidity in a cave due to less dripping activity caused by less precipitation. However, the $\delta^{18}O_{calcite}$ signal of the speleothem is influenced by the $\delta^{18}O$ value of the drip water and by isotopic fractionation processes that take place during calcite precipitation. Thereby, the relationship between temperature and the $\delta^{18}O_{calcite}$ value resulting from isotopic fraction during calcite precipitation is negative and compensate the positive relationship between temperature and the $\delta^{18}O$ value of

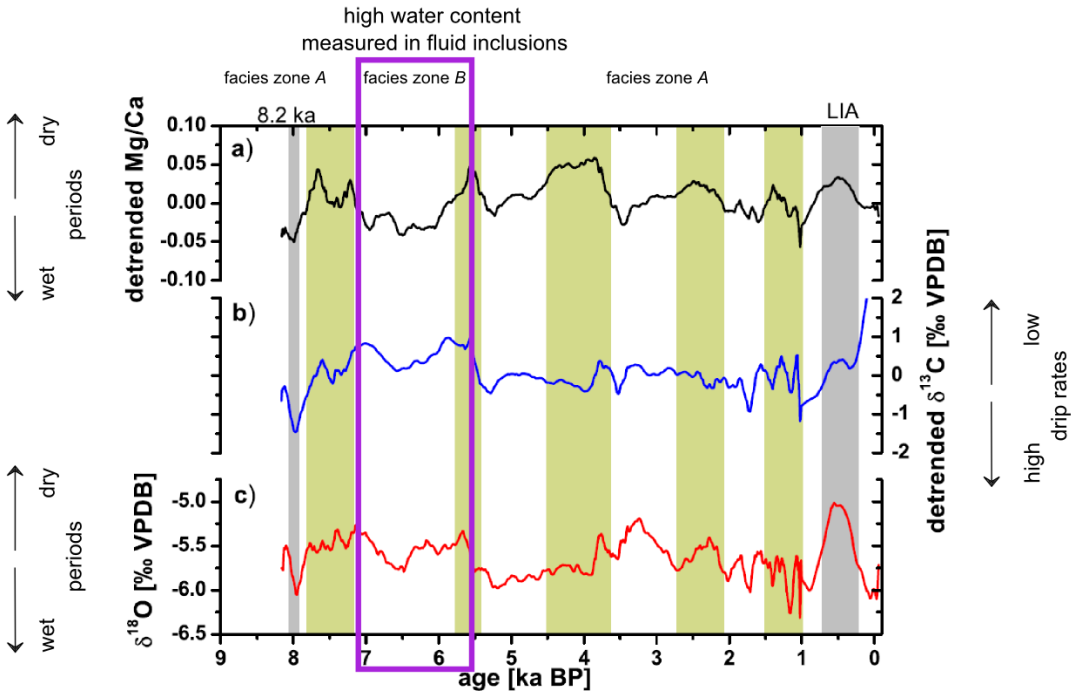

Figure 5.4: Bu4 data adapted and modified from *Fohlmeister et al.* [2012]. Shown is the deviation from the mean for the Mg/Ca ratio (black) and the δ^{13}C signal (blue), which are both detrended and smoothed. The smoothed $\delta^{18}O_{calcite}$ signal is shown in red and the green boxes are related to dry and cold periods. The section where I measured a high water content in the fluid inclusions is illustrated as purple box.

the meteoric precipitation [*Wackerbarth et al.*, 2010]. Since the signals of stable isotopes are influenced by various processes, the $\delta^{18}O_{calcite}$ signal should be interpreted carefully.

In summary, the measurements of an increased water content in facies zone *B* are consistent with the theoretical considerations of *Riechelmann* [2010]. The findings, that the water content is an indirect indicator for changing climatic conditions are supported by the investigations of *Niggemann et al.* [2003b, a] for Holocene stalagmites from Sauerland. Dark compact laminae (facies zone *A*) develop under constant drip water supply and thus under preferentially more humid climatic conditions. While the white porous laminae (facies zone *B*), which developed during frequent dripping interruptions, are favoured in drier cave environments and probably reflect periods of stronger evaporation and/or higher supersaturation. The trace element ratio Mg/Ca as well as the $\delta^{18}O_{calcite}$ signal do not show the expected accordance.

However, the more positive $\delta^{13}C_{calcite}$ signal for the period 7.1 to 5.5 ka indicates lower drip rates, increased kinetics and temporary drying, which is consistent with the water content measurements of Bu4.

5.4.2 Water stable isotopes in fluid inclusions - evaporation signal

Of the 19 measured samples, I could only use 13 for a detailed analysis of the stable water isotopes in the fluid inclusions, as only these samples have released more than 0.2 μl water. This water volume is considered to be the threshold value for a reliable evaluation (see section3.6). These 13 samples are in an age range of 7.7 to 5.0 ka (185 to 140 mm dft). For the oldest sample (7.7 ka) a correction due to a different sea level, which corresponds to a different isotopic composition of the global ocean would result only in a correction of -0.05 ‰ for δ^{18}O and -0.40 ‰ for δ^{2}H in VSMOW [*Waelbroeck et al.*, 2002]. This correction is so minor that it is not considered in the further discussion. Nevertheless, the corrected data is listed in table A.26. This correction is an important aspect for samples formed during the Last Glacial Period (115 – 11.7 ka BP [*Dansgaard et al.*, 1993]), since the changing ocean as a reservoir for the resulting precipitation and therefore drip water has a oxygen glacial - interglacial amplitude of $\sim$1 ‰ VSMOW [*Waelbroeck et al.*, 2002].

The fluid inclusion data indicate more positive values in both, δ^{18}O and δ^{2}H, with respect to the current drip water composition (see figure 5.5). This suggests that fractionation occurs. I performed a linear regression (red line) considering the x - and y - uncertainties and obtained a slope of $(+2.27 \pm 1.12)$ δ^{2}H/δ^{18}O. *Hu et al.* [2009] performed evaporation experiments in which the water vapour was not recycled. They found deuterium to be fractionated more strongly than oxygen by a factor of 3.432 with the correlation coefficient (R^2) of 0.845 [*Hu et al.*, 2009]. Accordingly, I performed a linear regression (blue line) with a fixed slope of 3.4 δ^{2}H/δ^{18}O. The actual mean drip water composition over the intersection point of the evaporation line (linear regression with a fixed slope) and the GMWL could be calculated. The resulting values close to the modern - day drip water isotope ratios suggest that the deviation from the original stable isotopic composition of the fluid inclusions was caused by evaporation. This is consistent with the consideration of drier climatic conditions during the period between 7.7 - 5.0 ka and therefore a lower drip rate or even a complete stop of dripping. It would allow long residence times on top of the stalagmite surface, which would favour evaporation [*Niggemann et al.*, 2003b]. As already mentioned, the two coralloid layers could only form under extremely dry conditions. Accordingly, it could be possible that the drip water on the stalagmite top has evaporated and thus experienced kinetic fractionation. The hypothesis that the isotopic composition of the fluid inclusions was effected by evaporation seems to be realistic, considering the related evaporation line of $y = (3.7 \pm 0.2) \cdot x + (5.1 \pm 1.8)$ ‰ which I found for a stalagmite from a different climatic region (see section 6).

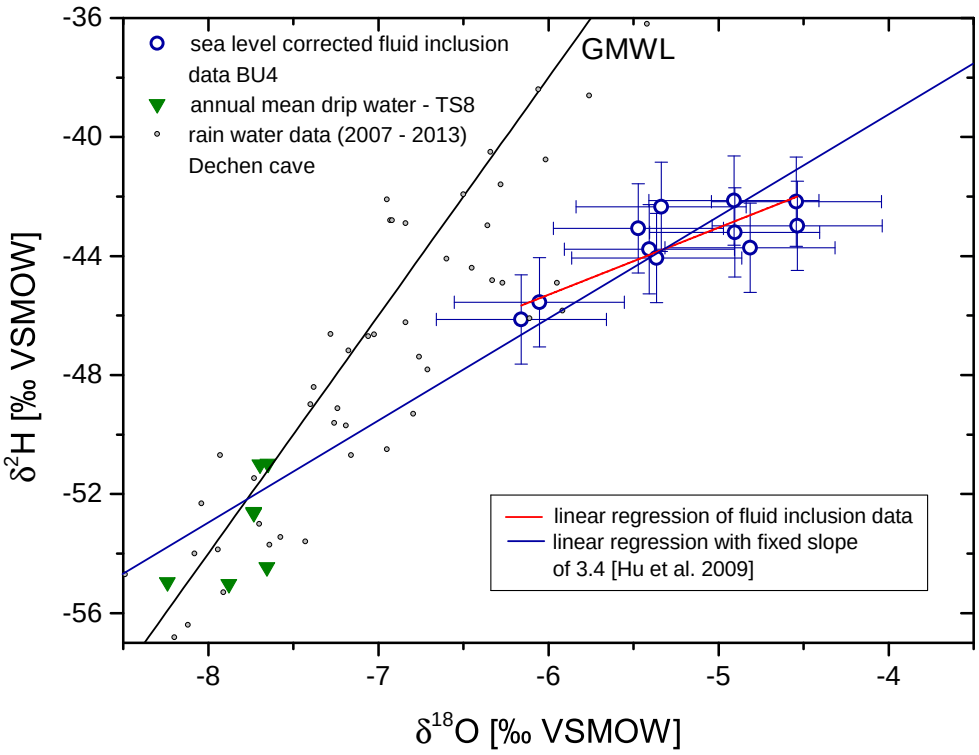

Figure 5.5: Water stable isotopes of Bu4 (blue circles) together with mean annual drip water (green triangles) and rain water data (light grey dots). The linear regression (red line) for Bu4 fluid inclusion data taking x- and y-uncertainties into account results to a slope of $+2.27 \pm 1.12\,\delta^2\mathrm{H}/\delta^{18}\mathrm{O}$. Considering the findings of *Hu et al.* [2009] for fractionation under evaporation with a slope of $3.4\,\delta^2\mathrm{H}/\delta^{18}\mathrm{O}$, the point of intersection between the GMWL and the resulting linear regression (blue line) predicts the actual drip water composition.

Where occurs evaporation - soil or stalagmite surface ?

I detect a clear evaporation signal in stable isotopic composition of the fluid inclusions of the stalagmite Bu4. The question arises where this evaporation takes place. Does evaporation already occur in the infiltration process or does it only take place in the cave. Evapotranspiration in the soil above the Bunker Cave was detected by *Münsterer et al.* [2012] through the analysis of cosmogenic $^{36}\mathrm{Cl}$ in drip water. Furthermore, the occurrence of PCP at the drip site TS8 indicates a previous change in the chemical composition of the drip water [*Riechelmann et al.*, 2013]. This mechanism is possible when the water percolates through the air-filled soil/epikarst and an initial CO_2 outgassing is enabled. However, previous outgassing does not affect the oxygen and hydrogen isotopic composition of the drip water, because it is representing the mean annual rainwater composition and does not deviate from the GMWL (see figure A.31).

Watch glass experiments today show kinetically fractionated $\delta^{18}O_{calcite}$ values below TS8, which are not completely understood [*Riechelmann et al.*, 2013]. *Riechelmann et al.* [2013] exclude evaporation today, because the average humidity in the cave varies around $93 \pm 2\,\%$. Still, increased residence times on the stalactite tip or the stalagmite surface could lead to evaporation and has not been investigated so far. Assuming dry climatic conditions in the time period from 7.1 to 5.5 ka, it cannot be excluded that the humidity in the cave was lower than today. In a homogeneously ventilated cave, like Bunker Cave (see figure A.28), the evaporation increases proportional to (1 - h) for a humidity below 95 % and significant effects altering the isotope ratio are possible [*Dreybrodt and Deininger*, 2014]. If the mean deviation of the current drip water to the measured fluid inclusions is considered, an enrichment of approximately 2 ‰ VSMOW for $\delta^{18}O_{fluid}$ can be identified. This enrichment due to evaporation would theoretically be possible in a moderately ventilated cave with a mean cave temperature of 10 °C, a wind speed of 0.1 m/s and a mean humidity of 80 % [*Deininger et al.*, 2012]. The possibility that evaporation in the cave effects the isotopic composition of the fluid inclusions is also supported by speleothem studies of Holocene stalagmites from Sauerland. *Niggemann et al.* [2003b, a] suspect that areas with white porous lamina (the region of Bu4, which contains water - filled inclusions) were precipitated during periods of low humidity in the cave, which enhances evaporation from the thin water film. This assumption is confirmed by significantly increased $\delta^{18}O_{calcite}$ values ($> +1$ ‰) and the correlation of $\delta^{18}O_{calcite}$ and $\delta^{13}C_{calcite}$, which gives evidence of periodic kinetic fractionation due to evaporation and fast degassing CO_2 [*Niggemann et al.*, 2003a].

In summary, I exclude the possibility of evaporation in the soil or epikarst, as the current drip water data does not provide any indication of this effect. The measured isotopic signal in the fluid inclusions shows a clear evaporation signal, which was probably imprinted during the residence time on the stalagmite surface. Evaporation was favoured by a very thin water film and partial drying of the stalagmite surface. With regard to the interpretation of $\delta^{18}O_{calcite}$ signals in stalagmites, the effect of kinetic fractionation induced by evaporation should be discussed more intensively.

Findings for the Holocene stalagmite from Central Europe - Bunker Cave

- A strongly changing water content is an indirect indicator for varying climatic conditions.
- I observe a high water content in the facies zone *B* (white porous laminae), which is preferred under drier climatic conditions and slow drip rates and probably reflect periods of stronger evaporation and/or higher supersaturation.

- For facies zone A (dark compact laminae) no water - filled inclusions could be found. The compact crystals develop under constant drip water supply and therefore resulting from a very regular crystal growth under more humid climatic conditions.
- I detect a clear evaporation signal in the stable isotopic composition of the fluid inclusions of the stalagmite Bu4 with a linear regression slope of $+2.27 \pm 1.12$ (δ^2H/δ^{18}O), which is comparable to other evaporation experiments [*Hu et al.*, 2009].
- I assume that the $\delta^{18}O_{fluid}$ - δ^2H_{fluid} evaporation signal was imprinted during the residence time on the stalagmite surface.

6 Case study III: Tropical stalagmite (15 - 46 ka BP) from Puerto Rico - Cueva Larga

In tropical regions, the isotopic composition of precipitation is mainly controlled by the amount effect [*Dansgaard*, 1964], in contrast to the relationship between precipitation and land surface temperature for the continental northern hemisphere. For this reason, after a detailed examination of the two European stalagmites, I have chosen a tropical stalagmite from Puerto Rico covering parts of the Last Glacial Period (LGP) (15 - 110 ka), which was characterized by rapid climatic fluctuations from cold (stadial) to warmer (interstadial) conditions recurring on millennial time scales. The instability of large ice sheets in the northern hemisphere led to a large input of fresh water into the North Atlantic, followed by a weakening of the Atlantic Meridional Overturning Circulation (AMOC) [*Heinrich*, 1988; *Bond et al.*, 2001; *Böhm et al.*, 2015]. The so called Heinrich events are well documented in the Northern Hemisphere by ice - core records, but the global imprint and the strength of the different HS (Heinrich stadials) events might vary [*Hemming*, 2004]. For the tropics, the increased input of freshwater into the North Atlantic and the weakening of the AMOC led to a southward shift of the ITCZ (Inter - Tropical Convergence Zone). The consequences are colder and drier climate conditions for the western Atlantic tropics as has been shown in various paleostudies on stalagmites, ocean sediment or lake sediment cores [*Lachniet et al.*, 2009; *Hodell et al.*, 2012; *Grauel et al.*, 2016; *Escobar et al.*, 2012; *Deplazes et al.*, 2013; *Arienzo et al.*, 2015]. Similarly, the Greenland stadials are interrupted by interstadials, in which an abrupt warming is followed by a gradual cooling. These interstadial warming events are better known as Dansgaard Oeschger (D/O) events [*Dansgaard et al.*, 1984]. The typical saw - tooth pattern is well preserved in oxygen stable isotope records of ice cores from North Greenland *Andersen et al.* [2004], whereas the process behind these D/O events and their timing is still debated [*Clement and Peterson*, 2008]. For the tropics, a northward shift of the ITCZ is expected during the interstadials, which will be accompanied by warmer and wetter climatic conditions [*Deplazes et al.*, 2013]. Furthermore, it is questionable how pronounced these events appear in the tropics, since in some stalagmite records no characteristic of D/O events can be found, although HS events are very clearly represented [*Carolin et al.*, 2013; *Arienzo et al.*, 2017]. This is also evident for the findings of *Deplazes et al.* [2013], who suggest that a general adaptation period of the tropical North Atlantic SST to the forcing at high latitudes can lead to a considerable smoothing of the tropical reaction.

Here I present a detailed stable isotope study of fluid inclusions from stalagmite LA-1 covering the interval between 15.4 to 46.2 ka, including HS 1 to 4 and D/O 2 to 12 [*Warken et al.*, 2020]. Some events are not represented in the stalagmite record due to a growth stop of LA-1, between 41.1 and 35.5 ka. I conducted in total 64 fluid inclusion measurements on samples based on a selection following prominent $\delta^{18}O_{calcite}$ changes. The fluid inclusion data show a strong variation of the water content as well as two different clusters for the stable isotopic composition with respect to the GMWL. The reconstructed paleotemperatures with the classic carbonate thermometer are in accordance with local SST reconstructions [*Ziegler et al.*, 2008] and a cooling of ~ 3°C during HS 2 and HS 3, which is comparable to a Bahamian speleothem record [*Arienzo et al.*, 2015] and lake sediment records of northern Guatemala [*Grauel et al.*, 2016].

6.1 Site description - Cueva Larga in Puerto Rico

Cueva Larga is located 350 m above sea level in the north central karst region of Puerto Rico, which is the easternmost island of the Great Antilles (see left side of figure 6.1). Puerto Rico is surrounded by the Atlantic Ocean to the north and the Caribbean Sea to the south. The area around Cueva Larga with a total rainfall of 2 137 mm per year [*Vieten et al.*, 2018] is a developed holokarst, characterized by sinkholes and mogotes, with the cave located in dense oligocene lares limestone [*Monroe*, 1980]. Thus, the overburden limestone reaches a depth of 30 to 100 m and is covered by a thin layer of soil and vegetation consisting of dense tropical forest. The main passage in the cave

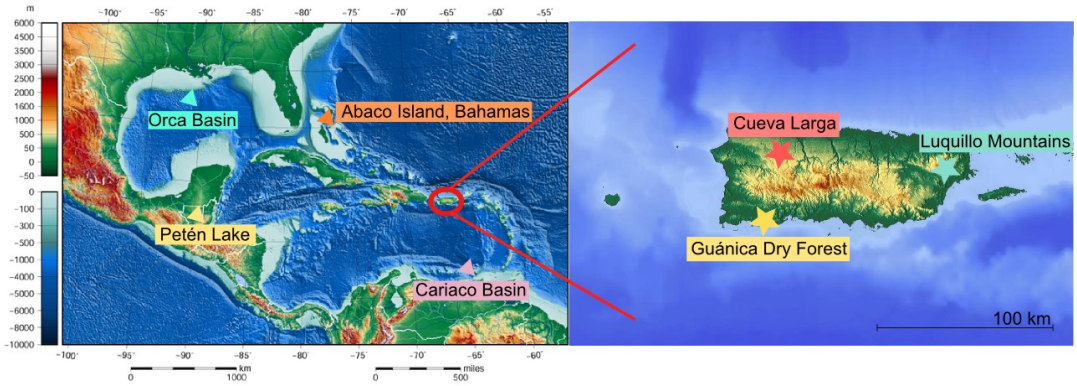

Figure 6.1: Left: Gulf of Mexico and the Caribbean Sea with the location of Puerto Rico marked as red circle. The positions of two ocean sediment cores (green and red triangle) as well as the position of the speleothem record (brown triangle) and the lake sediment core (yellow triangle) are shown, which will be discussed in the following (map is adapted and modified after *Wikimedia* [accessed January 26, 2020]). Right: Map of Puerto Rico showing the position of the Cueva Larga cave (red star) and the two locations of the LMWL stations (map is adapted and modified after *maps for free* [accessed January 26, 2020]).

is almost horizontal and has a total length of 1400 m with a ceiling height of up to 30 m, for details see cave map A.33 [*Miller*, 2010]. Since 2012 cave parameters have been recorded and show a constant cave temperature of 22.5 ± 0.2 °C and a humidity close to 100 % [*Vieten et al.*, 2018]. The cave air pCO_2 varies depending on the season, with high values of up to 1800 ppm in summer and low values of around 550 ppm in winter at drip site SW-2 close to the sampling location of stalagmite LA-1 [*Vieten et al.*, 2016]. This seasonal pattern indicates a very well ventilated cave environment in winter and low ventilation in summer, which can be explained by the temperature differences inside and outside the cave. In winter, the outside temperature is below the cave temperature, allowing the air to circulate, whereas in summer, the cave temperature is similar to the outside temperature and ventilation is stagnant.

As is typical for the location, there is also a seasonal variation in precipitation above the cave, with a bimodal maximum (peaks in May and September/October) in summer and dry season in winter. For the summer months (April to November), with increased precipitation, more negative values in the isotopic composition of the rain are observed than during the winter months (December to March) [*Vieten et al.*, 2016, 2018]. This pattern (see figure A.35) is mainly due to the relationship between rain water isotopes and atmospheric temperature with different types of precipitation that form at different altitudes and temperatures [*Scholl et al.*, 2009]. The dry season (December to March) in the Caribbean is characterized by orographic precipitation from clouds not higher than 3 km. This precipitation from frontal system rain (cold fronts from North America) and orographic processes of trade winds accounts for only one third of the total precipitation [*Scholl and Murphy*, 2014]. In orographic precipitation isotopically heavier (more positive) values are found than in convective rainfall which is characterized by isotopically lighter (more negative) values (see figure A.36). Convective precipitation, which originates from clouds extending above 5 km in the atmosphere, is formed by low pressure systems during the rainy season (April to November) and accounts for half of the total precipitation. This pressure system can develop into tropical storms and hurricanes, with the hurricane season starting in June and ending in November [*Taylor et al.*, 2002]. Despite the increased convective precipitation in the rainy season, *Scholl and Murphy* [2014] showed that the groundwater contains an increased input of orographic precipitation formed during the winter months of the dry season. Indeed, the seasonal variation of isotopic composition in the rainfall above the cave is not reflected in the drip water data in the cave. For example, for the drip water composition at drip site SW-2 in close proximity to stalagmite LA-1 no seasonal variation is recognisable between 2013 - 2019 with a mean value and corresponding standard deviation of $\delta^{18}O$ as -2.59 ± 0.27 ‰ and $\delta^{2}H$ as -9.49 ± 0.11 ‰ in VSMOW [*Vieten et al.*, 2018]. The individual drip water data of drip site SW-2 is listed in table A.28. It can be assumed that the seasonal variation in isotope composition is smoothed by the soil and the epikarst above the cave with a mixing time of at least several months to years [*Vieten et al.*, 2018].

On the right side of figure 6.1 the two positions of weather stations on Puerto Rico are shown where a LMWL is available. *Govender et al.* [2013] collected rain water data in a monthly interval (2008 - 2011) at the station Guánica Dry Forest (yellow star) and determined a LMWL to $\delta^2H = 7.79 \cdot \delta^{18}O + 10.85\,‰$ VSMOW. The station Guánica Dry Forest is located in the southwest of Puerto Rico with less annual precipitation than typical for the area around Cueva Larga (see figure A.34). In contrast, the Luquillo Mountain station is located in the northeast of the island. This region is characterized by particularly high precipitation. *Scholl and Murphy* [2014] found the LMWL to $\delta^2H = 8.2 \cdot \delta^{18}O + 14\,‰$ VSMOW.

6.2 Stalagmite LA - 1

The stalagmite LA-1 (left side of figure 6.2) with a total length of 1.85 m was collected between 2012 and 2013 in several field trips. It was found lying on the cave floor close to the drip site SW-2 in the main passage where the rock overburden is 40 to 80 m depth (see cave map A.33). *Warken et al.* [2020] dated LA-1 with ^{230}Th/U - dating

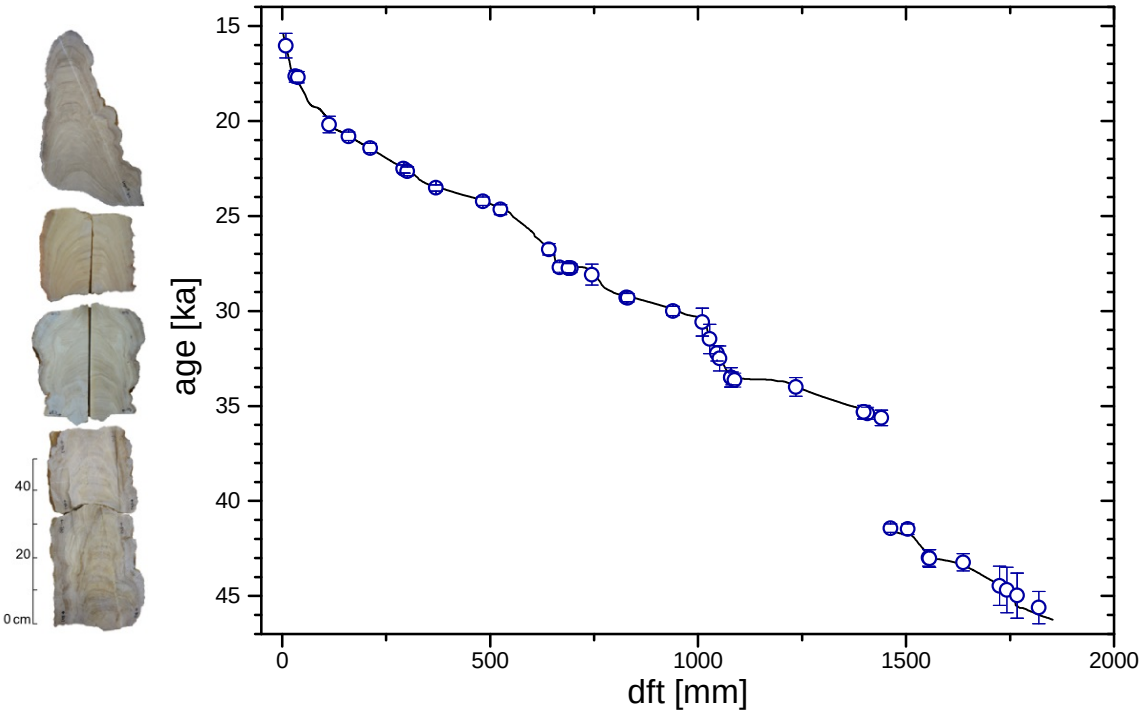

Figure 6.2: Left: Sample slabs of stalagmite LA-1 with a total length of 1.85 m [*Warken*, 2017]. Right: Age model calculated using "StalAge" with the position of fluid inclusion samples (blue circles) [*Warken et al.*, 2020]. In total, I analysed 64 fluid inclusion samples for different depths of LA-1. For a better overview, only the age intervals resulting from the depth uncertainty of the fluid samples are shown

and the calculated age model results in growth periods from 15.4 to 46.2 ka before present with a hiatus between 35.5 and 41.1 ka. The right side of figure 6.2 shows the age model as well as the position of the fluid inclusion samples (blue circles). Growth rates vary from phases of rapid growth (50 to 100 μm/yr) to phases of slower growth (10 to 30 μm/yr). As shown in figure 6.2, the stalagmite LA-1 consists of whitish translucent calcite, which in most parts has a convex shaped lamination. However, the lower part shows an irregular growth ("donut" shaped) with a depression in the middle. *Warken et al.* [2020] analysed LA-1 in detail and showed that Greenland stadials and interstadials are recorded in the stable isotopes ($\delta^{18}O_{calcite}$ and $\delta^{13}C$) of the calcite and in the trace elements (e.g. Mg/Ca). Furthermore, *Warken et al.* [2020] conducted an inverse model (I - STAL) to asses potential drivers of trace element variability.

6.3 Results

6.3.1 δ^{18}O and δ^{2}H of fluid inclusions - pool spar A4

As a modern analogue, pool spar samples were collected during a field trip in 2019 out of the pool A4 of Cueva Larga (see figure A.33) with a water stable isotope composition of $\delta^{18}O = -2.59 \pm 0.11$ ‰ and $\delta^{2}H = -9.49 \pm 0.27$ ‰ in VSMOW. I performed a total of six replicate measurements for the pool spar samples. The results of the stable water isotopes are shown in figure 6.3 with the corresponding mean value and standard deviation of -0.76 ± 0.76 ‰ for oxygen and 3.34 ± 1.83 ‰ for hydrogen in VSMOW.

6.3.2 δ^{18}O and δ^{2}H of fluid inclusions - stalagmite LA-1

I sampled 30 different time periods of the stalagmite LA-1, which, including replicate measurements, yielded a total of 64 fluid inclusion measurements (see figure 6.4). At the appropriate depth, or age, samples were mainly taken from areas where Heinrich events or D/O events are suspected. These intervals are assumed to be characterized by internally small variable $\delta^{18}O_{calcite}$ isotopes, but strongly varying signals before and after the respective section. Since some samples had a very low water content, B samples were re - sampled with slightly offset depth. It becomes apparent that the measurements of the stable isotopes in the fluid inclusions can be divided into two clusters. One cluster of samples is located on the GMWL or scatters around it, another one shows increased isotopic values in both δ^{18}O and δ^{2}H.

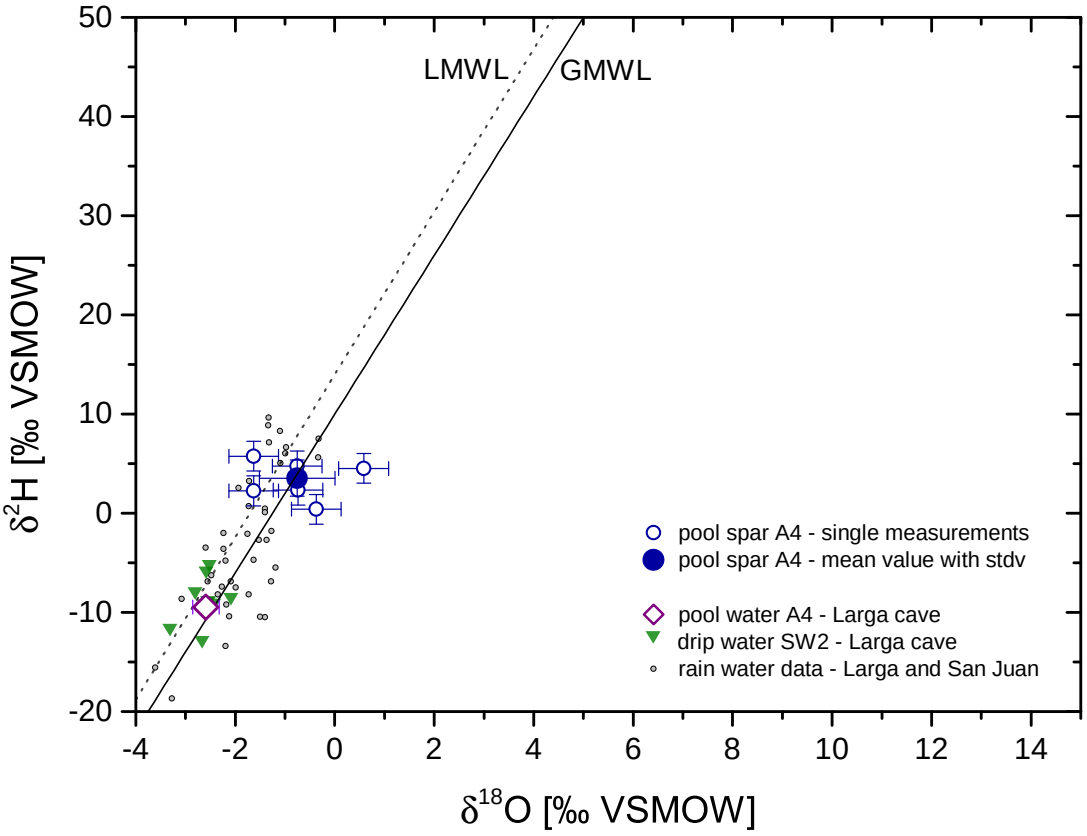

Figure 6.3: Water stable isotopes of fluid inclusions from pool spar out of the pool A4 from the Cueva Larga. For direct comparison of the results, the same axis scaling as in figure 6.4 was chosen. Single values (blue circles) and resulting mean value with corresponding standard deviation (blue dot) are shown together with pool water (purple diamond), drip water SW-2 (2013 - 2019, green triangles) close to the pool A4 and rain water data (2012 - 2019, grey dots) above the cave [*Vieten et al.* [2018] and personal correspondence Sophie Warken, 30.01.2020]. The LMWL with $\delta^2H = 8.2 \cdot \delta^{18}O + 14$ ‰VSMOW [*Scholl and Murphy*, 2014] as well as the GMWL are shown for a better classification. The data of the single measurements are listed in table A.27.

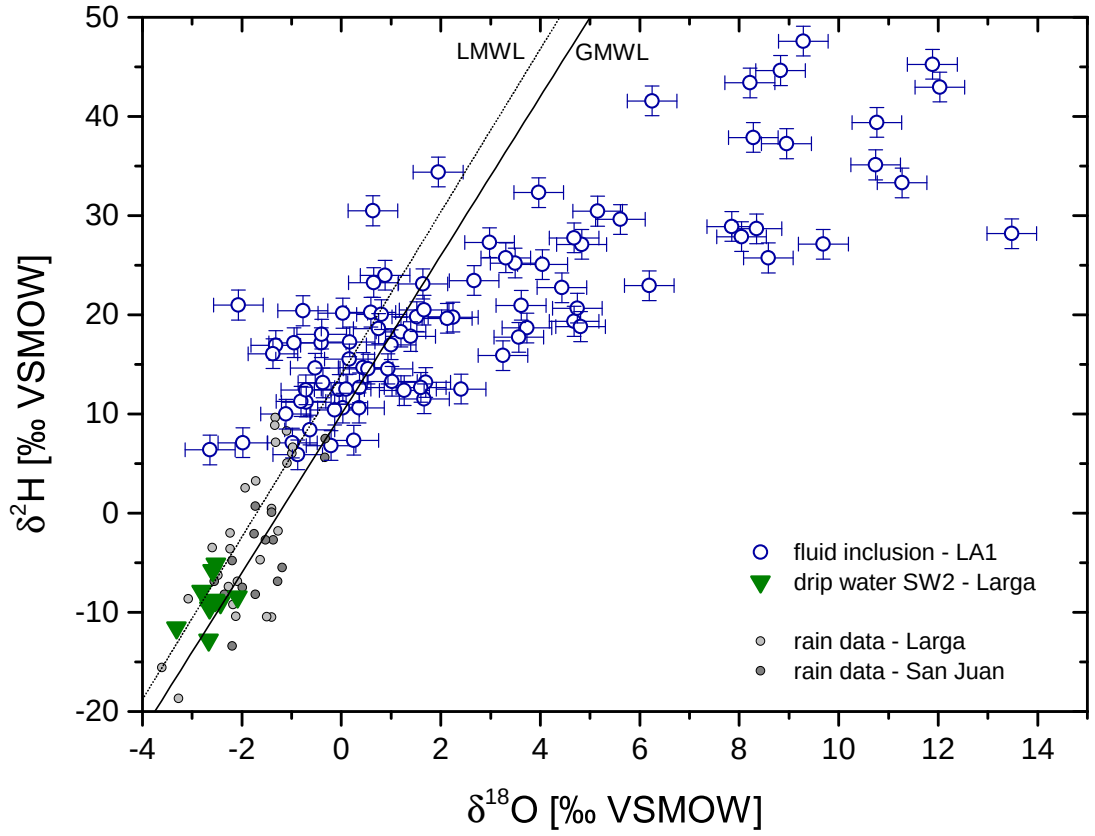

Figure 6.4: δ^{18}O and δ^{2}H of fluid inclusions from stalagmite LA-1 (blue circles). The drip water of drip site SW-2 close to the sampling location of LA-1 is shown as green triangles. For a better classification, rain water data collected above the cave (light grey circles, 2012 - 2019) [*Vieten et al.*, 2018] and close to it (grey circles) at San Juan (GNIP station, 1968 - 1970, downloaded from GNIP's WISER data-platform https://nucleus.iaea.org/wiser IAEA/WMO, 2015) as well as the LMWL after *Scholl and Murphy* [2014] are shown. The results of the stable isotope measurements as well as the water content of all single samples with corresponding depth and age are listed in the tables (A.29, A.30, A.31, A.32 and A.33).

6.4 Discussion

6.4.1 Modern precipitation conditions of pool spar A4

Vieten et al. [2018] measured oxygen isotope values of -2.9 ± 0.2 ‰VPDB in recent precipitated calcite at drip site SW-2 near LA-1. Unfortunately, no information about the oxygen isotope composition of the calcite or the age is available for the measured pool spar samples yet. The samples were taken at the edge of pool A4, i.e. not under the current water surface. However, since the individual measurements scatter around the GMWL and the mean value is located on it, I regard kinetic fractionation due to evaporation as not very likely. The measured stable isotope values of the fluid inclusions from the pool spar differ from the current isotopic composition of the pool water from which they were sampled by approximately $+2/12$ ‰ for $\delta^{18}O/\delta^{2}H$. Assuming that $\delta^{18}O_{calcite}$ corresponds to the value of the recently precipitated calcite (-2.9 ± 0.2 ‰VPDB) and the average $\delta^{18}O_{fluid}$ value (-0.76 ± 0.76 ‰ VSMOW), a precipitation temperature of 24 °C would be obtained using the classic carbonate oxygen isotope thermometer with isotope fractionation factors according to *Kim and O'Neil* [1997]. For the same isotope values and with isotope fractionation factors according to *Tremaine et al.* [2011], a temperature of 31.5 °C would be obtained. *Vieten et al.* [2018] recorded a mean temperature of up to 23.43 ± 0.19 °C in the back area of the cave at site C-2 near pool A4 (see figure A.33). The calcite precipitation temperature according to *Kim and O'Neil* [1997] corresponds roughly to the current cave air temperature. Even this result is promising and suggests that the applied method is feasible, the final interpretation of this result remains speculative, since so far no data of the $\delta^{18}O_{calcite}$ of pool A4 are available.

6.4.2 Variation of the water content - LA-1

Measurements of the fluid inclusions of LA-1 show a variation of the water content from close to 0 up to 3 μl/g. In figure 6.5 I compare the averaged water contents with the simulated growth rates. I separate the water content into high (stars) and low (half filled stars) with the threshold for high set at 0.4 μl/g. The growth rates of LA-1, which are derived from the age model ("StalAge" [*Scholz and Hoffmann*, 2011]) vary over more than an order of magnitude from less than 10 to up of 2000 μm per year. Some sections (e..g. at dft of 745 mm or 1 440 mm) with a high water content also show a high growth rate or a highly variable one, and similarly, parts (at dft of 642 mm or 1 046 mm) with a very low water content are found mainly in sections with lower growth rates relative to the immediate surroundings. However, no correlation can be identified between growth rate and the water content. This may be also related to the difficulties of "StalAge" to simulate realistic growth rate patterns [*Scholz and Hoffmann*, 2008]. On average, the samples which are clearly allocated to Heinrich stadials show a water content of 0.60 ± 0.13 μl/g and samples which are from sections of Greenland interstadials show a water content of 1.02 ± 0.47 μl/g. For the tropics, HS are associated with rather dry and cold climatic conditions, which is reflected in a

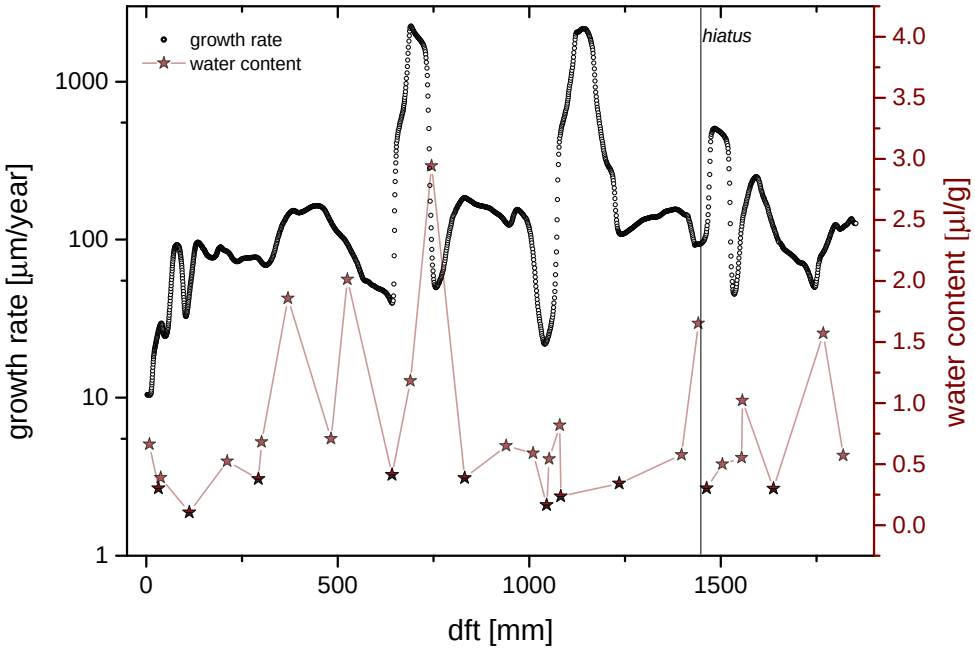

Figure 6.5: The mean measured water content for LA-1 compared to the modelled growth rate. The water content is divided into high (brown stars) and low (half filled stars) with a threshold value of 0.4 μl/g. The modelled growth rate using "StalAge" is shown as black circles on a logarithmic scale [*Warken et al.*, 2020]. The vertical line at 1 445.8 mm indicates the growth stop of LA-1.

lower water content compared to the interstadials, which are regarded as more humid and warmer.

6.4.3 Interpretation of δ^{18}O and δ^{2}H values of the fluid inclusions

The measured mean values ($\delta^{18}O_{fluid}$ and $\delta^{2}H_{fluid}$) for the individual depths are shown in figure 6.6 with the division into high (blue circles) and low (orange circles) water content, with the threshold value set to 0.4 μl/g. As already observed for the δ^{2}H over δ^{18}O plot of the individual measurements (figure 6.4), two clusters are obtained.

One group of fluid inclusion samples is located on the GMWL or scatters around it, the other group shows increased isotopic composition. It is noticeable that oxygen is more strongly fractionated than hydrogen. I performed a linear regression taking x - and y - errors into account, which results to $y = (7.2 \pm 0.8) \cdot x + (13.6 \pm 0.6)$ ‰ shown as blue line for the cluster of high water content. The slope of 7.2 ± 0.8 corresponds to that of the LMWL, which *Govender et al.* [2013] derived to 7.8. The measured mean values indicate heavier isotope values compared to current drip water data, as already observed in the results of the pool spar samples. For the second group with low water

contents, certain samples released water volumes below 0.2 μl. The isotopic data of samples, which have released water below this threshold are only considered in the evaluation if the values were reproduced by several replicate measurements. This has been verified for the samples presented see table A.29 - A.33. These samples show a clear deviation from the GMWL as already observed for the fluid inclusion measurements of Bu4 (see section 5.4.2). If I perform a linear regression taking x - and y - errors into account, the function: $y = (3.7 \pm 0.2) \cdot x + (5.1 \pm 1.8)$ ‰ is obtained shown as orange line. The slope of 3.7 for the cluster of low water contents deviates significantly from the other samples. Nevertheless, it corresponds with the findings of *Hu et al.* [2009] for evaporation experiments, where they derived a significantly lower slope than that of

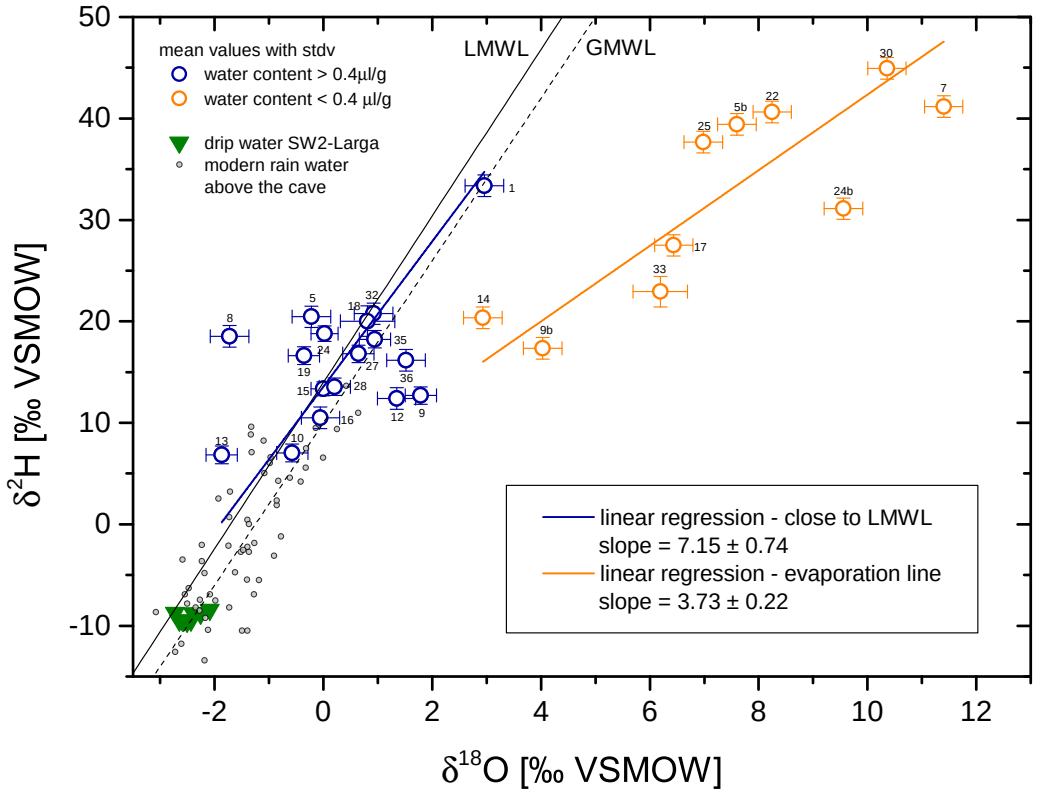

Figure 6.6: δ^{18}O and δ^{2}H of fluid inclusions from stalagmite LA-1. Shown are the mean values of the respective depths divided into high (blue circles) and low (orange circles) water content. The sample identification is the same as in table A.29 - A.33. The LMWL (solid line) after *Scholl and Murphy* [2014] as well as the GMWL (dotted line) are shown. In addition, drip water data at site SW-2 (green triangles) as well as the rain water (grey dots) above the cave are shown. Both groups of samples were fitted with a linear regression, whereby a comparable slope to the one of the GMWL results for the samples with a high water content. The samples with a low water content show fractionation due to evaporation.

the GMWL with a value of 3.4. For the samples with a low water content, the stable isotopic composition is interpreted to show kinetic fractionation, which was probably caused by evaporation. No conclusions can be derived from the stable isotopic composition of the fluid inclusions as to whether the evaporation took place in the cave or in the soil above the cave. The temperature-driven cave ventilation, which occurs when the outside temperature is lower than the cave temperature, might have been more pronounced in colder periods [*Vieten et al.*, 2016]. Strong ventilation and low drip rates during stadials favour the possibility of evaporation. Furthermore, *Warken et al.* [2020] shows that the stable isotopes in the calcite ($\delta^{18}O_{calcite}$ and $\delta^{13}C$) as well as the trace elements indicate partly strong kinetic fractionation, which could have been caused by evaporation.

Correction due to the changing isotopic composition of the ocean

To compare the measured stable isotope results of fluid inclusions with the actual precipitation above the cave or the drip water in the cave, the values must be corrected. Since during the growth period of LA-1 variations in continental ice volume led to a changed global $\delta^{18}O$ composition of the ocean, because ice formation preferentially removed H_2^{16}O from the ocean. In addition, the evaporation/precipitation ratio in the western tropical Atlantic varied due to changing atmospheric circulation patterns, which also affects the $\delta^{18}O_{sw}$ composition of the surface water. For the transitions between glacial-interglacial for the last 136 ka, *Schmidt et al.* [2004] found an amplitude of the local $\delta^{18}O_{sw}$ of about 1.5 ‰ for the Colombian basin, which is considerably larger than the global δ^{18}O change due to ice volume ($\delta^{18}O_{sl} \sim 1$ ‰). However, on glacial time scales $\delta^{18}O_{sw}$ is also affected by the variation of the continental ice volume. If these two corrections are applied to the results of the measurements of the stable isotopes of the fluid inclusions, the values of δ^{18}O and δ^{2}H would be shifted to lighter isotopes because the global ocean from which the precipitation is formed was heavier (see figure A.40). For the overall mean value of the $\delta^{18}O$ results for all samples with a high water content, this correction would shift the result from $+0.37 \pm 1.17$ ‰ to -1.13 ± 1.17 ‰ in VSMOW. This $\delta^{18}O_{fluid}$ value is still heavier compared to the present-day drip water isotopic composition at site SW-2, with a mean δ^{18}O value of -2.59 ± 0.27 ‰ VSMOW. Nevertheless, the overall pattern, that samples with a high water content are located on the GMWL and samples with a low water content are showing evaporation effects does not change. The analysis of the isotope values ($\delta^{18}O_{sl}$ and $\delta^{2}H_{sl}$) corrected for the changing sea level also results in comparable slopes of the derived linear regressions (see figure A.37). For the following application of the classic carbonate thermometer these corrections are not required, because here only the fractionation between $\delta^{18}O_{fluid}$ and $\delta^{18}O_{calcite}$ is considered. Hence, both signals are equally affected by a changed $\delta^{18}O_{sw}$.

Can a climatic signal be distinguished in the isotopic pattern of $\delta^{18}O_{fluid}$ and $\delta^{2}H_{fluid}$?

In figure 6.7 each sample is associated with the respective climatic condition through the analysis of the $\delta^{18}O_{calcite}$ signal and the trace elements [*Warken et al.*, 2020], whereby a distinction is made between cold phases (HS, LGM, GS) and warm phases (GI). All samples that clearly represent a Greenland interstadial (red triangle) show a uniform pattern, with the stable isotopic composition located on the GMWL or correspondingly on the linear regression close to the LMWL. This corresponds to the expectations for a relatively warm and moist climatic period. In contrast, I would expect a deviation in the isotopic composition of samples formed during colder climatic conditions, with precipitation decreasing during Heinrich stadials for the tropical regions of the western Atlantic [*Deplazes et al.*, 2013]. In figure 6.7 no uniform cluster on the GMWL or shifted towards higher isotope values can be identified for the $\delta^{18}O_{fluid}$

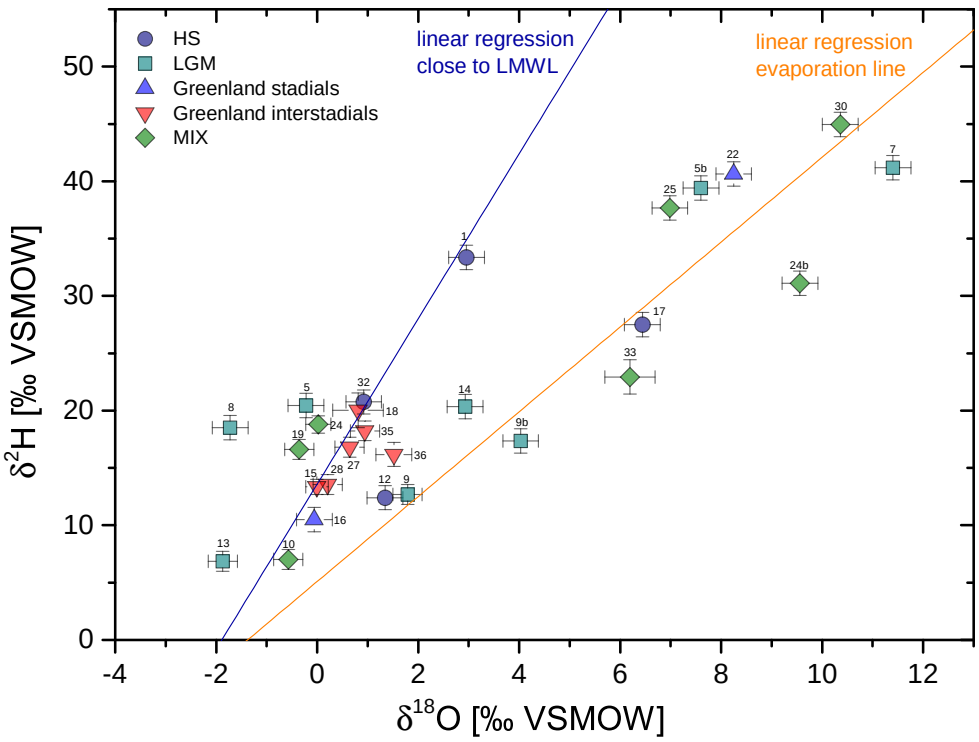

Figure 6.7: Water stable isotope data of all measured fluid inclusion samples from LA-1, with the mean values categorized according to the warm or cold periods in which they were formed. Thereby a distinction is made between Heinrich stadials (blue dots), LGM (green square), Greenland stadials (blue triangle), Greenland interstadials (red triangle) and samples whose depths covers several events (green diamond).

and $\delta^2 H_{fluid}$ data formed during HS (blue circle) or GS (blue triangle). Over the period of the LGM (24 - 18 ka) I measured at 6 different depths, but also in this interval no clear pattern with regard to the GMWL could be identified. Unfortunately, some samples appear to accumulate depths intervals with highly variable $\delta^{18}O_{calcite}$ signal and, therefore, potentially mix different climatic conditions.

HS, LGM and Greenland stadials - increased d - excess during colder and drier climatic conditions

A further parameter that can give information about the formation conditions of precipitation when analysing stable water isotopes is the d - excess [*Craig*, 1961; *Dansgaard*, 1964; *Gat*, 1996; *Froehlich et al.*, 2002]. It is related to evaporative fractionation of isotopes and the temperature and humidity conditions during evaporation and can vary due to local climate, land cover and history of the air mass producing rain [*Merlivat and Jouzel*, 1979]. The d - excess can be both an indicator for ocean evaporation or an indicator for moisture recycling. In the case of atmospheric vapour of oceanic origin, the deuterium excess, generally reflects the climatic conditions where the water evaporates [*Merlivat and Jouzel*, 1979]. The d - excess increases with decreasing relative humidity (h_s) and increasing SST in the evaporation flux above the ocean [*Craig*, 1961; *Uemura et al.*, 2008]. However, the influence of locally evaporated vapour could also lead to higher d - values (> 10 ‰) for precipitation originating from an air mass into which this re-evaporated water vapour is admixed, the so called moisture recycling [*Gat et al.*, 1994]. If water vapour from precipitation with an average d - value of 10 ‰ is re-evaporated, the lighter $^2H^1H^{16}O$ molecule may again contribute preferentially to the isotopic composition of the vapour and this, in turn, leads to an enhanced deuterium excess in precipitation. Accordingly, d - excess is not only influenced by humidity (h_s) during evaporation above the ocean, but also by local evapotranspiration [*Aemisegger et al.*, 2014].

Considering the stable isotope results of the fluid inclusions measured for LA-1, figure 6.8 focuses on the samples which could be clearly associated to colder and drier climatic conditions (HS, LGM and GS). The observed pattern may be explained by a simple conceptual model, which takes into account evaporation on the one hand and a varying d - excess on the other hand. If I examine these samples relative to an evaporation line which originates from the present - day drip water composition, a clear offset towards higher $\delta^2 H_{fluid}$ values becomes evident. Because it is not possible to determine the exact origin of these samples during the LGP. I decided to choose the mean isotopic composition of present - day drip water and thus determine a maximum possible deuterium excess. This vertical offset from the GMWL, the so - called d - excess quantifies the degree of moisture recycling or a lower humidity above the ocean during evaporation. In this case, the offset does not refer to the GMWL, but to the evaporation line (orange line) since these samples probably experienced additional evaporation. The maximum possible d - excess with respect to the evaporation line for each sample is

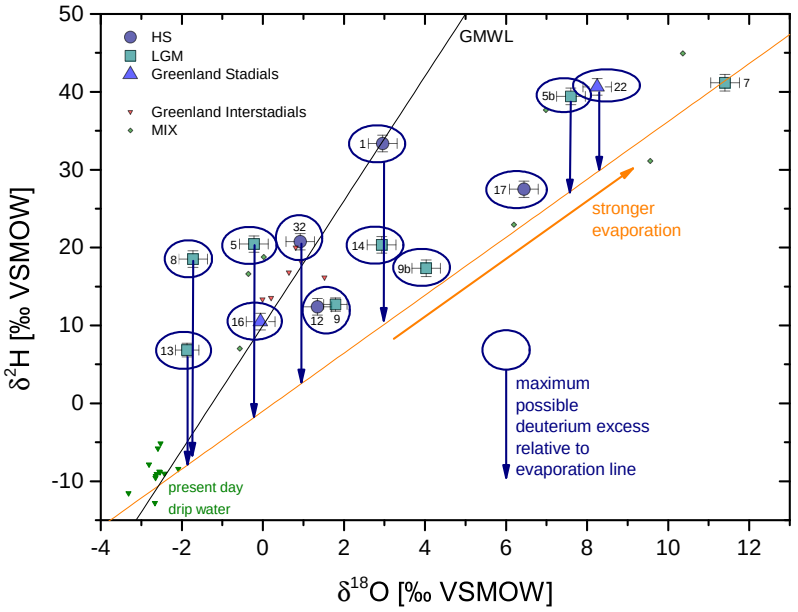

sample ID	possible d-excess [‰]
1	22.9
5	21.9
5b	11.9
7	0.0
8	26.0
9	6.3
9b	3.3
12	8.2
13	14.7
14	10.8
16	11.2
17	4.4
22	10.9
32	18.2

Figure 6.8: Possible d-excess relative to an evaporation line for samples associated with Heinrich stadials (blue circle), LGM (green square) or Greenland stadials (blue triangle). The intersection between the evaporation line ($y = 3.72 \cdot x - 1$, orange) and the GMWL (black line) reflects the present-day drip water composition. Possible d-excess relative to the evaporation line is illustrated as blue circles with approximate values listed in the table on the right.

illustrated as blue circle and the possible d-value is listed in figure 6.8. It is likely that the isotopic composition of the samples selected here was influenced by a combination of several processes, which are explained in the following.

Firstly, an increased deuterium excess, which shifts the samples to higher $\delta^2 H_{fluid}$ values, exceeding 10 ‰ due to an increased moisture recycling or less humidity above the ocean. It could be assumed that during colder and drier climatic conditions, a larger humidity gradient between the saturated layer directly at the ocean surface and the sub-saturated atmosphere above, leading to strong non-equilibrium fractionation and thus higher d-values in the evaporating moisture [*Pfahl and Sodemann*, 2014]. Furthermore, dry climatic conditions favour evaporation, particularly under unsaturated air conditions. Therefore, precipitation from air masses that have undergone considerable incorporation of evaporated water will present higher d-values [*Froehlich et al.*, 2002; *Pfahl and Wernli*, 2008; *Ampuero et al.*, 2020]. The assumption that an increased deuterium-excess can be expected under drier climatic conditions is further confirmed by the results of *Vieten et al.* [2018] for today's precipitation above the cave, with significant higher d-values (> 15 ‰) for the dry season (winter months). According to the theoretical considerations of *Merlivat and Jouzel* [1979] and a SST of

22 °C [*Schmidt et al.*, 2010], the highest d - value of 26 ‰ for sample 8 (21.43 ka) would theoretically be possible at a humidity at the sea surface of approximately 50 %. It is quite conceivable that the humidity during the Greenland stadials was significantly lower than the present - day average humidity above the ocean´s surface, which today varies between 65 % and 80 % for the tropics of the western Atlantic depending on the season [*Aemisegger et al.*, 2014].

Both stable water isotopes are influenced by evaporation, which fractionates oxygen more than hydrogen, with the characteristic slope of ~ 3.4. This possible evaporation, which has already been discussed, shifts the samples to both higher $\delta^{18}O_{fluid}$ and $\delta^{2}H_{fluid}$ values. The superposition of the variable d - excess and the evaporation causes some samples to be shifted from the evaporation line (orange) towards the GMWL (black), see figure 6.8. This would also explain why HS 1 (sample 1), which is actually the most pronounced Heinrich event for LA-1 considering the $\delta^{18}O_{calcite}$ signal [*Warken et al.*, 2020], does not show a clear evaporation pattern because it seems to lie on the GMWL. Furthermore, some samples show an atypical position above the GMWL (e.g. 5, 8 and 13), which could also be due to an increased deuterium excess relative to the evaporation line.

It is possible that for samples from Greenland stadials, HS and LGM different factors are superimposed which influence the d - excess to different strengths. Both low humidity over the ocean and increased moisture recycling can be favoured by rather dry climatic conditions [*Froehlich et al.*, 2002; *Masson-Delmotte et al.*, 2005; *Jouzel et al.*, 2007; *Pfahl and Sodemann*, 2014]. In such a scenario, the varying d - excess may shift samples that are actually on the evaporation line towards the GMWL, which makes it difficult to identify a uniform pattern. Considering the measured deuterium excess of the Greenland interstadials and stadials, the possible deuterium excess relative to an evaporation line shifts the very negative d - values of the stadials to more realistic d - values compared to the interstadials (see figure A.38).

Greenland interstadials - $\delta^{18}O_{fluid}$ compared to present - day rainfall

If I consider the samples of the presumably warm and moist Greenland interstadials, a clear pattern scattered around the GMWL with a d - value around 10 ‰ can be observed. In comparison to modern cave drip water ($\delta^{18}O = -2.6 \pm 0.2$ ‰) the mean $\delta^{18}O_{fluid}$ value shows an average enrichment of 3.3 ± 0.5 ‰ in VSMOW, see figure 6.9. If the results are corrected for the changing ice sheets (data of sea level corrected values see table A.34) and thus for the changed isotopic composition of the ocean, the average enrichment is 2.1 ± 0.43 ‰ VSMOW. As discussed before, this correction is questionable and does not change the overall pattern that the paleodrip water is isotopically enriched compared to modern day drip water. I suppose that the precipitation and thus the drip water that fed the stalagmite during the LGP was different from modern drip water. These findings are similar to the results of *Millo et al.* [2017], which found

an enrichment of about 4 ‰ VSMOW for paleodrip water compared to modern cave water for a subtropical stalagmite covering parts of the LGP from Brazil.

Regarding recent precipitation in Puerto Rico, *Scholl and Murphy* [2014] have shown that isotopically enriched precipitation is associated with trade wind orographic rain and isotopically lighter precipitation with convective rain such as hurricanes and tropical storms (see figure A.36). Accordingly, the paleoprecipitation during the Greenland interstadials of LA-1 could be characterized rather by orographic rain than by convective rain. These results are further supported by findings of *Winter et al.* [2020] for the hydroclimatic regime in Central America during the transition from the Last Glacial Period into the Holocene. The authors argue, that the type of precipitation (convective or orographic) depends on the location of the ITCZ and the related Caribbean SST. The exceeding of an SST threshold in the nearby tropical ocean triggered a deep atmospheric convection during the Holocene, which lead to a shift of the regime from drought during the LGP to humidity over Central America. In contrast, during the

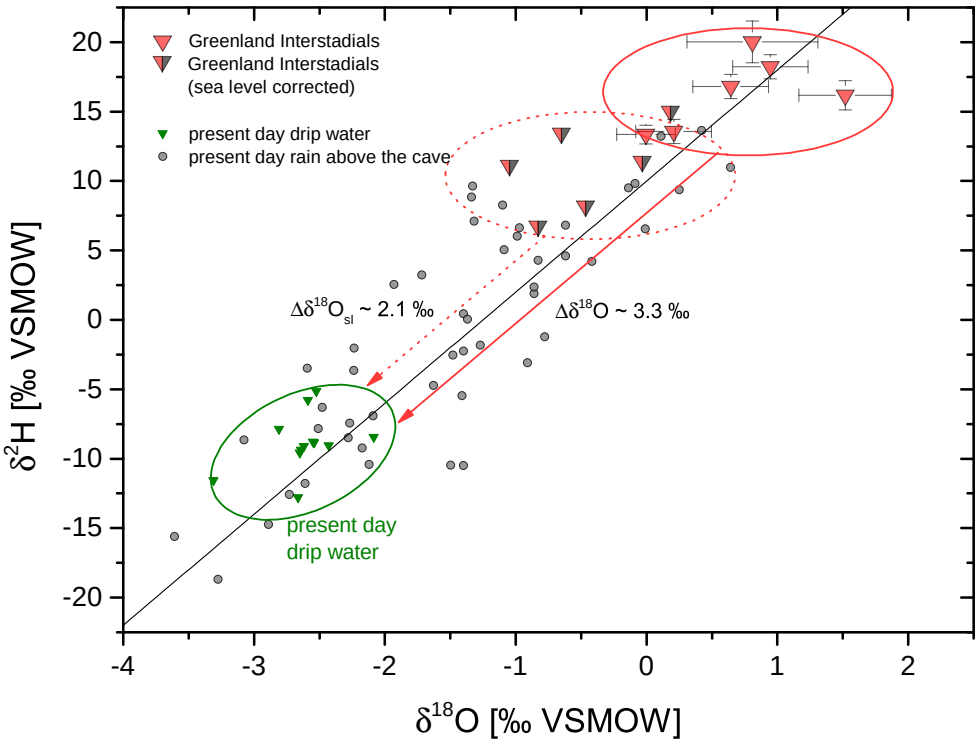

Figure 6.9: Mean δ^{18}O deviation for samples of the Greenland interstadial to present-day rainfall (mean $\delta^{18}O = -2.6 \pm 0.2$ ‰). The uncorrected isotopic composition (red triangles) results to a mean $\delta^{18}O_{fluid}$ value of 0.69 ± 0.49 ‰, whereas the sea level corrected (half filled triangle) oxygen values results to -0.47 ± 0.43 ‰ in VSMOW. The paleodrip water is isotopically enriched compared to present-day cave water, which indicates that orographic precipitation is more pronounced.

glacial period relatively cold Caribbean SST (approximately 2 - 3 °C colder [*Schmidt et al.*, 2010]) in the Guatemalan region could not sustain strong convective activity [*Winter et al.*, 2020]. Consequently, during the LGP with rather colder SST than today the precipitation is interpreted to be of more orographic origin.

Observations by *Rozanski et al.* [1993] on the relationship between the amount and isotopic composition of precipitation for tropical regions between 20°S and 20°N show a shift towards more positive (heavier) δ^{18}O values with decreasing amounts of precipitation (see figure A.39). Above the cave with an annual precipitation of 2130 mm per year a δ^{18}O value of $\sim 3 \pm 1$ ‰ VSMOW would be expected according to *Rozanski et al.* [1993], which agrees within the uncertainty with the mean isotopic signal of present - day drip water. Accordingly, it could be assumed that for Greenland interstadial the amount of rainfall has been reduced to 600 - 800 mm per year with an average $\delta^{18}O_{fluid}$ value which is about 2 ‰ heavier than present - day drip water taking the more positive sea water into account. This assumption of a drastic reduction of rainfall during the Greenland stadials of the LGP may be too extreme. However, the shift of δ^{18}O values to more positive values may indicate not only a change in the type of precipitation but also a reduction of the amount during the Greenland stadials compared to today.

Findings of the fluid inclusion δ^{18}O and δ^{2}H interpretation

- The stable isotope measurements of $\delta^{18}O_{fluid}$ and $\delta^{2}H_{fluid}$ for LA-1 show two characteristic patterns. Samples with a water content above 0.4 μl/g are located on the GMWL or scatter around it with a slope of 7.2 ± 0.8, whereas samples with a lower water content deviate significantly from that with a slope of 3.7 ± 0.2 indicating evaporation effects.
- For HS, LGM and Greenland stadials: The varying deuterium excess shifts some samples that experienced evaporation and should follow the evaporation line towards the GMWL, which may lead to misinterpretation.
- For Greenland interstadials: The samples exhibit no increased d - excess and are located on the GMWL, accordingly, an isotopic modification due to evaporation can be excluded.
- For Greenland interstadials: The $\delta^{18}O_{fluid}$ values are up to 3 ‰ VSMOW more positive than δ^{18}O of modern drip water, which is similar to findings of late glacial fossil drip water from a subtropical Brazilian stalagmite [*Millo et al.*, 2017].

- For Greenland interstadials: The isotopically enriched $\delta^{18}O_{fluid}$ values indicate paleodrip water that was dominated by orographic rain and perhaps the amount of precipitation was significantly reduced.

6.4.4 Application of the classic carbonate thermometer for samples with a high water content

For the samples with a high water content, where the isotopic composition of the fluid inclusion measurements are located on the GMWL, it can be assumed that they have not experienced kinetic fractionation due to evaporation. For the calculation of paleotemperatures with the classic carbonate thermometer (see section 2.2.3), the $\delta^{18}O_{fluid}$ and $\delta^{18}O_{calcite}$ values need to be harmonized to the equivalent depth range, since the $\delta^{18}O_{calcite}$ data were measured with a much higher resolution than the isotopes of the fluid inclusion samples. Figure 6.10 shows the high resolution $\delta^{18}O_{calcite}$ signal in grey with the averaged values (green circles) for the respective depth of the corresponding fluid sample pieces with the uncertainty resulting from the standard deviation of the fluid isotope analysis. For the $\delta^{18}O_{fluid}$ measurements, only the mean values with a high water content are shown (blue circle) together with the overall mean (dotted line). I decided to parametrize the classic oxygen isotope carbonate thermometer with isotope fractionation factors according to *Johnston et al.* [2013] with $1000 \cdot ln(\alpha_{calcite-water}) = 17.66 \cdot (10^3/T) - 30.16$, which derived the most realistic temperature patterns. For comparison with other parametrizations, temperatures calculated after *Kim and O'Neil* [1997] and *Tremaine et al.* [2011] are listed in table A.36 and shown in figure A.41.

The paleotemperatures were calculated for 17 individual depths using the classic carbonate thermometer, with temperatures varying between 15.2 ± 1.7 °C (sample 8, 21.43 ± 0.25 ka) and 33.5 ± 1.5 °C (sample 9, 22.65 ± 0.23 ka). Samples which can be clearly assigned to cold and dry climatic conditions due to their calcite signal (higher $\delta^{18}O_{calcite}$ values) are e.g. samples 1 (24.9 ± 1.8 °C), 12 (22.5 ± 1.8 °C) and 18 (17.6 ± 1.7 °C). In contrast, samples which clearly originate from a warmer and wetter climatic period are for example sample 9 (33.6 ± 1.6 °C), 24 (24.0 ± 1.3 °C), 27 (29.3 ± 1.5 °C) and 32 (29.9 ± 2.6 °C). Here the interstadials show higher temperatures on average compared to the stadials, but temperatures strongly exceeding present - day cave air temperature (22.5°C) and are rather unrealistic even for Greenland interstadials of the LGP.

The green bars in figure 6.10 illustrate intervals during the LGP, when LA-1 shows elevated $\delta^{18}O_{calcite}$ values (HS 1 (17.2 - 15.5 ka), HS 2 (24.3 - 23.8 ka) and HS 3 (29 - 30 ka)), which are associated with cold and dry climatic conditions. The calculated paleotemperatures for HS 2 are 21.4 ± 1.4 °C (sample 10), 22.5 ± 1.8 °C (sample 12) and

16.51 ± 1.4 °C (sample 13) and for HS 3 are 17.6 ± 1.7 °C (sample 18) and 18.7 ± 1.4 °C (sample 19), respectively. Accordingly, a mean cooling compared to the present cave air temperature of 2.4 ± 2.6 °C for HS 2 and 4.4 ± 0.6 °C for HS 3 could be obtained. In contrast, HS 1 shows no temperature decrease, although *Arienzo et al.* [2015] has found the most pronounced cooling (~ 4 °C) for HS 1 for a Bahamian stalagmite record. However, considering the $\delta^{18}O_{calcite}$ signal of LA-1, it appears that HS 1 is characterized by the most extreme conditions (cold and dry) in Puerto Rico [*Warken et al.*, 2020]. It is likely that very slow drip rates and enhanced PCP (Prior Calcite Precipitation) were dominant here, which may have also influenced the isotopic composition of the fluid inclusions. Considering figure 6.8 for HS 1, a strong possible d - excess ($d = 22.9$ ‰) is visible relative to the evaporation line for HS 1, which shifts the sample from the evaporation line towards the GMWL. Therefore, I hypothesize that HS 1 has experienced very strong evaporation, which is not obviously visible with the misleading location on

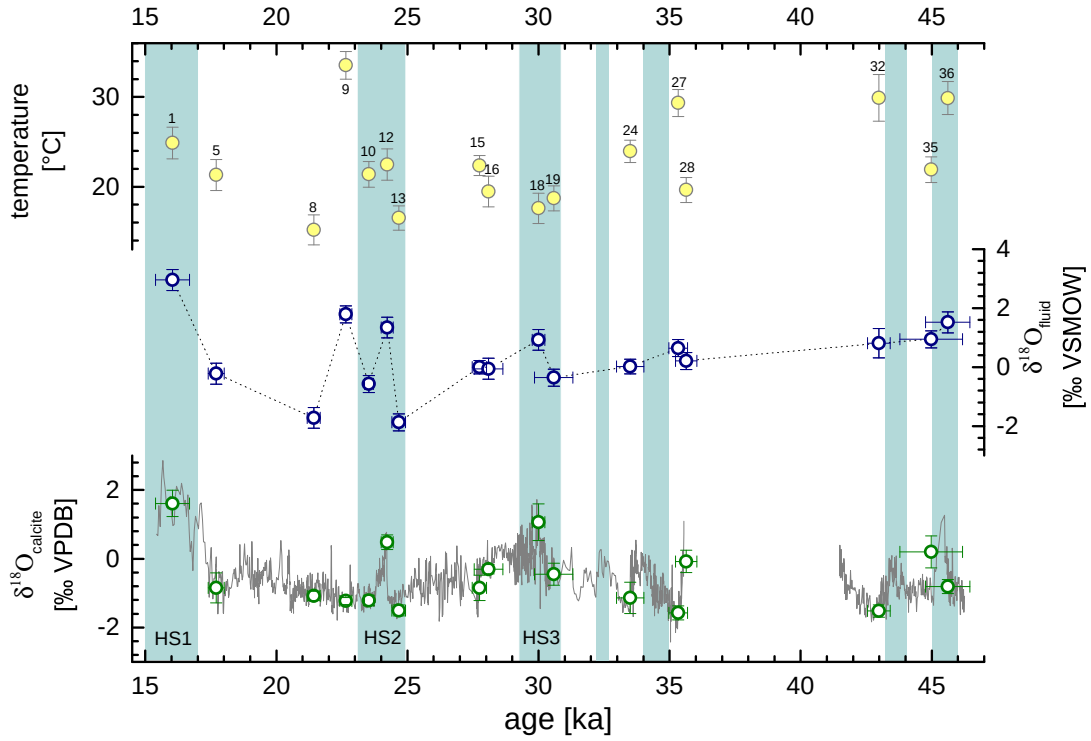

Figure 6.10: Measured $\delta^{18}O_{calcite}$ signal in grey with harmonized to fluid inclusion sample depth mean values (green circles). The $\delta^{18}O_{fluid}$ results with a high water content are shown as blue circles and the calculated paleotemperatures via the classic carbonate thermometer according to *Johnston et al.* [2013] as light yellow dots. For a better orientation presumably relatively dry and/or cool periods during the Last Glacial Period are illustrated as light blue bars. The corresponding time intervals of the colder periods refer to the clearly pronounced HS events with increased $\delta^{18}O_{calcite}$ values according to *Warken et al.* [2020].

the GMWL, but has shifted the $\delta^{18}O_{fluid}$ to a heavier (more positive) value. Accordingly, sample 1 (HS 1) should be excluded from the discussion of paleotemperatures. This is not the case for all samples which are formed during a Heinrich stadial, for example sample 13, which is assigned to HS 2. Here a clear d - excess can be recognized, but no strong evaporation. Accordingly, the $\delta^{18}O_{fluid}$ value is not modified and the obtained temperature of $16.5 \pm 1.4\,°C$ (see figure 6.10) can be considered realistic.

When the reconstructed paleotemperatures are examined more closely, a temperature fluctuation between 15 °C and 33 °C can be observed in particularly conspicuous samples (1, 8, 9, 27, 32 and 36). The samples 1, 8, 9, and 32 are to be excluded from the data set, because they have a misleading positions on the GMWL (see figure 6.8) despite a high water content. It can be assumed that these samples were affected by the evaporation of the drip water after precipitation of the calcite and therefore did not preserve the original $\delta^{18}O_{fluid}$ signal. Another effect which is often observed in caves and which extensively alters the signal in stalagmites is PCP. This leads to an accumulation of Mg and Sr in the drip water as well as to increased $\delta^{18}O_{calcite}$ and $\delta^{13}C$ values, at the same time PCP leads to slower growth [*Stoll et al.*, 2012]. The growth rates of LA-1 vary from 10 to up to 2000 μm per year [*Warken et al.*, 2020] suggesting the presence of PCP as modulator for the growth rate changes and correspondingly a modified $\delta^{18}O_{calcite}$ signal, which is not only controlled by temperature. To what extent PCP changes the isotope composition of the drip water is difficult to determine. However, the presence of PCP indicates a very difficult temperature reconstruction, because the temperature signal is additionally superimposed by kinetic effects. Noticeable are two additional samples, which show significantly higher temperatures than the present cave temperature. Samples 27 and 36 were taken in sections of LA-1 with a highly variable $\delta^{18}O_{calcite}$ signal and may not have been accurately sampled.

6.4.5 Comparison between classic carbonate thermometer with Bahamian speleothem, SST and Lake temperature records

I compare the $\delta^{18}O_{fluid}$ - carbonate precipitation temperatures (after *Johnston et al.* [2013]) for the samples with a high water content and where kinetic fractionation due to evaporation can be excluded with temperature records from marine and terrestrial archives. The locations of the individual studies are shown in figure 6.1. Figure 6.11 shows the different temperature reconstructions, with the fluid inclusion derived temperatures of LA-1 (light yellow dots) together with a Bahamian speleothem record [*Arienzo et al.*, 2015], marine SST (Sea Surface Temperature) reconstructions [*Schmidt et al.*, 2010; *Ziegler et al.*, 2008] and land surface temperatures records from lake sediments from central America [*Grauel et al.*, 2016]. For the paleotemperatures derived from $\delta^{18}O_{fluid}$ measurements of LA-1, samples (15, 24 and 35) associated with Greenland interstadials agree very well with the reconstruction of the SST of the Gulf of Mexico. Compared to the rather constant SST of the Cariaco Basin in the Caribbean, the SST record of the Gulf of Mexico shows a much stronger temperature variation

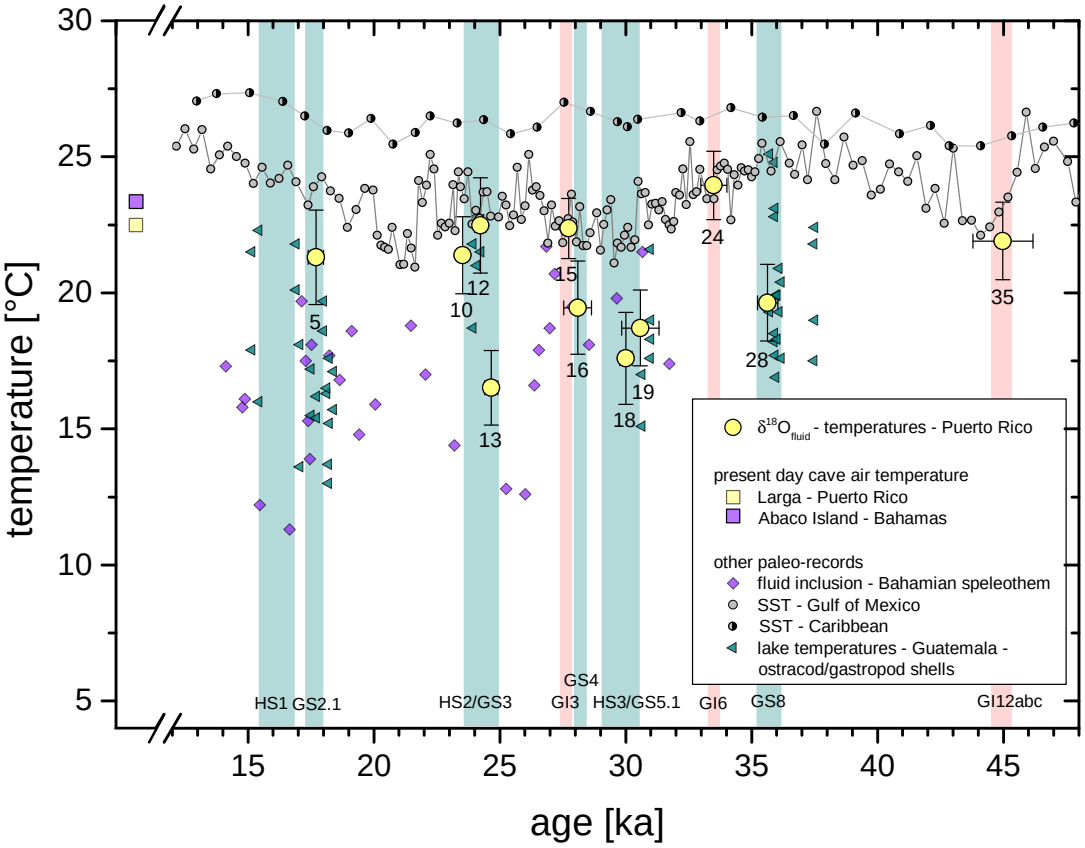

Figure 6.11: Fluid inclusion derived temperatures after *Johnston et al.* [2013] with sample ID are shown in light yellow. For comparison another speleothem record (diamond), two marine records (dots) and one terrestrial record (triangles) are shown. The temperature reconstruction of the Bahamian speleothem record is also based on the analysis of fluid inclusions, with a temperature uncertainty of $\pm 2.7\,°C$ [*Arienzo et al.*, 2015]. The present-day cave air temperature of Larga (yellow square) and Abaco Island (purple square) is given for a better comparison. The SST are derived from a sediment core located in the Cariaco Basin (Caribbean after *Schmidt et al.* [2010]) in dark grey and from the Orca Basin (Gulf of Mexico after *Ziegler et al.* [2008]) in light grey, based on the Mg/Ca ratio of surface-dwelling foraminifera. The terrestrial record from Lake Petén Itzá (Guatemala) after *Grauel et al.* [2016] using two different biogenic carbonates, with benthic ostracod limnocythere opesta (green triangle) and gastropods Cochliopinasp and Tryonia exigua (blue triangle). In the tropical Atlantic, Heinrich stadials (1 to 3) as well as Greenland stadials are associated with cold and dry conditions (light blue bars) and Greenland interstadials are associated with warmer and more humid climatic conditions (light red bars) [*Peterson et al.*, 2000].

of about 4.5 °C for the time period shown here. It is notable that both SST records indicate no significant cooling for HS 1, although this event is the most pronounced event in the terrestrial records after *Arienzo et al.* [2015] and *Grauel et al.* [2016]. In fact, the fluid inclusion derived temperature for HS 1 (24.9 ± 1.8 °C) corresponds to the SST of the Gulf of Mexico within the uncertainty (see figure A.42). However, this sample was excluded from interpretation due to evaporation, as well as the samples 9, 27, 32, and 36 which indicate significant higher temperatures than present - day cave air temperature. In contrast, sample 8 (21.43 ± 0.25 ka) with $T = 15.2 \pm 1.7$ °C shows a significantly lower temperature, which is consistent with the SST according to *Ziegler et al.* [2008] as this record shows a temperature minima around 21 ka (see figure A.42). In order to remain consistent and stringent in the argumentation that evaporation leads to kinetic fractionation and therefore no paleotemperatures can be determined with the classic carbonate thermometer, these samples must be excluded.

For intervals during the LGP, when LA-1 shows elevated $\delta^{18}O_{calcite}$ values, the paleotemperatures indicate significantly lower values. These are, however, not as pronounced as *Arienzo et al.* [2015] found for a Bahamian speleothem (temperature variation between 12 °C and 22 °C) or as terrestrial lake paleotemperature reconstructions for central America (temperature variation between 13 °C and 25 °C) demonstrate [*Grauel et al.*, 2016]. For the reconstruction of the lake temperatures ostracodes are used, these are bottom dwellers which archive hypolimnetic temperatures that are recorded during winter mixing [*Grauel et al.*, 2016]. So it is questionable if a lake sediment record is suitable to compare the formation of a stalagmite in a cave. Furthermore, because of the geographical location of Puerto Rico in respect to the two terrestrial records, located further south than the Bahamas and no continental influence as for Lake Petén Itzá, I would expect less pronounced temperature variations between glacial and interglacial and a more maritime Atlantic climate. For our measurements the temperature decrease during HS 3 was the most pronounced one, with both individual measurements indicating a cooling of about ∼4.4°C. This temperature decrease is consistent with the results of *Arienzo et al.* [2015], which found an average temperature decrease of ∼ 4°C across the Heinrich stadials 1 to 3.

In summary, the reconstructed paleotemperatures based on the fluid inclusion measurement show a variation of 7.5 °C between a minimum temperature of 16.5 ± 1.4 °C (24.6 ka) and a maximum temperature of 24.0 ± 1.3 °C (33.5 ka). This temperature variation between Greenland stadials and interstadials is more pronounced than the variation of the SST after *Ziegler et al.* [2008] and less pronounced than the variation of the Bahamian speleothem record after *Arienzo et al.* [2015]. I could show that during HS 2 a temperature decrease of ∼ 2.4 °C and during HS 3 an even more pronounced cooling of ∼ 4.4 °C occurred, which is consistent with the results of *Arienzo et al.* [2015] for an average temperature decrease of ∼ 4 °C during HS 1 to 3. This much stronger temperature decrease on land compared to the sea surface is consistent with other findings of speleothem records [*Arienzo et al.*, 2015] or lake sediments from

Central America [*Grauel et al.*, 2016]. For the reconstructed paleotemperatures during the Greenland interstadials I could show that they correspond to the temperatures of the sea surface of the Gulf of Mexico.

Findings for the paleotemperature reconstruction using the classic carbonate thermometer

- A paleotemperature reconstruction using the classic carbonate thermometer is useful if kinetic fraction during calcite formation can be excluded. Therefore, the measured stable water isotopes should be analysed with respect to possible evaporation and/or a varying deuterium excess.
- In many terrestrial paleorecords Heinrich stadial 1 is the most pronounced one [*Arienzo et al.*, 2015], which is also the case for the $\delta^{18}O_{calcite}$ signal of LA-1 [*Warken et al.*, 2020]. In contrast, SST reconstructions show no significant temperature decrease for HS 1, which agrees with the results of the fluid inclusion measurements. Therefore, I assume that the $\delta^{18}O_{fluid}$ and $\delta^{2}H_{fluid}$ values mainly indicate an evaporation signal with a strong deuterium excess due to dry climatic conditions.
- For Greenland interstadials: Reconstructed paleotemperatures match with sea surface temperatures from the Gulf of Mexico.
- For Greenland stadials: A mean temperature decrease compared to the present-day cave air temperature of $2.37 \pm 2.59\,°C$ for HS 2 and $4.35 \pm 0.56\,°C$ for HS 3 could be obtained.

7 Conclusion and Outlook

7.1 Conclusion

7.1.1 Fluid inclusion line

A major goal of this work was the design and development of the *fluid inclusion line* for the simultaneous measurement of the stable water isotopes of fluid inclusions of speleothems by absorption spectroscopy. The determination of the $\delta^{18}O$ and $\delta^{2}H$ value of fluid inclusion water is complicated by the small amount of released water in the μl to sub-μl range. So far, only a few laboratories have set up suitable systems (IRMS [*Vonhof et al.*, 2006; *Dublyansky and Spötl*, 2009] or CRDS [*Arienzo et al.*, 2013; *Affolter et al.*, 2014] / OA-ICOS [*Czuppon et al.*, 2014]) to perform these measurements. Consequently, the potential for detailed studies is severely limited by the small number of laboratories. Therefore, I have built up a line, which follows the basic idea of *Affolter et al.* [2014] to generate a continuous water vapour background with known isotopic composition on which the aliquots of water of the crushed speleothems are measured. The measurement precision of the Picarro analyser used in this thesis (*L2130-i*) for the single water isotopes is independent of water volumes. Therefore, I am able to work with significant lower water vapour background concentrations (6 000 - 8 000 ppmV) compared to *Affolter et al.* [2014] and could measure released water volumes down to 0,2 μl with high precision. The achieved precision of 0.5 ‰ for oxygen and 1.5 ‰ for hydrogen, VSMOW respectively, is comparable to the precision of classic mass spectrometer measurements and also to those with comparable laser absorption based setups. I have verified the accuracy of my measurements with inter-laboratory comparisons. Regarding the future exchange between laboratories measuring stable isotopes in fluid inclusions, I have developed a water amount calibration method using glass capillaries. These glass capillaries can be used to check the water amount calibration as well as the isotopic accuracy. In this context, an evaluation routine is made available, which helps laboratories with comparable measurement methods to evaluate the data in a fast and standardized manner. Thus, laboratory internal evaluation can be adjusted and the measured data can be compared more consistently.

Furthermore, I have considered different effects, which could influence the measurement of the stable water isotopes. I was able to show that both adsorption and memory effects can be excluded for laser adsorption measurements when working with a saturated water vapour background. However, a crucial point with regard to the generated water vapour background is the selection of the isotopic composition of this background water. If this deviates significantly from the isotopic composition of the speleothem, shifts of up to 0.4 ‰ for oxygen and 3 ‰ for hydrogen can be observed. Nevertheless, if the isotopic signal of the water vapour background is within a range of $\pm$ 10 ‰ for

$\delta^{18}O$ and $\pm 50\,‰$ for $\delta^{2}H$ from the analysed speleothem, no significant deviation can be observed. This requirement is usually fulfilled when stalagmites from mid-latitudes are measured with a water vapour background generated from tap water.

7.1.2 Different paleotemperature reconstructions using fluid inclusions

I have applied two different methods to reconstruct paleotemperatures using the stable isotopes of fluid inclusions. Firstly by means of the classic application of the carbonate thermometer and secondly by means of the $\delta^{2}H/T$ relationship. However, both applications can only be used under certain circumstances. For the application of the classic carbonate thermometer the calcite precipitation must take place in equilibrium, which proves to be problematic for several stalagmite studies. Kinetic fractionation occurs for fast growing stalagmites or for rapidly changing growth rates. This is partly the case for Stam 4 from Cloşani, where the traditional carbonate thermometer leads to unrealistic temperature variations of 10 °C for the last 100 years. Another factor that enhances kinetic fractionation is a drip rate that is too fast or too slow. In case of a very slow or even interrupted drip rate, evaporation in the cave can be enhanced and causes kinetic fractionation during calcite precipitation. For this reason I excluded a large number of samples for the temperature reconstruction of LA-1 (Puerto Rico). I have found that the use of the carbonate thermometer can only be applied under a suitable pre-selection and exclusion of fractionation effects. I could show that for the westerly tropical Atlantic during the Heinrich stadial a significant cooling of about 3.5°C has occurred, which is more pronounced than expected by SST reconstructions. For the interstadials, temperatures were reconstructed that are comparable to the present day cave air temperature and the reconstructed sea surface temperatures.

In contrast, the application of the $\delta^{2}H/T$ relation is a suitable approach for stalagmites that have grown under continental climatic influence. This means that the isotopic composition of the precipitation is mainly controlled by the Rayleigh rainout effect and not by other isotopic effects such as the amount effect, which excludes tropical stalagmites. If the relationship between the $\delta^{18}O$ value of precipitation and surface temperature is well characterized, the deuterium signal in the fluid inclusions can determine temperatures with a precision of ± 0.45°C. With this I was able to resolve the temperature increase due to anthropogenic climate change for southern Romania for the second half of the 20th century using the fluid inclusion measurement. The reconstructed temperature increase of 1.02 ± 0.63 °C for the period between 1950 to 2010 is in excellent agreement with local temperature records. Thus, the newly applied deuterium-temperature relationship proves to be a suitable method to determine mean annual temperatures for mid-latitude stalagmites.

7.1.3 Climatic imprint on isotopic compositions of fluid inclusions

I was able to demonstrate the extent to which a climate signal is imprinted in stable isotopes of fluid inclusion in addition to the temperature information. For two different climatic regions (continental and tropical) I have found significantly increased isotope values in comparison to the isotopic composition of the present day drip water. Fractionation was more pronounced for oxygen than for hydrogen with a slope ($\delta^2H/\delta^{18}O$) of $+2.27 \pm 1.12$ for Bu4 (Germany) and $+3.73 \pm 0.22$ for LA-1 (Puerto Rico). This clear deviation from the GMWL with slopes of 2.3 and 3.7 indicates fractionation due to evaporation. This effect has never been reported before in stable isotope measurements of fluid inclusions. In fact, evaporation effects in caves are usually only marginally discussed due to the typically high humidity in the cave. However, that the same evaporation pattern can be found for these two different stalagmites shows, that evaporation in caves is an important phenomenon that can lead to disequilibrium conditions during calcite precipitation. The findings obtained in this thesis on the analysis of fluid inclusions make an important contribution to the better characterization of kinetic fractionation due to evaporation. For both stalagmites it was further shown that evaporation was favoured by dry climatic conditions, so the position of the stable isotopes of the fluid inclusions relative to the GMWL can be used as an indicator for dry or humid climatic conditions.

With the simultaneous measurement of $\delta^{18}O$ and δ^2H, the deuterium excess can be determined, which provides information about the conditions of formation or possible moisture recycling of the precipitation [*Froehlich et al.*, 2002]. Here I could show that with respect to the δ^2H signature very dry climatic conditions can lead to a strongly varying deuterium excess. Furthermore, the varying deuterium excess shifts some samples that experienced evaporation and should follow the evaporation line towards the GMWL, which may lead to misinterpretation. Although deuterium excess has no influence on the $\delta^{18}O$ signal and thus does not concern the use of the classic carbonate thermometer, it should be discussed in detail as it can provide important information on the formation conditions of precipitation.

A further conclusion is, that the source of precipitation can be derived from the fluid inclusions. I was able to identify $\delta^{18}O$ values for the tropical stalagmite that are significantly higher than the isotopic composition of today's drip water, which indicates a change in the type of precipitation. The measured fluid inclusion data of LA-1 indicates that there was a shift from convective rain to more orographic rain during the Greenland interstadials. For the stalagmite from Cloşani, I could show that significantly increased (more positive) isotope values and concurrently positively correlated NAO and EAWR modes indicate a shift of the precipitation source towards Mediterranean influence. Regarding the interpretation of circulation patterns (Cloşani - Romania), kinetic effects during calcite formation are excluded and it is assumed that the signal stored in the fluid inclusions is purely atmospheric.

7.1.4 Water content as climate proxy

Apart from the isotopic analysis of the fluid inclusions, I was able to measure the volume of the released water and thus the water content per gram of calcite. This can also be used to reconstruct possible climate changes. I could identify that for the Holocene stalagmite Bu4, rather dry climatic conditions with sporadic or seasonal water supply tend to be associated with a higher water content and more humid climatic conditions with a lower water content. The fact that less precipitation is associated with a higher water content seems counter-intuitive at first. In fact, reduced drip rates lead to irregular crystal growth and thus to more possibilities for incorporating fluid inclusions. This signal is not always completely clear, as I would expect LA-1 to have a high water content during the Greenland stadials, as these periods are associated with rather cold and dry climatic conditions, which, however, is not the case. Indeed, I measure a high water content for the Greenland interstadials, which are associated with rather humid and warmer climatic conditions. Accordingly, the results of the water content in relation to the climatic conditions for Bu4 and LA-1 are contradictory. More studies need to be carried out to identify whether a changing water content can be used to reconstruct varying climatic conditions

7.2 Summary and Outlook

In summary, with the construction of the *fluid inclusion line* I was able to measure stable isotopes of the fluid inclusions very precisely (± 0.5 ‰ for δ^{18}O and ± 1.5 ‰ for δ^{2}H) with a simple and robust method. The measuring method based on absorption spectroscopy has proven to be low-cost and effective with an average measuring time of 2 h per sample. However, influences of the background water's isotopic composition on the actual sample measurement need to be investigated in more detail. In addition, other available CRDS analysers are able to measure δ^{17}O, which can be used as an additional proxy to identify the relative humidity at the moisture source [*Uemura et al.*, 2010] and has not been studied intensively in continental archives so far [*Affolter et al.*, 2015]. I have developed a calibration method based on water-filled glass capillaries, which simplifies inter-laboratory comparison. Furthermore, this technique allows for a simultaneous calibration of isotopic and water amount measurements. In this context an evaluation protocol was developed, which is publicly accessible to for better comparison of measurement results.

With the application of this new technique to three different stalagmites, I have demonstrated the advantage of using fluid inclusions to learn about the climatic conditions in various settings. The analysis of stable isotopes of fluid inclusions is suitable for the determination of paleotemperatures (classic carbonate thermometer or δ^{2}H/T relation) and changing climatic conditions can be reconstructed. Here the isotopic composition of the fluid inclusions shows distinct evaporation effects for rather dry climatic conditions, which is an important contribution to the understanding of kinetic fractionation

during speleothem formation. Regarding the stalagmites presented here, a subsequent analysis of the oxygen isotopes of the already crushed fluid inclusion samples could be performed for the Romanian stalagmite. For Stam 4, the application of the classic carbonate thermometer was hampered by the fact that the fluid inclusion measurements were not taken at the growth axis and therefore the fractionation between $\delta^{18}O_{calcite}$ and $\delta^{18}O_{fluid}$ could not be determined. Here subsequent measurements could clarify whether sampling away from the growth axis has an influence on the kinetic fractionation leading to the resulting unrealistic temperatures. In order to demonstrate possible evaporation in the present day monitoring range, the isotopic composition of thin water films on stalagmites could be sampled. Concerning the stalagmite Bu4, both water film and fluid inclusion measurements could be performed on the recently precipitated calcite samples of the watch glasses under the drip site TS8 (location of Bu4). Here the calcite precipitation shows clear evidence of isotopic disequilibrium with significantly higher $\delta^{18}O_{calcite}$ values than expected [*Riechelmann et al.*, 2013]. For Puerto Rico, additional pool spar measurements of the $\delta^{18}O_{calcite}$ signal would help to better characterise present day calcite precipitation in the cave, as there is as significant deviation in isotope values between fluid inclusions and pool water.

I conclude, that measurements of stable isotopes of fluid inclusions provide an important contribution for reconstructing the past climate. The here developed analytical technique should therefore be routinely incorporated in already existing standard analyses of stable isotopes of the carbonate in order to obtain a comprehensive picture of the speleothem under investigation.

A | Appendix

A.1 Theoretical background

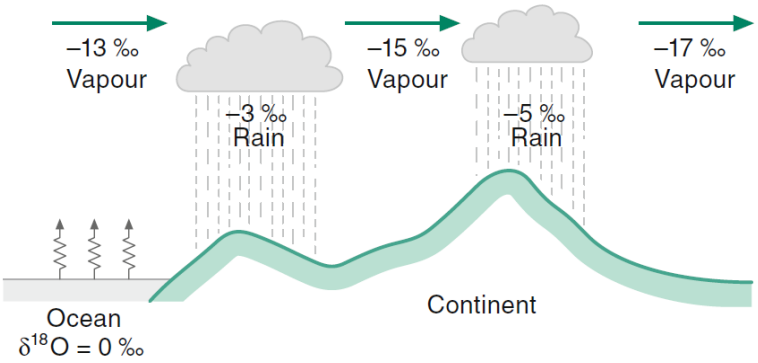

Figure A.1: Rainout effect on δ^{18}O values of atmospheric water [*Hoefs*, 2009].

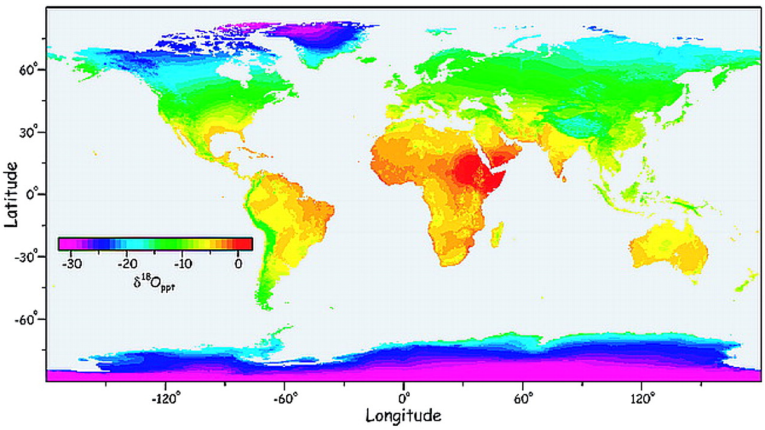

Figure A.2: The global distribution of mean annual δ^{18}O values show a spatial variation, with δ^{18}O values decreasing from low to high latitudes and heights [*Bowen and Wilkinson*, 2002].

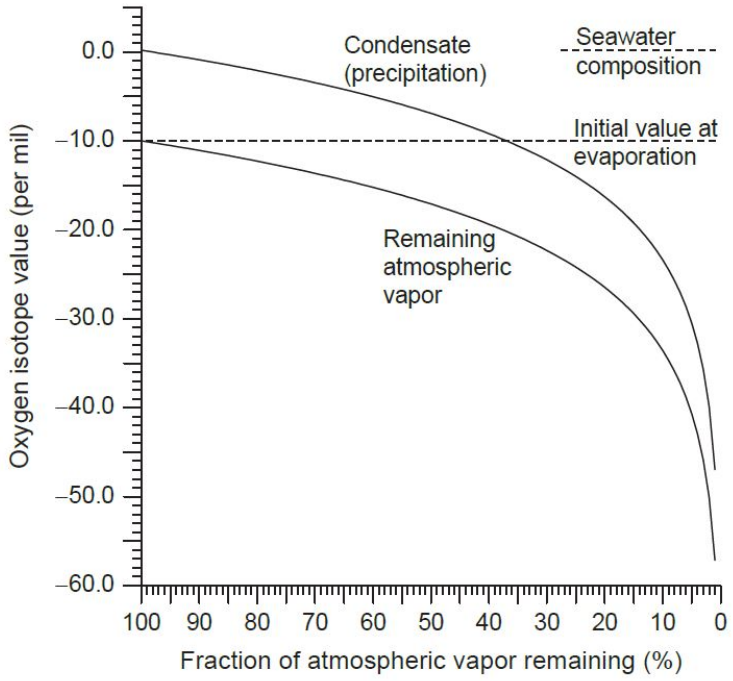

Figure A.3: The Rayleigh distillation process describes the relationship between the isotopic composition of atmospheric vapour and precipitation. Here, the isotopic composition of the first condensate (rain) is close to the local seawater composition, with ongoing rain - out the isotope values become more and more depleted (lighter) [adapted from [*Rohling*, 2013]]. The isotopic composition of the atmospheric vapour (AV) is approximated by $\delta^{18}O_{AV} = \delta^{18}O_E + 10^3(\alpha - 1)ln(f)$, where $\delta^{18}O_E$ denotes the evaporated water, α the fractionation and f is the fraction reaming after rain - out. The isotopic composition of the precipitation formed at equilibrium is given to: $\delta^{18}O_P = \delta^{18}O_{AV} + 10^3 ln(\alpha)$ [*Dansgaard*, 1964].

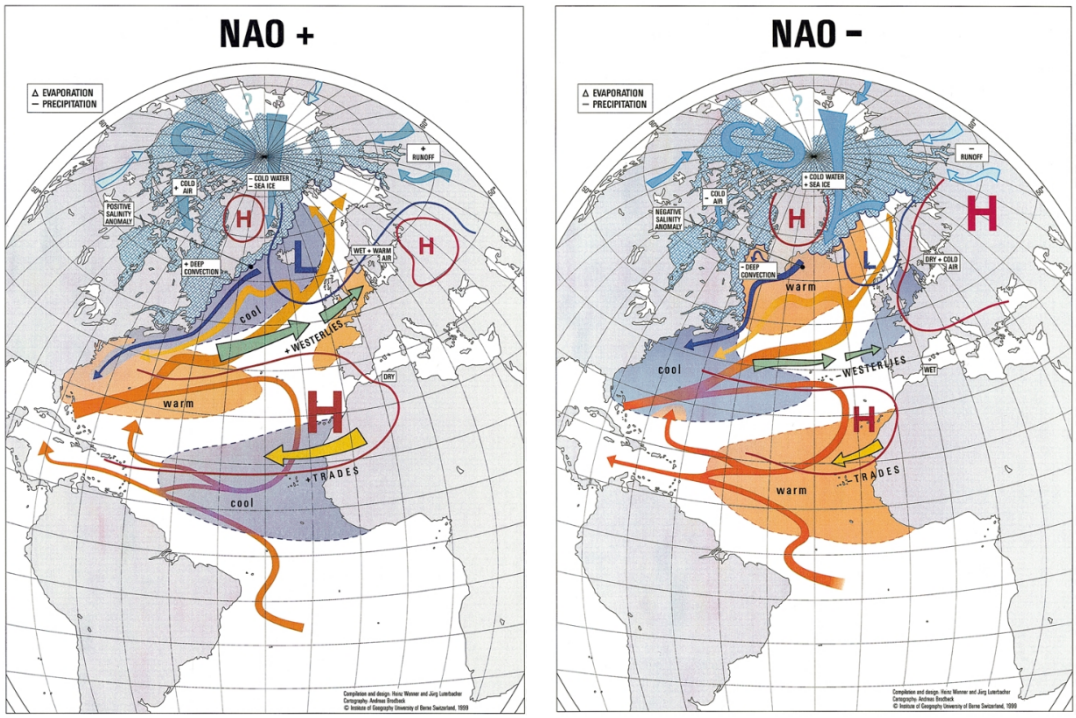

Figure A.4: Graphical representation of the two modes of the North Atlantic Oscillation (positive and negative). The NAO index describes the pressure gradient of the normalised sea level pressure values at two different location (Gibraltar and south-west Iceland) [*Jones et al.*, 1997]. The respective effects on the flow systems are shown as arrows, with the corresponding impacts of the NAO index on the European winter climate [*Wanner et al.*, 2001]. In case of NAO + conditions a strong Low above Iceland and a strong High above the Azores is found, while in NAO − conditions the highs and lows are weaker and the westerlies are less pronounced [*Hurrell*, 1995].

A.2 *Fluid inclusion line* - setup, data evaluation, calibration and intercomparison

Preparation line - effect on stability by different components of the preparation line

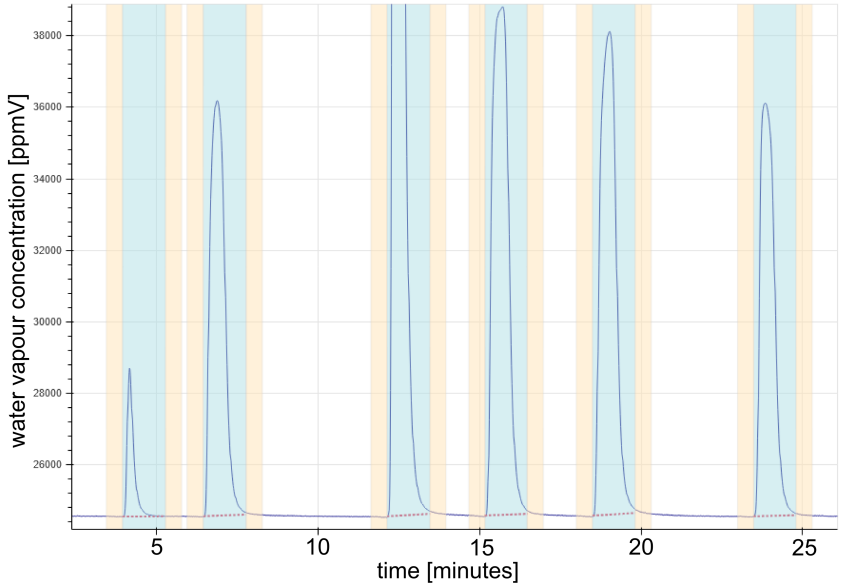

Figure A.5: The water vapour concentration in ppmV of six equal injections is not reproduced. Although always 1 μl is injected, the actual measured signal varies between 0.1 and 0.8 μl. Without an installed reflux valve, the reproducibility of the released water volumes cannot be guaranteed. Additionally, a 2 ml mixing cavity is installed, accordingly the peak duration is approximately one minute.

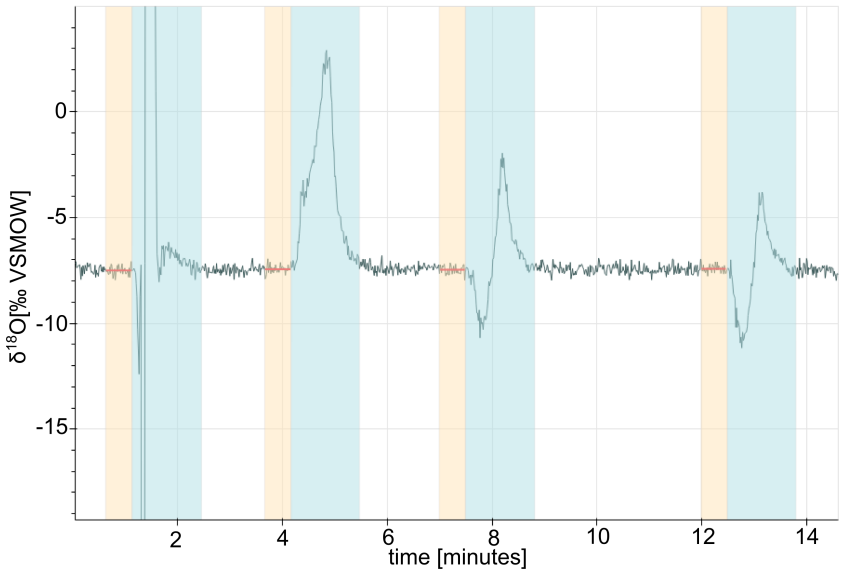

Figure A.6: The recorded $\delta^{18}O$ signal with a small mixing cavity (2 ml). The signal is measured within one minute, since only every 0.8 sec a data point is recorded. Despite the injection of isotopic equal water, the signal does not reproduce, because no reflux valve is installed.

Preparation line - setup with individual components

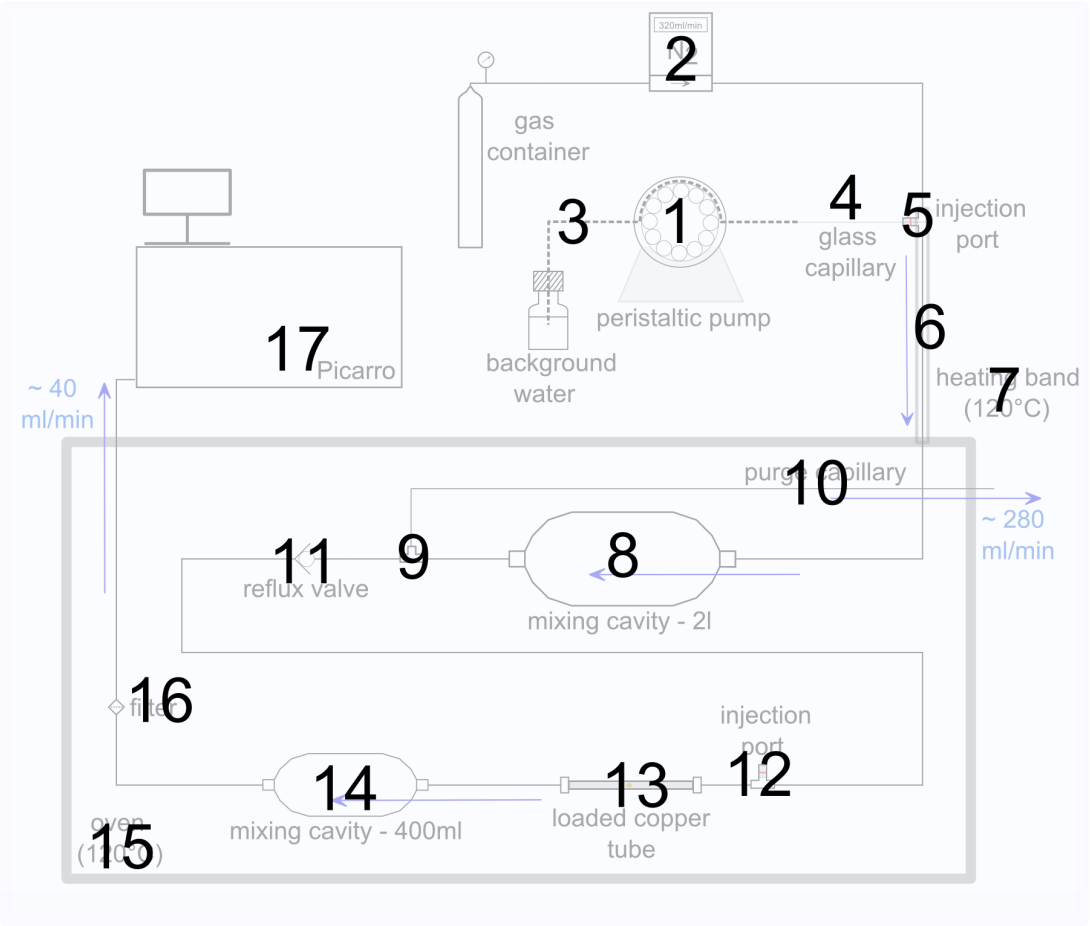

Figure A.7: Construction of the *Fluid inclusion line* line with the numbering of the single components used as listed in table A.1.

numbering preparation line	component	company	specification
1	peristaltic pump	Cole Parmer	Reglo Digital ISM 597D
2	flow controller	ANALYT-MTC	electronic mass flow controller GFC-17
3	tygon tubing	Cole Parmer	3-STP LMT55 0.13MMID
4	FS - capillary	BGB	TSP standard FS tubing, 50 μm ID, 363 μm OD
5	injection port	CS	injector nut 1/8 in connection (492EN2SI)
	with septum	CS	replacement septa, 350C, 1/4 in OD low bleed
6	seamless tubing	Swagelok	1/8 in OD (SS-T2-S-028-6ME)
7	heating tape	HORST	HS - 450° C with very small winding radius
	temperature regulator	HORST	HT 30 - desktop regulator
8	mixing cavity	FESTO	CRVZS-2.0 - 2 l
9	union tee	Swagelok	Swagelok Tube Fitting (SS-200-3)
10	purge capillary	Swagelok	tubing 1/16 in OD x 0.02 in (SS-T1-S-020-6ME)
11	reflux valve	Swagelok	poppet 6000 psig (SS-CHS2-1/3)
12	injection port	CS	injector nut 1/8 in connection (492EN2SI)
13	copper tube	C. Fischer GmbH	cuprofrio 10x1 mm
	brass ferrule set	Swagelok	B-10M0-SET
	tube fitting	Swagelok	reducer, 10 mm x 3/8 in (SS-10M0-R-6)
	tube fitting	Swagelok	reducing Union, 3/8 in x 1/8 in (SS-600-6-2)
14	mixing cavity	FESTO	CRVZS-0.4 - 400 ml
15	oven	SALVIS LAB	old oven with glass door
16	filter	Swagelok	in-line particulate filter (SS-2F-7)
17	Picarro	Picarro	L2130-i Isotopic Water Analyzer

Table A.1: Components with corresponding companies for the setup of the *Fluid inclusion line* based at Heidelberg University. The numbering can be seen in figure A.7.

component	company	specification
hydraulic crusher		
stainless steal jack	workshop IUP	self built
piston	FTP Krevet	ENERPAC - low height hydraulic cylinder (RCS101)
hand pump	FTP Krevet	ENERPAC - lightweight hydraulic hand pump (P142)
syringes		
Hamilton - 1.0 μl	VWR	7000 series μl syringes - 7001KH
Hamilton - 5.0 μl	VWR	700 series μl syringes - 75 N
SGE - 1.0 μl	VWR	plunger in needle syringes - 1BR-7RAX
SGE - 5.0 μl	VWR	plunger in needle syringes - 5BR-7RAX
ILS - 1.0 μl	ILS	1 μl syringe T-AG RN 0.47c70
ILS - 5.0 μl	ILS	5 μl syringe T-Ag RN 0.50d70
other components		
glass capillary	Hirschmann	ringcaps
micro pipettor	Hirschmann	to fill ringcaps
temperature sensor	HORST	Pt100 insertion sensor
glass wool	VWR	glass wool, superfine

Table A.2: Additional components with corresponding companies for the setup of the *Fluid inclusion line*.

Particle size analysis - test of crushing efficiency

For the *Analysette 22* two lasers are implemented, a green laser for small particles ($< 600\,\text{nm}$) and an infrared laser for larger particles ($> 600\,\text{nm}$). The system is calibrated before each measurement with aluminiumoxid, of which the grain size distribution is well known. The measuring process consists of several steps: First the sample is weighed and a suspension is prepared. This consists of deionised water to which a surfactant and an alcohol are added. Hereby, the surfactant does prevent the individual particles from sticking together. The alcohol reduces the surface tension and thus bubble formation. This would interfere with the actual analysis as bubbles appear like particles. Afterwards, the suspension is well mixed in an ultrasonic bath and then added to the analyser.

sample #	name	weight [g]	dilution [%]	number of measurements #
1_a	Closani_II_C1	0.251	10	5
1_b	Closani II_C1	0.251	5	10
2	Closani_II_B2	0.261	7	10
3	LA-1-24_B	0.303	14	10
4	LA-1-13_B	0.309	16	10
5	LA-1-1_A	0.315	14	10

Table A.3: The speleothem samples used for the particle size analysis. All samples have already been crushed and analysed for stable isotopes in fluid inclusions. The dilution and the number of measurements refer to the measuring procedure for particle size analysis.

D values %	I [μm]	II [μm]	III [μm]	IV [μm]	V [μm]
D5	2.0	2.1	2.0	2.2	2.4
D10	5.4	5.7	5.4	5.9	6.4
D25	17.3	17.5	16.3	17.0	17.7
D50	48.7	43.8	39.8	41.2	44.4
D75	207.1	171.7	146.9	146.4	164.4
D90	368.5	346.0	290.1	326.8	344.8
D95	439.5	417.5	356.9	407.6	423.0
D99	551.7	533.9	459.8	535.3	545.7

Table A.4: For the speleothem sample *Closani_II_C1* the results of the grain size analysis are given, with D values in μm. Thereby stands the D-value for the % of sample material which contains particles with a diameter below the given value in μm. The first measurement run was performed without an ultrasonic bath. Numbering I to V indicates the repetition of the measuring process.

D values %	I [μm]	II [μm]	III [μm]	IV [μm]	V [μm]	VI [μm]	VII [μm]	IIX [μm]	IX [μm]	X [μm]
D5	1.6	1.5	1.7	1.6	1.6	1.6	1.6	1.6	1.7	1.7
D10	3.8	3.6	4.1	3.7	3.8	3.7	3.7	3.7	3.7	3.8
D25	14.0	13.6	14.4	13.0	13.3	12.7	12.5	12.3	12.1	12.5
D50	32.5	30.4	32.2	28.6	28.9	27.1	27.0	27.1	25.7	26.0
D75	82.3	67.9	79.1	63.5	64.2	61.6	60.7	66.0	57.7	58.7
D90	226.3	205.0	292.1	142.9	177.3	151.3	141.0	208.0	123.6	142.7
D95	291.2	283.4	399.9	210.1	256.8	244.6	232.8	347.9	198.5	216.6
D99	393.2	395.8	554.0	302.6	361.1	357.7	344.6	512.8	304.6	316.5

Table A.5: Repetition of the measurement of the speleothem sample *Closani_II_C1* with an ultrasonic bath. The results of the grain size analysis are given, with D values in μm. Numbering I to X indicates the repetition of the measuring process.

D values %	I [μm]	II [μm]	III [μm]	IV [μm]	V [μm]	VI [μm]	VII [μm]	IIX [μm]	IX [μm]	X [μm]
D5	2.4	2.7	2.7	2.6	2.7	2.7	2.6	2.6	2.6	2.6
D10	6.9	7.7	7.3	6.8	6.7	6.9	6.5	6.5	6.2	6.2
D25	21.0	21.8	20.8	19.8	19.7	19.2	18.9	18.5	17.8	17.9
D50	84.5	87.9	76.2	73.7	67.3	63.1	61.3	55.8	56.2	51.8
D75	293.0	296.3	266.4	270.6	240.2	217.5	221.6	196.3	214.2	194.0
D90	436.7	441.2	421.3	445.3	412.0	405.6	391.2	369.4	420.5	371.8
D95	505.3	511.7	492.8	524.2	488.5	487.1	466.1	445.3	503.0	448.9
D99	623.1	631.9	609.1	653.7	609.9	617.1	590.3	567.6	640.2	575.0

Table A.6: For the speleothem sample *Closani_II_B2* the results of the grain size analysis are given, with D values in μm. The measurement was performed with an ultrasonic bath. Numbering I to X indicates the repetition of the measuring process.

D values %	I [μm]	II [μm]	III [μm]	IV [μm]	V [μm]	VI [μm]	VII [μm]	IIX [μm]	IX [μm]	X [μm]
D5	1.3	1.4	1.4	1.5	1.4	1.5	1.5	1.5	1.6	1.5
D10	3.1	3.2	3.4	3.4	3.1	3.6	3.5	3.5	3.5	3.2
D25	14.5	14.3	14.7	14.7	13.1	14.5	14.1	13.8	13.7	12.5
D50	50.3	43.8	42.3	41.6	36.8	40.0	38.5	37.0	36.3	31.6
D75	208.8	155.8	136.7	134.3	115.2	127.2	120.8	116.8	117.6	91.7
D90	383.8	363.9	321.5	340.3	250.8	311.2	322.4	306.7	329.6	197.8
D95	459.4	448.6	408.7	436.5	323.9	404.7	420.8	407.7	437.5	268.0
D99	584.8	582.1	544.0	579.9	437.9	544.0	561.9	552.1	589.5	386.1

Table A.7: For the speleothem sample *LA-1-24_B* the results of the grain size analysis are given, with D values in μm. The measurement was performed with an ultrasonic bath. Numbering I to X indicates the repetition of the measuring process.

D values %	I [μm]	II [μm]	III [μm]	IV [μm]	V [μm]	VI [μm]	VII [μm]	IIX [μm]	IX [μm]	X [μm]
D5	1.0	1.0	1.0	1.1	1.1	1.2	1.1	1.3	1.2	1.2
D10	1.9	2.0	2.2	2.3	2.3	2.6	2.4	2.8	2.5	2.6
D25	8.9	9.5	10.1	10.7	10.1	11.6	10.5	12.0	10.2	10.9
D50	28.4	28.8	29.7	31.4	29.0	31.9	29.3	32.2	27.8	28.1
D75	108.2	91.7	98.4	109.0	90.1	103.6	92.1	114.3	84.3	82.1
D90	287.9	248.3	258.7	315.8	225.2	292.6	244.0	342.1	214.1	204.6
D95	361.7	326.8	336.9	409.7	303.6	395.4	329.4	443.6	295.1	283.1
D99	474.5	443.0	452.8	547.4	423.7	540.6	452.1	590.2	420.7	407.3

Table A.8: For the speleothem sample *LA-1-13_B* the results of the grain size analysis are given, with D values in μm. The measurement was performed with an ultrasonic bath. Numbering I to X indicates the repetition of the measuring process.

D values %	I [μm]	II [μm]	III [μm]	IV [μm]	V [μm]	VI [μm]	VII [μm]	IIX [μm]	IX [μm]	X [μm]
D5	1.2	1.3	1.3	1.4	1.4	1.4	1.4	1.4	1.5	1.5
D10	2.7	3.0	2.9	3.1	3.1	3.2	3.3	3.1	3.4	3.4
D25	13.0	13.6	13.3	13.6	13.0	13.2	13.4	12.8	13.5	13.7
D50	42.7	44.6	40.0	40.7	37.8	36.3	38.2	35.2	36.1	36.0
D75	241.1	240.5	167.8	183.1	154.5	130.7	155.2	131.8	134.1	134.9
D90	419.3	425.9	359.7	402.9	375.8	326.4	368.4	330.9	337.5	339.5
D95	494.2	502.5	440.8	485.1	456.7	411.9	452.2	421.0	428.2	432.1
D99	614.0	632.2	569.7	611.6	586.4	544.1	584.8	553.2	561.9	568.4

Table A.9: For the speleothem sample *LA-1-1_A* the results of the grain size analysis are given, with D values in μm. The measurement was performed with an ultrasound bath. Numbering I to X indicates the repetition of the measuring process.

CRDS analyser - Picarro *L2130-i*

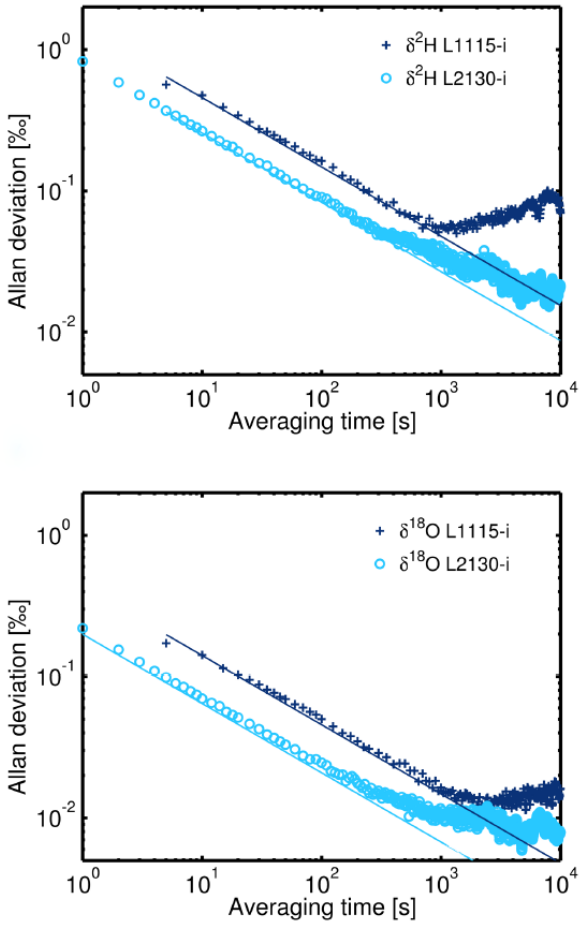

Figure A.8: Allan deviation plot adapted from *Aemisegger et al.* [2012] for *L2130-i* (light blue), with the short-term stability for $\delta^{18}O$ (bottom) and $\delta^{2}H$ (top) measurements at a water vapour concentration of 15 700 ppmV. Two different CRDS analyser from the company Picarro are shown. The Allan deviation is shown as a function of integration time on a log-log scale.

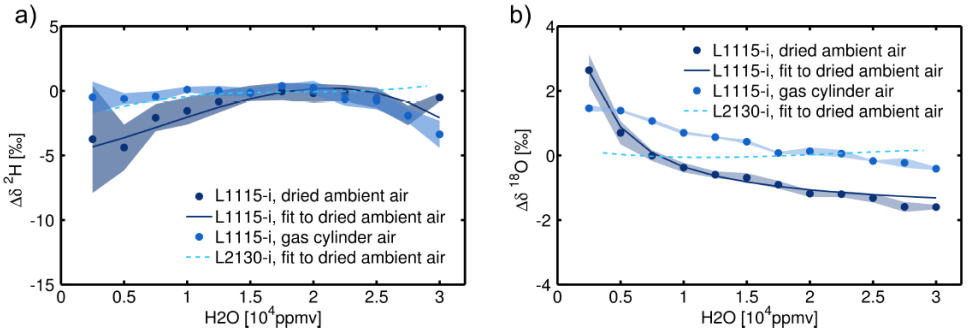

Figure A.9: Adapted from *Aemisegger et al.* [2012], shown is the dependency of isotope measurements on water vapour concentrations in ppmV. For the *L2130-i*, shown as a light blue dotted line, the dependence between isotopic accuracy and water vapour concentration is very small. The measured isotope values for oxygen and hydrogen require no correction for a varying water content.

time [min]	time [s]	σ (δ^{18}O) [‰VSMOW]	σ (δ^{2}H) [‰VSMOW]
0.2	10	0.2733	1.1052
0.8	50	0.2205	0.9038
1.7	100	0.2293	0.7943
8.3	500	0.2128	0.7629
16.7	1000	0.2119	0.7335
60.0	3600	0.2078	0.7311
83.3	5000	0.2081	0.7353
100.0	6000	0.2086	0.7380
141.7	8500	0.2117	0.7598
170.0	10200	0.2087	0.7499
14166.7	850000	0.2118	0.7598

Table A.10: Variation of the standard deviation for isotopic measurements with increasing integration time. Thereby, the standard deviation are calculated exemplary only for a couple of time intervals for the *L2130-i* analyser. For our measurement σ (δ^{18}O) and σ (δ^{2}H) is lowest for an integration interval of 60 min.

Long-term drift for the isotope calibration - *L2130-i*

date	δ^{18}O [‰]	stdv [‰]	δ^{2}H [‰]	stdv [‰]
CC				
28.05.2018	-17.65	0.20	-105.33	0.71
16.07.2018	-17.54	0.20	-105.40	0.72
19.09.2019	-17.61	0.21	-104.87	0.75
VE				
21.06.2019	-11.16	0.21	-54.67	0.80
17.09.2019	-11.13	0.21	-54.52	0.75
VCL				
29.05.2018	-15.53	0.20	-92.95	0.70
14.05.2019	-15.47	0.20	-92.73	0.69
NG				
16.05.2018	-29.13	0.20	-209.28	0.66
17.05.2018	-29.10	0.20	-208.90	0.66

Table A.11: Analysis of long-term drift for the isotope calibration for the *L2130-i* analyser. With a selection of the standard waters used (*CC* (Colle Alps), *VE* (tap water), *VCL* (Alps) and *NG* (North Greenland)). The results are uncalibrated and averaged values over a time interval of 60 min. Since the isotope calibration standards are measured at regular intervals, no deviation of the measured isotope signals can be identified even over several months.

Long-term measurement (22 h) for the *L2130-i*

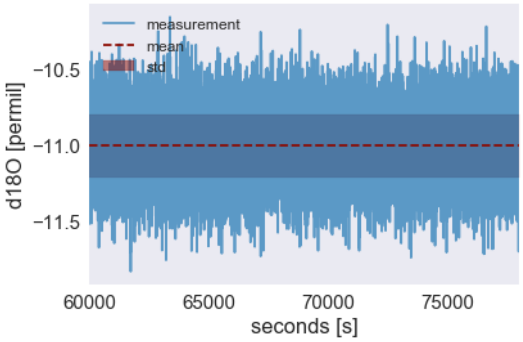

Figure A.10: A: $\delta^{18}O$ mean = -11.00 ‰ / stdv = 0.21 ‰ (30 min)

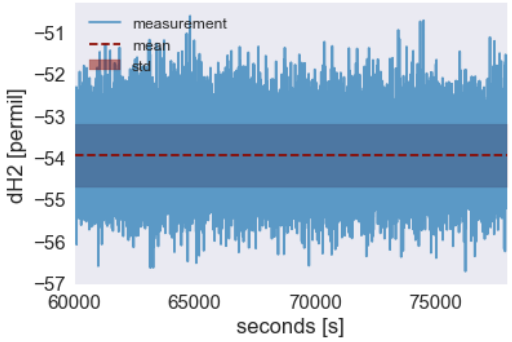

Figure A.11: B: $\delta^{2}H$ mean = -53.96 ‰ / stdv = 0.75 ‰ (30 min)

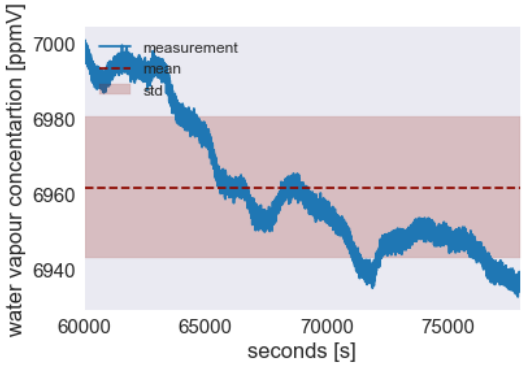

Figure A.12: C: H_2O mean = 6961 ppmV / stdv = 18 ppmV (30 min)

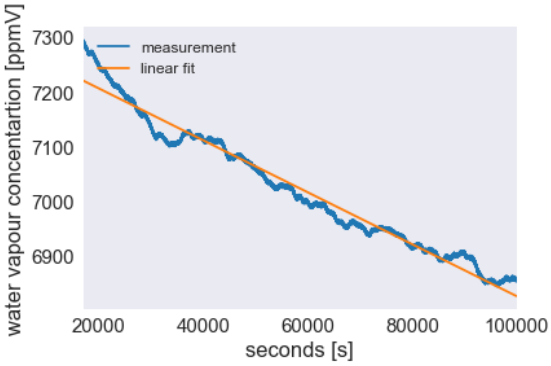

Figure A.13: D: H_2O slope = -72 ppmV/h (22 h)

Figure A.14: Short-term stability measurement over 22 hours. *A*, *B* and *C* show stability over the last 30 minutes, with ‰in VSMOW standard. *D* shows the 22 hour trend of water vapour concentration with a linear decreasing trend, resulting in a total decrease of 1 584 ppmV.

Desorption signal during sample change

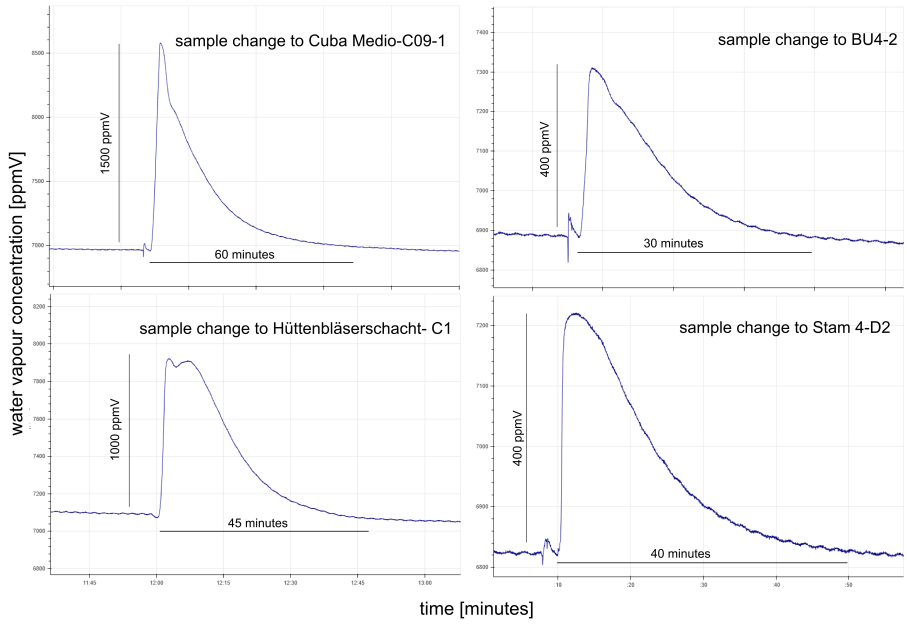

Figure A.15: Variation in water vapour concentration induced by sample change. Therefore, the line must be opened, visible as the first irregularity of the water content. As soon as the line is closed again and the sample is heated, the water content rises rapidly. This is due to the desorption of water molecules from the sample surface. The peak height varies depending on the characteristics of the sample piece. For example, the pool spar (Hüttenbläserschacht Cave) has a relatively large surface area, while the stalagmite from the Bunker Cave was a compact sample piece. This difference is reflected in the peak height. In addition, no spikes can be observed, so that a cracking of fluid inclusions can be excluded. A further proof that the chosen temperature (120°C) is not too high.

Evaluation Protocol - How to use the Python script

Figure A.16: Jupyter notebook interface to operate the Python script for evaluating fluid inclusion measurements. Shown are the different parameters which can be adjusted for evaluation.

In the following, the handling of the Python script (*IsoFluid*) will be explained briefly. *IsoFluid* can be operated via the web interface, called Jupyter Notebook, which allows a fast and easy data evaluation.

A shortcut of the interface is shown in figure A.16, where all the available parameters are listed. First, to evaluate the data is imported. This is done within the global configuration via the import function. The Picarro analyser stores a text file every hour. Afterwards, the criteria for peak-start and peak-end are defined. Therefore the slope (*start_slope*/*end_slope*) must be specified and the interval of data points which are used for the calculation. Since a running mean is used at the end of the peak to filter out the disturbing pump cycles, this interval (*runnin_mean_n*) must also be defined. Furthermore, it is possible to specify intervals (*ignore_intervals*) at which a peak is searched for, thus excluding peaks occurring during sample change. The selection of how the water background should be fitted is done via *bg_model*, either

linear or exponential. All the other parameters are shown in figure A.16. This evaluation protocol is intended to make data evaluation simpler and faster. Laboratories, which also perform fluid inclusion measurements with Picarro analysers and therefore have to evaluate small amounts of water, could use this evaluation method too. This could also help to better compare fluid inclusion data between laboratories by avoiding different evaluation routines.

Calibration - all measured glass capillaries

Date	Water type	Volume [μl]	Error [μl]	δ^{18}O [‰]	Error [‰]	δ^{2}H [‰]	Error [‰]
02.08.2018	WW	0.470	0.025	1.31	0.50	-17.88	1.50
03.08.2018	WW	0.700	0.025	-0.40	0.50	-18.36	1.50
10.09.2018	WW	4.280	0.025	-0.38	0.50	-18.99	1.50
11.09.2018	WW	1.170	0.025	-0.27	0.50	-18.08	1.50
12.09.2018	WW	1.510	0.025	-0.51	0.50	-19.23	1.50
13.09.2018	WW	2.630	0.025	-0.35	0.50	-19.01	1.50
14.09.2018	WW	4.220	0.025	-0.38	0.50	-18.90	1.50
23.10.2018	WW	2.920	0.025	-0.35	0.50	-18.83	1.50
31.10.2018	WW	3.800	0.025	-0.34	0.50	-18.80	1.50
02.11.2018	WW	1.730	0.025	-0.31	0.50	-18.77	1.50
23.11.2018	WW	1.640	0.025	-0.20	0.50	-18.27	1.50
12.03.2019	WW	0.685	0.025	-0.27	0.50	-18.75	1.50
13.03.2019	WW	0.317	0.025	0.01	0.50	-19.46	1.50
14.03.2019	WW	2.425	0.025	-0.37	0.50	-18.71	1.50
21.05.2019	WW	0.932	0.025	-0.31	0.50	-18.24	1.50
22.05.2019	WW	3.056	0.025	-0.32	0.50	-18.81	1.50

Table A.12: Results of the glass capillaries used for volume calibration. The results of the water volumes are given in μl and the stable water isotope data is given in VSMOW.

Date	Water type	Volume [μl]	Error [μl]	δ^{18}O [‰]	Error [‰]	δ^{2}H [‰]	Error [‰]
27.07.2018	CC	0.810	0.025	-14.53	0.50	-111.23	1.50
31.07.2018	CC	0.440	0.025	-14.34	0.50	-108.31	1.50
08.08.2018	Kona	0.910	0.025	0.12	0.50	1.89	1.50
10.08.2018	Kona	0.230	0.025	0.70	0.50	7.49	1.50
09.08.2018	NG	0.890	0.025	-29.52	0.50	-240.73	1.50
05.12.2018	NG	3.600	0.025	-30.28	0.50	-244.29	1.50
09.01.2019	NG	2.496	0.025	-30.42	0.50	-244.66	1.50
06.08.2018	VCL	0.360	0.025	-11.96	0.50	-95.73	1.50
07.08.2018	VCL	0.300	0.025	-12.10	0.50	-93.89	1.50
04.09.2018	VCL	2.871	0.025	-13.07	0.50	-99.30	1.50
05.09.2018	VCL	2.218	0.025	-13.26	0.50	-99.55	1.50
07.09.2018	VCL	2.140	0.025	-13.31	0.50	-99.30	1.50
18.05.2018	VE	0.436	0.025	-8.22	0.50	-58.74	1.50
18.05.2018	VE	0.367	0.025	-8.46	0.50	-58.76	1.50
22.05.2018	VE	1.058	0.025	-8.63	0.50	-61.26	1.50
23.05.2018	VE	0.526	0.025	-8.45	0.50	-60.62	1.50
28.05.2018	VE	0.310	0.025	-8.63	0.50	-58.63	1.50
29.05.2018	VE	0.261	0.025	-8.79	0.50	-58.37	1.50
30.05.2018	VE	1.318	0.025	-8.62	0.50	-61.20	1.50
18.06.2018	VE	0.356	0.025	-8.24	0.50	-59.80	1.50
19.06.2018	VE	1.488	0.025	-8.65	0.50	-61.43	1.50
20.06.2018	VE	1.675	0.025	-8.67	0.50	-60.71	1.50
21.06.2018	VE	1.482	0.025	-8.75	0.50	-60.85	1.50
20.07.2018	VE	2.515	0.025	-8.62	0.50	-61.28	1.50
23.07.2018	VE	0.264	0.025	-8.59	0.50	-62.77	1.50
25.07.2018	VE	0.338	0.025	-7.96	0.50	-58.99	1.50
12.07.2019	VE	2.640	0.025	-8.43	0.50	-60.15	1.50
15.07.2019	VE	4.082	0.025	-8.54	0.50	-60.77	1.50
15.07.2019	VE	0.341	0.025	-7.64	0.50	-62.52	1.50

Table A.13: Results of the glass capillaries used for volume calibration. The results of the water volumes are given in μl and the stable water isotope data is given in VSMOW.

Precision of isotope measurement - VE injections via syringes

volume	number of injections	δ^{18}O mean	δ^{18}O stdv	δ^{2}H mean	δ^{2}H stdv
[μl]	#	[‰]	[‰]	[‰]	[‰]
small					
0.1	6	-8.60	0.54	-60.76	1.83
0.2	6	-8.76	0.34	-60.96	1.58
0.3	6	-8.76	0.49	-61.19	1.64
0.4	6	-8.45	0.53	-60.57	1.06
0.5	6	-8.62	0.58	-61.53	1.43
0.6	6	-7.97	0.56	-60.82	1.00
large					
1.0	16	-8.53	0.17	-60.71	0.42
2.0	11	-8.35	0.21	-60.39	0.41
3.0	11	-8.56	0.16	-60.86	0.41
4.0	9	-8.62	0.10	-60.98	0.11
expected					
VE		-8.57	0.08	-61.04	0.70

Table A.14: Precision measurements with several syringe injections. The mean values with corresponding standard deviation are given in VSMOW. The injections spanning a volume range form 0.1 up to 4.0 μl, whereby reliable isotopic results are achieved with a released water volume above 0.2 μl. The expected value for *VE* water is independently measured with the *LGR* analyser.

water type	volume [μl]	δ^{18}O [‰VSMOW]	error [‰VSMOW]	δ^{2}H [‰VSMOW]	error [‰VSMOW]
test A					
VE	3.48	-8.32	0.50	-60.41	1.50
NG	2.31	-30.13	0.50	-243.54	1.50
NG	3.51	-29.99	0.50	-243.59	1.50
NG	3.54	-30.08	0.50	-244.08	1.50
NG	3.54	-30.08	0.50	-243.87	1.50
test B					
VE	3.38	-8.48	0.50	-60.75	1.50
NG	3.44	-30.35	0.50	-244.70	1.50
NG	3.55	-30.37	0.50	-244.92	1.50
NG	4.13	-30.36	0.50	-244.40	1.50
test C					
VE	2.48	-8.09	0.50	-59.92	1.50
NG	3.22	-30.03	0.50	-242.97	1.50
NG	3.22	-29.95	0.50	-242.97	1.50
NG	3.21	-29.94	0.50	-243.07	1.50
test D					
VE	0.39	-8.73	0.50	-58.91	1.50
NG	0.46	-29.65	0.50	-242.87	1.50
NG	0.50	-29.73	0.50	-240.00	1.50
NG	0.49	-29.88	0.50	-244.08	1.50
NG	0.40	-29.91	0.50	-242.37	1.50
test E					
VE	2.46	-8.40	0.50	-60.41	1.50
NG	2.55	-29.99	0.50	-243.96	1.50
NG	2.51	-30.44	0.50	-242.99	1.50
NG	2.48	-30.03	0.50	-243.60	1.50
test F					
VE	0.99	-8.23	0.50	-60.54	1.50
NG	1.00	-29.77	0.50	-242.94	1.50
NG	1.00	-29.89	0.50	-242.14	1.50
NG	1.00	-29.90	0.50	-242.79	1.50

Table A.15: The measurement to examine the memory effect were repeated six times (A to F), whereby after a first VE injection, water with significantly different isotopic composition was injected (NG). The volumes of the injection were varied in the range of 0.4 to 4.0 μl. The independently measured isotope data for *VE_II* are $\delta^{18}\mathrm{O} = -8.22\,‰$ and $\delta^{2}\mathrm{H} = -60.53\,‰$ and for *NG* they are $\delta^{18}\mathrm{O} = -30.24\,‰$ and $\delta^{2}\mathrm{H} = -242.15\,‰$ in VSMOW.

Possible disturbance effects during stable isotope measurement

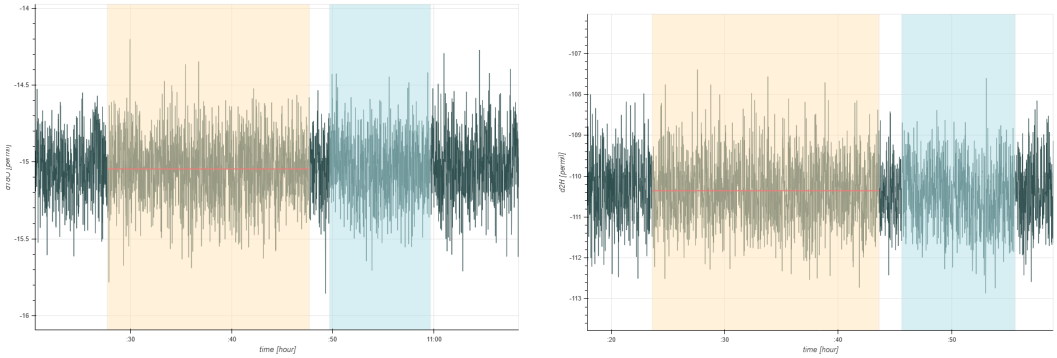

Figure A.17: Isotopic signal evolution for the measurement of pure Iceland Spar with a sample weight of 0.2524 g. The integrated background signal is shown in light brown, with the resulting mean in red. The interval of the actual sample signal is shown in light blue. There are no significant differences in the oxygen or hydrogen signal, both in dark green. The water vapour background is *CC* - Colle Alps with $\delta^{18}\mathrm{O} = -15.13\,‰$ and $\delta^{2}\mathrm{H} = -110.58\,‰$, in VSMOW.

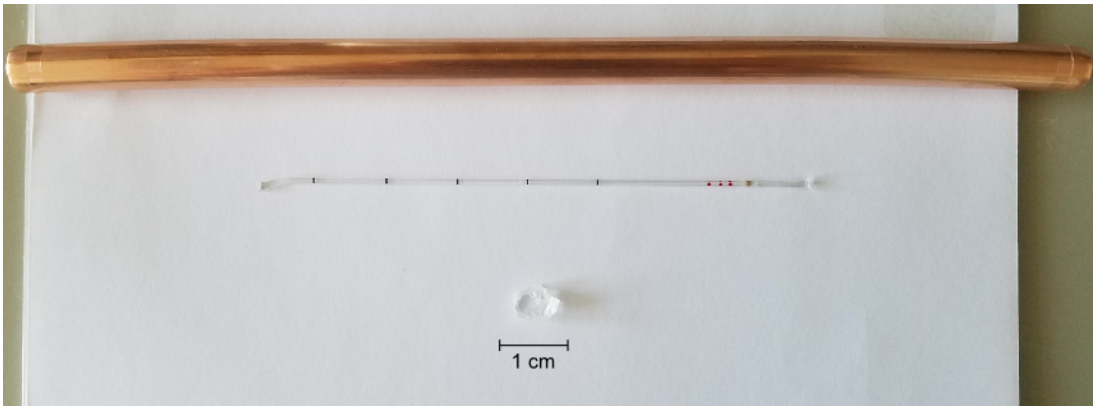

Figure A.18: Image of the sample configuration for testing whether adsorption influences the isotopic sample signal. Iceland Spar is measured together with a water-filled glass capillary, which is mounted together in a copper tube.

	δ^{18}O		δ^{2}H		volume	mass
	value [‰]	error [‰]	value [‰]	error [‰]	[μl]	[g]
only capillaries						
I	-8.54	0.50	-60.77	1.50	4.04	-
II	-8.43	0.50	-60.15	1.50	2.65	-
capillaries plus Iceland spar						
I	-8.47	0.50	-60.16	1.50	3.49	0.58
II	-8.58	0.50	-60.46	1.50	2.63	0.61
III	-8.49	0.50	-60.77	1.50	3.67	0.55
IV	-8.58	0.50	-60.46	1.50	3.52	0.45
V	-8.51	0.50	-60.17	1.50	2.89	0.56
mean with stdv	-8.52	0.05	-60.40	0.22	-	-

Table A.16: Results for the measurement whether adsorption influences the isotopic sample signal. First (I and II), water-filled glass capillaries (*VE*) were measured alone to check the precision of the isotope measurement. Afterwards, glass capillaries filled with the same standard water (*VE*) were measured together with Iceland Spar. Isotopic results are given in VSMOW. The isotopic signal for the measurement together with Iceland Spar does not differ from the measurements with only glass capillaries. The independently measured data for *VE* - tap water is -8.50 ‰VSMOW for δ^{18}O and -60.70 ‰VSMOW for δ^{2}H.

injection on background	water volume [μl]	δ^{18}O [‰VSMOW]	error [‰VSMOW]	δ^{2}H [‰VSMOW]	error [‰VSMOW]
VE on *NG*					
	2.76	-8.07	0.5	-57.82	1.50
	2.79	-8.13	0.5	-57.87	1.50
	2.84	-8.15	0.5	-57.71	1.50
	2.76	-8.11	0.5	-57.84	1.50
	2.81	-8.05	0.5	-57.93	1.50
mean with stdv		-8.10	0.04	-57.83	0.07
VE on *CC*					
	2.78	-8.53	0.5	-59.79	1.50
	2.27	-8.46	0.5	-59.82	1.50
	2.64	-8.47	0.5	-60.08	1.50
	2.88	-8.49	0.5	-59.67	1.50
	3.13	-8.45	0.5	-59.77	1.50
mean with stdv		-8.48	0.03	-59.83	0.14
VE on *VE*					
	2.81	-8.53	0.5	-60.36	1.50
	2.31	-8.54	0.5	-60.48	1.50
	2.69	-8.41	0.5	-60.22	1.50
	3.10	-8.48	0.5	-60.97	1.50
	3.05	-8.50	0.5	-60.48	1.50
mean with stdv		-8.49	0.05	-60.50	0.25
VE on *WW*					
	3.07	-8.65	0.5	-60.92	1.50
	3.11	-8.58	0.5	-60.88	1.50
	2.79	-8.72	0.5	-61.09	1.50
	2.91	-8.66	0.5	-60.99	1.50
	2.90	-8.63	0.5	-61.21	1.50
mean with stdv		-8.65	0.04	-61.02	0.12

Table A.17: *VE* injections to analyse the effect of the selected isotopic background on the actually measured isotopic signal. On four different isotope backgrounds (*NG*, *CC*, *VE* and *WW*) the same standard water (*VE*) was injected five times. The independently measured data for *VE* - tap water are $\delta^{18}O = -8.50\,‰$ and $\delta^{2}H = -60.70\,‰$, in VSMOW.

First test speleothem samples - reproducibility measurements

	sample ID	mass [g]	water volume [μl]	water content [μl/g]	δ^{18}O [‰]	error [‰]	δ^{2}H [‰]	error [‰]
A pond								
	1	0.52	0.24	0.46	-7.46	0.50	-53.15	1.50
	2	0.52	0.31	0.60	-7.92	0.50	-51.86	1.50
	mean	-	-	-	-7.69	0.35	-52.50	1.06
B pond								
	1	0.57	0.43	0.76	-7.60	0.50	-49.65	1.50
	2	0.65	0.42	0.64	-7.84	0.50	-48.56	1.50
	mean	-	-	-	-7.72	0.35	-49.11	1.06
C little pond								
	1	0.59	1.78	3.02	-7.25	0.50	-51.08	1.50
	2	0.45	0.48	1.08	-7.68	0.50	-50.95	1.50
	mean	-	-	-	-7.46	0.35	-51.01	1.06

Table A.18: Results of stable isotope measurements in fluid inclusions for pool spar speleothems in Hüttenbläserschacht Cave are given in VSMOW. The mean values with corresponding error, calculated after propagation of uncertainty, are given as well. The mean drip water values of the Bunker Cave, which is located nearby, are: $\delta^{18}O = -8.0 \pm 0.2$ ‰ and $\delta^{2}H = -54.5 \pm 1.5$ ‰, in VSMOW [*Riechelmann et al.*, 2011].

First test speleothem samples - accuracy measurements

	sample ID	mass [g]	water volume [μl]	water content [μl/g]	δ^{18}O [‰]	error [‰]	δ^{2}H [‰]	error [‰]
HUAGAPO								
Band 1								
	a	0.32	0.62	1.9	-16.61	0.5	-122.18	1.50
	b	0.39	0.67	1.7	-17.34	0.5	-125.81	1.50
	c	0.34	0.69	2.0	-16.84	0.5	-124.47	1.50
	d	0.32	0.52	1.6	-15.68	0.5	-123.62	1.50
	e	1.18	1.90	1.6	-17.92	0.5	-125.66	1.50
Band 2								
	a	0.66	0.68	1.0	-17.46	0.5	-128.46	1.50
	b	0.56	0.62	1.1	-18.60	0.5	-128.17	1.50
	c	0.59	0.75	1.3	-18.31	0.5	-131.37	1.50
	d	0.48	0.50	1.1	-16.69	0.5	-127.28	1.50

Table A.19: Results of stable isotope measurements in fluid inclusions for speleothem samples Huagapo Band 1 and 2 are given in VSMOW. Speleothems were analysed for inter lab comparison with IRMS technique (Hubert Vonhof, Max Planck Institute for Chemistry in Mainz).

A.3 Case study I: Late Holocene stalagmite (1911 - 2010) in the transitional climatic zone - Romania, Cloșani Cave

Site description - the Cloșani Cave and late Holocene stalagmite - Stam 4

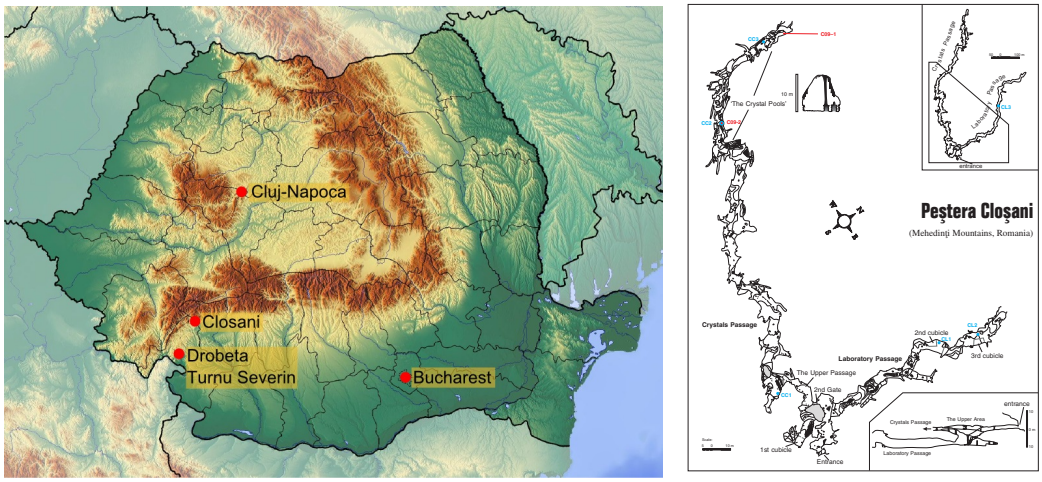

Figure A.19: Left: Topographic map of Romania [*Vidiani* [accessed November 17, 2019]], the red points mark the following locations: Cloşani (location of the cave), Drobeta (location of the station), Cluj-Napoca (location of GNIP station) and Bucharest, the capital. Right: Map of the Cloşani cave (45.1°N, 22.8°E) [*Constantin and Lauritzen*, 1999], Stam 4 was sampled near to the drip site CL3, which is located in the deeper sector of the *Laboratory Passage*.

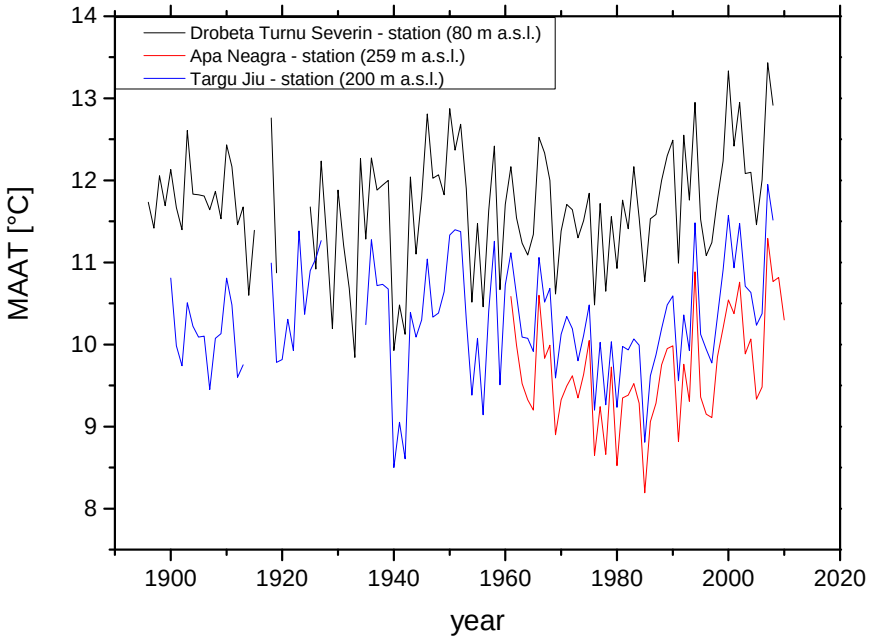

Figure A.20: Mean annual air temperature records for three meteorological stations close to the Cloşani Cave. The longest record (1896 - 2008) from the station Drobeta Turnu Severin gives a mean annual air temperature for the last 100 years of 11.7 °C. The station Apa Neagra, with a record from 1961 up to 2010 gives a mean MAAT of 9.7 °C and Targu Jiu (1900 - 2008) with a mean MAAT of 10.3 °C [*Klein Tank et al.*, 2002]. All stations show an increase in temperature between 1980 - 2010.

sample ID	sample point	date	δ^{18}O VSMOW [‰]	error VSMOW [‰]	δ^{2}H VSMOW [‰]	error VSMOW [‰]
CL3.10-05	CL3	25.04.2010	-9.74	0.15	-65.40	1.00
CL3.10-09	CL3	28.08.2010	-9.14	0.15	-69.00	1.00
CL3.10-11	CL3	05.11.2010	-9.62	0.15	-65.90	1.00
CL3.11-01	CL3	11.01.2011	-9.76	0.15	-69.40	1.00
CL3.11-07	CL3	14.07.2011	-9.84	0.15	-64.79	1.00
CL3.12-03	CL3	04.03.2012	-9.75	0.15	-66.80	1.00
CL3.12-05	CL3	13.05.2012	-9.51	0.15	-66.20	1.00
CL3.12-07	CL3	13.07.2012	-9.61	0.15	-64.70	1.00
CL3.12-09	CL3	13.09.2012	-9.58	0.15	-64.70	1.00
		mean	-9.62	0.20	-66.32	1.68

Table A.20: Drip water isotopic composition for the site CL3 in the Cloşani Cave, where Stam 4 was collected 1 m nearby. Drip water was measured from 2010 to 2015 in bimonthly intervals [*Warken et al.*, 2018]. There are 8 data pairs of drip water isotopic composition available for site CL3, covering both the summer and the winter months.

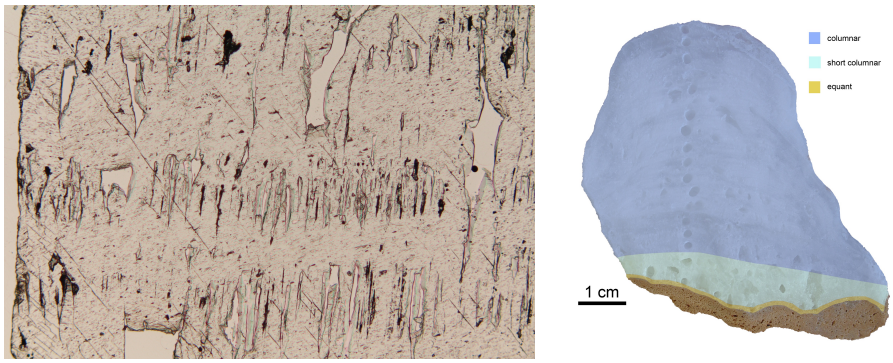

Figure A.21: On the left side a thin section of Stam 4 is shown, where the width of the image is 3 mm. The individual layers can be distinguished by the presence of inclusions. Winter layers showing very little inclusions, while summer layers are showing air-filled and water-filled inclusions. On the right side, the crystal fabrics with predominantly columnar is shown. Both pictures were provided by Dana Riechelmann.

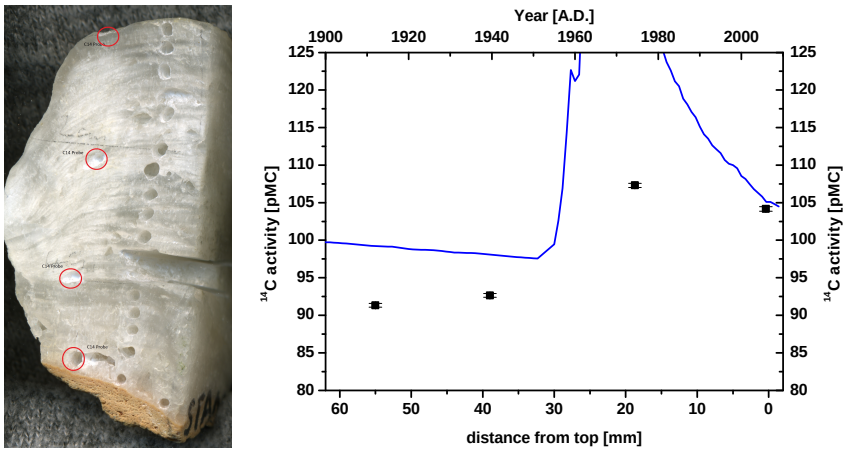

Figure A.22: Left: Stam 4 with the four sampling points for radio carbon dating. Right: ^{14}C results for Stam 4, with the atmospheric input curve in blue (unpublished data, personal correspondence Jens Fohlmeister, 18.12.2019). The increase of the atmospheric ^{14}C anomaly (bomb-peak) can be found in the depth between 1.9 and 3.9 cm distance from top.

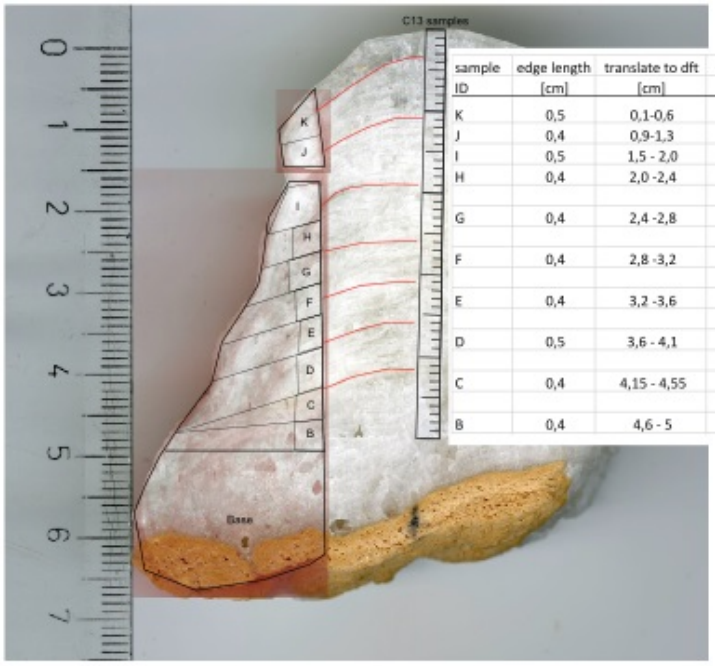

sample ID	edge length [cm]	translate to dft [cm]	translate to age range	comment
K	0,5	0,1-0,6	1999-2008	edge
J	0,4	0,9-1,3	1985-1994	edge
I	0,5	1,5 - 2,0	1972-1982	edge
H	0,4	2,0 -2,4	1964-1971	plateau
				but still on the edge
G	0,4	2,4 -2,8	1957-1963	plateau
				but still on the edge
F	0,4	2,8 -3,2	1947-1956	plateau
				but still on the edge
E	0,4	3,2 -3,6	1941-1946	plateau
				stratification schematically
D	0,5	3,6 - 4,1	1933-1940	plateau
				stratification schematically
C	0,4	4,15 - 4,55	1924-1932	plateau
				stratification schematically
B	0,4	4,6 - 5	1912-1923	stratification is not detectable

Figure A.23: Graphical age distribution for Stam 4, where the sample piece (marked in light red) is located at the age of the stalagmite and far away from the growth axis. For this reason, the age determined should not be understood as absolute, but as an age range with large uncertainty.

Fluid inclusion results - Stam 4

sample ID	mass [g]	water volume [μl]	water amount [μl/g]	δ^{18}O VSMOW [‰]	error VSMOW [‰]	δ^{2}H VSMOW [‰]	error VSMOW [‰]
part II							
A1	0.69	0.34	0.49	-8.72	0.50	-62.95	1.50
B1	0.61	0.40	0.65	-9.40	0.50	-66.59	1.50
B2	0.30	0.22	0.72	-9.54	0.50	-66.62	1.50
B3	0.37	0.34	0.91	-8.71	0.50	-63.10	1.50
B4	0.38	0.29	0.75	-9.41	0.50	-64.55	1.50
C1	0.38	0.33	0.87	-10.63	0.50	-63.50	1.50
C2	0.40	0.15	0.38	-8.65	0.50	-62.87	1.50
C3	0.44	0.42	0.95	-9.70	0.50	-65.00	1.50
D1	0.41	0.56	1.35	-9.65	0.50	-65.03	1.50
D2	0.47	0.33	0.70	-10.01	0.50	-65.65	1.50
E1	0.23	0.27	1.19	-9.34	0.50	-64.15	1.50
E2	0.22	0.26	1.19	-9.36	0.50	-63.88	1.50
F	0.28	0.39	1.38	-9.59	0.50	-63.58	1.50
G	0.28	0.26	0.92	-9.05	0.50	-64.76	1.50

Table A.21: Fluid inclusion data for Stam 4 from Cloşani Cave - part II. Samples marked in blue are not used for the interpretation because the water volume is below the critical evaluation limit, which is 0.2 μl.

sample ID	mass [g]	water volume [μl]	water amount [μl/g]	δ^{18}O VSMOW [‰]	error VSMOW [‰]	δ^{2}H VSMOW [‰]	error VSMOW [‰]
part I							
A1	0.58	0.30	0.52	-9.53	0.50	-65.36	1.50
A2	0.49	0.29	0.59	-9.76	0.50	-59.66	1.50
B1	0.42	0.40	0.95	-9.62	0.50	-64.14	1.50
B2	0.49	0.37	0.75	-9.55	0.50	-64.72	1.50
B3	0.53	0.40	0.76	-8.87	0.50	-64.85	1.50
B4	0.52	0.29	0.56	-9.07	0.50	-66.31	1.50
B5	0.42	0.19	0.45	-9.41	0.50	-68.45	1.50
C1	0.49	0.81	1.66	-7.98	0.50	-57.61	1.50
C2	0.42	0.51	1.21	-8.52	0.50	-59.63	1.50
C3	0.54	0.44	0.81	-8.97	0.50	-60.41	1.50
D1	0.32	0.18	0.57	-8.45	0.50	-63.79	1.50
D2	0.51	0.42	0.83	-9.95	0.50	-63.80	1.50
D3	0.56	0.50	0.89	-10.43	0.50	-63.68	1.50
D4	0.55	0.54	0.98	-10.13	0.50	-63.95	1.50
D5	0.40	0.35	0.88	-8.97	0.50	-61.69	1.50
E1	0.49	0.38	0.78	-10.25	0.50	-62.93	1.50
E2	0.58	0.46	0.78	-9.41	0.50	-62.51	1.50
E3	0.54	0.44	0.82	-10.39	0.50	-62.75	1.50
E4	0.53	0.32	0.60	-9.95	0.50	-63.14	1.50
E5	0.25	0.14	0.55	-9.03	0.50	-59.40	1.50
F1	0.47	0.35	0.75	-9.59	0.50	-63.52	1.50
F2	0.58	0.82	1.40	-9.42	0.50	-63.22	1.50
F3	0.56	0.87	1.56	-8.33	0.50	-59.81	1.50
G1	0.46	0.40	0.87	-9.03	0.50	-61.96	1.50
G2	0.50	0.76	1.53	-8.85	0.50	-61.82	1.50
H1	0.40	0.46	1.16	-9.08	0.50	-61.57	1.50
H2	0.35	0.46	1.30	-8.80	0.50	-60.96	1.50
I	0.39	0.28	0.72	-9.29	0.50	-60.34	1.50
J	0.50	0.43	0.86	-8.72	0.50	-59.20	1.50
K	0.46	0.43	0.94	-8.37	0.50	-59.38	1.50

Table A.22: Fluid inclusion data for Stam 4 from Cloşani Cave - part I. Samples marked in blue are not used for the interpretation because the water volume is below the critical evaluation limit, which is 0.2 μl.

sample ID	dft [cm]	error [cm]	$\delta^{18}O_{fluid}$ VSMOW [‰]	error VSMOW [‰]	$\delta^{18}O_{calcite}$ VSMOW [‰]	error VSMOW [‰]	$\Delta(\alpha)$	error	T [K]	error [K]	Δ(T) [K]	error [K]
B1	4.82	0.20	-9.62	0.50	22.36	0.19	31.78	0.50	280.83	2.19		
C1	4.39	0.20	-7.98	0.50	22.92	0.28	30.67	0.50	285.79	2.26	4.96	1.55
D2	3.90	0.25	-9.95	0.50	22.83	0.10	32.57	0.50	277.42	2.13	-3.42	1.57
E1	3.45	0.20	-10.25	0.50	22.71	0.14	32.76	0.50	276.61	2.12	-4.22	1.58
F1	3.01	0.20	-9.59	0.50	22.55	0.19	31.94	0.50	280.15	2.18	-0.68	1.50
G1	2.62	0.20	-9.03	0.50	22.51	0.22	31.33	0.50	282.83	2.22	2.00	1.54
H1	2.21	0.20	-9.08	0.50	23.03	0.20	31.89	0.50	280.35	2.18	-0.48	1.57
I	1.78	0.25	-9.29	0.50	22.90	0.20	31.98	0.50	279.98	2.17	-0.85	1.54
J	1.09	0.20	-8.72	0.50	22.78	0.16	31.28	0.50	283.06	2.22	2.23	1.55
K	0.39	0.25	-8.37	0.50	22.59	0.15	30.74	0.50	285.46	2.26	4.63	1.54

Table A.23: Results for classical carbonate thermometer Stam 4 - *part I*, with calcite oxygen values averaged over the edge length of the fluid inclusion sample piece (typically 5 mm) and corresponding standard deviation. To calculate the fractionation factor α(calcite - water), $\delta^{18}O_{calcite}$ must be converted to the VSMOW scale. α(calcite - water) is defined as $(1000 + \delta^{18}O_{calcite})/(1000 + \delta^{18}O_{fluid})$. The temperature dependence of α is used to determine relative temperature changes (Δ(T)) to the sample level B. *Kim and O'Neil* [1997] obtained a relation between $\Delta\,(10^3 ln(\alpha))$ and temperature, with the following parameters: $\Delta = 18.03(10^3/T) - 32.42$ (for calcium carbonate). The errors were calculated by error propagation, adding the squared contributions of the individual uncertainties.

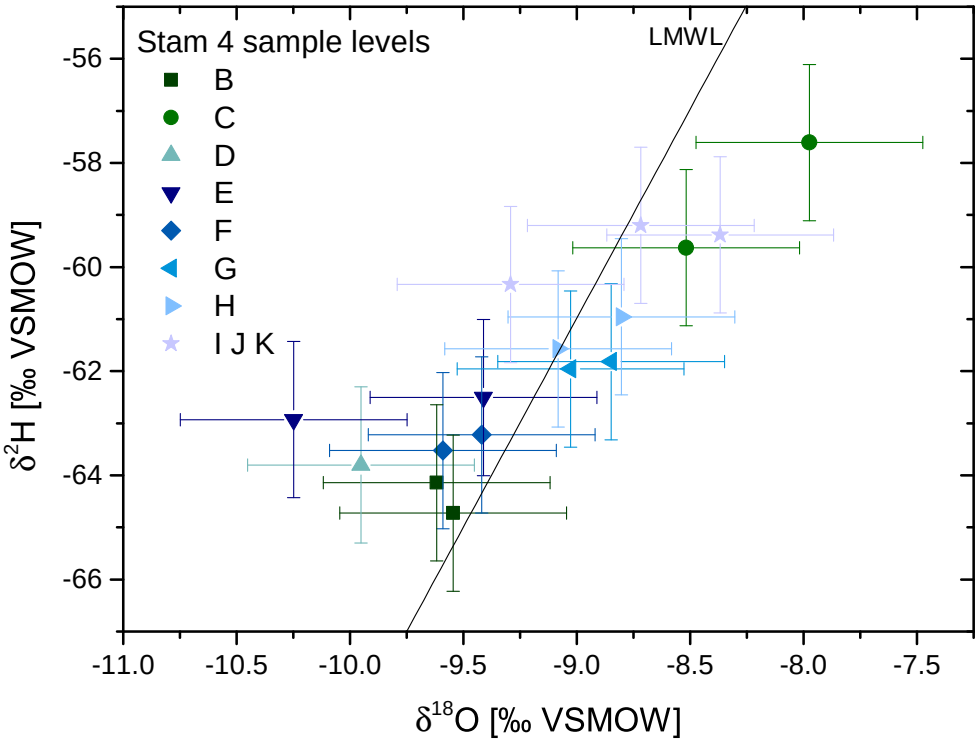

Figure A.24: Fluid inclusion results for *part I* all sample levels (B to K) with numbering *1* and *2* are shown. The LMWL of Cluj-Napoca with $\delta^2H = 8.03 \cdot \delta^{18}O + 11.29$ ‰VSMOW is shown as back line [*Cozma et al.*, 2017].

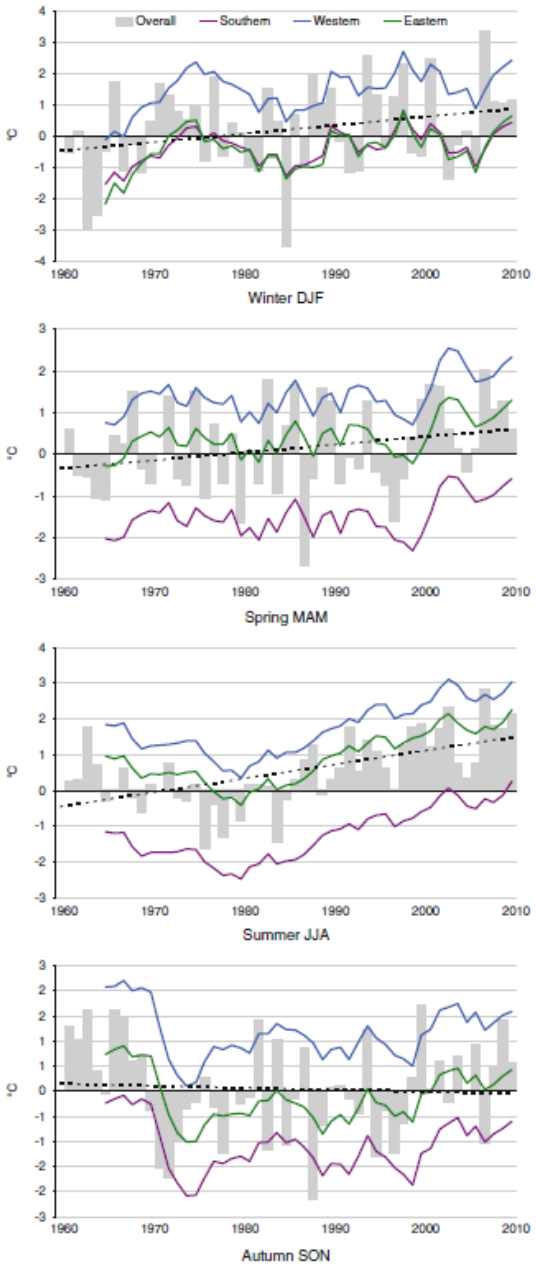

Fig. 8.3 Regional seasonal mean temperature anomalies (5-year moving averages) in the Romanian Carpathians (1961–2010) relative to 1961–1990. The columns show the general seasonal anomalies over the region

Figure A.25: Temperature anomalies in the Romanian Carpathians after *Micu et al.* [2016]. A total number of 35 weather stations were analysed (statistical details see *Micu et al.* [2016]) for the period between 1960 - 2010. The temperature variation is more significant in winter than in summer with an overall increase of 1°C for the period between 1960 - 2010.

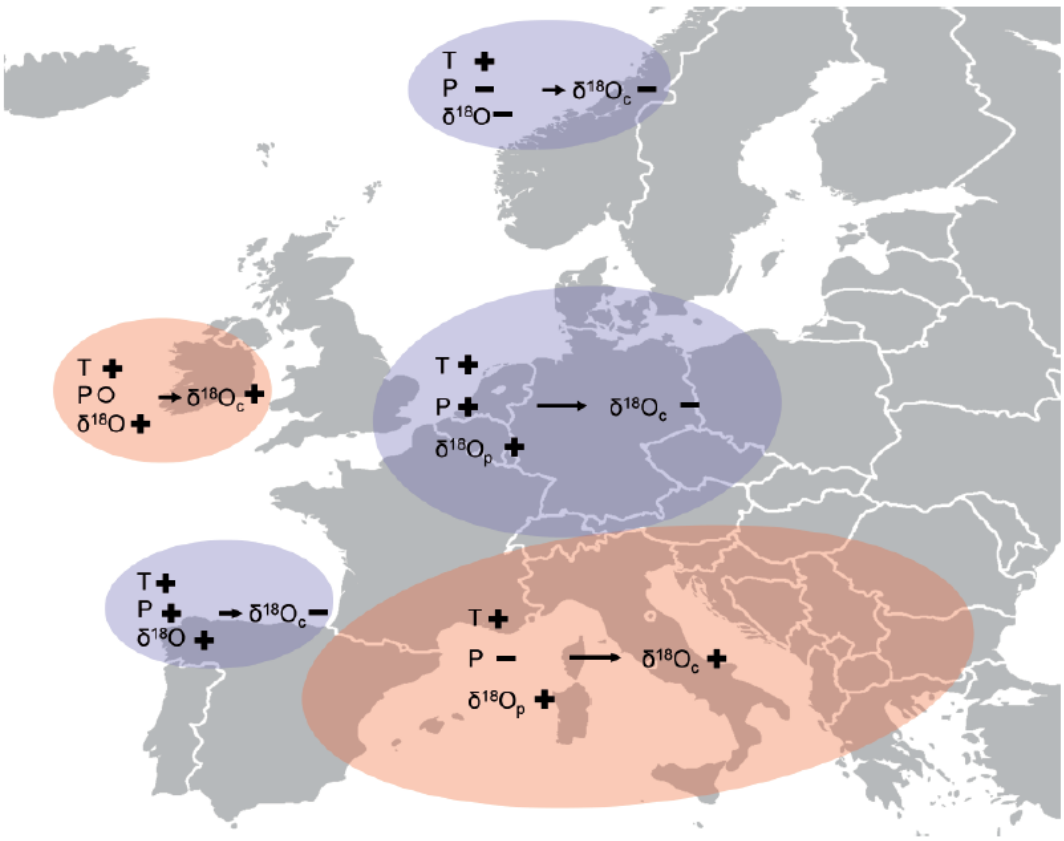

Figure A.26: European climate pattern (temperature, isotopic composition and amount of precipitation) for a positive NAO mode. For the Closani Cave with its location in Romania a positive NAO mode shows a decrease in the amount of precipitation and isotopically heavier precipitation, due to the warmer Mediterranean Sea as source of precipitation. Schematic illustration adapted from *Wackerbarth* [2011].

A.4 Case study II: Holocene stalagmite (present - 8.6 ka BP) from Central Europe - Bunker Cave

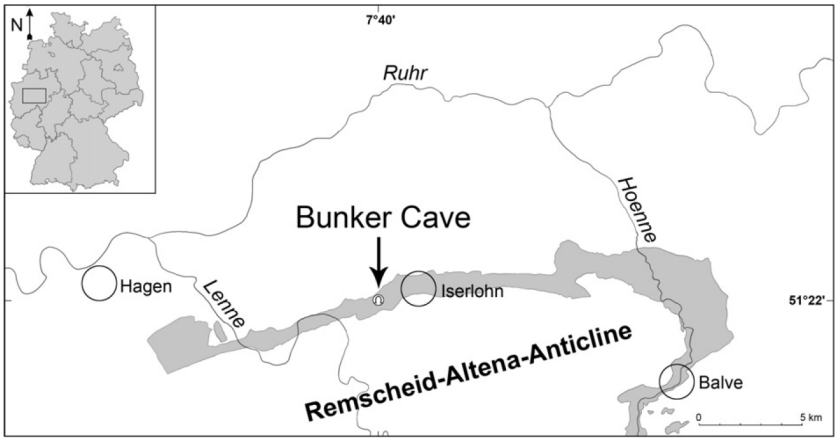

Figure A.27: Location of Bunker Cave close to the city Iserlohn. The grey shading indicating Middle to Upper Devonian limestone [*Riechelmann et al.*, 2011]. Bunker Cave is located in the federal state of North Rhine-Westphalia, see black square in the small map of Germany.

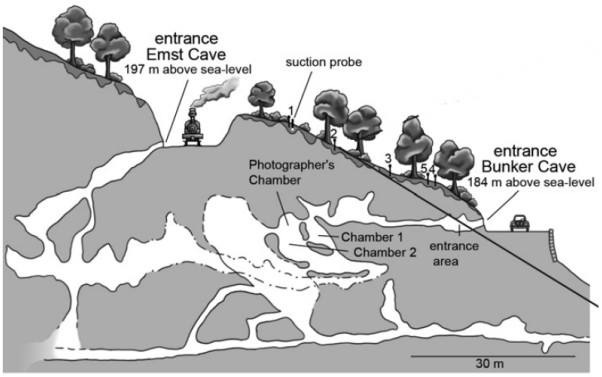

Figure A.28: Longitudinal section of Bunker Cave with the two entrances, adapted from *Riechelmann et al.* [2011]

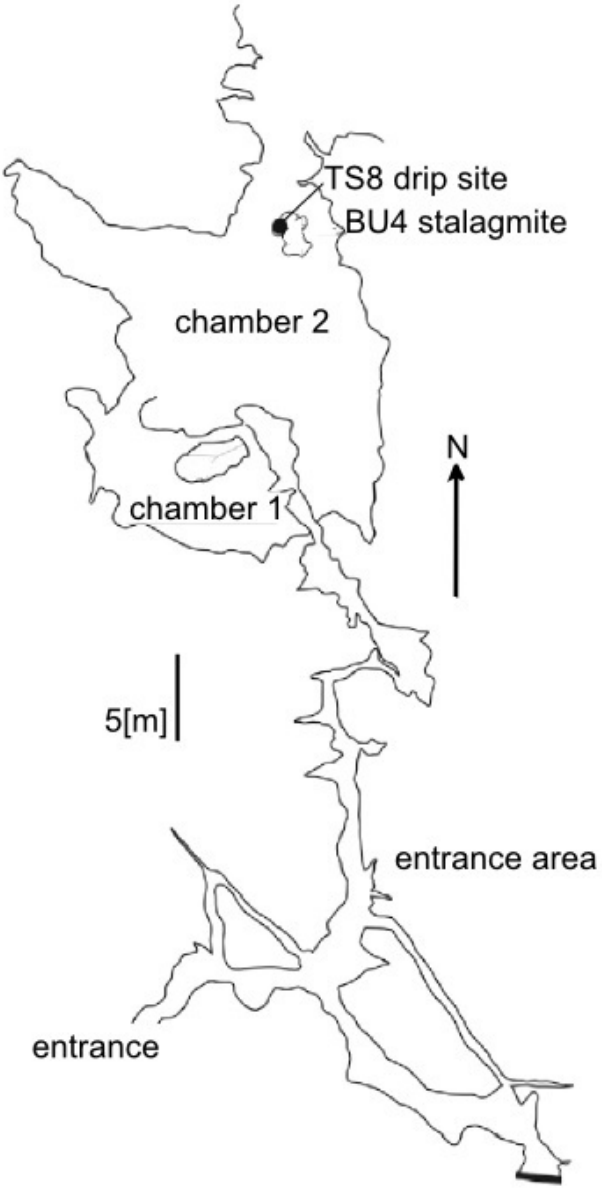

Figure A.29: Cave map of the Bunker Cave, with the location of the drip site TS8 and the sampling site of the stalagmite Bu4 in chamber 2. The map is modified after *Riechelmann et al.* [2013].

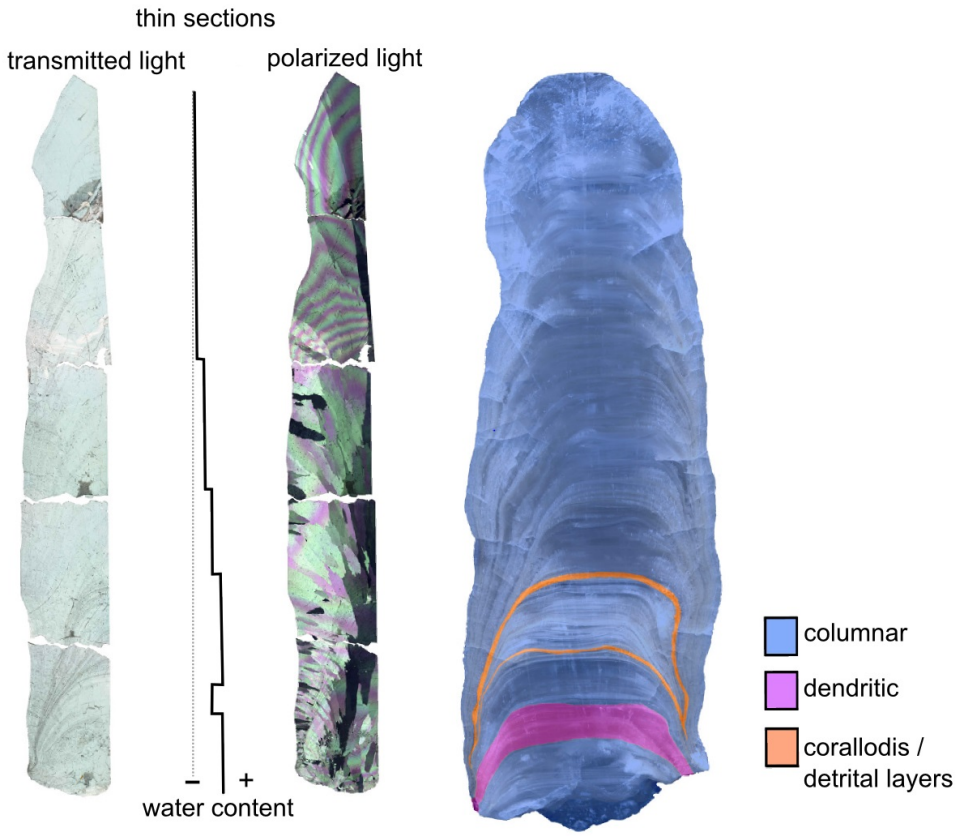

Figure A.30: Thin sections, left with plane-polarized light and right with cross - polarized light (Nicol prism). In the middle the theoretically expected water content of the stalagmite Bu4 after the analysis of thin sections. A high water content is expected between the two detrital layers. On the right side the crystallographic fabrics of Bu4 are shown with coralloids and/or detrital layers in orange, columnar fabrics in blue and dendritic fabrics in pink [*Riechelmann*, 2010].

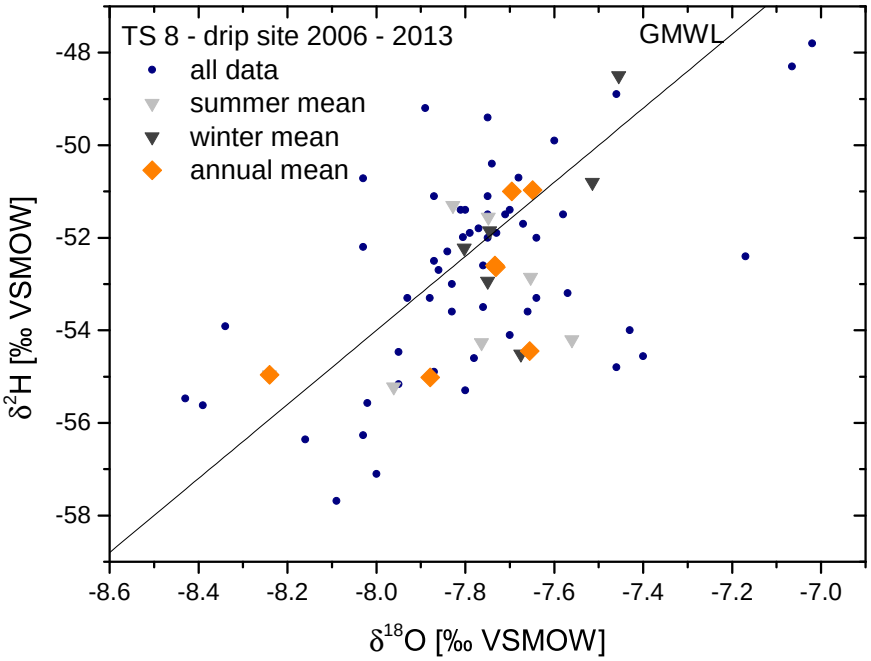

Figure A.31: TS8 drip water isotopic composition with the individual measurements (blue dots), summer means (light grey triangles), winter means (dark grey triangles) and annual means (orange diamond). No seasonal pattern can be distinguished. The trip water isotopic composition was measured with mass spectrometry ($1\,\sigma$ reproducibility) with an uncertainty of $\pm 0.09\,‰$ for $\delta^{18}O$ and $\pm 1.0\,‰$ for $\delta^{2}H$, in VSMOW [*Riechelmann et al.*, 2017].

sample ID	DFT (total) [mm]	error [mm]	mass [g]	water volume [μl]	water content [μl/g]	δ^{18}O [‰]	error [‰]	δ^{2}H [‰]	error [‰]	crystal fabric
1	2.75	2.75								cl
2	8.25	2.75	0.74	0.17	0.23	-4.95	-	-46.72	-	cl
3	16.75	3.25								cl
4	24.00	4.00								cl
5	35.50	2.50								cl
6	48.00	3.00								cl
7	55.00	4.00								cl
8	60.25	1.25								cl
9	64.25	2.75								cl
10	70.50	3.50								cl
11	75.75	1.75	0.61	0.06	0.10	0.87	-	-39.25	-	cl
12	80.50	3.00								cl
13	85.75	2.25								cl
14	89.50	1.50								cl
15	97.25	3.25								cl
16	103.25	2.75								cl
17	108.25	2.25								cl
18	113.00	2.50								cl
19	117.75	2.25	0.77	0.38	0.49	-5.46	0.5	-42.99	1.5	cl

Table A.24: Part 1: All available sample pieces for Bu4 with depth information (distance from top), weight, water volume and water content. The stable isotope values are given in VSMOW, if no uncertainty is specified the released water volume was beneath the threshold (0.2 μl) for a reliable evaluation. The abbreviation of the crystal fabric stands for: *cl* for columnar, *d* for dendritic and *dl* for detrial layers.

sample ID	DFT (total) [mm]	error [mm]	mass [g]	water volume [μl]	water content [μl/g]	δ^{18}O [‰]	error [‰]	δ^{2}H [‰]	error [‰]	crystal fabric
20_A	122.50	2.50								cl
20_B	122.50	2.50								cl
21_A	127.00	2.00	0.50	0.18	0.35	-3.11	-	-40.54	-	cl
21_B	127.00	2.00	0.32	0.08	0.24	-2.91	-	-41.01	-	cl
22	132.00	3.00								cl
23_A	142.50	2.50	0.32	0.25	0.77	-6.32	0.5	-43.84	1.5	cl
23_B	142.50	2.50	0.36	0.39	1.08	-5.32	0.5	-42.18	1.5	cl
24_A	149.00	2.00	0.36	0.63	1.76	-6.03	0.5	-45.35	1.5	cl
24_B	149.00	2.00	0.36	0.56	1.58	-4.51	0.5	-42.78	1.5	cl
25_A	153.25	2.25	0.33	2.08	6.23	-5.38	0.2	-43.53	0.5	cl
25_B	153.25	2.25								cl
26_A	157.75	2.25	0.41	2.49	6.09	-5.32	0.2	-43.74	0.5	cl
26_B	157.75	2.25	0.39	1.19	3.08	-4.87	0.2	-41.82	0.5	cl
27_A	162.50	2.50	0.77	7.32	9.52	-4.78	0.2	-43.40	0.5	cl
27_B	162.50	2.50	0.90	24.17	26.79	-4.50	0.2	-41.85	0.5	cl
28_A	167.50	2.50	0.83	6.26	7.52	-4.86	0.2	-42.81	0.5	dl
28_B	167.50	2.50	0.82	5.35	6.51	-6.11	0.2	-45.73	0.5	dl
29_A	172.50	2.50	0.79	0.11	0.14	-0.08	-	-40.56	-	cl
29_B	172.50	2.50								cl
30_A	177.50	2.50								cl
30_B	177.50	2.50								cl
31_A	182.50	2.50	0.74	0.55	0.75	-9.54	0.5	-49.54	1.5	d
31_B	182.50	2.50								d
32_A	187.50	2.50								d
32_B	187.50	2.50								d
33_A	192.50	2.50								d
33_B	192.50	2.50								d
34_A	197.50	2.50	0.83	0.01	0.01	18.37	-	-24.89	-	cl
34_B	197.50	2.50								cl
35_A	202.50	2.50								cl
35_B	202.50	2.50								cl

Table A.25: Part 2: See previous label.

Water content - changing climate condition

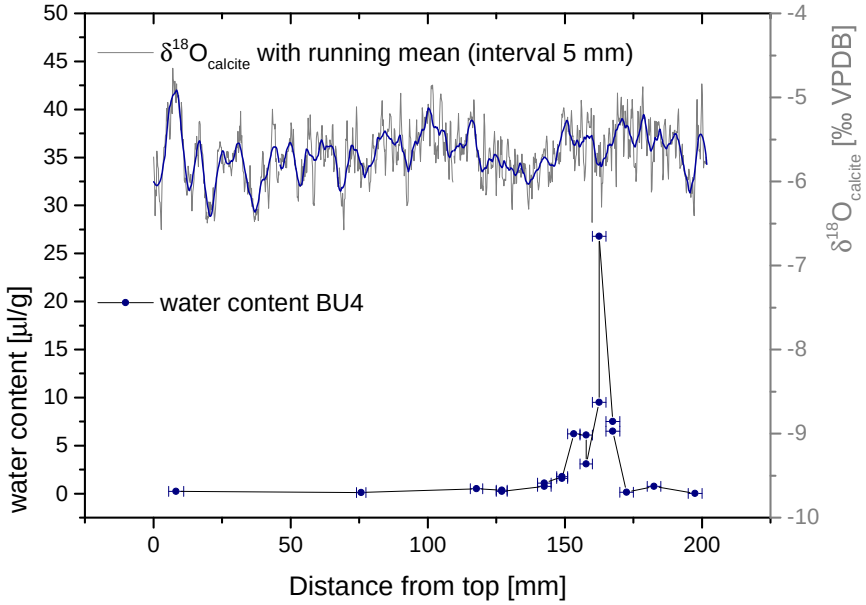

Figure A.32: Measured water content (μl per g calcite) in direct comparison to the smoothed $\delta^{18}O_{calcite}$ signal (blue line) of Bu4. The running mean interval (5 mm) is equal to the edge length of fluid inclusion sample pieces. After *Vogel et al.* [2013] higher $\delta^{18}O_{calcite}$ values are associated with a higher water content and vice versa. However, this accordance is not distinguishable for Bu4.

Sea level corrected stable isotope results

sample ID	DFT [mm]	mass [g]	water volume [μl]	water content [μl/g]	$\delta^{18}O_{sl}$ [‰]	error [‰]	$\delta^{2}H_{sl}$ [‰]	error [‰]
19	115.5 - 120	0.77	0.38	0.49	-5.47	0.5	-43.07	1.5
23_A	140 - 145	0.32	0.25	0.77	-6.34	0.5	-44.00	1.5
23_B		0.36	0.39	1.08	-5.34	0.5	-42.34	1.5
24_A	147 - 151	0.36	0.63	1.76	-6.05	0.5	-45.55	1.5
24_B		0.36	0.56	1.58	-4.54	0.5	-42.98	1.5
25_A	151 - 155.5	0.33	2.08	6.23	-5.41	0.5	-43.77	1.5
26_A	155.5 - 160	0.41	2.49	6.09	-5.36	0.5	-44.06	1.5
26_B		0.39	1.19	3.08	-4.91	0.5	-42.14	1.5
27_A	160 - 165	0.77	7.32	9.52	-4.82	0.5	-43.72	1.5
27_B		0.90	24.17	26.79	-4.54	0.5	-42.17	1.5
28_A	165 - 170	0.83	6.26	7.52	-4.91	0.5	-43.21	1.5
28_B		0.82	5.35	6.51	-6.16	0.5	-46.13	1.5
31_A	180 - 185	0.74	0.55	0.75	-9.59	0.5	-49.94	1.5

Table A.26: Stable isotope results for Bu4 samples with a released water volume above 0.2 μl, which is set as a threshold for a reliable evaluation. I corrected these δ^{18}O and δ^{2}H values for sea level change after *Waelbroeck et al.* [2002], in VSMOW.

A.5 Case study III: Tropical stalagmite (15 - 46 ka BP) from Puerto Rico - Cueva Larga

Site description - Cueva Larga cave

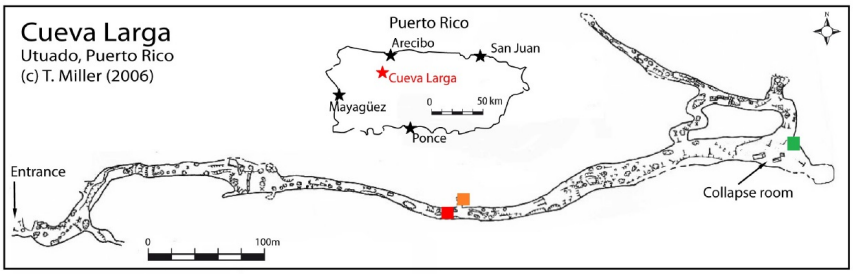

Figure A.33: Cueva Larga map from *Warken* [2017] position of LA-1 (red square), the closet drip site SW-2 (orange square) and site A4 with the location of pool A4 (green square).

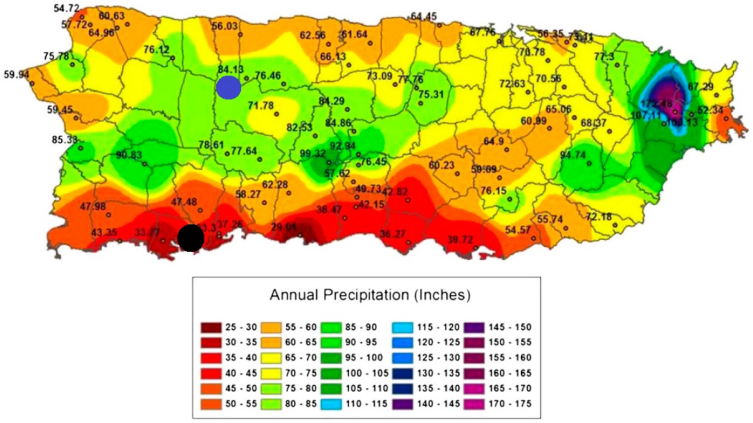

Figure A.34: Mean annual rainfall for Puerto Rico (1981-2010) after *Govender et al.* [2013]. The black dot shows the location of the study site Boca Station (Guánica Dry Forest) and the blue dot the location of the Cueva Larga cave. *Govender et al.* [2013] derived a LMWL as $\delta^2H = 7.0 \cdot \delta^{18}O + 10.3$ ‰ VSMOW for rainwater in dry months and a LMWL as $\delta^2H = 7.37 \cdot \delta^{18}O + 8.0$ ‰ VSMOW for rainwater in wet months.

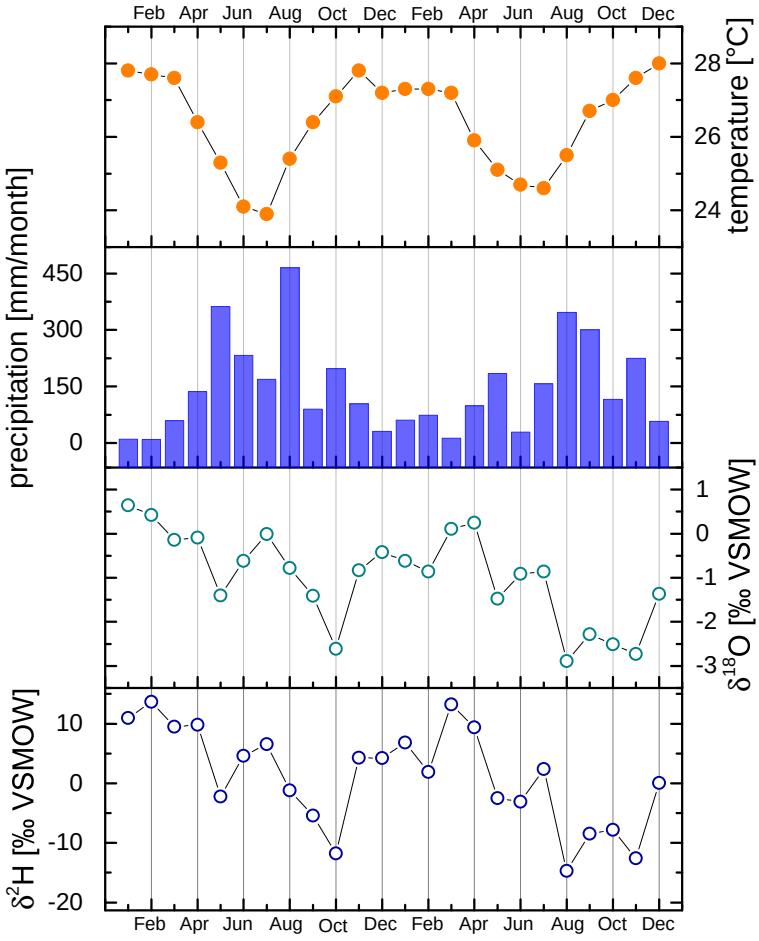

Figure A.35: Monthly rainwater samples from Mayagüez (GNIP station) for a two-year record of oxygen and hydrogen values of precipitation, as well as the amount of rainfall and the air temperature (adapted from [*Vieten et al.*, 2018]).

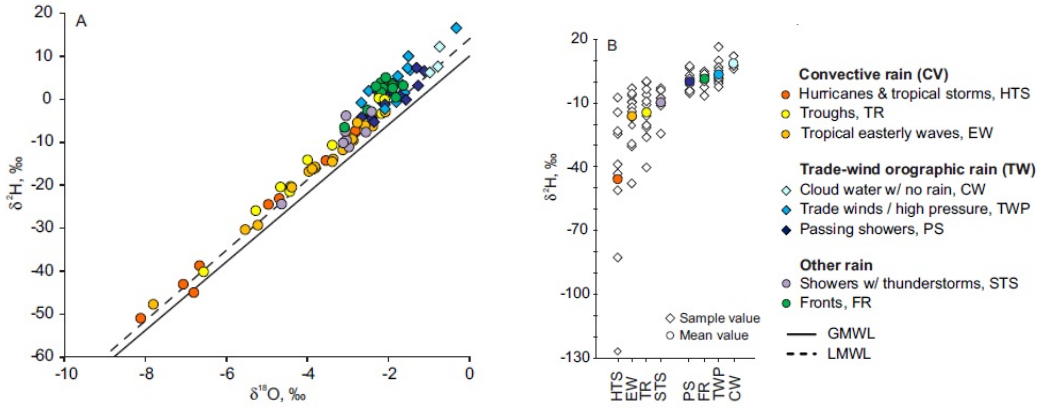

Figure A.36: Stable isotopes of precipitation (Pico del Este) in Puerto Rico adapted from *Scholl and Murphy* [2014]. Composition of the weekly collected rain water samples in Puerto Rico: 52 % convective rain (with 14 % cyclonic low-pressure systems, 8 % named tropical storms and hurricanes, 15 % troughs and 15 % tropical easterly waves), 25 % orographic rain (with 13 % trade wind showers and 12 % passing showers) and 10 % cold fronts and showers with thunderstorms.

sample ID	mass [g]	water volume [μl]	water content [μl/g]	δ^{18}O VSMOW [‰]	error VSMOW [‰]	δ^{2}H VSMOW [‰]	error VSMOW [‰]
LA4_A	0.36	0.01	0.03	12.64	0.50	51.80	1.50
LA4_B	0.51	0.02	0.04	23.38	0.50	63.57	1.50
A4_A	0.36	0.20	0.55	-0.37	0.50	0.40	1.50
A4_B	0.45	0.19	0.42	0.11	0.50	4.72	1.50
A4_C	0.79	0.40	0.51	-1.63	0.50	5.75	1.50
A4_D	1.54	1.04	0.68	-0.74	0.50	2.32	1.50
A4_E	1.63	1.13	0.70	-0.76	0.50	4.77	1.50
A4_F	1.54	0.91	0.59	-1.63	0.50	2.25	1.50
A4_G	1.40	1.35	0.96	0.58	0.50	4.53	1.50
mean with stdv				-0.76	0.76	3.34	1.83

Table A.27: Water stable isotope results of fluid inclusions for pool spar from the pool A4 and LA4 in the Cueva Larga. The ones marked in blue released a water volume below the critical threshold value ($< 0.2\,\mu$l) for a reliable evaluation. For the samples with sufficient released water, the mean value and the corresponding standard deviation was calculated.

	date	δ^{18}O VSMOW [‰]	error VSMOW [‰]	δ^{2}H VSMOW [‰]	error VSMOW [‰]
LA-SW2					
	02.09.13	-2.66	0.08	-12.79	0.50
	08.04.14	-3.31	0.08	-11.54	0.50
	31.05.14	-2.81	0.08	-7.86	0.50
	07.10.15	-2.52	0.08	-5.14	0.50
	16.12.15	-2.59	0.08	-5.77	0.50
	20.03.16	-2.54	0.08	-8.83	0.50
	16.07.16	-2.65	0.08	-9.56	0.50
	21.09.16	-2.62	0.08	-9.08	0.50
	13.12.16	-2.64	0.08	-9.34	0.50
	25.06.17	-2.55	0.08	-8.77	0.50
	03.12.17	-2.43	0.08	-9.03	0.50
	12.03.19	-2.09	0.08	-8.43	0.50
LA-A4					
	21.11.19	-2.72	0.26	-9.17	0.17

Table A.28: Water stable isotope results for drip site SW-2 close to the location where the stalagmite LA-1 was collected [*Vieten et al.*, 2018]. Drip water was measured in Innsbruck using a Picarro L2140-i analyser. The stable isotope composition of pool water from A4 was measured at the Institute of Environmental Physics, Heidelberg [personal correspondence Sophie Warken, 30.01.2020].

sample ID	dft [mm]	error [mm]	age [ka]	error plus [ka]	error minus [ka]	mass [g]	water volume [μl]	water content [μl/g]	δ^{18}O VSMOW [‰]	error VSMOW [‰]	δ^{2}H VSMOW [‰]	error VSMOW [‰]
1_A	9.00	3.00	16.04	16.61	15.32	0.51	0.33	0.66	1.95	0.50	34.39	1.50
1_B	9.00	3.00	16.04	16.61	15.32	0.42	0.28	0.67	3.97	0.50	32.32	1.50
5_A	32.00	2.00	17.65	17.97	17.35	0.35	0.11	0.31	8.95	0.50	37.26	1.50
5_B	32.00	2.00	17.65	17.97	17.35	0.47	0.14	0.30	6.25	0.50	41.57	1.50
5b_A	38.00	2.00	17.70	18.01	17.40	1.06	0.45	0.42	0.88	0.50	24.00	1.50
5b_B	38.00	2.00	17.70	18.01	17.40	1.03	0.37	0.36	-1.32	0.50	16.91	1.50
7_A	112.75	0.75	20.19	20.54	19.67	0.30	0.04	0.12	10.77	0.50	39.40	1.50
7_B	112.75	0.75	20.19	20.54	19.67	0.27	0.02	0.08	12.03	0.50	42.96	1.50
7b_A	160.00	2.00	20.81	21.00	20.56	0.74	0.47	0.64	-0.71	0.50	11.20	1.50
7b_B	160.00	2.00	20.81	21.00	20.56	1.34	2.98	2.21	4.68	0.50	19.34	1.50
8_A	212.00	2.00	21.43	21.66	21.16	0.36	0.20	0.57	-1.38	0.50	16.07	1.50
8_B	212.00	2.00	21.43	21.66	21.16	0.61	0.29	0.48	-2.07	0.50	20.99	1.50
9a_A	293.00	1.50	22.54	22.74	22.31	0.33	0.10	0.31	4.81	0.50	18.81	1.50
9a_B	293.00	1.50	22.54	22.74	22.31	0.25	0.11	0.45	3.25	0.50	15.89	1.50
9b_A	291.50	1.50	22.52	22.72	22.29	0.40	0.22	0.54	1.70	0.50	13.18	1.50
9b_B	301.00	4.00	22.65	22.86	22.39	0.21	0.18	0.85	0.25	0.50	7.34	1.50
9c_A	301.00	4.00	22.65	22.86	22.39	0.70	0.46	0.66	1.27	0.50	12.37	1.50
9c_B	301.00	4.00	22.65	22.86	22.39	0.77	0.65	0.84	2.41	0.50	12.52	1.50

Table A.29: Results of stable isotope measurements for the fluid inclusions of the stalagmite Larga LA-1, with the corresponding depth (distance from top) and age (personal correspondence Sophie Warken). The capital letters (A to C) indicate the replicate measurements. Whereas the small letters (a to c) indicate repeated measurements with a slight depth offset. They were performed when the initial water content was too low and the released water volume was below the evaluation limit of 0.2 μl.

sample ID	dft [mm]	error [mm]	age [ka]	error plus [ka]	error minus [ka]	mass [g]	water volume [μl]	water content [μl/g]	δ^{18}O VSMOW [‰]	error VSMOW [‰]	δ^{2}H VSMOW [‰]	error VSMOW [‰]
10_A	370.00	1.00	23.53	23.73	23.39	0.43	0.78	1.81	-0.21	0.50	6.81	1.50
10_B	370.00	1.00	23.53	23.73	23.39	0.38	0.60	1.56	-0.64	0.50	8.39	1.50
10_C	370.00	1.00	23.53	23.73	23.39	0.32	0.70	2.21	-0.88	0.50	5.90	1.50
12_A	482.50	2.50	24.23	24.42	23.97	0.47	0.34	0.71	1.02	0.50	13.29	1.50
12_B	482.50	2.50	24.23	24.42	23.97	0.63	0.44	0.71	1.67	0.50	11.53	1.50
13_A	525.00	2.50	24.67	24.91	24.39	0.57	0.72	1.27	-2.64	0.50	6.38	1.50
13_B	525.00	2.50	24.67	24.91	24.39	0.51	1.06	2.07	-0.99	0.50	7.08	1.50
13_C	525.00	2.50	24.67	24.91	24.39	0.50	1.34	2.70	-1.98	0.50	7.10	1.50
14_A	642.00	2.00	26.76	27.03	26.43	0.34	0.16	0.47	3.61	0.50	20.96	1.50
14_B	642.00	2.00	26.76	27.03	26.43	0.23	0.08	0.35	2.25	0.50	19.76	1.50
15_A	689.50	19.50	27.74	28.01	27.46	0.57	0.84	1.49	-0.37	0.50	13.15	1.50
15_B	667.50	2.50	27.72	27.96	27.45	0.51	0.17	0.33	1.52	0.50	19.80	1.50
15b_A	689.50	19.50	27.74	28.01	27.46	0.41	0.26	0.62	1.60	0.50	12.67	1.50
15b_B	689.50	19.50	27.74	28.01	27.46	0.75	1.15	1.53	-0.81	0.50	11.27	1.50
15b_C	694.50	2.50	27.75	27.97	27.50	0.33	0.17	0.50	-0.78	0.50	20.41	1.50
15c_A	689.50	19.50	27.74	28.01	27.46	0.71	0.99	1.39	-0.04	0.50	12.47	1.50
15c_B	689.50	19.50	27.74	28.01	27.46	0.74	0.65	0.88	-0.40	0.50	17.18	1.50
16_A	745.00	2.00	28.09	28.78	27.68	0.24	0.74	3.05	0.02	0.50	10.59	1.50
16_B	745.00	2.00	28.09	28.78	27.68	0.33	0.93	2.83	-0.14	0.50	10.41	1.50
17_A	827.50	1.50	29.29	29.51	29.07	0.44	0.12	0.27	5.15	0.50	30.45	1.50
17_B	827.50	1.50	29.29	29.51	29.07	0.65	0.34	0.52	1.64	0.50	23.11	1.50

Table A.30: Stable isotope results of fluid inclusion measurements for Larga LA-1, with labelling see table above.

sample ID	dft [mm]	error [mm]	age [ka]	error plus [ka]	error minus [ka]	mass [g]	water volume [μl]	water content [μl/g]	δ^{18}O VSMOW [‰]	error VSMOW [‰]	δ^{2}H VSMOW [‰]	error VSMOW [‰]
17b_A	831.50	3.50	29.31	29.52	29.07	0.61	0.23	0.38	8.04	0.50	27.88	1.50
17b_B	831.50	3.50	29.31	29.52	29.07	0.62	0.25	0.40	4.83	0.50	27.10	1.50
18_A	940.00	2.50	30.00	30.23	29.75	0.46	0.24	0.53	0.65	0.50	23.25	1.50
18_B	940.00	2.50	30.00	30.23	29.75	0.30	0.14	0.45	2.98	0.50	27.29	1.50
18_C	940.00	2.50	30.00	30.23	29.75	0.38	0.29	0.77	1.20	0.50	18.26	1.50
19_A	1010.50	11.50	30.58	31.55	30.08	0.58	0.25	0.44	0.59	0.50	20.26	1.50
19_B	1010.50	11.50	30.58	31.55	30.08	0.58	0.43	0.74	-0.96	0.50	17.19	1.50
20_A	1010.50	11.50	30.58	31.55	30.08	0.54	1.21	2.24	-0.71	0.50	12.43	1.50
21b_A	1028.00	3.00	31.48	31.93	30.40	0.69	1.19	1.74	0.44	0.50	14.67	1.50
21b_B	1028.00	3.00	31.48	31.93	30.40	0.75	0.39	0.53	4.43	0.50	22.73	1.50
22_A	1045.50	1.50	32.22	32.59	31.78	0.45	0.08	0.18	8.21	0.50	43.40	1.50
22_B	1045.50	1.50	32.22	32.59	31.78	0.43	0.07	0.15	8.28	0.50	37.87	1.50
23_A	1052.00	2.00	32.49	33.32	32.01	0.31	0.17	0.55	3.50	0.50	25.21	1.50
23_B	1052.00	2.00	32.49	33.32	32.01	0.24	0.13	0.53	3.30	0.50	25.75	1.50
24_A	1079.50	9.50	33.50	33.98	32.95	0.61	0.29	0.48	0.03	0.50	20.17	1.50
24_B	1079.50	9.50	33.50	33.98	32.95	0.56	0.22	0.39	0.64	0.50	30.49	1.50
24b_A	1082.00	2.00	33.55	33.89	33.22	0.81	0.32	0.40	7.85	0.50	28.91	1.50
24b_B	1082.00	2.00	33.55	33.89	33.22	0.80	0.06	0.08	11.27	0.50	33.31	1.50
24c_A	1079.50	9.50	33.50	33.98	32.95	0.64	0.83	1.30	0.53	0.50	14.53	1.50
24c_B	1079.50	9.50	33.50	33.98	32.95	0.69	0.76	1.10	-1.12	0.50	9.99	1.50
24c_C	1088.00	2.00	33.64	33.99	33.26	0.49	0.24	0.48	10.74	0.50	35.12	1.50

Table A.31: Stable isotope results of fluid inclusion measurements for Larga LA-1, with labelling see table above.

sample ID	dft [mm]	error [mm]	age [ka]	error plus [ka]	error minus [ka]	mass [g]	water volume [μl]	water content [μl/g]	δ^{18}O VSMOW [‰]	error VSMOW [‰]	δ^{2}H VSMOW [‰]	error VSMOW [‰]
25_A	1235.00	1.50	34.00	34.53	33.54	0.44	0.12	0.27	9.29	0.50	47.60	1.50
25_B	1235.00	1.50	34.00	34.53	33.54	0.65	0.27	0.42	4.68	0.50	27.75	1.50
27_A	1398.00	10.00	35.33	35.70	35.00	0.35	0.27	0.79	0.94	0.50	14.55	1.50
27_B	1398.00	10.00	35.33	35.70	35.00	0.70	0.27	0.38	-0.40	0.50	18.05	1.50
27b_A	1407.00	3.00	35.39	35.72	35.09	0.54	0.20	0.37	2.13	0.50	19.65	1.50
27b_B	1398.00	10.00	35.33	35.70	35.00	1.20	0.69	0.57	1.39	0.50	17.81	1.50
28_A	1441.00	2.00	35.63	36.05	35.24	0.48	0.58	1.21	0.16	0.50	15.53	1.50
28_B	1441.00	2.00	35.63	36.05	35.24	0.37	0.56	1.50	0.36	0.50	12.66	1.50
28_C	1441.00	2.00	35.63	36.05	35.24	0.49	1.11	2.24	0.09	0.50	12.49	1.50
30_A	1463.00	2.00	41.43	41.67	41.24	0.49	0.18	0.36	11.88	0.50	45.26	1.50
30_B	1463.00	2.00	41.43	41.67	41.24	0.47	0.11	0.24	8.83	0.50	44.63	1.50
31_A	1504.50	2.50	41.48	41.81	41.26	0.29	0.12	0.42	4.04	0.50	25.07	1.50
31_B	1504.50	2.50	41.48	41.81	41.26	0.75	0.37	0.50	5.61	0.50	29.62	1.50
32_A	1554.50	2.50	42.98	43.40	42.53	0.44	0.15	0.35	0.74	0.50	18.60	1.50
32_B	1554.50	2.50	42.98	43.40	42.53	0.56	0.31	0.55	0.81	0.50	20.03	1.50
32b_A	1556.00	4.50	43.02	43.46	42.52	0.77	0.93	1.22	8.59	0.50	25.74	1.50
32b_B	1556.00	4.50	43.02	43.46	42.52	0.61	0.50	0.82	8.35	0.50	28.68	1.50
32b_C	1556.00	4.50	43.02	43.46	42.52	0.70	0.26	0.37	4.75	0.50	20.67	1.50
33_A	1637.50	2.50	43.23	43.68	42.78	0.39	0.18	0.47	0.36	0.50	10.61	1.50
33_B	1637.50	2.50	43.23	43.68	42.78	0.73	0.22	0.30	6.19	0.50	22.94	1.50

Table A.32: Stable isotope results of fluid inclusion measurements for Larga LA-1, with labelling see table above.

sample ID	dft [mm]	error [mm]	age [ka]	error plus [ka]	error minus [ka]	mass [g]	water volume [μl]	water content [μl/g]	δ^{18}O VSMOW [‰]	error VSMOW [‰]	δ^{2}H VSMOW [‰]	error VSMOW [‰]
34_A	1725.00	2.00	44.46	45.68	43.63	0.47	0.32	0.68	13.48	0.50	28.18	1.50
34_B	1725.00	2.00	44.46	45.68	43.63	0.82	0.37	0.46	2.67	0.50	23.45	1.50
34b_A	1742.50	4.50	44.69	46.03	43.65	0.75	1.19	1.57	9.69	0.50	27.12	1.50
34b_B	1742.50	4.50	44.69	46.03	43.65	0.72	0.66	0.92	3.73	0.50	18.67	1.50
35_A	1767.50	1.50	44.98	46.14	43.75	0.34	0.63	1.83	1.00	0.50	16.97	1.50
35_B	1767.50	1.50	44.98	46.14	43.75	0.31	0.58	1.84	0.17	0.50	17.27	1.50
35_C	1767.50	1.50	44.98	46.14	43.75	0.31	0.32	1.04	1.66	0.50	20.48	1.50
36_A	1819.50	3.50	45.61	46.51	44.81	0.42	0.25	0.60	-0.53	0.50	14.63	1.50
36_B	1819.50	3.50	45.61	46.51	44.81	0.55	0.30	0.54	3.56	0.50	17.73	1.50

Table A.33: Stable isotope results of fluid inclusion measurements for Larga LA-1, with labelling see table above.

	sample ID	number of replicate	water content [μl/g]	age [ka]	error [ka]	$\delta^{18}O_{sl}$ VSMOW [‰]	error VSMOW [‰]	$\delta^{2}H_{sl}$ VSMOW [‰]	error VSMOW [‰]	d-excess VSMOW [‰]
high water content										
	1	2	0.66	16.04	0.64	2.04	0.35	26.00	1.06	9.70
	5	2	0.39	17.70	0.30	-1.21	0.35	12.50	1.06	22.22
	8	2	0.52	21.43	0.25	-2.74	0.35	10.36	1.06	32.32
	9	3	0.68	22.65	0.23	0.79	0.29	4.66	0.87	-1.63
	10	3	1.86	23.53	0.17	-1.56	0.29	-0.85	0.87	11.63
	12	2	0.71	24.23	0.22	0.38	0.35	4.68	1.06	1.66
	13	3	2.01	24.67	0.26	-2.82	0.29	-0.77	0.87	21.81
	15	5	1.18	27.74	0.27	-0.83	0.22	6.75	0.67	13.38
	16	2	2.94	28.09	0.55	-0.86	0.35	4.06	1.06	10.95
	18	2	0.65	30.00	0.24	0.21	0.35	15.09	1.06	13.38
	19	3	0.59	30.58	0.73	-1.05	0.29	11.11	0.87	19.49
	24	4	0.82	33.50	0.52	-0.65	0.25	13.44	0.75	18.63
	27	3	0.58	35.33	0.35	-0.03	0.29	11.40	0.87	11.66
	28	3	1.65	35.63	0.40	-0.47	0.29	8.19	0.87	11.91
	32	1	0.55	42.98	0.43	0.18	0.50	15.01	1.50	13.56
	35	3	1.57	44.98	1.19	0.32	0.29	13.23	0.87	10.67
	36	2	0.57	45.61	0.85	0.90	0.35	11.22	1.06	4.03

Table A.34: Mean stable isotope results for fluid inclusion measurements of LA-1. Only samples with a mean water content above 0.4 μl/g are listed. The isotopic data is corrected for a changing isotopic composition of the ocean due to changing sea levels after *Waelbroeck et al.* [2002].

	sample ID	number of replicate	water content [μl/g]	age [ka]	error [ka]	$\delta^{18}O_{sl}$ VSMOW [‰]	error VSMOW [‰]	$\delta^{2}H_{sl}$ VSMOW [‰]	error VSMOW [‰]	d-excess VSMOW [‰]
low water content										
	5	2	0.30	17.65	0.31	6.62	0.35	31.58	1.06	-21.38
	7	2	0.10	20.19	0.43	10.36	0.35	32.87	1.06	-50.03
	9	2	0.38	22.54	0.21	3.02	0.35	9.30	1.06	-14.88
	14	2	0.41	26.76	0.30	2.06	0.35	13.42	1.06	-3.08
	17	2	0.39	29.31	0.22	5.71	0.35	21.65	1.06	-24.01
	22	2	0.17	32.22	0.41	7.58	0.35	35.26	1.06	-25.35
	24b	2	0.24	33.55	0.33	8.89	0.35	25.75	1.06	-45.37
	25	2	0.34	34.00	0.49	4.00	0.50	22.37	1.50	-9.66
	30	2	0.30	41.43	0.21	9.77	0.35	40.23	1.06	-37.91
	33	1	0.30	43.23	0.45	5.56	0.50	17.90	1.50	-26.61

Table A.35: Mean stable isotope results for fluid inclusion measurements of LA-1. Only samples with a mean water content below 0.4 μl/g are listed. The isotopic data is corrected for a changing isotopic composition of the ocean due to changing sea levels after *Waelbroeck et al.* [2002].

δ^{18}O and δ^{2}H of fluid inclusions with sea level correction - stalagmite LA-1

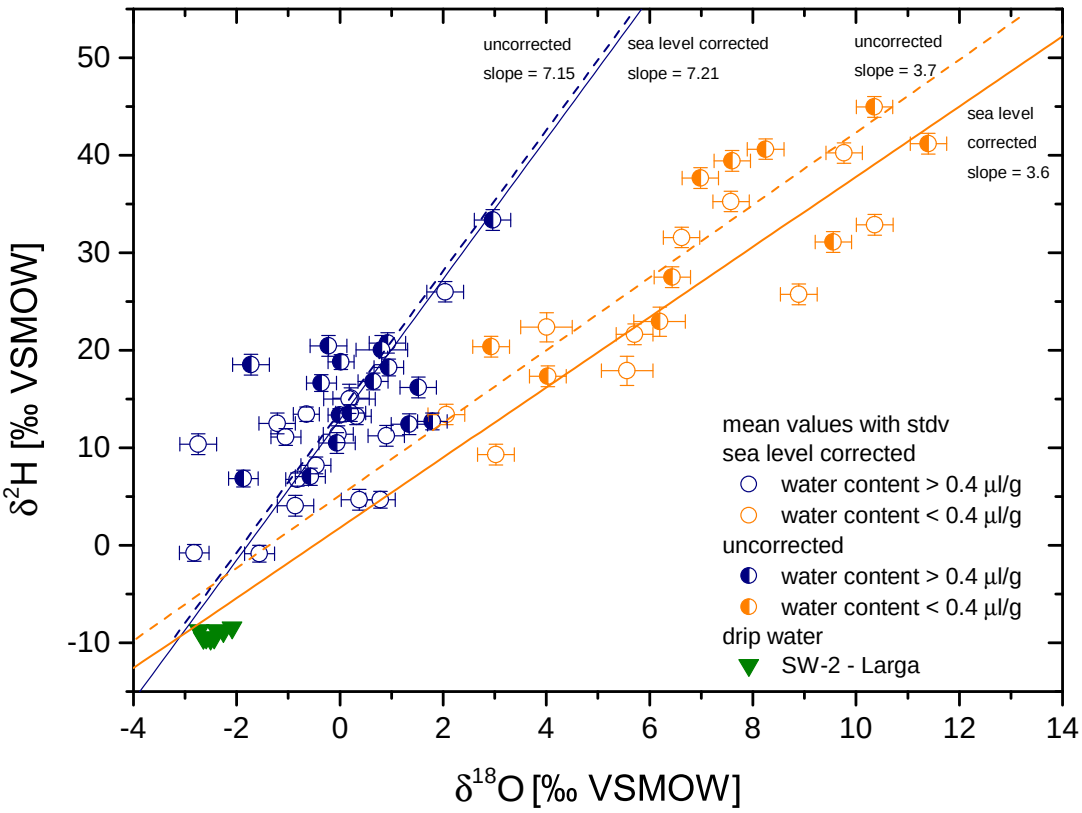

Figure A.37: Results of the stable water isotopes from LA-1 fluid inclusion measurements with the correction for the changing sea level (open circles) and the uncorrected results (half filled circles). Shown are the mean values of the respective depths divided into high (blue) and low (orange) water content. The drip water data at side SW-2 is shown as green triangle. Both groups of samples were fitted with a linear regression, whereby a comparable slope to the one of the GMWL results for the samples with a high water content. The samples with a low water content show fractionation due to evaporation.

δ^{18}O and δ^{2}H of fluid inclusions with possible deuterium excess

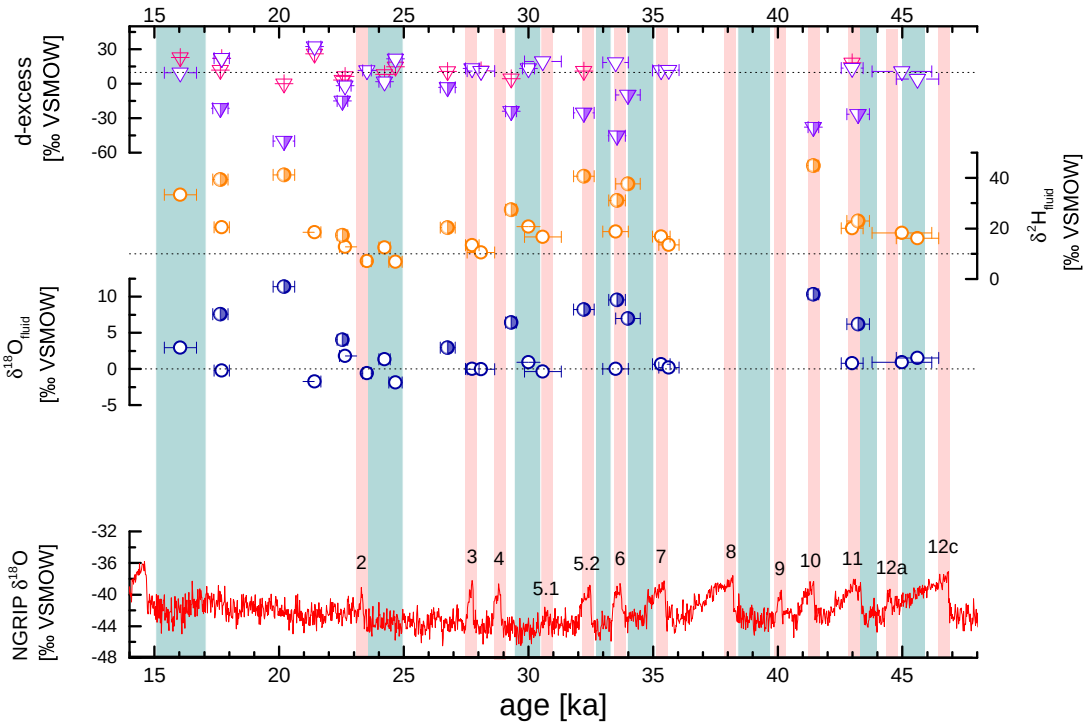

Figure A.38: Mean stable isotope values (δ^{18}O and δ^{2}H) for all sampled depths of LA-1 are shown in blue (oxygen) and orange (hydrogen). Half filled circles indicate samples with a water content below 0.4 μl/g which are labelled as low water content. The measured deuterium excess (purple triangle) calculated via the relationship of the GMWL as well as the the possible d - excess relative to an evaporation line (pink triangle) are shown. The the oxygen isotope record of an ice core from North Greenland NGRIP (red) is shown to identify cold and warm periods [*Andersen et al.*, 2004] with the numbers indicating D/O events (light red bars) according *Capron et al.* [2010]. The HS events and Greenland stadials are illustrated as light green bars.

Amount effect for tropical island

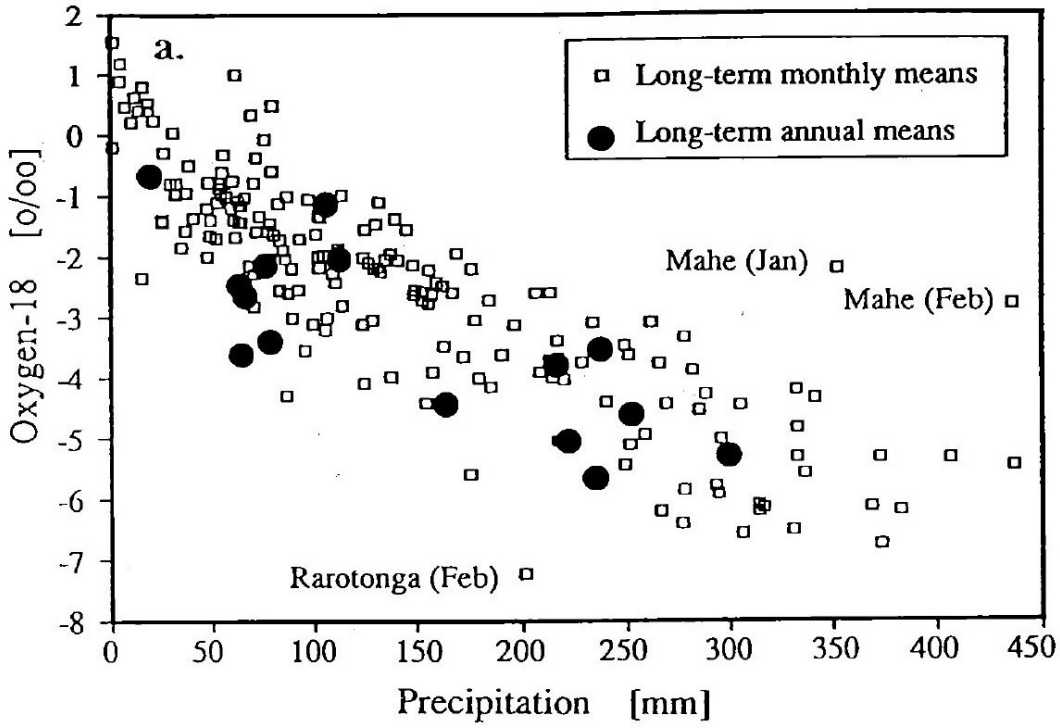

Figure A.39: Long - term monthly and annual mean $\delta^{18}O$ values for tropical island stations (20°S to 20°N) are shown against the amount of monthly precipitation [*Rozanski et al.*, 1993].

Correction due to the changing isotopic composition of the ocean

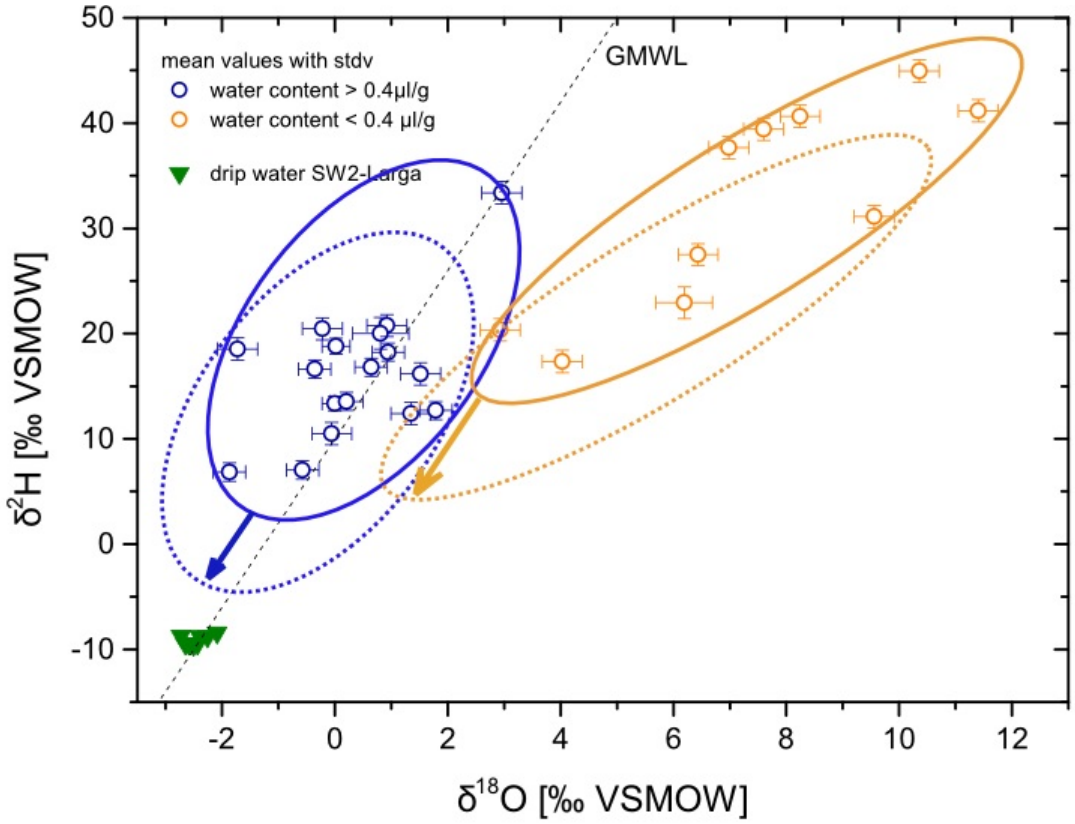

Figure A.40: Fluid inclusion results with possible correction for local Caribbean sea surface $\delta^{18}O_{sw}$ variability [*Schmidt et al.*, 2004]. The stable water isotopes from LA-1 fluid inclusion measurements are divided into high (blue) and low (orange) water content, with the identification of the two clusters. The possible effects due to $\delta^{18}O_{sw}$ changes in the Cariaco Basin are illustrated as dotted circles. Thereby the change of the isotopic composition of the surface water is mainly due to a varying evaporation/precipitation ratio over the western tropical Atlantic.

Application of the classic carbonate thermometer for samples with parametrizations after *Kim and O'Neil* [1997]; *Tremaine et al.* [2011]; *Johnston et al.* [2013]

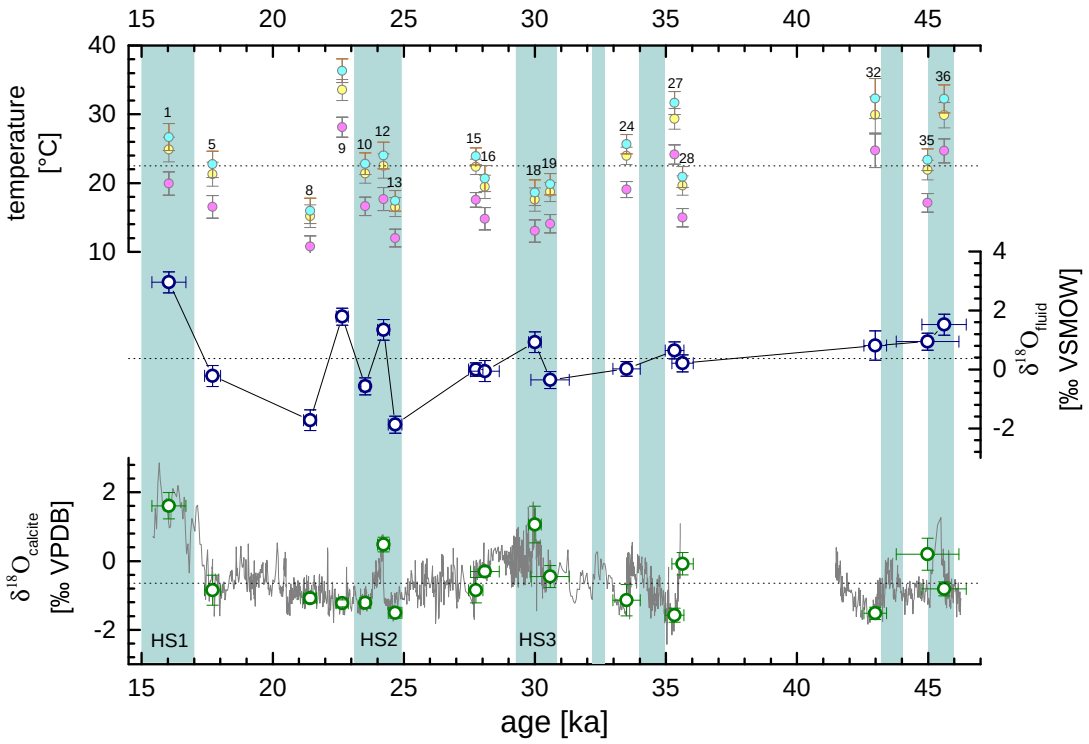

Figure A.41: Measured $\delta^{18}O_{calcite}$ signal in grey with harmonized to fluid inclusion sample depth mean values (green circles). The $\delta^{18}O_{fluid}$ results with a high water content are shown as blue circles and the calculated paleotemperatures via the classical carbonate thermometer with different parametrizations as dots. Thereby, *Kim and O'Neil* [1997] is shown in pink, *Tremaine et al.* [2011] in light blue and *Johnston et al.* [2013] in yellow. The dotted line represents the present day cave air temperature (22.5°C). For a better orientation presumably relatively dry and/or cool periods during the last Glacial are illustrated as light green bars. The overall means of $\delta^{18}O_{fluid}$ and $\delta^{18}O_{calcite}$ are shown as dotted line, respectively.

							Kim O'Neil		Tremaine		Johnston	
sample ID	$\delta^{18}O_{fluid}$ [‰]	error [‰]	$\delta^{18}O_{calcite}$ [‰]	stdv [‰]	α_{cc-w}	error	T [°C]	error [°C]	T [°C]	error [°C]	T [°C]	error [°C]
1	2.96	0.35	32.57	0.39	1.03	0.36	19.94	1.68	26.68	1.97	24.88	1.78
5	-0.22	0.35	30.04	0.45	1.03	0.36	16.56	1.65	22.72	1.92	21.31	1.74
8	-1.72	0.35	29.80	0.14	1.03	0.36	10.76	1.58	15.97	1.84	15.19	1.66
9	1.79	0.29	29.64	0.11	1.03	0.30	28.14	1.45	36.33	1.72	33.54	1.54
10	-0.57	0.29	29.66	0.15	1.03	0.30	16.63	1.34	22.81	1.57	21.38	1.42
12	1.34	0.35	31.40	0.22	1.03	0.36	17.67	1.66	24.03	1.94	22.48	1.75
13	-1.87	0.29	29.36	0.17	1.03	0.30	12.01	1.30	17.42	1.51	16.51	1.37
15	0.00	0.22	30.04	0.38	1.03	0.23	17.56	1.05	23.90	1.23	22.37	1.11
16	-0.06	0.35	30.60	0.14	1.03	0.36	14.80	1.63	20.67	1.90	19.45	1.71
18	0.92	0.35	32.00	0.55	1.03	0.36	13.03	1.61	18.61	1.87	17.59	1.69
19	-0.36	0.29	30.45	0.33	1.03	0.30	14.09	1.32	19.85	1.54	18.71	1.39
24	0.02	0.25	29.73	0.47	1.03	0.26	19.06	1.18	25.66	1.39	23.95	1.25
27	0.64	0.29	29.29	0.21	1.03	0.30	24.17	1.42	31.64	1.67	29.34	1.50
28	0.21	0.29	30.83	0.34	1.03	0.30	14.98	1.33	20.88	1.55	19.64	1.40
32	0.81	0.50	29.34	0.18	1.03	0.51	24.71	2.46	32.29	2.90	29.92	2.60
35	0.95	0.29	31.11	0.48	1.03	0.30	17.13	1.35	23.39	1.58	21.91	1.42
36	1.52	0.35	30.08	0.21	1.03	0.36	24.68	1.74	32.25	2.05	29.88	1.84

Table A.36: Temperature reconstruction after *Kim and O'Neil* [1997] with $1000 \cdot ln(\alpha_{cc-w}) = 18.03(10^3/T) - 32.42$, *Tremaine et al.* [2011] with $1000 \cdot ln(\alpha_{cc-w}) = 16.1(10^3/T) - 24.6$ and after *Johnston et al.* [2013] with $1000 \cdot ln(\alpha_{cc-w}) = 17.66(10^3/T) - 30.16$. In order to calculate α we averaged the calcite oxygen isotope, measured at a considerably higher resolution than the $\delta^{18}O_{fluid}$ data. Thereby the intervals for averaging the data correspond to the depth errors of the fluid inclusion sample pieces. Both $\delta^{18}O_{fluid}$ and $\delta^{18}O_{calcite}$ are given in VSMOW.

All samples for $\delta^{18}O_{fluid}$ temperature reconstruction compared to SST and lake sediments - LA-1 - Cueva Larga

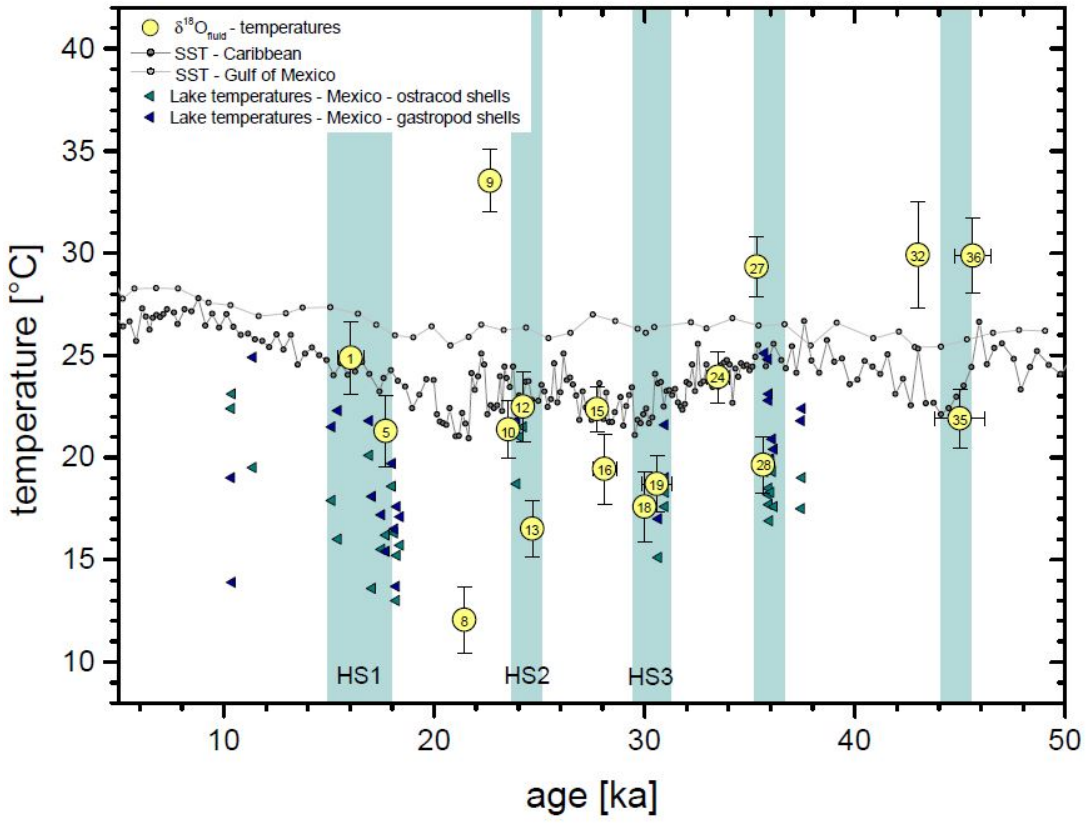

Figure A.42: Fluid inclusion derived temperatures after *Johnston et al.* [2013] as shown in figure 6.11 with all measured samples.

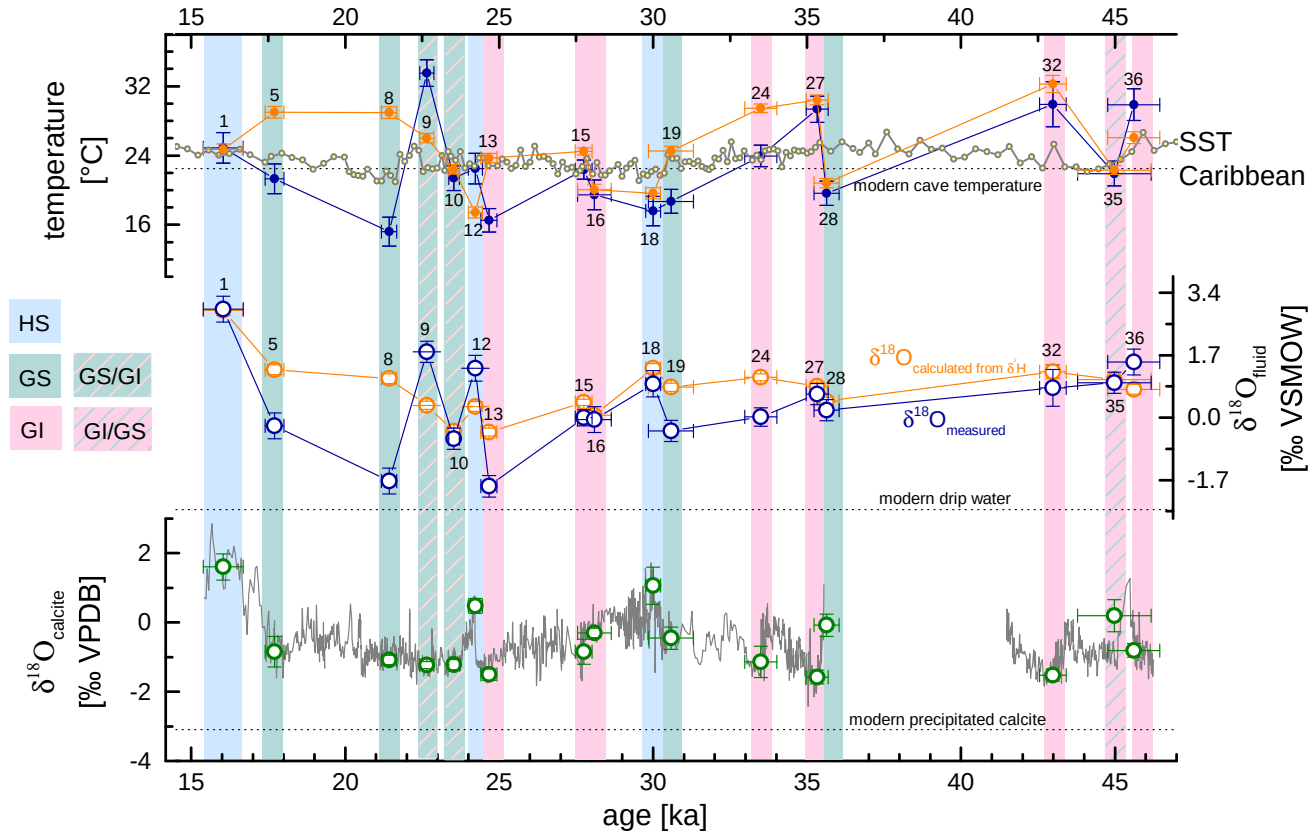

Figure A.43: Comparison between $\delta^{18}O_{fluid}$ and $\delta^{18}O_{based\,on\,\delta^2H}$ with coloured bars in the back identifying the events which can be associated due to the $\delta^{18}O_{calcite}$ signal.

Contents

B List of Figures

C | List of Tables

Bibliography - own publications

The following manuscripts have been published or submitted in peer-reviewed journals and were co-authored by Therese Weissbach. The content of the manuscripts listed here has not been used in this thesis.

- Under submission in peer-reviewed journals
  - Nehme, C., et al. (including Weissbach,T.), Speleothem record from Pentadactylos cave (Cyprus): high-resolution insight into climatic variations during MIS 6 and MIS 5, *Quaternary Science Reviews*, 2020
- Published in peer-reviewed journals
  - Raidla, V., et al. (including Weissbach,T.), Intrusion of Saline Water into a Coastal Aquifer Containing Palaeogroundwater in the Viimsi Peninsula in Estonia. *Geosciences, 9(1)*, 47, 2019.
  - Pärn, J., et al. (including Weissbach,T.), Dating of glacial palaeogroundwater in the Ordovician-Cambrian aquifer system, northern Baltic Artesian Basin. *Applied geochemistry, 102*, 64-76, 2019.
  - Gerber, C., et al. (including Weissbach,T.), Using 81Kr and noble gases to characterize and date groundwater and brines in the Baltic Artesian Basin on the one-million-year timescale. *Geochimica et cosmochimica acta, 205*, 187-210, 2017.

Bibliography

Aemisegger, F., P. Sturm, P. Graf, H. Sodemann, S. Pfahl, A. Knohl, and H. Wernli, Measuring variations of δ^{18}O and δ^{2}H in atmospheric water vapour using two commercial laser-based spectrometers: an instrument characterisation study, *Atmospheric Measurement Techniques*, *5*(7), 1491–1511, 2012.

Aemisegger, F., S. Pfahl, H. Sodemann, I. Lehner, S. I. Seneviratne, and H. Wernli, Deuterium excess as a proxy for continental moisture recycling and plant transpiration, *Atmospheric Chemistry and Physics*, *14*(8), 4029–4054, 2014.

Affek, H. P., M. Bar-Matthews, A. Ayalon, A. Matthews, and J. M. Eiler, Glacial/interglacial temperature variations in Soreq cave speleothems as recorded by 'clumped isotope' thermometry, *Geochimica et Cosmochimica Acta*, *72*(22), 5351–5360, 2008.

Affolter, S., D. Fleitmann, and M. Leuenberger, New-on-line method for water isotope analysis of speleothem fluid inclusions using laser absorption spectroscopy (WS-CRDS), *Climate of the Past*, *10*, 1291–1304, 2014.

Affolter, S., A. D. Häuselmann, D. Fleitmann, P. Häuselmann, and M. Leuenberger, Triple isotope (δD, δ^{17}O, δ^{18}O) study on precipitation, drip water and speleothem fluid inclusions for a Western Central European cave (NW Switzerland), *Quaternary Science Reviews*, *127*, 73–89, 2015.

Affolter, S., A. Häuselmann, D. Fleitmann, R. L. Edwards, H. Cheng, and M. Leuenberger, Central Europe temperature constrained by speleothem fluid inclusion water isotopes over the past 14,000 years, *Science advances*, *5*(6), eaav3809, 2019.

Ampuero, A., et al., The forest effects on the isotopic composition of rainfall in the northwestern amazon basin, *Journal of Geophysical Research: Atmospheres*, p. e2019JD031445, 2020.

Andersen, K. K., et al., High-resolution record of Northern Hemisphere climate extending into the last interglacial period, *Nature*, *431*(7005), 147, 2004.

Arienzo, M. M., P. K. Swart, and H. B. Vonhof, Measurement of δ^{18}O and δ^{2}H values of fluid inclusion water in speleothems using cavity ring-down spectroscopy compared with isotope ratio mass spectrometry, *Rapid Communications in Mass Spectrometry*, *27*(23), 2616–2624, 2013.

Arienzo, M. M., P. K. Swart, A. Pourmand, K. Broad, A. C. Clement, L. N. Murphy, H. B. Vonhof, and B. Kakuk, Bahamian speleothem reveals temperature decrease associated with Heinrich stadials, *Earth and Planetary Science Letters*, *430*, 377–386, 2015.

Arienzo, M. M., P. K. Swart, K. Broad, A. C. Clement, A. Pourmand, and B. Kakuk, Multi-proxy evidence of millennial climate variability from multiple Bahamian speleothems, *Quaternary Science Reviews*, *161*, 18–29, 2017.

Arps, J., Towards ε-precision of U-series age determinations of secondary carbonates, Ph.D. thesis, The Combined Faculties for the Natural Sciences and for Mathematics of the Ruperto-Carola University of Heidelberg, Germany, 2017.

Baker, A., P. L. Smart, R. L. Edwards, and D. A. Richards, Annual growth banding in a cave stalagmite, *Nature*, *364*(6437), 518–520, 1993.

Baker, A., I. Flemons, M. S. Andersen, K. Coleborn, and P. C. Treble, What determines the calcium concentration of speleothem-forming drip waters?, *Global and Planetary Change*, *143*, 152–161, 2016.

Baldini, L. M., F. McDermott, A. M. Foley, and J. U. Baldini, Spatial variability in the European winter precipitation δ^{18}O-NAO relationship: Implications for reconstructing NAO-mode climate variability in the Holocene, *Geophysical Research Letters*, *35*(4), 2008.

Bar-Matthews, M., A. Ayalon, A. Matthews, E. Sass, and L. Halicz, Carbon and oxygen isotope study of the active water-carbonate system in a karstic Mediterranean cave: Implications for paleoclimate research in semiarid regions, *Geochimica et Cosmochimica Acta*, *60*(2), 337–347, 1996.

Bar-Matthews, M., A. Ayalon, A. Kaufman, and G. J. Wasserburg, The Eastern Mediterranean paleoclimate as a reflection of regional events: Soreq cave, Israel, *Earth and Planetary Science Letters*, *166*(1-2), 85–95, 1999.

Baskaran, M., and R. Krishnamurthy, Speleothems as proxy for the carbon isotope composition of atmospheric CO_2, *Geophysical Research Letters*, *20*(24), 2905–2908, 1993.

Benetti, M., G. Reverdin, C. Pierre, L. Merlivat, C. Risi, H. C. Steen-Larsen, and F. Vimeux, Deuterium excess in marine water vapor: Dependency on relative humidity and surface wind speed during evaporation, *Journal of Geophysical Research: Atmospheres*, *119*(2), 584–593, 2014.

Berden, G., R. Peeters, and G. Meijer, Cavity ring-down spectroscopy: Experimental schemes and applications, *International Reviews in Physical Chemistry*, *19*(4), 565–607, 2000.

Beuselinck, L., G. Govers, J. Poesen, G. Degraer, and L. Froyen, Grain-size analysis by laser diffractometry: comparison with the sieve-pipette method, *Catena*, *32*(3-4), 193–208, 1998.

Boch, R., C. Spötl, and S. Frisia, Origin and palaeoenvironmental significance of lamination in stalagmites from Katerloch Cave, Austria, *Sedimentology*, *58*(2), 508–531, 2011.

Böhm, E., et al., Strong and deep Atlantic meridional overturning circulation during the last glacial cycle, *Nature*, *517*(7532), 73–76, 2015.

Böhm, R., P. D. Jones, J. Hiebl, D. Frank, M. Brunetti, and M. Maugeri, The early instrumental warm-bias: a solution for long central European temperature series 1760-2007, *Climatic Change*, *101*(1-2), 41–67, 2010.

Bojariu, R., and D.-M. Paliu, North Atlantic Oscillation projection on Romanian climate fluctuations in the cold season, in *Detecting and Modelling Regional Climate Change*, pp. 345–356, Springer, 2001.

Bond, G., et al., Persistent solar influence on North Atlantic climate during the Holocene, *science*, *294*(5549), 2130–2136, 2001.

Bottinga, Y., and M. Javoy, Comments on oxygen isotope geothermometry, *Earth and Planetary Science Letters*, *20*(2), 250–265, 1973.

Bowen, G. J., and B. Wilkinson, Spatial distribution of δ^{18}O in meteoric precipitation, *Geology*, *30*(4), 315–318, 2002.

Bowen, G. J., Z. Cai, R. P. Fiorella, and A. L. Putman, Isotopes in the water cycle: regional-to global-scale patterns and applications, *Annual Review of Earth and Planetary Sciences*, *47*, 453–479, 2019.

Brand, W. A., H. Geilmann, E. R. Crosson, and C. W. Rella, Cavity ring-down spectroscopy versus high-temperature conversion isotope ratio mass spectrometry; a case study on δ^{2}H and δ^{18}O of pure water samples and alcohol/water mixtures, *Rapid Communications in Mass Spectrometry: An International Journal Devoted to the Rapid Dissemination of Up-to-the-Minute Research in Mass Spectrometry*, *23*(12), 1879–1884, 2009.

Capron, E., et al., Millennial and sub-millennial scale climatic variations recorded in polar ice cores over the last glacial period, *Climate of the Past*, *6*, 345–365, 2010.

Carolin, S. A., K. M. Cobb, J. F. Adkins, B. Clark, J. L. Conroy, S. Lejau, J. Malang, and A. A. Tuen, Varied response of western Pacific hydrology to climate forcings over the last glacial period, *Science*, *340*(6140), 1564–1566, 2013.

Casado, M., et al., Continuous measurements of isotopic composition of water vapour on the East Antarctic Plateau, *Atmospheric Chemistry and Physics*, *16*(13), 8521–8538, 2016.

Chacko, T., and P. Deines, Theoretical calculation of oxygen isotope fractionation factors in carbonate systems, *Geochimica et Cosmochimica Acta*, *72*(15), 3642–3660, 2008.

Cheng, H., et al., Improvements in ^{230}Th dating, ^{230}Th and ^{234}U half-life values, and U-Th isotopic measurements by multi-collector inductively coupled plasma mass spectrometry, *Earth and Planetary Science Letters*, *371*, 82–91, 2013.

Clark, I., and P. Fritz, The environmental isotopes, *Environmental Isotopes in Hydrogeology*, pp. 2–34, 1997.

Clement, A. C., and L. C. Peterson, Mechanisms of abrupt climate change of the last glacial period, *Reviews of Geophysics*, *46*(4), 2008.

Comas-Bru, L., F. McDermott, and M. Werner, The effect of the East Atlantic pattern on the precipitation δ^{18}O-NAO relationship in Europe, *Climate dynamics*, *47*(7-8), 2059–2069, 2016.

Constantin, S., and S. Lauritzen, Speleothem datings in SW Romania. Part 1: evidence for a continuous speleothem growth in Peștera Cloșani during oxygen isotope stages 5–3 and its paleoclimatic significance, *Theor Appl Karstol*, pp. 11–12, 1999.

Coplen, T. B., Reporting of stable hydrogen, carbon, and oxygen isotopic abundances (technical report), *Pure and Applied Chemistry*, *66*(2), 273–276, 1994.

Coplen, T. B., Calibration of the calcite–water oxygen-isotope geothermometer at Devils Hole, Nevada, a natural laboratory, *Geochimica et Cosmochimica Acta*, *71*(16), 3948–3957, 2007.

Coplen, T. B., A. L. Herczeg, and C. Barnes, Isotope engineering—using stable isotopes of the water molecule to solve practical problems, in *Environmental tracers in subsurface hydrology*, pp. 79–110, Springer, 2000.

Cozma, A. I., C. Baciu, D. Papp, G. Roșian, and C.-I. Pop, Isotopic composition of precipitation in western Transylvania (Romania) reflected by two local meteoric water lines, *Carpathian J Earth Environ Sci*, *12*, 357–364, 2017.

Craig, H., Isotopic variations in meteoric waters, *Science*, *133*(3465), 1702–1703, 1961.

Craig, H., and L. I. Gordon, Deuterium and oxygen 18-variations in the ocean and the marine atmosphere, *Stable Isotopes in Oceanographic Studies and Paleotemperatures*, pp. 1–22, 1965.

Czuppon, G., et al., Stable (H, O, C) and noble-gas (He and Ar) isotopic compositions from calcite and fluorite in the Speewah Dome, Kimberley Region, Western Australia: implications for the conditions of crystallization and evidence for the influence of crustal-mantle fluid mixing, *Mineralogy and Petrology*, *108*(6), 759–775, 2014.

Daëron, M., R. N. Drysdale, M. Peral, D. Huyghe, D. Blamart, T. B. Coplen, F. Lartaud, and G. Zanchetta, Most Earth-surface calcites precipitate out of isotopic equilibrium, *Nature communications*, *10*(1), 429, 2019.

Dai, A., I. Y. Fung, and A. D. Del Genio, Surface observed global land precipitation variations during 1900–88, *Journal of climate*, *10*(11), 2943–2962, 1997.

Dansgaard, W., Stable isotopes in precipitation, *Tellus*, *16*(4), 436–468, 1964.

Dansgaard, W., S. Johnsen, H. Clausen, D. Dahl-Jensen, N. Gundestrup, C. Hammer, and H. Oeschger, North Atlantic climatic oscillations revealed by deep Greenland ice cores, *Climate processes and climate sensitivity*, *29*, 288–298, 1984.

Dansgaard, W., J. White, and S. Johnsen, The abrupt termination of the Younger Dryas climate event, *Nature*, *339*(6225), 532–534, 1989.

Dansgaard, W., et al., Evidence for general instability of past climate from a 250-kyr ice-core record, *nature*, *364*(6434), 218–220, 1993.

de Boer, G. B., C. de Weerd, D. Thoenes, and H. W. Goossens, Laser diffraction spectrometry: Fraunhofer diffraction versus Mie scattering, *Particle & Particle Systems Characterization*, *4*(1-4), 14–19, 1987.

Deininger, M., J. Fohlmeister, D. Scholz, and A. Mangini, Isotope disequilibrium effects: The influence of evaporation and ventilation effects on the carbon and oxygen isotope composition of speleothems–A model approach, *Geochimica et Cosmochimica Acta*, *96*, 57–79, 2012.

Demény, A., et al., Stable isotope compositions of speleothems from the last interglacial–Spatial patterns of climate fluctuations in Europe, *Quaternary Science Reviews*, *161*, 68–80, 2017.

Demtröder, W., Neuere Entwicklungen in der Laserspektroskopie, in *Laserspektroskopie 2*, pp. 371–466, Springer, 2013.

Dennis, P., P. Rowe, and T. Atkinson, The recovery and isotopic measurement of water from fluid inclusions in speleothems, *Geochimica et Cosmochimica Acta*, *65*(6), 871–884, 2001.

Denniston, R. F., L. A. González, R. G. Baker, Y. Asmerom, M. K. Reagan, R. L. Edwards, and E. C. Alexander, Speleothem evidence for Holocene fluctuations of the prairie-forest ecotone, north-central USA, *The Holocene*, *9*(6), 671–676, 1999.

Deplazes, G., et al., Links between tropical rainfall and North Atlantic climate during the last glacial period, *Nature Geoscience*, *6*(3), 213–217, 2013.

Diaconu, G., *Closani Cave: Mineralogical and genetic study of carbonates and clays*, Institutul de speologie" Emil Racoviţă", 1990.

Dietzel, M., J. Tang, A. Leis, and S. J. Köhler, Oxygen isotopic fractionation during inorganic calcite precipitation—Effects of temperature, precipitation rate and pH, *Chemical Geology*, *268*(1-2), 107–115, 2009.

Dorale, J. A., and Z. Liu, Limitations of Hendy test criteria in judging the paleoclimatic suitability of speleothems and the need for replication, *Journal of cave and karst studies*, *71*(1), 73–80, 2009.

Dorale, J. A., L. A. González, M. K. Reagan, D. A. Pickett, M. T. Murrell, and R. G. Baker, A high-resolution record of Holocene climate change in speleothem calcite from Cold Water Cave, northeast Iowa, *Science*, *258*(5088), 1626–1630, 1992.

Dredge, J., et al., Cave aerosols: distribution and contribution to speleothem geochemistry, *Quaternary Science Reviews*, *63*, 23–41, 2013.

Dreybrodt, W., Deposition of calcite from thin films of natural calcareous solutions and the growth of speleothems, *Chemical Geology*, *29*(1-4), 89–105, 1980.

Dreybrodt, W., *Processes in karst systems: physics, chemistry, and geology*, vol. 4, Springer Science & Business Media, 2012.

Dreybrodt, W., and M. Deininger, The impact of evaporation to the isotope composition of DIC in calcite precipitating water films in equilibrium and kinetic fractionation models, *Geochimica et Cosmochimica Acta*, *125*, 433–439, 2014.

Dreybrodt, W., and D. Scholz, Climatic dependence of stable carbon and oxygen isotope signals recorded in speleothems: From soil water to speleothem calcite, *Geochimica et Cosmochimica Acta*, *75*(3), 734–752, 2011.

Dublyansky, Y. V., and C. Spötl, Hydrogen and oxygen isotopes of water from inclusions in minerals: design of a new crushing system and on-line continuous-flow isotope ratio mass spectrometric analysis, *Rapid Communications in Mass Spectrometry: An International Journal Devoted to the Rapid Dissemination of Up-to-the-Minute Research in Mass Spectrometry*, *23*(17), 2605–2613, 2009.

Duplessy, J.-C., J. Labeyrie, C. Lalou, and H. Nguyen, Continental climatic variations between 130,000 and 90,000 years BP, *Nature*, *226*(5246), 631–633, 1970.

Edwards, R. L., J. Chen, and G. Wasserburg, ^{238}U-^{234}U-^{230}Th-^{232}Th systematics and the precise measurement of time over the past 500,000 years, *Earth and Planetary Science Letters*, *81*(2-3), 175–192, 1987.

Epstein, S., R. Buchsbaum, H. A. Lowenstam, and H. C. Urey, Revised carbonate-water isotopic temperature scale, *Geological Society of America Bulletin*, *64*(11), 1315–1326, 1953.

Escobar, J., et al., A ∼43-ka record of paleoenvironmental change in the Central American lowlands inferred from stable isotopes of lacustrine ostracods, *Quaternary Science Reviews*, *37*, 92–104, 2012.

Fairchild, I., et al., Speleophysiology: a key to understanding high-resolution information in speleothems, in *Archives of Climate Change in Karst: Proceedings of the Symposium: Climate Change the Karst Record, IV. Karst Waters Institute Special Publication*, vol. 10, p. 249, 2006a.

Fairchild, I. J., and A. Baker, *Speleothem science: from process to past environments*, vol. 3, John Wiley & Sons, 2012.

Fairchild, I. J., and P. C. Treble, Trace elements in speleothems as recorders of environmental change, *Quaternary Science Reviews*, *28*(5-6), 449–468, 2009.

Fairchild, I. J., A. Borsato, A. F. Tooth, S. Frisia, C. J. Hawkesworth, Y. Huang, F. McDermott, and B. Spiro, Controls on trace element (Sr–Mg) compositions of carbonate cave waters: implications for speleothem climatic records, *Chemical Geology*, *166*(3-4), 255–269, 2000.

Fairchild, I. J., G. W. Tuckwell, A. Baker, and A. F. Tooth, Modelling of dripwater hydrology and hydrogeochemistry in a weakly karstified aquifer (Bath, UK): Implications for climate change studies, *Journal of Hydrology*, *321*(1-4), 213–231, 2006b.

Fleitmann, D., S. J. Burns, M. Mudelsee, U. Neff, J. Kramers, A. Mangini, and A. Matter, Holocene forcing of the Indian monsoon recorded in a stalagmite from southern Oman, *science*, *300*(5626), 1737–1739, 2003a.

Fleitmann, D., S. J. Burns, U. Neff, A. Mangini, and A. Matter, Changing moisture sources over the last 330,000 years in Northern Oman from fluid-inclusion evidence in speleothems, *Quaternary Research*, *60*(2), 223–232, 2003b.

Fohlmeister, J., et al., Bunker Cave stalagmites: an archive for central European Holocene climate variability, *Climate of the Past*, *8*(5), 1751–1764, 2012.

Frisia, S., Petrographic evidences of diagenesis in speleothems: some examples, *Speleochronos*, *7*, 21–30, 1996.

Frisia, S., Microstratigraphic logging of calcite fabrics in speleothems as tool for palaeoclimate studies, *International Journal of Speleology*, *44*(1), 1, 2014.

Frisia, S., Stalactites and stalagmites, in *Encyclopedia of Caves*, pp. 1041–1048, Elsevier, 2019.

Frisia, S., and A. Borsato, Chapter 6 Karst, *Developments in Sedimentology*, *61*, 269–318, 2010.

Frisia, S., A. Borsato, I. J. Fairchild, and F. McDermott, Calcite fabrics, growth mechanisms, and environments of formation in speleothems from the Italian Alps and southwestern Ireland, *Journal of Sedimentary Research*, *70*(5), 1183–1196, 2000.

Froehlich, K., J. Gibson, and P. Aggarwal, Deuterium excess in precipitation and its climatological significance, *Tech. rep.*, International Atomic Energy Agency, Vienna (Austria), 2002.

Gao, J., T. Yao, V. Masson-Delmotte, H. C. Steen-Larsen, and W. Wang, Collapsing glaciers threaten Asia's water supplies, 2019.

Gat, J. R., Comments on the stable isotope method in regional groundwater investigations, *Water resources research*, *7*(4), 980–993, 1971.

Gat, J. R., Oxygen and hydrogen isotopes in the hydrologic cycle, *Annual Review of Earth and Planetary Sciences*, *24*(1), 225–262, 1996.

Gat, J. R., and E. Matsui, Atmospheric water balance in the Amazon Basin: an isotopic evapotranspiration model, *Journal of Geophysical Research: Atmospheres*, *96*(D7), 13,179–13,188, 1991.

Gat, J. R., C. J. Bowser, and C. Kendall, The contribution of evaporation from the Great Lakes to the continental atmosphere: estimate based on stable isotope data, *Geophysical Research Letters*, *21*(7), 557–560, 1994.

Genty, D., and Y. Quinif, Annually laminated sequences in the internal structure of some Belgian stalagmites; importance for paleoclimatology, *Journal of Sedimentary Research*, *66*(1), 275–288, 1996.

Genty, D., B. Vokal, B. Obelic, and M. Massault, Bomb ^{14}C time history recorded in two modern stalagmites–importance for soil organic matter dynamics and bomb ^{14}C distribution over continents, *Earth and Planetary Science Letters*, *160*(3-4), 795–809, 1998.

Genty, D., V. Plagnes, C. Causse, O. Cattani, M. Stievenard, S. Falourd, D. Blamart, R. Ouahdi, and S. Van-Exter, Fossil water in large stalagmite voids as a tool for paleoprecipitation stable isotope composition reconstitution and paleotemperature calculation, *Chemical Geology*, *184*(1-2), 83–95, 2002.

Genty, D., et al., Rainfall and cave water isotopic relationships in two South-France sites, *Geochimica et Cosmochimica Acta*, *131*, 323–343, 2014.

Gianfrani, L., G. Gagliardi, M. Van Burgel, and E. T. Kerstel, Isotope analysis of water by means of near-infrared dual-wavelength diode laser spectroscopy, *Optics Express*, *11*(13), 1566–1576, 2003.

Govender, Y., E. Cuevas, L. Sternberg, and M. Jury, Temporal variation in stable isotopic composition of rainfall and groundwater in a tropical dry forest in the northeastern Caribbean, *Earth Interactions*, *17*(27), 1–20, 2013.

Granger, O. E., Caribbean climates, *Progress in Physical Geography*, *9*(1), 16–43, 1985.

Grauel, A.-L., D. A. Hodell, and S. M. Bernasconi, Quantitative estimates of tropical temperature change in lowland Central America during the last 42 ka, *Earth and Planetary Science Letters*, *438*, 37–46, 2016.

Grebe, W., Die Bunkerhöhle in Iserlohn-Letmathe (Sauerland), *Mitteilung des Verbands der deutschen Höhlen-und Karstforscher, München*, *39*(2), 22–23, 1993.

Griffiths, M. L., et al., Younger Dryas–Holocene temperature and rainfall history of southern Indonesia from δ^{18}O in speleothem calcite and fluid inclusions, *Earth and Planetary Science Letters*, *295*(1-2), 30–36, 2010.

Grist, J. P., Easterly waves over Africa. Part I: The seasonal cycle and contrasts between wet and dry years, *Monthly Weather Review*, *130*(2), 197–211, 2002.

Grossman, E. L., T.-L. Ku, et al., Oxygen and carbon isotope fractionation in biogenic aragonite: temperature effects, *Chemical Geology*, *59*(1), 59–74, 1986.

Guan, H., X. Zhang, G. Skrzypek, Z. Sun, and X. Xu, Deuterium excess variations of rainfall events in a coastal area of South Australia and its relationship with synoptic weather systems and atmospheric moisture sources, *Journal of Geophysical Research: Atmospheres*, *118*(2), 1123–1138, 2013.

Gupta, P., D. Noone, J. Galewsky, C. Sweeney, and B. H. Vaughn, Demonstration of high-precision continuous measurements of water vapor isotopologues in laboratory and remote field deployments using wavelength-scanned cavity ring-down spectroscopy (WS-CRDS) technology, *Rapid Communications in Mass Spectrometry: An International Journal Devoted to the Rapid Dissemination of Up-to-the-Minute Research in Mass Spectrometry*, *23*(16), 2534–2542, 2009.

Hansen, M., D. Scholz, B. R. Schöne, and C. Spötl, Simulating speleothem growth in the laboratory: Determination of the stable isotope fractionation (δ^{13}C and δ^{18}O) between H_2O, DIC and $CaCO_3$, *Chemical Geology*, *509*, 20–44, 2019.

Harmon, R. S., H. P. Schwarcz, and D. C. Ford, Stable isotope geochemistry of speleothems and cave waters from the Flint Ridge-Mammoth Cave system, Kentucky: Implications for terrestrial climate change during the period 230,000 to 100,000 years BP, *The Journal of Geology*, *86*(3), 373–384, 1978.

Harmon, R. S., H. P. Schwarcz, and J. R. O'Neil, D/H ratios in speleothem fluid inclusions: a guide to variations in the isotopic composition of meteoric precipitation?, *Earth and Planetary Science Letters*, *42*(2), 254–266, 1979.

Heinrich, H., Origin and consequences of cyclic ice rafting in the northeast Atlantic Ocean during the past 130,000 years, *Quaternary research*, *29*(2), 142–152, 1988.

Hemming, S. R., Heinrich events: Massive late Pleistocene detritus layers of the North Atlantic and their global climate imprint, *Reviews of Geophysics*, *42*(1), 2004.

Hendy, C. H., The isotopic geochemistry of speleothems—I. The calculation of the effects of different modes of formation on the isotopic composition of speleothems and their applicability as palaeoclimatic indicators, *Geochimica et cosmochimica Acta*, *35*(8), 801–824, 1971.

Hill, C., and P. Forti, Cave minerals of the world: Huntsville, *Alabama, National Speleological Society*, pp. 285–287, 1997.

Hodell, D. A., et al., Late Glacial temperature and precipitation changes in the lowland Neotropics by tandem measurement of δ^{18}O in biogenic carbonate and gypsum hydration water, *Geochimica et Cosmochimica Acta*, *77*, 352–368, 2012.

Hoefs, J., *Stable isotope geochemistry*, vol. 285, Springer, 2009.

Hu, H.-y., W.-m. Bao, T. Wang, and S.-m. Qu, Experimental study on stable isotopic fractionation of evaporating water under varying temperature, *Water Science and Engineering*, *2*(2), 11–18, 2009.

Hurrell, J. W., Decadal trends in the North Atlantic Oscillation: regional temperatures and precipitation, *Science*, *269*(5224), 676–679, 1995.

IPCC, *Climate Change 2013: The Physical Science Basis. Contribution of Working Group I to the Fifth Assessment Report of the Intergovernmental Panel on Climate Change*, 1535 pp., Cambridge University Press, Cambridge, United Kingdom and New York, NY, USA, doi:10.1017/CBO9781107415324, 2013.

ISMATEC, *Tygon R-3603/R-3607 - Special properties*, `http://www.ismatec.com/int_e/tubing/misc/e_tygon_st.htm`, accessed January 09, 2020).

Johnston, V., A. Borsato, C. Spötl, S. Frisia, and R. Miorandi, Stable isotopes in caves over altitudinal gradients: fractionation behaviour and inferences for speleothem sensitivity to climate change, *Climate of the Past*, *9*(1), 99, 2013.

Jones, P. D., T. Jónsson, and D. Wheeler, Extension to the North Atlantic Oscillation using early instrumental pressure observations from Gibraltar and south-west Iceland, *International Journal of Climatology: A Journal of the Royal Meteorological Society*, *17*(13), 1433–1450, 1997.

Jouzel, J., M. Stievenard, S. J. Johnsen, A. Landais, V. Masson-Delmotte, A. Sveinbjornsdottir, F. Vimeux, U. Von Grafenstein, and J. W. White, The GRIP deuterium-excess record, *Quaternary Science Reviews*, *26*(1-2), 1–17, 2007.

Kendall, A. C., and P. L. Broughton, Origin of fabrics in speleothems composed of columnar calcite crystals, *Journal of Sedimentary Research*, *48*(2), 519–538, 1978.

Kim, S.-T., and J. R. O'Neil, Equilibrium and nonequilibrium oxygen isotope effects in synthetic carbonates, *Geochimica et cosmochimica acta*, *61*(16), 3461–3475, 1997.

Kim, S.-T., T. B. Coplen, and J. Horita, Normalization of stable isotope data for carbonate minerals: Implementation of IUPAC guidelines, *Geochimica et cosmochimica acta*, *158*, 276–289, 2015.

Klein Tank, A., et al., Daily dataset of 20th-century surface air temperature and precipitation series for the European Climate Assessment, *International Journal of Climatology: A Journal of the Royal Meteorological Society*, *22*(12), 1441–1453, 2002.

Kluge, T., and H. P. Affek, Quantifying kinetic fractionation in Bunker Cave speleothems using Δ_{47}, *Quaternary Science Reviews*, *49*, 82–94, 2012.

Kluge, T., T. Marx, D. Scholz, S. Niggemann, A. Mangini, and W. Aeschbach-Hertig, A new tool for palaeoclimate reconstruction: Noble gas temperatures from fluid inclusions in speleothems, *Earth and Planetary Science Letters*, *269*(3-4), 408–415, 2008.

Kluge, T., D. Riechelmann, M. Wieser, C. Spötl, J. Sültenfuß, A. Schröder-Ritzrau, S. Niggemann, and W. Aeschbach-Hertig, Dating cave drip water by tritium, *Journal of Hydrology*, *394*(3-4), 396–406, 2010.

Koster, R. D., D. P. De Valpine, and J. Jouzel, Continental water recycling and $H_2^{18}O$ concentrations, *Geophysical Research Letters*, *20*(20), 2215–2218, 1993.

Krichak, S., and P. Alpert, Signatures of the NAO in the atmospheric circulation during wet winter months over the Mediterranean region, *Theoretical and Applied Climatology*, *82*(1-2), 27–39, 2005.

Krüger, Y., D. Marti, R. H. Staub, D. Fleitmann, and M. Frenz, Liquid–vapour homogenisation of fluid inclusions in stalagmites: Evaluation of a new thermometer for palaeoclimate research, *Chemical geology*, *289*(1-2), 39–47, 2011.

Lachniet, M. S., Climatic and environmental controls on speleothem oxygen-isotope values, *Quaternary Science Reviews*, *28*(5-6), 412–432, 2009.

Lachniet, M. S., L. Johnson, Y. Asmerom, S. J. Burns, V. Polyak, W. P. Patterson, L. Burt, and A. Azouz, Late Quaternary moisture export across Central America and to Greenland: evidence for tropical rainfall variability from Costa Rican stalagmites, *Quaternary Science Reviews*, *28*(27-28), 3348–3360, 2009.

Leng, M. J., *Isotopes in palaeoenvironmental research*, vol. 10, Springer, 2006.

Levanič, T., I. Popa, S. Poljanšek, and C. Nechita, A 323-year long reconstruction of drought for SW Romania based on black pine (Pinus nigra) tree-ring widths, *International journal of biometeorology*, *57*(5), 703–714, 2013.

Lewis, S. C., et al., High-resolution stalagmite reconstructions of Australian–Indonesian monsoon rainfall variability during Heinrich stadial 3 and Greenland interstadial 4, *Earth and Planetary Science Letters*, *303*(1-2), 133–142, 2011.

Lis, G., L. Wassenaar, and M. Hendry, High-precision laser spectroscopy D/H and $^{18}O/^{16}O$ measurements of microliter natural water samples, *Analytical chemistry*, *80*(1), 287–293, 2008.

maps for free, *Topographic map of Puerto Rico*, `https://maps-for-free.com/`, accessed January 26, 2020).

Masson-Delmotte, V., J. Jouzel, A. Landais, M. Stievenard, S. J. Johnsen, J. White, M. Werner, A. Sveinbjornsdottir, and K. Fuhrer, GRIP deuterium excess reveals rapid and orbital-scale changes in Greenland moisture origin, *Science*, *309*(5731), 118–121, 2005.

Matthews, A., A. Ayalon, and M. Bar-Matthews, D/H ratios of fluid inclusions of Soreq cave (Israel) speleothems as a guide to the Eastern Mediterranean Meteoric Line relationships in the last 120 ky, *Chemical Geology*, *166*(3-4), 183–191, 2000.

Mayewski, P. A., et al., Holocene climate variability, *Quaternary research*, *62*(3), 243–255, 2004.

McCrea, J. M., On the isotopic chemistry of carbonates and a paleotemperature scale, *The Journal of Chemical Physics*, *18*(6), 849–857, 1950.

McDermott, F., Palaeo-climate reconstruction from stable isotope variations in speleothems: a review, *Quaternary Science Reviews*, *23*(7-8), 901–918, 2004.

McDermott, F., H. Schwarcz, and P. J. Rowe, Isotopes in speleothems, in *Isotopes in palaeoenvironmental research*, pp. 185–225, Springer, 2006.

McGarry, S., M. Bar-Matthews, A. Matthews, A. Vaks, B. Schilman, and A. Ayalon, Constraints on hydrological and paleotemperature variations in the Eastern Mediterranean region in the last 140 ka given by the δD values of speleothem fluid inclusions, *Quaternary Science Reviews*, *23*(7-8), 919–934, 2004.

Meckler, A. N., et al., Glacial–interglacial temperature change in the tropical West Pacific: A comparison of stalagmite-based paleo-thermometers, *Quaternary Science Reviews*, *127*, 90–116, 2015.

Merlivat, L., and J. Jouzel, Global climatic interpretation of the deuterium-oxygen 18 relationship for precipitation, *Journal of Geophysical Research: Oceans*, *84*(C8), 5029–5033, 1979.

Mickler, P. J., J. L. Banner, L. Stern, Y. Asmerom, R. L. Edwards, and E. Ito, Stable isotope variations in modern tropical speleothems: evaluating equilibrium vs. kinetic isotope effects, *Geochimica et Cosmochimica Acta*, *68*(21), 4381–4393, 2004.

Micu, D. M., A. Dumitrescu, S. Cheval, and M.-V. Birsan, *Climate of the Romanian Carpathians*, Springer, 2016.

Miller, T., Stream pirates of the Caribbean: Tanamá and Camuy Rivers in the northern karst of Puerto Rico, *Espeleorevista Puerto Rico*, *2*, 8–13, 2010.

Millo, C., N. M. Strikis, H. B. Vonhof, M. Deininger, F. W. da Cruz Jr, X. Wang, H. Cheng, and R. L. Edwards, Last glacial and Holocene stable isotope record of fossil dripwater from subtropical Brazil based on analysis of fluid inclusions in stalagmites, *Chemical Geology*, *468*, 84–96, 2017.

Ministry of Environment and Climate Change, Romania's Sixth National Communication on Climate Change and First Biennial Report, *Climate Report*, p. 44, 2013.

Monroe, W. H., *Some tropical landforms of Puerto Rico*, US Government Printing Office, 1980.

Mook, W., and K. Rozanski, Environmental isotopes in the hydrological cycle, *IAEA Publish*, *39*, 2000.

Moore, G., Speleothem — a new cave term, *National Speleological Society News*, *10*(6), 2, 1952.

Mühlinghaus, C., D. Scholz, and A. Mangini, Modelling stalagmite growth and δ^{13}C as a function of drip interval and temperature, *Geochimica et Cosmochimica Acta*, *71*(11), 2780–2790, 2007.

Mühlinghaus, C., D. Scholz, and A. Mangini, Modelling fractionation of stable isotopes in stalagmites, *Geochimica et Cosmochimica Acta*, *73*(24), 7275–7289, 2009.

Münsterer, C., J. Fohlmeister, M. Christl, A. Schröder-Ritzrau, V. Alfimov, S. Ivy-Ochs, A. Wackerbarth, and A. Mangini, Cosmogenic ^{36}Cl in karst waters from Bunker Cave North Western Germany–A tool to derive local evapotranspiration?, *Geochimica et Cosmochimica Acta*, *86*, 138–149, 2012.

Niggemann, S., A. Mangini, M. Mudelsee, D. K. Richter, and G. Wurth, Sub-Milankovitch climatic cycles in Holocene stalagmites from Sauerland, Germany, *Earth and Planetary Science Letters*, *216*(4), 539–547, 2003a.

Niggemann, S., A. Mangini, D. K. Richter, and G. Wurth, A paleoclimate record of the last 17,600 years in stalagmites from the B7 cave, Sauerland, Germany, *Quaternary Science Reviews*, *22*(5-7), 555–567, 2003b.

Oltmans, S., and D. Hofmann, Increase in lower-stratospheric water vapour at a mid-latitude Northern Hemisphere site from 1981 to 1994, *Nature*, *374*(6518), 146–149, 1995.

Peterson, L. C., G. H. Haug, K. A. Hughen, and U. Röhl, Rapid changes in the hydrologic cycle of the tropical Atlantic during the last glacial, *Science*, *290*(5498), 1947–1951, 2000.

Pfahl, S., and H. Sodemann, What controls deuterium excess in global precipitation?, *Climate of the Past*, *10*(2), 771–781, 2014.

Pfahl, S., and H. Wernli, Air parcel trajectory analysis of stable isotopes in water vapor in the eastern Mediterranean, *Journal of Geophysical Research: Atmospheres*, *113*(D20), 2008.

Picarro, *L2130i Analyzer Datasheet*, Picarro, Inc., picarro Certificate of Compliance, 2015.

Picarro, *Cavity Ring-Down Spectroscopy (CRDS)*, `https://www.picarro.com/company/technology/crds`, accessed February 28, 2020).

Popa, I., and Z. Kern, Long-term summer temperature reconstruction inferred from tree-ring records from the Eastern Carpathians, *Climate dynamics*, *32*(7-8), 1107–1117, 2009.

Prokhorov, I., T. Kluge, and C. Janssen, Optical clumped isotope thermometry of carbon dioxide, *Scientific reports*, *9*(1), 1–11, 2019.

Rayleigh, L., L. Theoretical considerations respecting the separation of gases by diffusion and similar processes, *The London, Edinburgh, and Dublin Philosophical Magazine and Journal of Science*, *42*(259), 493–498, 1896.

Richards, D. A., and J. A. Dorale, Uranium-series chronology and environmental applications of speleothems, *Reviews in Mineralogy and Geochemistry*, *52*(1), 407–460, 2003.

Riechelmann, D. F., Aktuospeläologische Untersuchungen in der Bunkerhöhle des Iserlohner Massenkalks (NRW/Deutschland): Signifikanz für kontinentale Klimaarchive, Dissertation, Fakultät für Geowissenschaften der Ruhr-Universität Mainz, 2010.

Riechelmann, D. F. C., A. Schröder-Ritzrau, D. Scholz, J. Fohlmeister, C. Spötl, D. K. Richter, and A. Mangini, Monitoring Bunker Cave (NW Germany): A prerequisite to interpret geochemical proxy data of speleothems from this site, *Journal of Hydrology*, *409*(3-4), 682–695, 2011.

Riechelmann, D. F. C., M. Deininger, D. Scholz, S. Riechelmann, A. Schröder-Ritzrau, C. Spötl, D. K. Richter, A. Mangini, and A. Immenhauser, Disequilibrium carbon

and oxygen isotope fractionation in recent cave calcite: Comparison of cave precipitates and model data, *Geochimica et Cosmochimica Acta*, *103*, 232–244, 2013.

Riechelmann, S., A. Schröder-Ritzrau, C. Spötl, D. F. C. Riechelmann, D. K. Richter, A. Mangini, N. Frank, S. F. Breitenbach, and A. Immenhauser, Sensitivity of Bunker Cave to climatic forcings highlighted through multi-annual monitoring of rain-, soil-, and dripwaters, *Chemical Geology*, *449*, 194–205, 2017.

Risi, C., D. Noone, C. Frankenberg, and J. Worden, Role of continental recycling in intraseasonal variations of continental moisture as deduced from model simulations and water vapor isotopic measurements, *Water Resources Research*, *49*(7), 4136–4156, 2013.

Roberts, M. S., P. L. Smart, and A. Baker, Annual trace element variations in a Holocene speleothem, *Earth and Planetary Science Letters*, *154*(1-4), 237–246, 1998.

Rohling, E. J., Oxygen isotope composition of seawater, *The Encyclopedia of Quaternary Science. Amsterdam: Elsevier*, *2*, 915–922, 2013.

Rozanski, K., L. Araguas-Araguas, and R. Gonfiantini, Relation between long-term trends of oxygen-18 isotope composition of precipitation and climate, *Science*, *258*(5084), 981–985, 1992.

Rozanski, K., L. Araguás-Araguás, and R. Gonfiantini, Isotopic patterns in modern global precipitation, *Climate change in continental isotopic records*, *78*, 1–36, 1993.

Salati, E., A. Dall'Olio, E. Matsui, and J. R. Gat, Recycling of water in the Amazon basin: an isotopic study, *Water resources research*, *15*(5), 1250–1258, 1979.

Schauble, E. A., P. Ghosh, and J. M. Eiler, Preferential formation of ^{13}C–^{18}O bonds in carbonate minerals, estimated using first-principles lattice dynamics, *Geochimica et Cosmochimica Acta*, *70*(10), 2510–2529, 2006.

Scheidegger, Y., H. Baur, M. S. Brennwald, D. Fleitmann, R. Wieler, and R. Kipfer, Accurate analysis of noble gas concentrations in small water samples and its application to fluid inclusions in stalagmites, *Chemical Geology*, *272*(1-4), 31–39, 2010.

Schellekens, J., F. Scatena, L. Bruijnzeel, A. Van Dijk, M. Groen, and R. Van Hogezand, Stormflow generation in a small rainforest catchment in the Luquillo Experimental Forest, Puerto Rico, *Hydrological Processes*, *18*(3), 505–530, 2004.

Schmidt, M., K. Maseyk, C. Lett, P. Biron, P. Richard, T. Bariac, and U. Seibt, Concentration effects on laser-based $\delta^{18}O$ and $\delta^{2}H$ measurements and implications for the calibration of vapour measurements with liquid standards, *Rapid Communications in Mass Spectrometry*, *24*(24), 3553–3561, 2010.

Schmidt, M. W., H. J. Spero, and D. W. Lea, Links between salinity variation in the Caribbean and North Atlantic thermohaline circulation, *Nature*, *428*(6979), 160–163, 2004.

Scholl, M. A., and S. F. Murphy, Precipitation isotopes link regional climate patterns to water supply in a tropical mountain forest, eastern Puerto Rico, *Water Resources Research*, *50*(5), 4305–4322, 2014.

Scholl, M. A., J. B. Shanley, J. P. Zegarra, and T. B. Coplen, The stable isotope amount effect: New insights from NEXRAD echo tops, Luquillo Mountains, Puerto Rico, *Water Resources Research*, *45*(12), 2009.

Scholz, D., and D. Hoffmann, ^{230}Th/U-dating of fossil corals and speleothems, *Quat. Sci. J*, *57*(1-2), 52–76, 2008.

Scholz, D., and D. L. Hoffmann, StalAge–An algorithm designed for construction of speleothem age models, *Quaternary Geochronology*, *6*(3-4), 369–382, 2011.

Schwarcz, H. P., R. S. Harmon, P. Thompson, and D. C. Ford, Stable isotope studies of fluid inclusions in speleothems and their paleoclimatic significance, *Geochimica et Cosmochimica Acta*, *40*(6), 657–665, 1976.

Shen, C.-C., K. Lin, W. Duan, X. Jiang, J. W. Partin, R. L. Edwards, H. Cheng, and M. Tan, Testing the annual nature of speleothem banding, *Scientific reports*, *3*, 2633, 2013.

Siegenthaler, U., and H. Oeschger, Correlation of ^{18}O in precipitation with temperature and altitude, *Nature*, *285*(5763), 314, 1980.

Sinclair, D. J., et al., Magnesium and strontium systematics in tropical speleothems from the Western Pacific, *Chemical Geology*, *294*, 1–17, 2012.

Sonntag, C., K. Muennich, C. Junghans, E. Klitzsch, U. Thorweihe, K. Weistroffer, E. Loehnert, E. El-Shazly, and F. Swailem, Palaeoclimatic information from deuterium and oxygen-18 in carbon-14-dated north Saharian groundwaters. Groundwater formation in the past, in *Isotope hydrology 1978*, International Atomic Energy Agency (IAEA), 1979.

Stoll, H. M., W. Müller, and M. Prieto, I-STAL, a model for interpretation of Mg/Ca, Sr/Ca and Ba/Ca variations in speleothems and its forward and inverse application on seasonal to millennial scales, *Geochemistry, Geophysics, Geosystems*, *13*(9), 2012.

Stríkis, N. M., et al., Abrupt variations in South American monsoon rainfall during the Holocene based on a speleothem record from central-eastern Brazil, *Geology*, *39*(11), 1075–1078, 2011.

Taylor, M. A., D. B. Enfield, and A. A. Chen, Influence of the tropical Atlantic versus the tropical Pacific on Caribbean rainfall, *Journal of Geophysical Research: Oceans*, *107*(C9), 10–1, 2002.

The University of Auckland, S. o. E., *World Map of Carbonate Rock Outcrops*, `https://www.fos.auckland.ac.nz/our_research/karst/index.html`, accessed March 20, 2020).

Tremaine, D. M., P. N. Froelich, and Y. Wang, Speleothem calcite farmed in situ: Modern calibration of δ^{18}O and δ^{13}C paleoclimate proxies in a continuously-monitored natural cave system, *Geochimica et Cosmochimica Acta*, *75*(17), 4929–4950, 2011.

Trouet, V., J. Esper, N. E. Graham, A. Baker, J. D. Scourse, and D. C. Frank, Persistent positive North Atlantic Oscillation mode dominated the medieval climate anomaly, *science*, *324*(5923), 78–80, 2009.

Uemura, R., Y. Matsui, K. Yoshimura, H. Motoyama, and N. Yoshida, Evidence of deuterium excess in water vapor as an indicator of ocean surface conditions, *Journal of Geophysical Research: Atmospheres*, *113*(D19), 2008.

Uemura, R., E. Barkan, O. Abe, and B. Luz, Triple isotope composition of oxygen in atmospheric water vapor, *Geophysical research letters*, *37*(4), 2010.

Uemura, R., Y. Kina, C.-C. Shen, and K. Omine, Experimental evaluation of oxygen isotopic exchange between inclusion water and host calcite in speleothems, *Climate of the Past*, *16*(1), 17–27, 2020.

Uemura, R., et al., Precise oxygen and hydrogen isotope determination in nanoliter quantities of speleothem inclusion water by cavity ring-down spectroscopic techniques, *Geochimica et Cosmochimica Acta*, *172*, 159–176, 2016.

Urey, H. C., Oxygen isotopes in nature and in the laboratory, *Science*, *108*(2810), 489–496, 1948.

Van Breukelen, M., H. Vonhof, J. Hellstrom, W. Wester, and D. Kroon, Fossil dripwater in stalagmites reveals Holocene temperature and rainfall variation in Amazonia, *Earth and Planetary Science Letters*, *275*(1-2), 54–60, 2008.

Varsányi, I., L. Palcsu, and L. Ó. Kovács, Groundwater flow system as an archive of palaeotemperature: noble gas, radiocarbon, stable isotope and geochemical study in the Pannonian Basin, Hungary, *Applied Geochemistry*, *26*(1), 91–104, 2011.

Vidiani, *Large topographical map of Romania*, `http://www.vidiani.com/large-topographical-map-of-romania/`, accessed November 17, 2019).

Vieten, R., A. Winter, S. F. Warken, A. Schröder-Ritzrau, T. E. Miller, and D. Scholz, Seasonal temperature variations controlling cave ventilation processes in Cueva Larga, Puerto Rico, *International Journal of Speleology*, *45*(3), 7, 2016.

Vieten, R., S. Warken, A. Winter, D. Scholz, T. Miller, C. Spötl, and A. Schröder-Ritzrau, Monitoring of Cueva Larga, Puerto Rico — A first step to decode speleothem climate records, in *Karst Groundwater Contamination and Public Health*, pp. 319–331, Springer, 2018.

Vodila, G., L. Palcsu, I. Futó, and Z. Szántó, A 9-year record of stable isotope ratios of precipitation in Eastern Hungary: Implications on isotope hydrology and regional palaeoclimatology, *Journal of Hydrology*, *400*(1-2), 144–153, 2011.

Vogel, N., Y. Scheidegger, M. Brennwald, D. Fleitmann, S. Figura, R. Wieler, and R. Kipfer, Stalagmite water content as a proxy for drip water supply in tropical and subtropical areas, *Climate of the Past*, *9*(1), 1–12, 2013.

von Freyberg, J., B. Studer, and J. W. Kirchner, A lab in the field: high-frequency analysis of water quality and stable isotopes in stream water and precipitation, *Hydrology and Earth System Sciences*, *21*, 1721–1739, 2017.

Vonhof, H. B., M. R. van Breukelen, O. Postma, P. J. Rowe, T. C. Atkinson, and D. Kroon, A continuous-flow crushing device for on-line δ^2H analysis of fluid inclusion water in speleothems, *Rapid Communications in Mass Spectrometry: An International Journal Devoted to the Rapid Dissemination of Up-to-the-Minute Research in Mass Spectrometry*, *20*(17), 2553–2558, 2006.

Wackerbarth, A., D. Scholz, J. Fohlmeister, and A. Mangini, Modelling the δ^{18}O value of cave drip water and speleothem calcite, *Earth and Planetary Science Letters*, *299*(3-4), 387–397, 2010.

Wackerbarth, A. K., Towards a better understanding of climate proxies in stalagmites-Modelling processes from surface to cave, Dissertation, The Combined Faculties for the Natural Sciences and for Mathematics of the Ruperto-Carola University of Heidelberg, Germany, 2011.

Waelbroeck, C., L. Labeyrie, E. Michel, J. C. Duplessy, J. McManus, K. Lambeck, E. Balbon, and M. Labracherie, Sea-level and deep water temperature changes derived from benthic foraminifera isotopic records, *Quaternary Science Reviews*, *21*(1-3), 295–305, 2002.

Wang, Y.-J., H. Cheng, R. L. Edwards, Z. An, J. Wu, C.-C. Shen, and J. A. Dorale, A high-resolution absolute-dated late Pleistocene monsoon record from Hulu Cave, China, *Science*, *294*(5550), 2345–2348, 2001.

Wanner, H., S. Brönnimann, C. Casty, D. Gyalistras, J. Luterbacher, C. Schmutz, D. B. Stephenson, and E. Xoplaki, North Atlantic Oscillation–concepts and studies, *Surveys in geophysics*, *22*(4), 321–381, 2001.

Wanner, H., O. Solomina, M. Grosjean, S. P. Ritz, and M. Jetel, Structure and origin of Holocene cold events, *Quaternary Science Reviews*, *30*(21-22), 3109–3123, 2011.

Warken, S. F., Potentials and limitations of multi-proxy records in speleothem research - Case studies in complex climate systems, Dissertation, The Combined Faculties for the Natural Sciences and for Mathematics of the Ruperto-Carola University of Heidelberg, Germany, 2017.

Warken, S. F., R. Vieten, A. Winter, C. Spötl, T. E. Miller, K. P. Jochum, A. Schröder-Ritzrau, A. Mangini, and D. Scholz, Persistent link between Caribbean precipitation and Atlantic Ocean circulation during the Last Glacial revealed by a speleothem record from Puerto Rico, *Earth and Space Science Open Archive*, p. 30, doi:10.1002/essoar.10502676.1, 2020.

Warken, S. F., et al., Reconstruction of late Holocene autumn/winter precipitation variability in SW Romania from a high-resolution speleothem trace element record, *Earth and Planetary Science Letters*, *499*, 122–133, 2018.

Wassenaar, L., S. Terzer-Wassmuth, C. Douence, L. Araguas-Araguas, P. Aggarwal, and T. B. Coplen, Seeking excellence: An evaluation of 235 international laboratories conducting water isotope analyses by isotope-ratio and laser-absorption spectrometry, *Rapid Communications in Mass Spectrometry*, *32*(5), 393–406, 2018.

Watkins, J., and J. Hunt, A process-based model for non-equilibrium clumped isotope effects in carbonates, *Earth and Planetary Science Letters*, *432*, 152–165, 2015.

Wikimedia, *Caribbean Sea Gulf of Mexico shaded relief bathymetry land map*, `https://commons.wikimedia.org/wiki/File:Caribbean_Sea_Gulf_of_Mexico_shaded_relief_bathymetry_land_map.png`, accessed January 26, 2020).

Winter, A., et al., Initiation of a stable convective hydroclimatic regime in Central America circa 9000 years BP, *Nature Communications*, *11*(1), 1–8, 2020.

WRI, W. R. I., *Aqueduct - Water Risk Atlas*, `https://www.wri.org/aqueduct`, accessed March 19, 2020).

Wurth, G., Klimagesteuerte Rhythmik in spät-bis postglazialen Stalagmiten des Sauerlandes, der Fränkischen Alb und der Bayerischen Alpen, Dissertation, Fakultät für Geowissenschaften der Ruhr-Universität Bochum, 2003.

Yonge, C. J., Stable isotope studies of water extracted from speleothems, Dissertation, McMaster University, 1982.

Yonge, C. J., D. Ford, J. Gray, and H. Schwarcz, Stable isotope studies of cave seepage water, *Chemical Geology: Isotope Geoscience Section*, *58*(1-2), 97–105, 1985.

Yu, T., and M. Lin, Kinetics of phenyl radical reactions studied by the cavity-ring-down method, *Journal of the American Chemical Society*, *115*(10), 4371–4372, 1993.

Zalicki, P., and R. N. Zare, Cavity ring-down spectroscopy for quantitative absorption measurements, *The Journal of chemical physics*, *102*(7), 2708–2717, 1995.

Ziegler, M., D. Nürnberg, C. Karas, R. Tiedemann, and L. J. Lourens, Persistent summer expansion of the Atlantic Warm Pool during glacial abrupt cold events, *Nature Geoscience*, *1*(9), 601–605, 2008.

Acknowledgments

Ich möchte mich zuerst bei Tobias Kluge bedanken, der mir dir Möglichkeit gegeben hat in seiner Nachwuchsgruppe zu promovieren. Vielen lieben Dank Tobias, dass Du dir immer die Zeit genommen hast mit mir über die technischen Details und Interpretationen zu diskutieren. Dein Verständnis und die Kommunikation auf Augenhöhe gaben mir die Möglichkeit sehr frei und selbstbestimmt meinen Weg zu gehen. Dafür möchte ich Dir von Herzen danken.
Danken, möchte ich auch Norbert Frank, der das zweite Gutachten übernommen hat und mich auch im Entstehungsprozess dieser Arbeit begleitet und immer unterstützt hat. Dafür möchte ich Dir danken und bin sehr froh, dass mir Deine Tür immer offenstand.
Ein weiteres Dankeschön möchte ich Werner Aeschbach aussprechen, mit dessen Gruppe ich seit meiner Masterarbeit sehr verbunden bin und der mich nicht nur in der Zeit des Antragschreibens, sondern auch während und in der Zeit des Abschlusses sehr unterstützt hat. Vielen Dank Werner, dass Du diese Idee für die Arbeit hattest und ich immer noch eine HydroTraperin bin, obwohl ich den Edelgasen den Rücken zugekehrt habe. Ohne Dich wäre diese Arbeit so nicht entstanden.
Danke auch an Prof. Dr. S. Hansmann - Menzemer und Jun. - Prof. Dr. S. Westhoff, dass sie sich bereit erklärt haben, Teil meines mündlichen Prüfungskomitees zu sein.
For the technical part of this thesis, I would like to thank Stéphane Affolter and Hubert Vonhof in particular. Thank you, Stéphane, for sharing your secret technical "hacks" with me and thank you, Hubert, for the comparative measurements and the helpful discussions in the laboratory.
Martina Schmidt möchte ich für die Messung der Wasserstandards und für all die beantworteten Fragen bezüglich CRDS Systemen danken. Vielen Dank Martina, dass Du immer ein offenes Ohr für mich hattest. Für die Partikelgrößen Analyse möchte ich mich bei André Bahr bedanken. Vielen Dank, dass ich das so unkompliziert durchführen konnte und vielen Dank, dass Du dir so viel Zeit für mich genommen hast.
In diese Arbeit sind eine Menge Kooperationspartner miteingeschlossen, ohne die ich nicht die Möglichkeit gehabt hätte so tolle Stalagmiten vermessen zu können. Zuerst einmal möchte ich mich bei Dana Riechelmann bedanken, dass sie mir die Möglichkeit gegeben hat an dem rumänischen Stalagmiten zu arbeiten. Vielen Dank Dana, für das unkomplizierte Bereitstellen aller notwendigen Daten und das Beantworten vieler E-Mails und persönlicher Fragen. In diesem Zuge möchte mich auch sehr bei Sophie Warken bedanken, die mir den tropischen Stalagmiten zur Verfügung gestellt hat und darüber hinaus viele Proben gesägt und noch viel mehr Stunden mit mir über die Ergebnisse der Messung gegrübelt und diskutiert hat. Vielen Dank Sophie, das war eine wirklich schöne Zeit und Zusammenarbeit mit Dir und tausend Dank für Dein sehr intensives Korrekturlesen. Ich möchte mich auch bei Andrea Schröder-Ritzrau bedanken, die mir viele Informationen über die Bunker Höhle hat zukommen lassen

und mir genauso lange grundlegend die "speleothem science" erklärt hat. Vielen Dank liebe Andrea, dass Du dir so viel Zeit für mich genommen hast und auch für das Korrekturlesen (und natürlich für den gemeinsamen Kaffeedienst). Jens Fohlmeister möchte ich danken, für seine Anmerkungen und Diskussionen zu den Ergebnissen von Bu4, vielen Dank Jens für Dein detailliertes Korrekturlesen. Weitere Menschen die mir sehr geholfen haben, den schriftlichen Teil dieser Arbeit besser zu machen sind meine Schwester, Arne, Sanam, Steffen und Halua. Vielen lieben Dank dafür. An dieser Stelle möchte ich mich noch bei Marie-Christin Juhl, die bei der Messung der Closani Proben im Rahmen ihrer Bachelorarbeit mitgeholfen hat und Benedikt Hemmer, mit welchem ich das Auswertungsprotokoll entwickelt habe, herzlich bedanken.

Dann gibt es noch viele liebe Menschen am IUP, die mir mein Arbeitsleben am Institut sehr angenehm gestaltet haben, sei es beim gemeinsamen Mittagessen oder den vielen Kaffee Pausen. Danke an die „HydroTraper“ und die „Environmental Archives“ Leute, dass ich Teil Eurer beiden Gruppen sein durfte. Danke auch an all die, die schon vor mir das IUP verlassen haben (Sanam, Patrick, Jan, Philipp, Lara, Jenny, Freya, Simon und Sabrina).
Natürlich auch ein großes Dankeschön an all meine Freunde außerhalb des IUPs. Danke, dass ihr trotz meiner sozialen Abstinenz der letzten (vielen) Monate noch meine Freude seid. Natürlich möchte ich mich bei meiner Familie bedanken, die hier an letzter Stelle genannt wird, die aber nichtsdestotrotz einen großen Anteil am Gelingen dieser Arbeit hat. Vielen Dank lieber Opa, für dein Interesse und deine Neugier an meiner Arbeit und vielen Dank für deine Unterstützung über all die Jahre. Caro, mein liebes Schwesterherz, vielen Dank für dein Korrekturlesen und dein offenes Ohr, wenn ich mal keine Lust hatte noch weiter zu promovieren. Und ganz besonders möchte ich meinem Mann danken. Danke Jörg, dass du mir immer den Rücken freigehalten hast und viele, (sehr) viele Familientage geopfert hast, damit ich in Ruhe schreiben kann. Ohne dich hätte ich das alles nicht in dieser Zeit geschafft. Ich bin dir unendlich dankbar und weiß wie hart diese Zeit für dich war. Ich könnte mir keinen besseren Partner wünschen und bin unendlich froh, dass wir einander haben. Danke auch an Gretel, du kleiner Wirbelwind für ein paar mehr graue Haare und die Gelassenheit zu erkennen was am Ende des Tages wirklich wichtig ist: Gummibärchen und Schokolade.